Theoretical and Experimental Analysis of Dissipative Buckling Restrained Braces

G. Palazzo
F. López Almansa
X. Cahís
F. Crisafulli

Monograph CIMNE IS-64, 2011

Monografías de Ingeniería Sísmica
Editor A. H. Barbat

Theoretical and Experimental Analysis of Dissipative Buckling Restrained Braces

G. Palazzo
F. López Almansa
X. Cahís
F. Crisafulli

Monograph CIMNE IS-64, 2011

CENTRO INTERNACIONAL DE MÉTODOS NUMÉRICOS EN INGENIERÍA
Edificio C1, Campus Norte UPC
Gran Capitán s/n
08034 Barcelona, España

MONOGRAFÍAS DE INGENIERÍA SÍSMICA
Editor A. H. Barbat

ISSN: 1134-3249

THEORETICAL AND EXPERIMENTAL ANALYSIS OF DISSIPATIVE BUCKLING RESTRAINED BRACES
Monografía CIMNE IS64

ISBN: 978-84-96736-98-6
Depósito legal: B-8120-2011

SUMMARY

Buckling restrained braces are passive energy dissipators used for seismic protection of building frames; such devices consist of slender steel bars connected usually to the frame to be protected either like conventional (concentric) diagonal braces or like chevron braces. Under horizontal seismic motions, the interstory drifts generate axial strains in the steel bars beyond their yielding points; such tension-compression cycles constitute the hysteresis loops. The buckling of the steel bars (core) is prevented by embedding them in a stockiest encasing; it consists usually of a steel tube filled with mortar. A crucial issue is to allow sliding between the core and the encasing to prevent relevant shear stress transfer.

This work aims to contribute to a better understanding of the behavior of buckling restrained braces; the final objective is to foster its mass use in developing countries (in earthquake prone regions), particularly for reinforced concrete building frames. The research approach consists of designing, producing and testing (in Argentina) five reduced scale dissipators (about 400 mm long) and of taking profit of the gained experience to design, to produce and to test (in Spain) four full size (near 3000 mm long) prototype devices. All these tests are individual, i.e. no subassemblies (accounting for the building frames) are considered.

The main conclusion is that it is possible to obtain a reasonably cheap (about 1000 US$ per unit; this amount corresponds to production in Spain (summer 2006) without optimizing the fabrication process), efficient, robust, low maintenance and durable prototype device requiring only a low-tech production process (suitable for developing countries). Moreover, the results show that the fatigue life of buckling restrained braces, even highly uncertain, can be significantly bigger than expected (according to some previously published results); it might allow extending the life of these devices after a number of strong seismic inputs.

A numerical analysis of the buckling behavior of these devices is performed; it allows formulating some design recommendations. Further research needs are identified.

RESUMEN

Las barras de pandeo restringido son elementos pasivos utilizados habitualmente para protección sismorresistente de pórticos de estructuras de edificación; consisten en barras esbeltas de acero conectadas o bien en forma de arriostramientos (concéntricos) diagonales o bien como arriostramientos en forma de “V” invertida (“chevron braces”). Cuando se producen movimientos sísmicos (horizontales), los desplazamientos relativos entre plantas generan deformaciones axiales plásticas en las barras y de esta manera se disipa energía (mediante ciclos de histéresis que involucran tracción y compresión). El pandeo de estas barras de acero se impide embebiéndolas en una barra robusta compuesta habitualmente por un tubo de acero relleno de hormigón o mortero. Es importante garantizar el libe deslizamiento entre el núcleo (barras de acero) y el revestimiento (tubo de acero relleno de hormigón) para evitar que se produzca una transferencia excesiva de tensiones tangenciales.

Este trabajo pretende contribuir a una mayor comprensión del comportamiento de las barras de pandeo restringido; el objetivo final es promover su uso (masivo) en países en desarrollo (ubicados en zonas de alta sismicidad), en particular para edificios de hormigón armado. La estrategia seguida consiste en proyectar, fabricar y ensayar (en Argentina) cinco disipadores a escala reducida (de unos 400 mm de longitud) y en aprovechar la experiencia obtenida para proyectar, fabricar y ensayar (en España) cuatro dispositivos prototipo (de unos 3000 mm de longitud). Los ensayos son individuales, es decir se efectúan sólo sobre los disipadores y no se utilizan elementos que representen las estructuras en que éstos se instalarían.

La principal conclusión que emana de este estudio es la posibilidad de obtener dispositivos (barras de pandeo restringido) que reúnan importantes cualidades: economía (unos 1000 US$ por unidad, este importe corresponde a fabricación en España durante el año 2006 sin optimizar el proceso de producción), eficiencia, robustez, bajos requerimientos de mantenimiento, durabilidad y producción sencilla (conveniente para países en desarrollo). Por otra parte, los resultados obtenidos muestran que la vida a fatiga de estos dispositivos, a pesar de ser bastante aleatoria, puede llegar a ser significativamente mayor que lo que podría ser esperado (de acuerdo con algunos resultados publicados previamente); su uso podría extenderse a varios movimientos sísmicos de elevada intensidad.

Se presenta un análisis numérico del comportamiento a pandeo de estos dispositivos formulándose algunos criterios de proyecto. Se identifican aspectos que requieren ser investigados en el futuro.

INDEX

1 INTRODUCTION

Energy dissipators are a convenient option for earthquake-resistant design of buildings and other civil engineering constructions since they absorb most of the input energy thus protecting the main structure from damage even under strong seismic motions [Soong & Dargush, 1997; Housner, Bergman, Caughey, Chassiakos, Claus, Masri, Skelton, Soong, Spencer and Yao, 1997] and many applications have been reported [Martelli, 2006]. Several types of devices have been proposed; those based on plastification of metals (commonly termed as hysteretic) are the simplest, cheapest and most reliable and have repeatedly shown their usefulness. Among them, the buckling restrained braces are one of the most used for seismic protection of building frames [Wada, Saeki, Takeuchi, and Watanabe, 1998; Watanabe, Hitomi, Saeki, Wada and Fujimoto, 1988; Clark, Aiken, Kasai, Ko and Kimura, 1999; Tremblay, Degrange and Blouin, 1999]. The use of such devices has been also (recently) considered for bridges [Kanaji, Hamada, Ishibashi, Suzuki, Mino, Durán and Sakugawa, 2004; Carden, Itani, Buckle & Aiken, 2004; Carden, Itani & Buckle, 2006; Usami, Lu and Ge, 2005], spherical tanks [European Commission, Indepth Project; Summers, Jacob, Martí, Bergamo, Dorfmann, Castellano, Poggianti, Karabalis, Silbe and Triantafillou, 2004] and even for intake towers for dams [Star Seismic]. The buckling restrained braces consist of slender steel bars connected usually to the frame to be protected either like conventional (concentric) diagonal braces (see the left sketch in Figure 1) or like chevron braces (V or V-inverted bracing, see the right sketch in Figure 1).

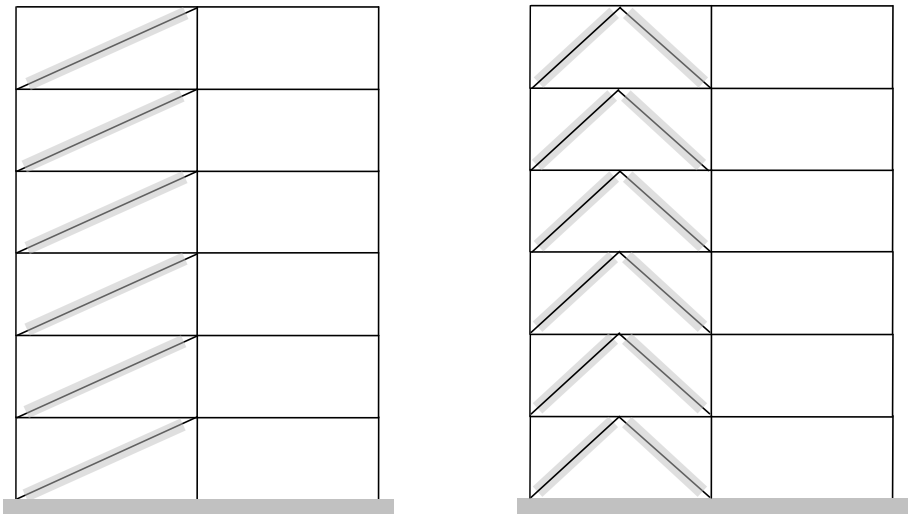

Figure 1. Building frames protected with buckling restrained braces

Figure 1 shows two sketch of six storey frames with buckling restrained diagonal braces (left) and V-inverted chevron braces (right) installed on their left bays.

It is remarkable that, beyond the layouts described by Figure 1, at [Tremblay, Ben Ftima & Sabelli, 2004] the use of buckling restrained braces as (dissipative) columns is proposed.

Under horizontal seismic motions, the interstory drifts generate axial strains in the steel bars beyond their yielding points; their tension-compression cycles constitute the hysteresis loops. The buckling of the steel bars is prevented by embedding them in a stockiest encasing. Such encasing is usually formed by steel elements [Iwata, 2004; Tsai, Lai, Hwang, Lin and Weng, 2004] sometimes filled with mortar; the most common solution for encasing is a steel tube filled with mortar. Figure 2 shows two common solutions for buckling restrained braces; the top sketch

depicts a cruciform core bar embedded in a mortar casing placed in a square steel tube while the bottom sketch represents a circular core embedded in a circular mortar casing.

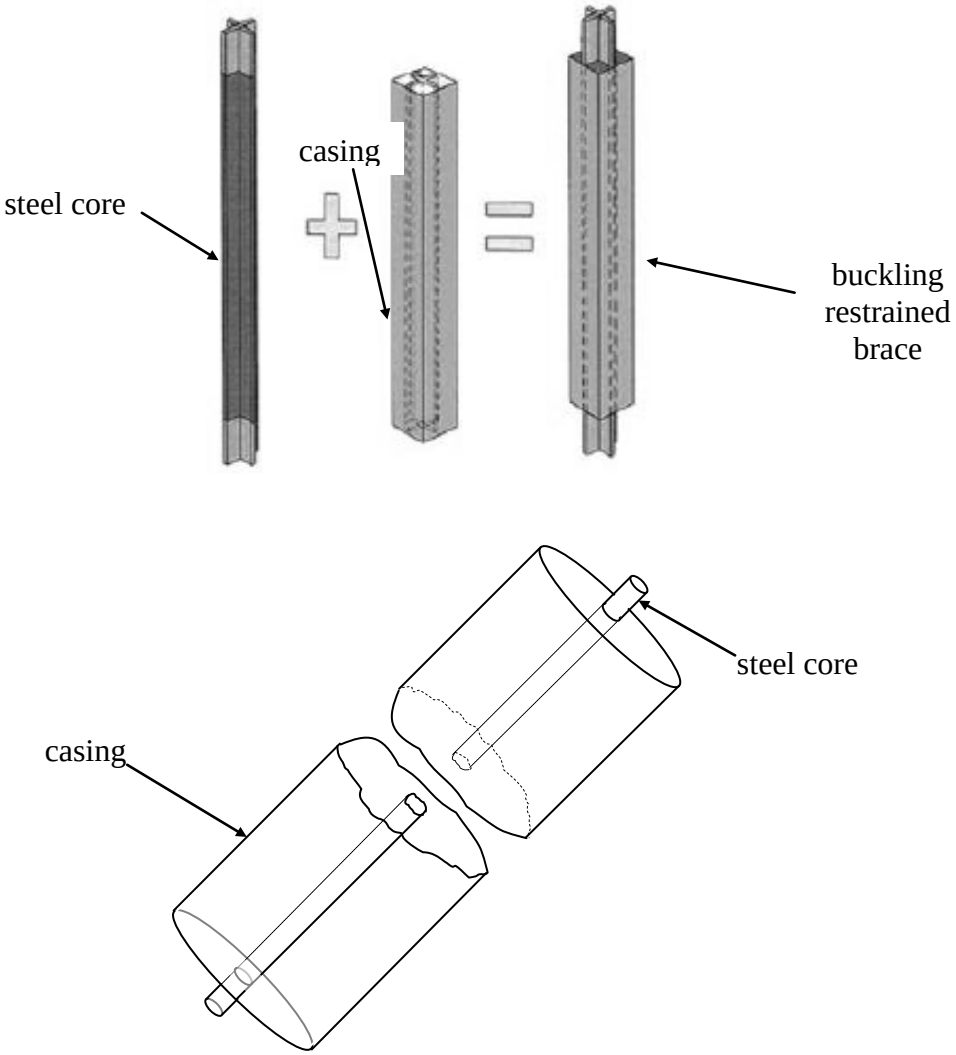

Figure 2. Common types of buckling restrained braces

Some sliding interface between the steel core and the surrounding mortar is required in order to prevent excessive shear stress transfer (it would reduce the longitudinal stress in the core thus impairing the dissipation of energy).

The buckling restrained braces posses several relevant advantages compared to other devices based also on plastification of metals:

- The ratio dissipated energy / added material (including dissipators, bracing and connections) is the highest in the comparative devices [Palazzo & Crisafulli, 2004]. The degree of plastification is uniform along the whole body of the core.
- The buckling restrained braces constitute themselves a bracing system and no additional braces are required to connect the device to the main frame.
- A relevant experience is available since a number of individual and subassemblage tests have been carried out [Black, Makris & Aiken, 2002; Merritt, Uang & Benzoni, 2003; Newell, Uang & Benzoni, 2006; Seismic Isolation Engineering for Nippon Steel Corporation, 1999;

Tsai & Huang, 2002; Tsai & Lin, 2003; Tsai, Lai, Hwang, Lin & Weng, 2004; Mahin, Uriz, Aiken, Field & Ko, 2004; Lopez, Gwie, Lauck & Saunders, 2004; Nishimoto, Nakata, Kimura, Aiken, Yamada & Wada, 2004; Tremblay, Poncet, Bolduc, Neville & De Vall, 2004; Carden, Itani, Buckle & Aiken, 2004; D'Aniello, Della Corte, Mazzolani & Landolfo, 2006; Wada & Nakashima, 2004; Lehman, Roeder & Yoo, 2004; Lee & Brunneau, 2005; Iwata, Kato & Wada, 2000; Konami, Sugihara, Narikawa, Huan, Maeda & Wada, 1999; Hasegawa, Takeuchi, Nakata, Iwata, Yamada & Akiyama, 1999; Wada, Saeki, Takeuch & Watanabe, 1989; Watanabe & Nakamura, 1992] and many realizations have been reported, mostly in Japan [Iwata, 2004], Taiwan [Tsai, Loh, Hwang & Weng, 2003; Tsai, Lai, Hwang, Lin & Weng, 2004], Canada [Tremblay, Degrange & Blouin, 1999] and the United States [Black, Makris, & Aiken, 2002]. Preliminary versions of design codes have been proposed [SEAONC, 2001, Sabelli & Aiken, 2004; Kasai & Kibayashi, 2004; Kibayashi, Kasai, Tsuji, Kikuchi, Kimura, Kobayashi, Nakamura & Matsuba, 2004] and many references about design procedures are available [Kim & Choi, 2004; Wada & Nakashima, 2004; Tremblay, Poncet, Bolduc, Neville & De Vall, 2004; Brockenbrough & Merritt, 2005; Taranath, 2004; Mahin, Uriz, Aiken, Field & Ko, 2004; Sabelli, Pottebaum, Brazier & López, 2005; Sabelli, Mahin & Chang, 2001; Fahnestock, Sause and Ricles, 2004; Astrella & Whittaker, 2005].

- Since the dissipative part of the device can encompass near the whole length of the brace, the required strain is rather low. Therefore, the plastic excursion is rather moderate, possibly providing high fatigue resistance.

Conversely, the buckling restrained braces exhibit some disadvantages (compared to other devices based also on plastification of metals):

- After a strong input, the whole dissipator has to be replaced (instead of merely a small part of it).
- Once the main layout has been selected (see Figure 1), there are few design parameters (basically, the area of the core, the steel yielding point and the length of the dissipative segment). This scarcity prevents highly tailored designs.

In spite of the relevant existent background about the buckling restrained braces, there are still some open questions which might require further research:

- **Design and production**. In spite that a number of devices based on axial plasticity of steel bars are commercially available, no full details about them have been reported, perhaps partially for confidentiality reasons. In particular, the solutions for the sliding interface between the steel core and the mortar have been reported only scarcely [Wada & Nakashima, 2004; Tsai et al., 2004] in the technical literature. As well, most of the relevant production issues have not been deeply discussed.
- **Buckling analysis**. The buckling design of the mortar-steel coating is based usually in simple second-order models [Black, Makris & Aiken, 2002; Wada & Nakashima, 2004]. Some of their parameters are not usually selected from the actual parameters of the device but merely from semi-empirical considerations; hence, the obtained results cannot be very accurate and it is uncertain than they are on the safe side. In other words, only over-conservative designs of the casing are feasible and even it is doubtful that the actual safety factor is greater than 1.
- **Experiments**. A number of tests have been carried out, both individually and on subassemblies accounting for the main frame. Perhaps, the only relevant lack is the absence of extensive information about the inner final condition of the devices.
- **Structural behavior**. The structural behavior of the device is rather complicated because of the coexistence of several coupled issues, mainly: (i) joint behavior of three materials (inner and outer steel, mortar and the sliding interface), (ii) plastic cyclic behavior of the core, (iii) partial sliding between the core and the encasing mortar and (iv) large strains and displacements. A reliable and accurate numerical model considering these issues has not been

reported. This lack requires that the design is based on over-conservative approaches and prevents the proposal of innovative and daring solutions.

- **Effectiveness**. In spite that several parametric studies have been reported in the technical literature [Sabelli & Mahin, 2003; Tremblay, Lacerte & Christopoulos, 2008], their authors still indicate a number of open questions. It is noted that most of the existing studies refer to steel buildings while this research is rather oriented to concrete frames, very common in developing countries.

This work addresses mainly the first three issues. Research focusing on the two last issues is in progress.

As stated in the previous paragraph the objective of this work is to contribute to increase the knowledge in the first three issues. The research approach consists basically of designing, producing and testing (individually) a number of (reduced scale) dissipators and taking advantage of the gained experience to better designing, producing and testing (individually) some (full size) prototype dissipators. The results are carefully analyzed to derive useful conclusions. A deeper description (classified according to the aforementioned three issues) of the research follows.

- **Design and production**. A new type of buckling restrained brace (yet similar to the existing ones) is designed and a number of (short) dissipators and of (full size) prototypes are produced. Main concerns of the design are: (i) efficient, simple, robust, low maintenance and durable device, (ii) low cost, (iii) simple production and (iv) easy to find materials. The **short dissipators** (see Figure 3) are formed by a rectangular steel core encased by a (round) tube (made of PVC or steel) filled with mortar or grouting [Palazzo, Crisafulli & López Almansa, 2006; Palazzo, Crisafulli, López Almansa & Cahís, 2006]. The dissipative segment of the core was wrapped with a polyethylene film (protected with an adhesive tape) to allow for the transverse expansion of the core (mainly during yielding) and to reduce the shear stress transfer between the core and the surrounding mortar. The **full scale prototypes** (see Figure 3) are composed of a slender steel bar (cylinder) as dissipative core and a round steel tube filled with high strength mortar (without shrinkage) as buckling restrainer system (casing). The sliding between the inner bar and the mortar is ensured by a three-layer interface: the core is coated with high strength Teflon®, is lubricated with grease and is wrapped with a thin rubber layer. Such core rod is made of conventional constructional steel and no welding is used in the dissipative segment (the portion out of the end connections) to avoid any local fragility (possibly) leading to premature failure. The connectors between the core and the frame are carefully designed to avoid stress concentrations in the core, to provide sound stress transfer mechanisms and to restrain the local buckling of the end parts of the core. Five short dissipators (its dissipative segment is about 175 mm) and four full size prototypes (its dissipative segment lies in between about 2.50 m and 2.20 m) are produced.
- **Buckling**. A simple yet reasonably accurate second order analysis has been performed for the prototypes. Instead of obtaining lower bounds of critical loads under ideal conditions (which are unable to provide lower bounds of design values under real conditions), the analysis considers (in a simplified way) both the geometrical imperfections and the nonlinear behavior of the steel core. All these simplifications are from the safe side.
- **Experiments**. Extensive individual testing has been carried out on the short dissipators and the full size prototypes. For both, the experiments have consisted of cycling axial loading until failure; the dissipators have been tested in the Centro Atómico Bariloche, Argentina, while the prototypes have been tested (mainly) in the University of Girona, Spain. The objectives of these proofs are: (i) to assess the performance of the proposed devices, (ii) to learn deeply about their structural behavior, (iii) to characterize their hysteretic behavior and (iv) to obtain a wide set of experimental results that might be useful to calibrate the numerical models (to be developed). Pseudo dynamic tests on prototype devices installed on concrete frames are in progress (subassemblies).

This work belongs to a bigger research whose objective is to promote the mass use of energy dissipators for seismic protection of buildings in developing countries located in seismic-prone regions. It is noteworthy that most of the up-to-date reported applications correspond to steel frames while in these countries the vast majority of building posses reinforced concrete frames.

2 DESIGN AND PRODUCTION

2.1 General remarks

In spite that a number of devices based on axial plasticity of steel bars are commercially available [CoreBrace, Fip Industriale, Nippon Steel Corporation, Read Jones Christoffersen, Star Seismic] no full details about them have been reported, perhaps partially for confidentiality reasons. The proposal of an "open source" device has several advantages, mainly: (i) the technical solutions will be revealed to the scientific community thus allowing for open discussion, (ii) the costs might be lowered (this is relevant for any emergent technology but, moreover, in this case it might foster its mass use in developing countries). One of the objectives of this research is to propose a new type of buckling restrained brace; the design and production issues have been addressed in an integrated way and a number of (short) dissipators and of (full size) prototypes are produced.

As described previously, the following qualities are sought:

- **Simplicity**. The device must be efficient, simple, robust, durable and requiring virtually no maintenance. These qualities are relevant to promote its use among people which are not familiar with advanced construction technologies; it is remarkable that in many countries there is little tradition in maintenance of buildings.
- **Low cost**. It should be kept on mind that the use of energy dissipators has to compete with other solutions and that in developing countries the economical issues are crucial.
- **Simple production**. It means that neither complex nor protected technologies are acceptable and the final result has to be robust with respect to production errors. Any developing country should be able to produce the devices by itself.
- **Basic materials**. Only easy-to-find and replaceable materials should be used. In particular, no particular requirements about the steel of the inner core are suitable.

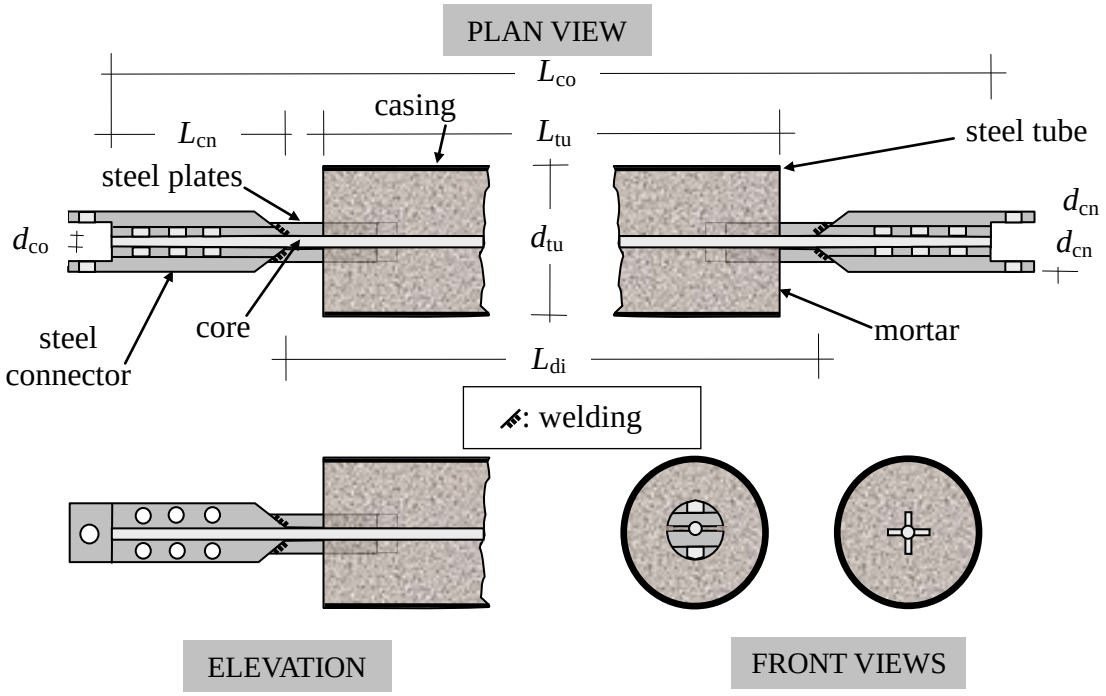

Figure 3. Considered prototypes of buckling restrained braces

The considered dissipator (see Figure 3) consists basically of a slender solid bar (cylinder) as dissipative steel core and a round thin-wall steel tube filled with high strength mortar (without shrinkage) as buckling restrainer (casing).

As shown by Figure 3 both the core and the tube have constant cross section because of simplicity and availability. A relevant decision is to select the section of the core; in the technical literature mainly rectangular (flat) and cruciform sections have been proposed [Black, Makris & Aiken, 2002; Tremblay, Boldue, Neville & De Vall, 2005] (see the top sketch in Figure 2) but round sections (see the bottom sketch in Figure 2) have been also considered [Sabelli, Mahin & Chang, 2002]. In the tests of the short dissipators (where the core had rectangular section) some stress concentrations were detected in the corners (leading to cracking in the mortar, see Figure E.5.c) [Palazzo, Crisafulli & López Almansa, 2006]; hence, for the full size devices it was decided to use a circular section for the core. Additional advantages that support this choice are the equal buckling strength (radius of gyration) in any direction (compared to flat sections) and the lack of risk of torsional buckling (compared to cruciform sections). For simplicity and coherence the tube is also round (even in the short dissipators).

The core can be made of ordinary construction steel; for the sake of simplicity and of moderate cost none surface treatment (aiming to reduce the risk of stress concentration) is required. Two steel connectors are placed at both ends of the core to ensure a proper anchoring to the building frame to be protected.

One of the key issues of the design is to ensure a proper sliding between the inner bar (core) and the surrounding mortar in order to avoid relevant shear stress transfer among them. For the short dissipators, this is ensured by wrapping the core with a polyethylene film. For the full size devices the sliding is ensured by a three-layer interface: the steel core is coated with Teflon® (this material gathers two relevant qualities: high strength and low friction coefficient), its outer surface is lubricated with grease and is wrapped with a thin rubber layer (to provide further axial flexibility and to guarantee an even sliding surface). The parameters of these elements (Teflon, grease and rubber) may vary from a device to another as one of the main concerns is to propose a device without strict technical requirements.

To avoid any local fragility (possibly) leading to premature failure of the core, neither welding nor (local) reductions of section are acceptable in the dissipative segment; hence, the connection with the elements fixed to the frame use only friction and bonding (with adhesive products). Welding is only acceptable as a redundant mechanism and is just used in the end portions of the core (where the stresses have been already transferred to the connectors). In the (short) dissipators conventional jaws are used while in the (longer) prototypes the axial forces are bigger and more sophisticated elements are required (steel connectors depicted in Figure 3).

The tubes with the core inside are placed vertically and filled with mortar by conventional gravity pouring.

These solutions yield devices which are easy to produce, robust, cheap, efficient and durable. All the materials are available almost everywhere and most of them can be replaced with similar products.

Five short dissipators were been designed, produced and tested; by taking profit of the gained experience, four full size prototype devices belonging to the typology described by Figure 3 have been designed, produced and tested. Both types of devices are described in the next subsections.

2.2 Reduced scale dissipators

Five short dissipators were produced in Argentina (in the National Technological University) along April 2006 [Palazzo, Crisafulli & López Almansa, 2006; Palazzo, Crisafulli, López Almansa & Cahís, 2006]. Such dissipators are termed SD1, SD2, SD3, SD4 and SD5 (accounting for "Short Dissipator"). They are formed by a steel core encased by a (round) tube filled with mortar. Figure 4 displays the five devices.

All these dissipators have the same external dimensions (length 400 mm and diameter 63 mm) and its inner steel core is alike; they differ in the material and thickness of the tube and in the parameters of the mortar. The value of the total length was selected as the maximum allowed by the testing machine; the diameter was chosen because of availability and easy filling with mortar.

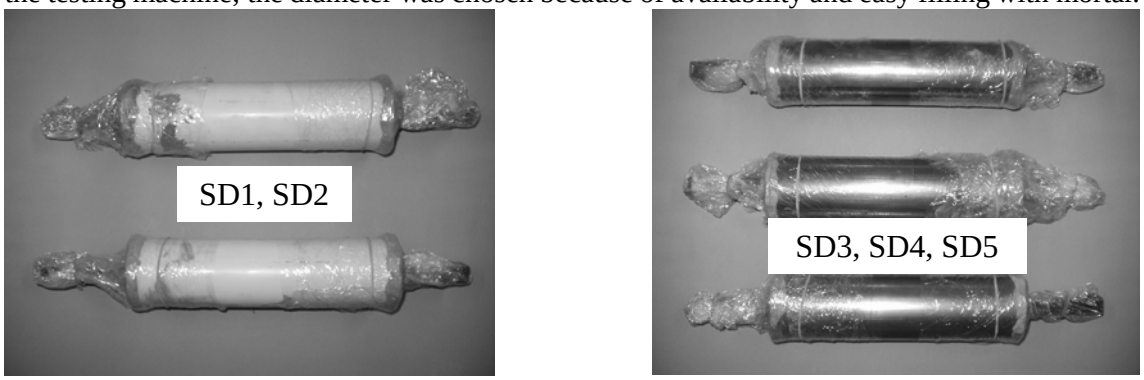

Figure 4. Dissipators SD1, SD2, SD3, SD4 and SD5

The steel core is a square section bar with side 15.90 mm (the nominal value is 16 mm); the central dissipative segment has been milled to form a rectangle 15.90 × 4.4 mm^2; no further surface smoothening treatment has been applied. The steel is A36 [ASTM A36/A36M, 2005]; the nominal values of the yielding point and of the ultimate strength are f_y = 330 MPa and f_u = 500 MPa, respectively. The total length of the core is L_{de} = 400 mm (as described in the previous paragraph) and the dissipative segment length is L_{di} = 175 mm. Seven cores were produced, five were used for the dissipators and the other two underwent tension tests to characterize their mechanical parameters, see Figure 17, Figure 18 and Table 7. Figure 5 displays two views of the completed cores.

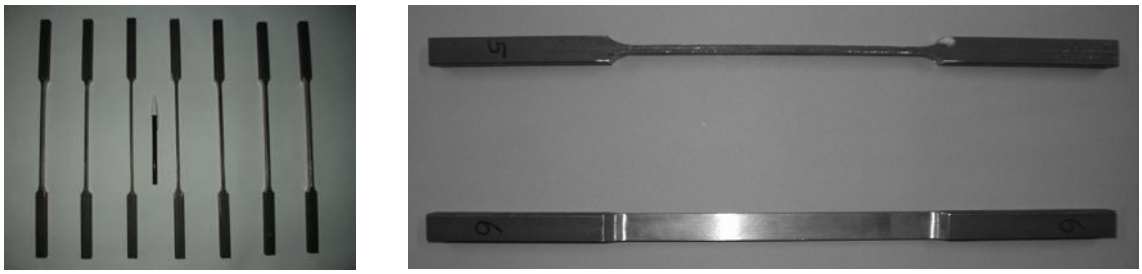

Figure 5. Steel core for dissipators SD1, SD2, SD3, SD4 and SD5

Left picture in Figure 5 displays a general view of the seven cores and right picture shows two lateral views of a core. The two end parts of the core have been slightly lowered (12.2 × 15.90 mm^2 along 126.8 mm) for easier connection to the jaws. The yielding (central) segment is rather coarse with (slight) marks from the milling machine and irregular thickness; moreover, the transition parts are not smooth enough to avoid any stress concentration. These facts might have a relevant impact on the fatigue life.

The dissipative segment of the core was wrapped with a polyethylene film (Ziplot type), protected with an adhesive tape, to allow the transverse expansion of the core (mainly during yielding) and to reduce the shear stress transfer between the core and the surrounding mortar (Tremblay, Poncet, Bolduc, Neville & De Vall, 2004). The cores for dissipators SD1, SD3 and SD4 were covered with four layers while the cores for dissipators SD2 and SD5 were wrapped with eight layers. Figure 6 displays a wrapped core.

Figure 6 shows that the two transition parts (between the extreme "integer" segments and the lowered dissipative central segment) were covered with expanded polystyrene (porexpan®) to create gaps that may allow longitudinal relative displacements between the core and the nearby mortar; such displacements are particularly necessary during the yielding of the dissipative segment.

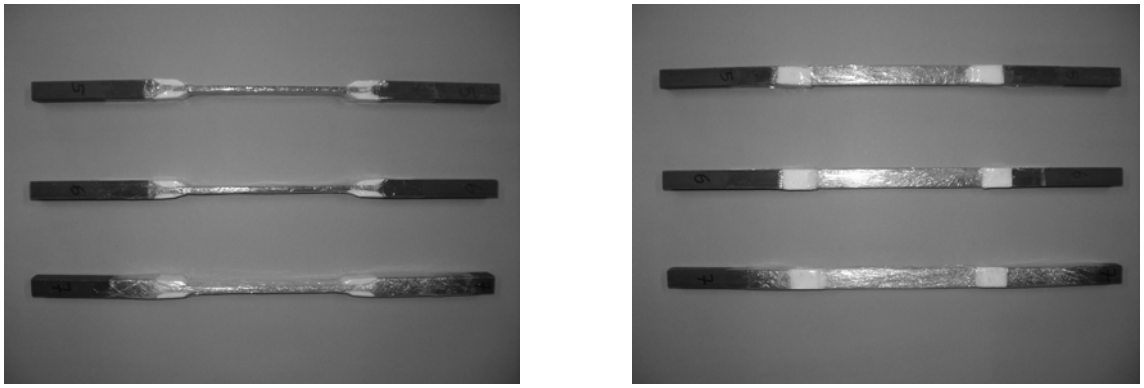

Figure 6. Core wrapped with a polyethylene film

As described previously, all these dissipators are encased by a 63 mm diameter tube (d_{tu} = 63 mm). As shown by Figure 4, for dissipators SD1 and SD2 such tube is made of PVC (thickness t_{tu} = 2 mm) while for SD3, SD4 and SD5 it is made of A36 [ASTM A36/A36M, 2005] steel (thickness t_{tu} = 1.2 mm); all the tubes are 230 mm long (L_{tu} = 230 mm). In the steel, the nominal values of the yielding point and of the ultimate strength are f_y = 330 MPa and f_u = 500 MPa. In the PVC, the deformation modulus is E_{PVC} = 700 MPa (as indicated by the supplier).

Dissipators SD1, SD2 and SD3 were filled with grout while dissipators SD4 and SD5 were filled with grout mixed with small size aggregate (sand). Figure 7 displays two dissipators to be filled with mortar.

Figure 7. Two (short) dissipators prior to mortar pouring

For dissipators SD1, SD2 and SD3 the dosage was 350 kg cement for 105 l water. For dissipators SD4 and SD5 the dosage was 300 kg cement, 120 l water, 3 l fluidizing (chemical) and 900 kg sand.

The most relevant parameters of these (short) dissipators are described by Table 6.

2.3 Prototypes

Four full size prototype devices have been produced in Barcelona (June 2006) according to the described technology (see Figure 3). The total length of the device is limited to L_{de} = 3 m because of restrictions in the testing laboratory. In two devices (termed in this work D1 and D2) the (nominal) diameters of the core and of the tube are d_{co} = 10 mm and d_{tu} = 90 mm, respectively; in the other two dissipators (termed in this work D3 and D4) such values are d_{co} = 22 mm and d_{tu} = 115 mm, respectively. In all the devices, the length of the core is L_{co} = 2808 mm and the thickness of the tube is t_{tu} = 3 mm. The lengths of the dissipative segment of the core (L_{di}) and of the tube (L_{tu}) are L_{di} = 2466 mm and L_{tu} = 2422 mm for dissipators D1 and D2 and L_{di} = 2196 mm and L_{tu} = 2152 mm for dissipators D3 and D4. The length (L_{cn}) and the diameter (d_{cn}) of the steel connectors are L_{cn} = 200 mm and d_{cn} = 80 mm for dissipators D1 and D2 and L_{cn} = 270 mm and d_{cn} = 85 mm for dissipators D3 and D4. Such values are summarized in Table 1.

Table 1. Main geometrical parameters of prototypes D1, D2, D3 and D4

Devices	L_{co} (mm)	L_{cn} (mm)	L_{tu} (mm)	L_{di} (mm)	d_{co} (mm)	d_{tu} (mm)	t_{tu} (mm)	d_{cn} (mm)
D1 & D2	2808	200	2422	2466	10	90	3	80
D3 & D4	2808	270	2152	2196	22	115	3	85

In Table 1 the difference between the length of the dissipative segment of the core L_{di} and the length of the tube L_{tu} is 44 mm for all the devices (22 mm each side); it is intended to allow the slide of the core with respect the tube. This value is about six times the yielding displacement at each end of the core, see Eqn. (22) and Eqn. (23); hence, this design largely allows ductility ratios (quotient between the yielding and the maximum displacements, see Appendix B) above 5.

For both the tube and the core, ordinary construction steel S275 JR has been used [EN 10025, 2002]; its yielding point is f_y = 275 MPa while the ultimate strength is f_u = 410 MPa (both are nominal values). Commercially available mortar without shrinkage has been used; the expectable compressive strength ranges between 45 and 50 MPa (at 28 days and with 14% water contents). The dosage of the mortar has been 30 kg of (dry) product for 3.30 l of water. Bolted steel connectors were placed at both ends of the core. According to this information dissipators D1 and D2, as well as D3 and D4 were designed to be alike; it will allow comparing their results.

The criteria for selecting the aforementioned design parameters are discussed next (when describing the structural design) more deeply.

Figure 8 depicts these four prototypes (D1, D2, D3 and D4) while standing after mortar pouring (see Figure 9).

The production started by coating the core with Teflon, by greasing its surface and by wrapping the coated bar with a layer (1.7 mm thick) of conventional rubber. As stated previously, the Teflon had high resistance to abrasion (because of the expected sliding with respect the surrounding

mortar during yielding). Besides providing shear flexibility, the rubber is intended also to allow the transverse expansion of the core, thus preventing cracking failure in the mortar. The core will expand mainly during yielding as its volume will be kept roughly constant and, therefore, the transversal strains will be similar to half of the longitudinal ones.

Next operation was placing the core inside the tube (positioned vertically) and pouring the mortar. Figure 9 depicts this action for dissipator D4. The mortar sliding was merely ensured by knocking and shaking the tube.

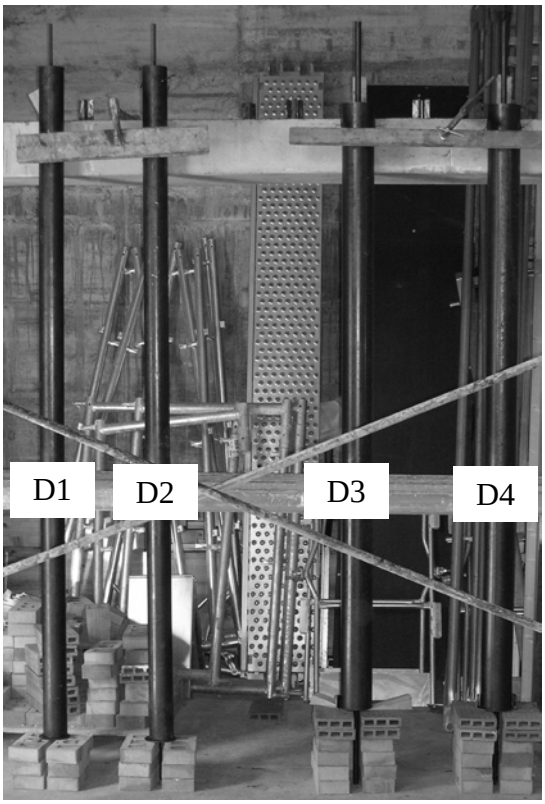

Figure 8. Prototype devices

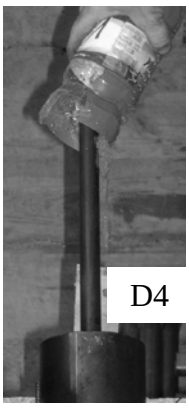

Figure 9. Pouring of the mortar on a prototype device

The connectors (minimally described in Figure 3) consisted of two-halved steel elements encasing the end parts of the core. Both halves were bolted each other (with high strength prestressed bolts) as shown by Figure 10.

Figure 10 displays four views of the connectors for dissipators D1 and D2 (left) and three views of the connectors for dissipators D3 and D4 (right). Upper pictures correspond to the two steel halves while lower pictures show the same connectors once installed in the dissipators. As shown by Figure 10, every half part of a connector is formed by a (rear) half cylinder segment and a (front) half cone segment. The rear segment is pierced transversally (by a 30 mm hole) to house a pin connected to the support. The front (cone) segment is intended to provide a smooth transition between the core and the (wider) cylinder segment. At the small connectors (for dissipators D1 and D2) the bolts are mainly placed in the cone segment while in the big connectors (for dissipators D3 and D4) the bolts are placed completely in the cylinder segment.

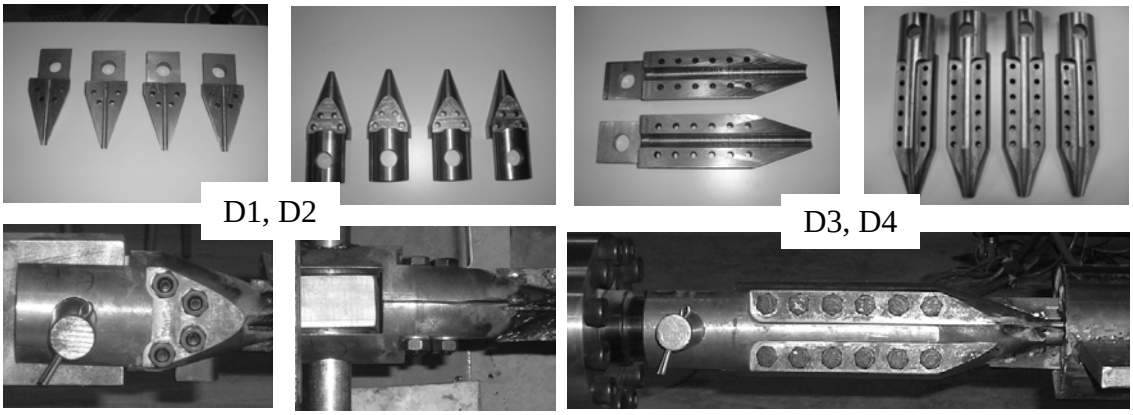

Figure 10. Steel connectors

As shown by Figure 10, the shear stress transfer between the core and the connectors was guaranteed by a dual mechanism: (i) the friction generated by the prestressed bolts and (ii) the bonding provided by a chemical adhesive (in the contact surface between the inner core and the connector) with high fatigue strength. Figure 11 depicts the application of such adhesive on a connector intended for dissipators D3 or D4. It is remarkable that, for a better bonding, the maximum recommended gap between the core and the connector was 0.25 mm.

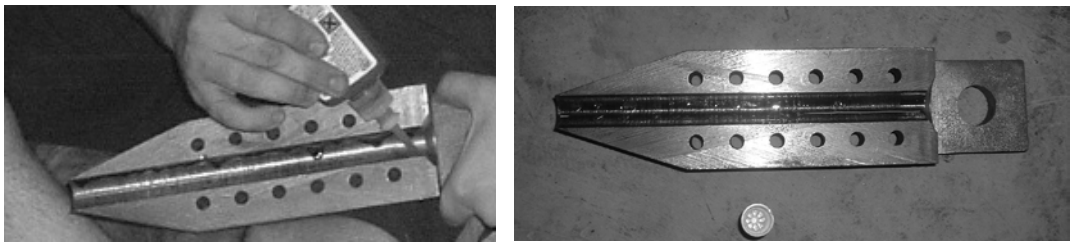

Figure 11. Application of the adhesive product

To restrain the local buckling of the bare (unrestrained) end segments of the core four (longitudinal) steel plates were welded to the connectors; to avoid the risk of premature failure, such plates were not welded to the core. These plates are alike for all the dissipators; Figure 12 depicts a plate.

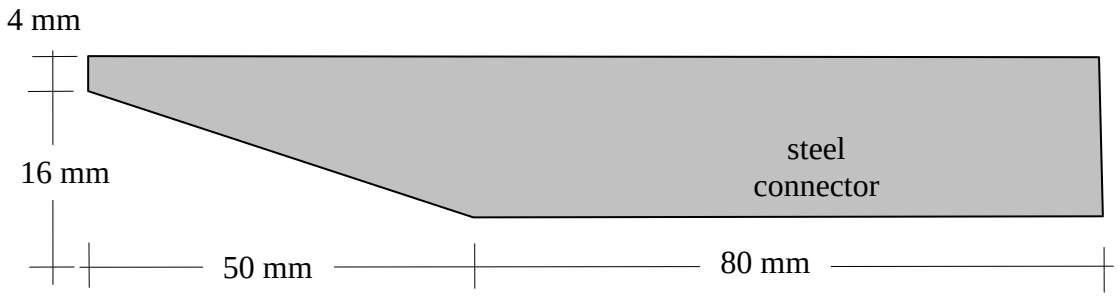

Figure 12. Trapezoidal steel plate

The trapezoidal plates described by Figure 12 are made of steel S275 JR [EN 10025, 2002]; its thickness is 3 mm.

Figure 13 depicts a connector (intended for dissipators D3 or D4) that incorporates the welded trapezoidal plates.

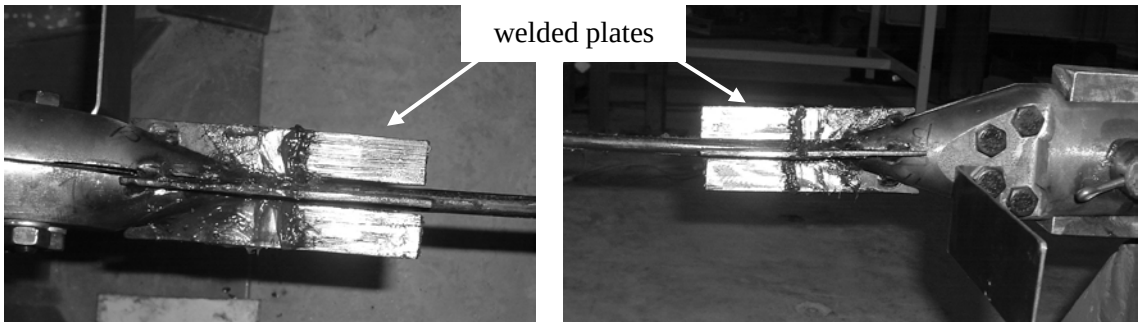

Figure 13. Steel plates welded to the connector

Figure 13 displays two images (the left one is a plan view while the right one is an elevation) of a connector (intended for dissipators D1 or D2) with the four (trapezoidal) welded plates. Figure 13 shows that the plates are distributed uniformly (symmetrically) to better restrain the buckling of the core.

The production cost (in Barcelona, during summer 2006) of the four prototypes D1, D2, D3 and D4 has been 3272.28 € (including 16% VAT). This quantity comprises the material, the labor (except some tasks carried out directly by the authors of this work) and transportation (about 100 km plus minor journeys) costs; the costs of the experiments are not included. It is remarkable that, under normal production conditions in developing countries, this amount might be dramatically lowered.

Table 2 shows a decomposition of the cost. Despite the items are classified under two broad categories (materials and execution), in some cases it is not possible to split exactly the total amount as such information is not always available (e.g. for Teflon®).

Results from Table 2 show that the costs of the (raw) materials are rather moderate (in spite that bulk purchases would further decrease them) while most of the expenditure is concentrated in the labor tasks. It confirms that a proper planning of the production will allow a significant cheapening. The execution cost for the steelwork (about 46% of the grand total) may be significantly lowered by a simpler design of the end connectors (see Figure 10) and by a more

systematic planning of the production. As well, all the labor costs (manpower) in developing countries will be significantly lower.

Another relevant conclusion from Table 2 is that, despite its good quality, the cost of the mortar is small (less than 3% of the grand total) while the benefits of using high strength mortar are seemingly important (e.g., see Figure 86, Figure 113, Figure 151 and Figure 176).

Table 2. Production costs of the dissipators D1, D2, D3 and D4

	Issue	Cost (€)
Materials (737.11 €)	Steel for cores and connectors	335.02
	Steel for tubes	158.10
	Bolts	42.00
	Rubber	7.25
	Mortar	93.26
	Glue, grease and minor items	101.48
Execution (2535.17 €)	Steelwork	1511.48
	Teflon®	543.62
	Mortar pouring and curing and local transportation	480.07
	TOTAL	3272.28

3 STRUCTURAL DESIGN

3.1 General remarks

This subsection describes the structural design of the major elements of the (full size) prototype dissipators D1, D2, D3 and D4 (see Figure 3): dissipative (inner) steel core, casing (steel tube filled with high strength mortar, see Figure 8) and steel connectors (half-cone-shaped twin elements, see Figure 11 and Figure 13). Next three subsections present the issues for these three members, respectively. For each member, the general formulation for designing dissipators for real applications is presented first and then the particular design of the testing prototypes D1, D2, D3 and D4 is discussed; such devices are designed as to represent actual devices while accounting for the testing constraints.

The design of the core is mainly governed by the global dissipative behavior of the device (with little input from the buckling issues since the transversal bending is prevented by the casing); conversely, the design of the casing is mostly driven by the transversal interaction forces arising during the core buckling. Consequently, the core design issues are common to most of the dissipators based on plastification of metals while the design of the casing is clearly specific of buckling restrained braces (and even of the proposed type of devices).

3.2 Dissipative core

The steel core is designed mainly to dissipate as much energy as possible while minimizing the risk of rupture. No buckling design is required as the transversal displacements are prevented by the mortar-steel encasing.

The incorporation of energy dissipators to a given building structure has two major effects: adding damping and stiffness. The effect of damping is always positive; hence, the main design criterion is to provide as much damping as possible. Conversely, the impact of the added stiffness is rather unclear as discussed next. The stiffness might not be useful for improving the seismic behavior since the stiffening effect can increase the equivalent static forces (as obtained from any standard pseudo-acceleration response spectrum); alternatively, by considering the input energy design approach [Akiyama, 2003; Bruneau and Wang, 1996; Uang and Bertero, 1990] the stiffening effect can decrease the natural period of the building and, hence, increase the input energy. As pointed out by Figure 1, the main frame and the dissipative bracing system behave, with respect to lateral motion, as statically-redundant and parallel-connected springs; therefore, the higher the stiffness of the dissipators, the higher the force they attract (for a given seismic input). Consequently, the optimum value of the added stiffness depends on the particular characteristics of the building and is a trade-off decision: small values of the stiffness of the dissipators (compared to the one of the main frame) correspond to low attracted forces (and, hence, to low energy dissipation capacity) and big values generate low interstory drifts (and again low energy dissipation capacity). Hence, it can be concluded that the bigger the stiffness of the frame, the bigger the optimum value of the added stiffness. By the other hand, in any frame (see Figure 1) the equivalent lateral forces are higher in the bottom floors than in the top ones; hence, in general, the distribution of stiffness of the dissipators should fit (at least, roughly) that pattern.

The influence of the design parameters of the core of the proposed devices in the added damping and stiffness is analyzed in the next paragraphs.

As discussed previously, the steel core is a (constant section) solid cylinder. Given that its total length cannot exceed (roughly) 3 m because of constraints in the testing laboratory, the only (independent) design parameters are the length of the dissipative segment (L_{di}, see Figure 3), the

diameter of the core (d_{co}, see Figure 3) and the steel type (mainly, the yielding point f_y). The selection of the optimum values of such parameters is discussed next.

- **Dissipative length**. The maximum dissipative volume, the minimum added stiffness and the minimum ductility demand on the dissipator (ratio between the yielding and the maximum strains) are obtained (for any given interstory drift) obviously if the whole length of the brace is dissipative ($L_{di} = L_{co} - 2\ L_{cn}$, see Figure 3). Moreover, the energy dissipation capacity is mainly governed by the amount of skeleton energy [Kato, Akiyama, Yamanouchi, 1973] (related to the cumulated plastic damage [Oller, 2003]) consumed (before the maximum strain is reached); obviously, the longer the bar, the shorter the strain. Consequently, it is generally convenient to design a brace whose dissipative length covers its whole length. It is remarkable that this decision further supports the use of a constant section bar as inner core.
- **Core diameter**. Given that all the length of the core is dissipative, the only remaining design parameter is the diameter of the core d_{co}; obviously, the bigger such diameter the bigger the added stiffness. Given that only four devices can be produced and tested, two values of the diameter will be used as dissipators D1 and D2, as well as D3 and D4 are designed to be alike to allow comparing their results. For rather stiff frames (and for bottom floors) a diameter d_{co} = 22 mm is considered adequate while for less stiff frames (and for top floors) a diameter d_{co} = 10 mm is selected [Palazzo & Crisafulli, 2004].
- **Steel type**. For practical reasons (coherent with the sought simplicity of the device), ordinary construction steel is used (S275 JR [EN 10025, 2002], yielding point f_y = 275 MPa).

3.3 Casing

3.3.1 General remarks

The casing (steel tube-mortar filling assembly, see Figure 3) has to be designed to withstand its self weight and the second order lateral forces exerted by the core when trying to buckle. Given the short length of the tube, the first load is unable to exert any significant demand and only the second one is relevant. To support this statement, the maximum deflections in the mid sections are computed next.

- **Devices D1 and D2**. The self-weight is approximately $q = 7850 \times \pi \times 0.09 \times 0.003 + 2300 \times \pi \times 0.042^2 = 19.41$ kg / m = 0.194 N / mm. In the 90 mm (diameter) tube the equivalent moment of inertia of the tube is $I_{tu} = \pi \times (45^4 - 42^4) / 4 + \pi \times 42^4 / 4 / 11.99 = 9.805 \times 10^5$ mm^4; in this calculation, the concrete has been transformed to steel by means of the equivalence coefficient $n = E_s / E_m = 210 / 17.52 = 11.99$ (the value of E_m has been obtained from Table 8). The vertical deflection in the mid section is $y = 5 \times 0.194 \times 2422^4 / (384 \times 2.1 \times 10^5 \times 9.805 \times 10^5) = 0.422$ mm.
- **Devices D3 and D4**. The self-weight is approximately $q = 7850 \times \pi \times 0.115 \times 0.003 + 2300 \times \pi \times 0.0545^2 = 27.68$ kg / m = 0.277 N / mm. In the 115 mm (diameter) tube the equivalent moment of inertia of the tube is $I_{tu} = \pi \times (57.5^4 - 54.5^4) / 4 + \pi \times 54.5^4 / 4 / 11.99 = 2.234 \times 10^6$ mm^4; in this calculation, the concrete has been transformed to steel by means of the equivalence coefficient $n = E_s / E_m = 210 / 17.52 = 11.99$ (the value of E_m has been obtained from Table 8). The vertical deflection in the mid section is $y = 5 \times 0.\ 277 \times 2152^4 / (384 \times 2.1 \times 10^5 \times 2.234 \times 10^6) = 0.165$ mm.

These results show that these deflections are extremely small. Moreover, even if the effect of the first load was significant, intermediate bearings might be of help to partially alleviate it.

Next subsections present the possible buckling modes and the analyses of each of them.

3.3.2 Buckling modes

In any buckling restrained brace three flexural buckling modes are feasible and must be accounted for [Black, Makris and Aiken, 2004]:

- Global buckling of the whole device. The buckling of the core (either in low or high modes) involves also the buckling of the filled tube (casing).
- Buckling of the core in higher modes. The buckling of the core (only in high modes) does not involve the buckling of the casing. The core behaves as a column embedded in an elastic medium. This phenomenon is termed as rippling.
- Local buckling of the naked core ends. When the core reaches its maximum extension their ends protrude beyond the protection of the casing. When the motion reverts, the core is compressed and both ends are in serious risk of buckling.

The analyses of these modes are presented next.

3.3.3 Global flexural modes

The considered formulation is based on a model of the second order behavior of the core-mortar-tube assembly which accounts (in a simplified way) for all the relevant issues. Such issues are: the initial geometrical imperfections, the nonlinear behavior of the core (while it is yielding, the actual value of the modulus of elasticity is hard to estimate as is significantly smaller than the ordinary modulus of elasticity of steel) and the interaction between the core and the mortar.

The following geometrical imperfections are considered:

- Initial gap (a) between the core and the surrounding mortar. It is conservatively assumed that this gap is constant along the length of the core and is equal to two times the rubber width (a = 3.4 mm). This assumption is equivalent to neglect the transversal stiffness of the rubber.
- Initial eccentricity of the core duct (e_{co}). The observation of the (broken) tested specimens (see Figure 86, Figure 113, Figure 151 and Figure 176) shows that this parameter is relevant and, hence, cannot be neglected.
- Initial eccentricity of the outer tube (e_{tu}). Compared to the other two parameters, this one can be neglected (e_{tu} = 0).

Figure 14 describes a case where the core buckles according to the first mode. The interaction between the core and the mortar is modeled as concentrated lateral forces (F_1) in the (three) sections where both elements are in contact.

In Figure 14, L_{tu} is the length of the tube (which is equal to the buckling length l_1 of the first mode). P is the axial compressive force, F_1 is the interaction force (exerted by the casing on the core) and M is the bending moment in the mid section of the core (see Figure 14, down). In the lower plot in Figure 14 y is the lateral mid span deflection of the core and of the casing due to their interaction. The sum of e_{co} and a is termed as e_1 which accounts for the effective initial eccentricity corresponding to the first buckling mode.

The second-order equilibrium equation of the left half of the core (Figure 14, down) can be written as

$$P\,(e_1 + y) = F_1\,l_1 / 4 + M \qquad \text{Eqn. (1)}$$

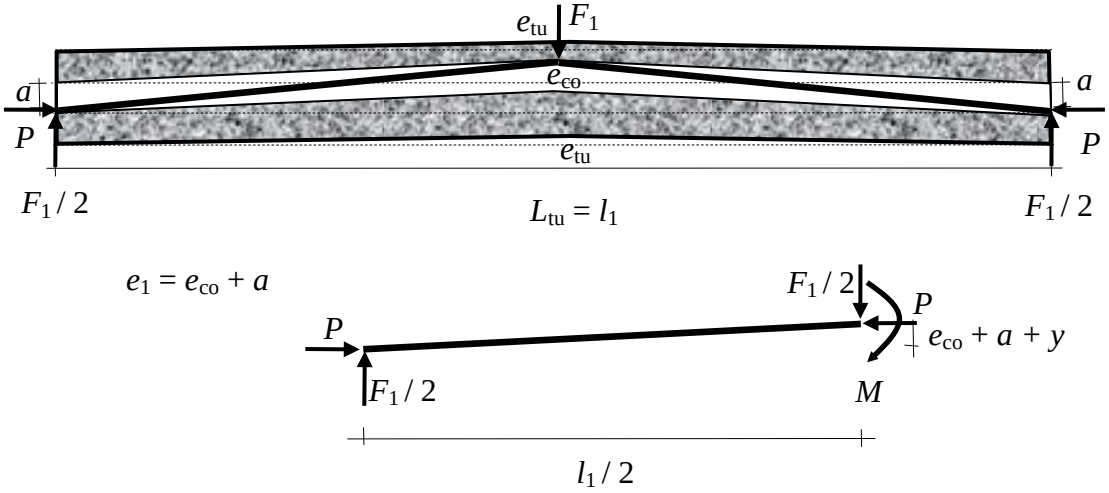

Figure 14. Buckling of the core (first mode)

It is remarkable that the eccentricity e_{tu} of the tube has no influence in this relation. As stated previously, y is the lateral deflection of the casing generated by F_1. Its constitutive equation relates F_1 and y as $F_1 = k_{tu}\, y$ where k_{tu} is the stiffness of the casing (filled tube; $k_{tu} = 48\, E_{tu}\, I_{tu} / L_{tu}^3$ where E_{tu} and I_{tu} are the deformation moduli and moments of inertia of the restraining filled tube). The substitution of this equation in Eqn. (1) yields the interaction force:

$$F_1 = [P\, e_1 - M] / (l_1 / 4 - P / k_{tu}) \qquad \text{Eqn. (2)}$$

As the core is compressed beyond the steel yielding point but the strain is far from the hardening region, it does not possess any significant bending strength and, consequently, it can be assumed that $M = 0$. The term P / k_{tu} represents the contribution of the flexibility of the filled tube: if $P / k_{tu} = l_1 / 4$, F_1 tends to infinity but, in ordinary cases, P / k_{tu} can be neglected compared to $l_1 / 4$ as it represents the deflection that would undergo the filled tube under a lateral load P; consequently

$$F_1 \approx P\, 4\, e_1 / l_1 << P \qquad \text{Eqn. (3)}$$

Hence, the casing (filled tube) has to be designed to resist a shear force V_1 and a bending moment M_1:

$$V_1 = F_1 / 2 = P\, 2\, e_1 / l_1 << P \qquad M_1 = F_1\, l_1 / 4 \approx P\, e_1 \qquad \text{Eqn. (4)}$$

The observation of Eqn. (4) shows that neither V_1 nor M_1 are able to exert any relevant demand on the tube (provided that P / k_{tu} can be neglected compared to $l_1 / 4$). It means that this buckling mode is not feasible. This preliminary conclusion is supported next by the verification of resistance of devices D1, D2, D3 and D4. The thinner and thicker tubes (with 90 and 115 mm diameter, respectively) are considered in the next paragraphs.

- **Thinner tube**. In the 90 mm (diameter) tube it is conservatively assumed that $e_1 = 20$ mm. The maximum possible value of the axial compressive force in the steel core is $P = f_u\, A_{co} = 428 \times 78.54 = 33.62$ kN (the value of the ultimate strength f_u of the steel core has been taken from the tested specimens, see Table 7). Eqn. (3) shows that the interaction force is F_1 =

P 4 e_1 / l_1 = 33.62 × 4 × 20 / 2422 = 1.11 kN. Eqn. (4) shows that the shear force is $V = F_1 / 2$ = 1.11 / 2 = 0.555 kN and the bending moment is $M = F_1\ l_1 / 4$ = 1.11 × 2422 / 4 = 0.672 kN m (these demanding values are not yet multiplied by any safety factor). European regulations [EN, 1994] state that the shear force has to be resisted by the steel tube alone (i.e. the contribution of mortar has to neglected) and that the design value of the shear (plastic) strength is given by $V_{pl\ Rd} = A_v\ f_y / \sqrt{3}\ \gamma_{M0}$ where A_v is the shear area and γ_{M0} = 1.1 is the material (steel) safety factor; for circular tubes $A_v = 2\ d_{tu}\ t_{tu}$. For the thinner tube $V_{pl\ Rd}$ = 2 × 90 × 3 × 275 / √3 / 1.1 = 77.94 kN; hence, the safety factor is 140 (even neglecting the contribution of mortar and reducing the strength of steel). The maximum (plastic) bending moment that can be resisted by the steel tube alone is $M_{pl\ Rd} = W_{pl}\ f_y / \gamma_{M0}$ where W_{pl} is the plastic section modulus, it is given by two times the first moment of area of half of the section with respect to the center axis: $W_{pl} = 2\ S_y = d_{tu}^2\ t = 90^2 \times 3 = 24300\ mm^3$; hence $M_{pl\ Rd}$ = 24300 × 275 / 1.1 = 6.075 kN m. Therefore, the safety factor is 9 (even neglecting the contribution of mortar). Since the demanding value of the shear force is smaller than half of the plastic resistance, the interaction between the shear force and the bending moment can be neglected [EN, 1993].

- **Thicker tube**. In the 115 mm (diameter) tube it is conservatively assumed that e_1 = 20 mm. The maximum possible value of the axial compressive force in the steel core is $P = f_u\ A$ = 423 × 380 = 160.80 kN (the value of the ultimate strength f_u of the steel core has been taken from the tested specimens, see Table 7). Eqn. (3) shows that the interaction force is $F_1 = P\ 4\ e_1 / l_1$ = 160.80 × 4 × 20 / 2152 = 5.98 kN. Eqn. (4) shows that the shear force is $V = F_1 / 2$ = 5.98 / 2 = 2.99 kN and the bending moment is $M = F_1\ l_1 / 4$ = 5.98 × 2152 / 4 = 3.217 kN m (these demanding values are not yet multiplied by any safety factor). The maximum shear force that can be resisted by the steel tube alone is $V_{pl\ Rd}$ = 2 × 115 × 3 × 275 / √3 / 1.1 = 99.59 kN; hence, the safety factor is 33. The maximum bending moment that can be resisted by the steel tube alone is $M_{pl\ Rd} = W_{pl}\ f_y / \gamma_{M0} = d_{tu}^2\ t\ f_y / \gamma_{M0}$ = 115² × 3 × 275 / 1.1 = 9.92 kN m; hence, the safety factor is 3 (even neglecting the contribution of mortar). Since the demanding value of the shear force is smaller than half of the plastic resistance, the interaction between the shear force and the bending moment can be neglected [EN, 1993].

These results show that the resistance of the casing is enough to restrain the buckling of the core according to the first mode. The safety margins are much wider for the thinner tube than for the thicker one.

Figure 15 describes the buckling of the core according to higher buckling modes; the considered i-th mode shape is composed of near-straight segments (the wave length is l_i; $l_i = L_{tu} / i$) joined by plastic hinges leaning alternatively on both inner sides of the hole housing the core. Similarly to Figure 14 the stiffness of the rubber is neglected. Conversely, there are two major differences with Figure 14: given that l_i is much smaller than l_1 the effects of the initial geometrical imperfections (mainly e_{co}) are not considered relevant and the transversal flexibility of the casing is neglected (given that the lateral interaction forces near counteract each others).

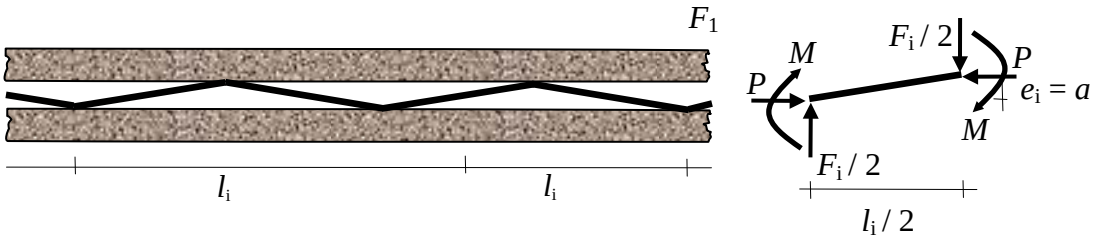

Figure 15. Buckling of the core (higher modes)

The second order equilibrium equation of any portion of the core between consecutive hinges can

be written as

$$P\,e_i = F_i\,l_i / 4 + 2\,M \qquad F_i = (P\,e_i - 2\,M) / (l_i / 4) \qquad \text{Eqn. (5)}$$

As the core is compressed beyond the steel yielding point but the strain is far from the hardening region, it does not possess any significant bending strength and, consequently, it can be assumed that $M = 0$. This result means that the transversal forces acting on the casing are given approximately by $F_i = 4\,P\,e_i / l_i$; hence, they are significantly bigger than those for the first buckling mode (F_1 in Figure 14): $F_i = i\,F_1$. The internal equilibrium equations of the casing (Figure 15) show that the maximum (internal) shear force V and bending moment M are

$$V = F_i / 2 = 2\,P\,e_i / l_i \qquad M = F_i\,l_i / 4 = P\,e_i \qquad \text{Eqn. (6)}$$

These results show that the filled tube can undergo extremely high shear forces (as l_i tends to zero, V tends to infinity) and the assumption that the lateral flexibility of the core is negligible must be released. By considering the lateral interaction between the core and the mortar [Wada, Saeki, Takeuch & Watanabe, 1989] and [Black, Makris & Aiken, 2002] have shown that, under ideal conditions, the critical axial load of the brace is

$$P_{cr} = \pi^2\,(E_{co}\,I_{co} + E_{tu}\,I_{tu}) / L_k^2 \qquad \text{Eqn. (7)}$$

At Eqn. (7) L_k is the effective length of the device (in this case $L_k = l_1$) and $E_{co}\,I_{co}$ and $E_{tu}\,I_{tu}$ are the deformation moduli and moments of inertia of the inner steel core and of the restraining filled tube (casing), respectively. As the casing is composed of two different materials (steel and concrete), E_{tu} and I_{tu} are equivalent values; however, usually the contribution of concrete is ignored and also $E_{co}\,I_{co}$ is neglected compared to $E_{tu}\,I_{tu}$. This conclusion can be also obtained by noting that the buckling situation of the core is equivalent to the one of a compressed liquid column (without any bending strength) in a hollow rigid column [Bazant and Cedolin, 1991].

[Black, Makris & Aiken, 2002; Watanabe et al., 1998] propose that the filled tube be designed to withstand this critical load multiplied by a safety factor. This factor accounts for the initial geometrical imperfections, the nonlinear behavior of the core (while yielding, the actual value of E_{co} is hard to estimate and is significantly smaller than the ordinary modulus of elasticity of steel) and the interaction between the core and the mortar. Not sound and comprehensive criteria to select the values of this factor have been reported; conversely, only over-conservative approaches are possible and, hence, the actual safety factor is unknown. A modification of the formulation by [Black, Makris & Aiken, 2002; Watanabe et al., 1998] is presented next; it incorporates explicitly the initial geometrical imperfections.

Figure 16 describes the interaction between the core (while trying to buckle) and the casing. The upper plot represents the initial position of the core (dashed line, y_0) and the final one (solid line, y). The lower plots represent the final (bent) configurations of the casing and of the core; the transversal (distributed) interaction forces are described by an unknown law $q(x)$.

The initial position of the core is described by the geometrical imperfection considered also in Figure 14 and by the rest of terms of the Fourier series decomposition:

$$y_0 = \sum_{i=1}^{\infty} e_i \sin\frac{\pi\,x}{l_i} = \sum_{i=1}^{\infty} e_i \sin\frac{\pi\,i\,x}{l_1} \qquad \text{Eqn. (8)}$$

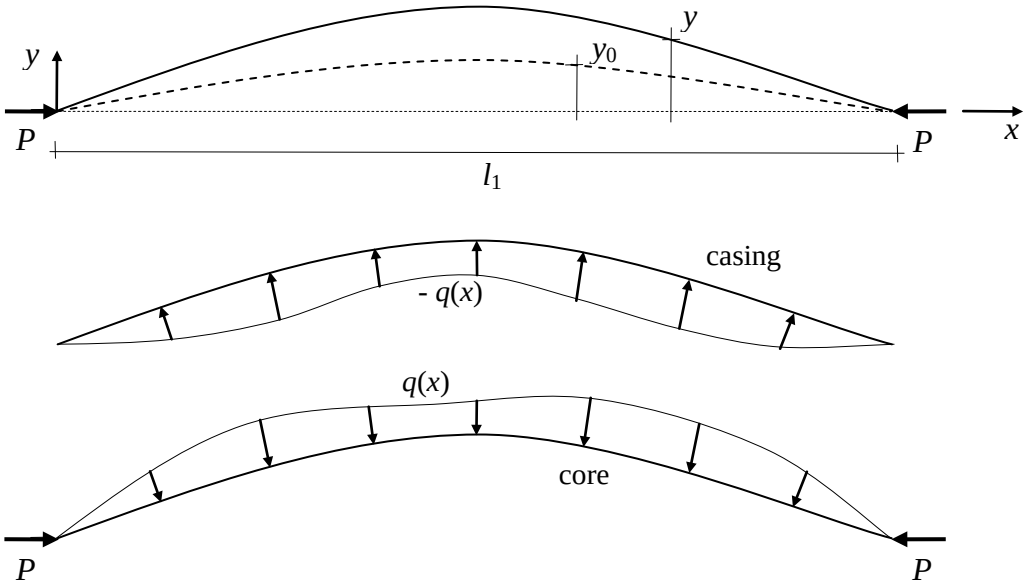

Figure 16. Lateral interaction between the core and the casing

Where $l_i = L_{tu} / i = l_1 / i$. The first initial eccentricity is given by $e_1 = e_{co} + a$ (see Figure 14); for the other terms it can be assumed that $e_i = a$ (see Figure 15).

The second order equilibrium differential equations of the casing and of the core can be written as

$$E_{tu} I_{tu} (y^{iv} - y_0^{iv}) = - q \qquad E_{co} I_{co} (y^{iv} - y_0^{iv}) + P y'' = q \qquad \text{Eqn. (9)}$$

By adding both equations the unknown interaction forces are eliminated and (taking into account Eqn. (8)) a single equation is derived

$$y^{iv} + k^2 y'' = \sum_{i=1}^{\infty} e_i \left(\frac{\pi}{l_i} \right)^4 \sin \frac{\pi x}{l_i} \qquad \text{Eqn. (10)}$$

Where the constant value k is given by $k^2 = P / (E_{tu} I_{tu} + E_{co} I_{co}) \approx P / E_{tu} I_{tu}$. By integrating two times, this fourth-order differential equations becomes a second-order one

$$y'' + k^2 y = - \sum_{i=1}^{\infty} e_i \left(\frac{\pi}{l_i} \right)^2 \sin \frac{\pi x}{l_i} \qquad \text{Eqn. (11)}$$

The general solution of this equation is

$$y = A \sin k x + B \cos k x + \sum_{i=1}^{\infty} q_i \sin \frac{\pi x}{l_i} \qquad \text{Eqn. (12)}$$

A and B are unknown integration constant vales and q_i are also unknown final eccentricities. By imposing the initial conditions $y(0) = 0$ and $y(l_1) = 0$, it follows that $A = B = 0$. By substituting Eqn. (12) into Eqn. (11) and taking into account that $\sin(\pi x / l_i)$ are linearly independent functions it

follows that the final maximum eccentricities q_i are given by

$$q_i = \frac{e_i}{i^2 - \frac{P}{P_E}} \qquad \text{Eqn. (13)}$$

P_E is the first critical Euler load of the casing given by $P_E = \pi^2 E_{tu} I_{tu} / l_1^2$.

Eqn. (13) shows that loads below the critical one can largely amplify the bending of the core, possibly leading to collapse.

For the first term, the maximum bending moment in the tube is determined as the value of $E_{tu} I_{tu} (y'' - y_0'')$ in the mid section ($x = l_1 / 2$):

$$M = E_{ca} I_{ca} e_1 \left(\frac{\pi}{l_1}\right)^2 \frac{\frac{P}{P_E}}{1 - \frac{P}{P_E}} = \frac{P e_1}{1 - \frac{P}{P_E}} \qquad \text{Eqn. (14)}$$

Eqn. (14) allows deriving similar conclusions than Eqn. (13).

The resistance of the casing to these demands is verified next. The thinner and thicker tubes (with 90 and 115 mm diameter, respectively) are considered in the next paragraphs.

- **Thinner tube**. The first critical Euler load of the casing is $P_E = \pi^2 E_{tu} I_{tu} / l_1^2 = \pi^2 \times 2.1 \times 10^5 \times 9.805 \times 10^5 / 2422^2 = 346$ kN. This value is more than ten times bigger than the maximum axial load ($P = 33.62$ kN); Eqn. (13) shows that the amplification factor for the first mode is $1 / (1 - P / P_E) = 1 / (1 - 33.62 / 346) = 1.107$. Eqn. (14) shows that the maximum bending moment (in the mid section of the tube) is $M = E_{tu} I_{tu} e_1 (\pi / l_1)^2 (P / P_E) / (1 - P / P_E) = 2.1 \times 10^5 \times 9.805 \times 10^5 \times 20 \times (\pi / 2422)^2 (33.62 / 346) / (1 - 33.62 / 346) = 0.7460$ kN m. As expectable, this value is similar to the one derived from the formulation described by Figure 14 ($M = 0.672$ kN m); the observed difference can be explained because there the lateral flexibility of the tube was neglected. Since $M_{pl\,Rd} = 6.075$ kN m, the safety factor is bigger than 8 (even neglecting the contribution of mortar).
- **Thicker tube**. The first critical Euler load of the casing is $P_E = \pi^2 E_{tu} I_{tu} / l_1^2 = \pi^2 \times 2.1 \times 10^5 \times 2.234 \times 10^6 / 2152^2 = 1000$ kN. This value is more than six times bigger than the maximum axial load ($P = 160.80$ kN); Eqn. (13) shows that the amplification factor for the first mode is $1 / (1 - P / P_E) = 1 / (1 - 160.80 / 1000) = 1.192$. Eqn. (14) shows that the maximum bending moment (in the mid section of the tube) is $M = E_{tu} I_{tu} e_1 (\pi / l_1)^2 (P / P_E) / (1 - P / P_E) = 2.1 \times 10^5 \times 2.234 \times 10^6 \times 20 \times (\pi / 2152)^2 (160.80 / 1000) / (1 - 160.80 / 1000) = 3.831$ kN m. As expectable, this value is similar to the one derived from the formulation described by Figure 14 ($M = 3.217$ kN m); as in the thinner tube, the observed difference can be explained because there the lateral flexibility of the tube was neglected. Since $M_{pl\,Rd} = 9.92$ kN m, the safety factor is bigger than 2.5 (even neglecting the contribution of mortar).

These results show again that the resistance of the casing is enough to restrain the buckling of the core. The safety margins are much wider for the thinner tube than for the thicker one.

These calculations show that the design of the smaller tube (for dissipators D1 and D2) is clearly over-conservative; a new design based on a more accurate analysis is presented next. As a

conservative safety measure, the contribution of the mortar to the resistance to shear force and to bending moment is neglected (as in the previous verifications). Only commercially available (in Spain) tubes are considered; the thickness is kept constant (t_{tu} = 3 mm) and only the diameter d_{tu} is modified. For tubes more slender than those in devices D1 and D2 it cannot be assumed anymore that P / k_{tu} can be neglected compared to $l_1 / 4$; hence, only the approach from Figure 16 is considered here.

A tube with thickness t_{tu} = 3 mm and diameter d_{tu} = 63 mm is considered next. The maximum shear force and bending moment that can be resisted by the steel tube alone are $V_{pl\,Rd} = 2 \times 63 \times 3 \times 275 / \sqrt{3} / 1.1 = 54.56$ kN and $M_{pl\,Rd} = W_{pl}\, f_y / \gamma_{M0} = 63^2 \times 3 \times 275 / 1.1 = 2.\,977$ kN m. The moment of inertia of the tube is $I_{tu} = \pi \times (31.5^4 - 28.5^4) / 4 + \pi \times 31.5^4 / 4 / 11.99 = 3.196 \times 10^5$ mm^4; in this calculation, the concrete has been transformed to steel by means of the equivalence coefficient $n = E_s / E_m = 210 / 17.52 = 11.99$ (the value of E_m has been obtained from Table 8). The first critical Euler load of the casing is $P_E = \pi^2 E_{tu} I_{tu} / l_1^2 = \pi^2 \times 2.1 \times 10^5 \times 3.196 \times 10^5 / 2422^2 = 112.92$ kN. This value is more than three times bigger than the maximum axial load (P = 33.62 kN); Eqn. (13) shows that the amplification factor for the first mode is $1 / (1 - P / P_E) = 1 / (1 - 33.62 / 112.92) = 1.424$. Eqn. (14) shows that the maximum bending moment (in the mid section of the tube) is $M = E_{tu} I_{tu} e_1 (\pi / l_1)^2 (P / P_E) / (1 - P / P_E) = 2.1 \times 10^5 \times 3.196 \times 10^5 \times 20 \times (\pi / 2422)^2 (33.62 / 112.92) / (1 - 33.62 / 112.92) = 0.957$ kN m. As expectable, this value is higher than the one for the 90 mm diameter tube (M = 0. 7460 kN m). The safety factor is bigger than 3 (even neglecting the contribution of mortar).

3.3.4 Buckling of the core in higher modes

The buckling of the core (only in high modes) does not involve the buckling of the casing. The core behaves as a column embedded in an elastic medium. This phenomenon is commonly termed as rippling.

It is considered that the interaction distributed transversal load (see Figure 16) is proportional to the lateral deflection:

$$q = \beta\, y \qquad \text{Eqn. (15)}$$

Where β is the distributed spring constant. [Timoskenko and Gere, 1961] (following an energy approach) and [Black, Makris and Aiken, 2002] (by direct integration of the second order equilibrium equations) have shown that the critical load is given by

$$P_{cr} = 2\, (\beta\, E_{co}\, I_{co})^{1/2} \qquad \text{Eqn. (16)}$$

The core tends to buckle according to sinusoidal waves; the number i of semi-waves inside the tube length is

$$i = (L_{tu} / \pi)\, (\beta / E_{co}\, I_{co})^{1/4} \qquad \text{Eqn. (17)}$$

By neglecting the restraint exerted by the rubber coating, the value of the spring coefficient can be estimated from the computed unidirectional deformation modulus E_m (see Table 8) taking into account than the mortar is completely confined (by the surrounding mortar and by the steel core):

$$\beta = E_m (1 - \nu) / (1 + \nu) (1 - 2 \nu) \qquad \text{Eqn. (18)}$$

By assuming $\nu = 0.35$, $\beta = 17.52 (1 - 0.35) / (1 + 0.35) (1 - 2 \times 0.35) = 28.12$ GPa. This value is comparable (yet slightly lower) than those reported by [Wada, Saeki, Takeuch and Watanabe, 1989] and by [Black, Makris and Aiken, 2002]. By substituting this result into Eqn. (15), the value of the critical load of the core is obtained. For devices D1 and D2: $P_{cr} = 2 \times (28120 \times 2.1 \times 10^5 \times \pi \times 5^4 / 4)^{½} = 3405$ kN. For devices D3 and D4: $P_{cr} = 2 \times (28120 \times 2.1 \times 10^5 \times \pi \times 11^4 / 4)^{½} = 16481$ kN. Both values are several orders of magnitude bigger than the maximum possible axial forces (given by $A_{co} f_y$). Hence, it can be clearly concluded that this buckling mode is not feasible. However, it should be kept on mind that the core can buckle against the rubber; this fact is confirmed by the inspection of the broken specimens (see Figure 86, Figure 113, Figure 151 and Figure 176).

3.3.5 Buckling of the naked core ends

When the core reaches its maximum extension their ends protrude beyond the protection of the casing (see, for instance, Figure 153). When the motion reverts, the core is compressed and both ends are in serious risk of buckling. This phenomenon can be easily analyzed by conventional Euler analysis of beam-column models.

In the considered experiments (see Figure 57) the bare segments are hinged at their outer end while the inner ends can be considered as moving clamped connections for devices D1 (see Figure 58), D2 (see Figure 89) and D4 (see Figure 152). Conversely, in device D3 (see Figure 115) the added intermediate supports are intended to prevent the transversal displacements and, hence, the inner ends can be considered as fixed clamped connections. For devices D1, D2 and D4 the buckling length is $2 L_0$ (where L_0 is the length of the bare segment) while for device D3 it is $0.7 L_0$; it means than the critical load is eight times higher, this confirms the usefulness of such supports. On the other hand (as discussed previously), the effective value of the modulus of elasticity is hard to estimate since the steel has yield. Consequently, this buckling mode is extremely dangerous since L_0 cannot be reduced and the steel deformation modulus can be extremely small.

The local buckling of the “naked” (end) portions of the core is restrained by four trapezoidal steel plates welded to the final (narrower) part of the (cone) connectors as shown by Figure 3, Figure 12 and Figure 13. These plates are designed to resist 2% of the axial force carried by the core [EN, 1993]. It is remarkable that this design proved to be insufficient during the experiments as shown by Figure 175 (for dissipator D4). Conversely the intermediate supports in device D4 proved very efficient.

3.4 Connectors

The steel end connectors (see Figure 10) are designed to transmit the axial forces from the core to the frame.

As discussed previously, the forces are transferred from the core to the connectors by a dual shear mechanism: (i) friction generated by high strength prestressed bolts and (ii) bonding provided by a chemical adhesive (see Figure 11) with high resistance to fatigue. Each of these two systems is (independently) designed to be able to transmit alone the whole axial force; the screws are designed according to European regulations [EN, 1993] and the adhesive is designed following the producer’s recommendations. About the bolts, the design parameters are the number, diameter of the screws and the steel type (the friction coefficient has been assumed as $\mu = 0.30$

corresponding to little treated rough surface); four bolts are used for the smaller connectors (for dissipators D1 and D2, see Figure 10 left) and twelve for the bigger ones (for dissipators D3 and D4, see Figure 10 right), all the bolts are M10 (10 mm diameter) and the steel of the screws is 12.9 [EN ISO 4014, 2000] (its yielding point is f_y = 1080 MPa and its ultimate strength is f_u = 1200 MPa). About the adhesive product, the only design parameter is the length of the grooves in the connectors (providing contact surface, see Figure 11); as indicated in Table 1, the length of the smaller connectors (for dissipators D1 and D2, see Figure 10 left) is L_{cn} = 200 mm and the length of the bigger connectors (for dissipators D3 and D4, see Figure 10 right) is L_{cn} = 270 mm. In their turn, the connectors are assumed to be fixed to the main frame by any conventional method (e.g. welding or bolts); in the experiments they were joined by a 30 mm diameter pin (see Figure 10, bottom left and Figure 13).

4 INDIVIDUAL EXPERIMENTS ON SHORT DISSIPATORS

4.1 Characterization of materials

4.1.1 General description

The steel (of the core) and the mortar were tested to characterize their most relevant parameters. Such experiments are described in the subsequent subsections.

4.1.2 Characterization of the steel of the core

The characterization experiments about the steel of the core consisted of conventional (monotonic) tension tests on two specimens which are alike to the cores of the (short) dissipators (see Figure 5); such specimens are termed SCS1 and SCS2, accounting for "Short Core Specimen". The effective lengths of each specimen were 336.6 mm; such measures correspond to the distance among the centers of the parts encased by the jaws. Moreover, it should be kept on mind that the section of the specimen is not constant as the (central) yielding segment is significantly thinner. Only the test of the first specimen (SCS1) provided useful results.

Figure 17 displays a steel core mounted of the testing rig (left) and a broken core (right).

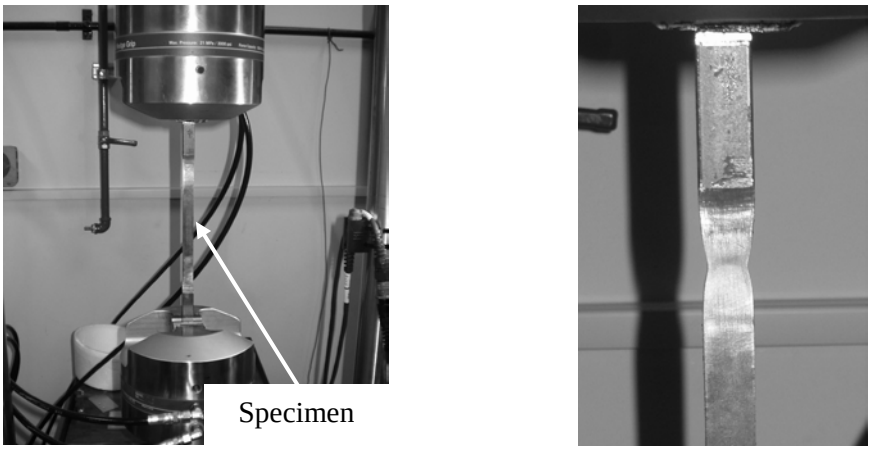

Figure 17. Testing of the steel core of the (short) dissipators

The right picture in Figure 17 shows that the failure arose near the transition zone. It confirms the pernicious effect of the change of section. The test was stopped after the formation of the necking shown by the right picture in Figure 17.

Figure 18 displays the force-displacement plots for specimen SCS1.

The main results of these characterization experiments are shown in Table 7. f_y is the yielding point, E_{co} is the deformation modulus and f_u and ε_u are the ultimate stress and strain, respectively; f_u and ε_u correspond to the maximum value of the stress-strain plot.

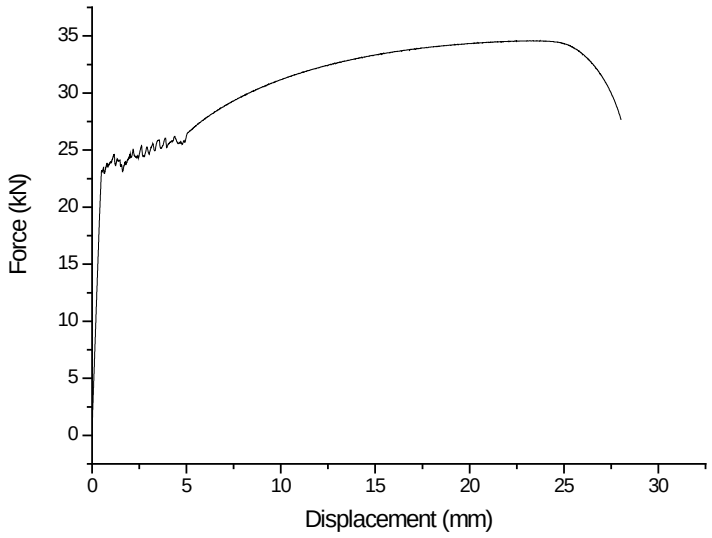

Figure 18. Force-displacement plots for specimen SCS1

Table 3. Measured parameters of the steel of the core for the dissipators SD1, SD2, SD3, SD4 and SD5

Specimen	f_y (MPa)	f_u (MPa)	ε_u (10^{-3})	E_{co} (GPa)
SCS1	330	494	124	165
SCS2	-	-	-	-

Results from Table 7 show no relevant differences between the measured and nominal values of the yielding point f_y and of the ultimate strength f_u (f_y = 330 MPa and f_u = 500 MPa). The ultimate deformation (ε_u) corresponds to f_u and has been determined assuming that all the deformation is concentrated in the central yielding segment (188 mm long). The deformation modulus (E_{co}) has been obtained from points 1 and 222 in the plot in Figure 18 according to the Hooke's law:

$$\frac{1}{E_{co}}\left(257.69\times188+\frac{257.69\times69.96}{252.81}\times85.2+\frac{257.69\times69.96}{193.98}\times\frac{126.8}{2}\right)=0.36649\ \text{mm} \quad \text{Eqn. (19)}$$

It is apparent that the obtained value (E_{co} = 164844 MPa) is not reliable; it confirms that the influence of the flexibility of the testing machine and of the slides in the jaws are not negligible. The nominal value (E_{co} = 200 GPa) is assumed instead.

4.1.3 Characterization of the mortar

The tests about grout (dissipators SD1, SD2 and SD3) and mortar (dissipators SD4 and SD5) consisted of axial compression loading tests of a number of specimens encased by segments of the PVC tube (120 mm tall, as to obtain an aspect ratio near to 2). These proofs were carried out in the National Technological University at Mendoza (Argentina).

Figure 19 displays PVC-coated specimens mounted of the testing machine (left) and a broken specimen (mid and right).

Figure 19. Testing of grout and mortar specimens coated with PVC

Four PVC-coated specimens were tested, two with grout and two with mortar; the collapse forces were 195 and 151 kN (grout) and 116 and 129 kN (mortar). Therefore, the mean stresses were f_{cm} = 63.28 MPa (grout) and f_{cm} = 44.81 MPa (mortar).

4.2 Testing of dissipators

As described previously, the five (short) dissipators were (individually) tested along April 2006 in the Centro Atómico Bariloche, Argentina. The experiments consisted of a certain protocol of cycling axial loading.

The objectives of the tests are (i) to assess the performance of the proposed devices (to validate their design and to investigate their energy dissipation capacity under different ductility demands), (ii) to learn deeply about their structural behavior, (iii) to characterize their hysteretic behavior and (iv) to obtain a wide set of experimental results that might be useful to calibrate the numerical models (to be developed). The experiments were designed to reach these goals.

Each of the dissipators SD1, SD2, SD3, SD4 and SD5 underwent three types of cyclic loading tests. Figure 20 displays two views of dissipators mounted (vertically) on the testing machine.

At Figure 20 the left image corresponds to a dissipator with PVC tube while the right one depicts a device with steel tube.

The registered magnitudes (at each test) were the axial force (measured by a load cell with 100 kN capacity) and the displacement of the hydraulic jack (measured by a displacement transducer with 200 mm range). The time was also recorded but it is not considered relevant as the behavior of the dissipator is assumed to be rather rate-independent (for the range of considered velocities). Positive values of the axial force and of the displacement correspond to tension and to elongation, respectively. Table 4 summarizes this information.

The imposed displacements (testing protocol) were similar for the five dissipators and consisted of three different types of loading cycles: the first one was a growing amplitude wave, the second one was an irregular wave with a sudden initial pulse and a permanent displacement (aiming to represent a near-fault seismic input [Hall, Heaton, Halling & Wald, 1995; Bray & Rodriguez-Marek, 2004]) and the third one was a constant amplitude wave. These three

sequences of cycles have been taken from [Black, Makris & Aiken, 2002] and [SEAONC, 2001]; they are intended to correspond to the effect of highly demanding earthquakes. Conversely, they provide little information about the final energy dissipation capacity of the devices as the first two cycles involve different (coupled) issues.

Table 4. Registered magnitudes on the experiments on (short) dissipators

Magnitude	Sensor	Units	Range	Positive if
Jack axial force	Load cell	kN	100	Tension
Axial displacement	LVDT	mm	200	Elongation

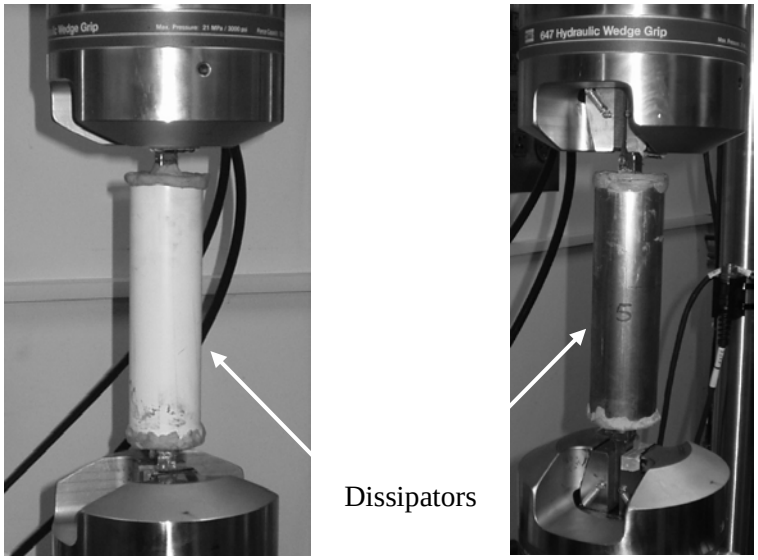

Figure 20. Cyclic testing of a (short) dissipator

The yielding displacement Δ_y is determined from the measured yielding point (see Table 3) and the approximate values of the lengths of each segment of the core according to the Hooke's law:

$$\Delta_y = \frac{1}{200000}\left(330\times188+\frac{330\times69.96}{252.81}\times85.2+\frac{330\times69.96}{193.98}\times\frac{126.8}{2}\right)=0.387\ \text{mm} \qquad \text{Eqn. (20)}$$

In this calculation the first term corresponds to the (central) yielding segment, the second term is the contribution of the intermediate (integer) segments and the third term represents the (outer) segments connected to the jaws. In the length of the inner segment (188 mm) the two transition parts (see Figure 5) have been included. It has been assumed than the effective length of these last segments is the half of their total length.

Figure 21 and Figure 22 display the first type of loading history (growing amplitude cycles) for dissipators SD1, SD2 and SD3 (Figure 21) and for dissipators SD4 and SD5 (Figure 22).

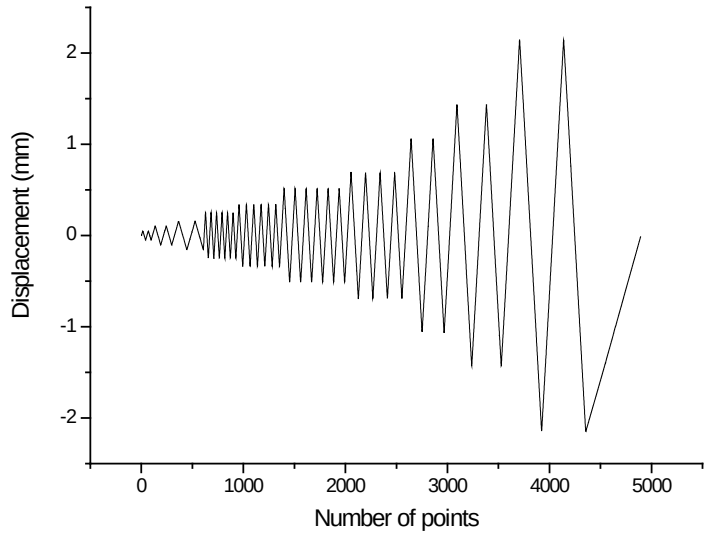

Figure 21. Growing amplitude cycles of dissipators SD1, SD2 and SD3

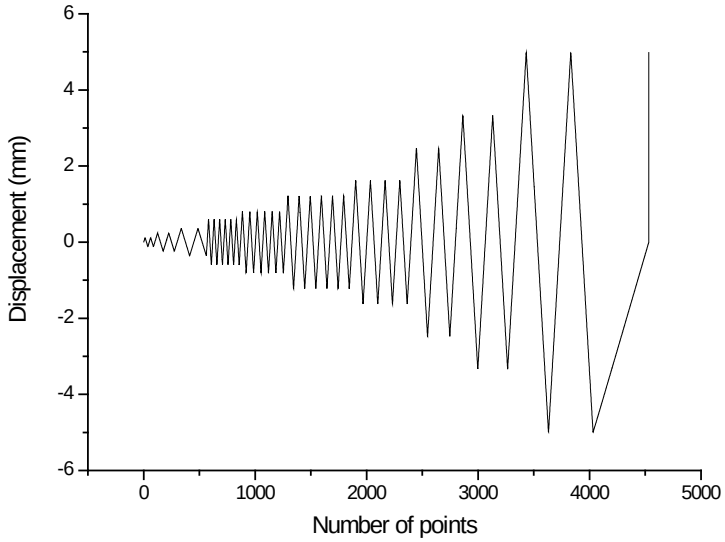

Figure 22. Growing amplitude cycles of dissipators SD4 and SD5

The observation of Figure 21 and Figure 22 shows that the sequence is alike in both cases but the amplitudes are bigger in Figure 22. At Figure 21 the ductility ratio (quotient between the maximum -at the two last cycles- and the yielding displacements, see Eqn. (20)) is 5.56 while in Figure 22 it is 12.92. For dissipators SD1 and SD3 the total duration of the cycles was 98 s, for dissipator SD2 it was 398 s and for dissipators SD4 and SD5 it was 227 s.

Figure 23 and Figure 24 display the second type of loading cycles (irregular wave with a pulse and a permanent displacement, representing near-source effects) for dissipators SD1, SD2 and SD3 (Figure 23) and for dissipators SD4 and SD5 (Figure 24).

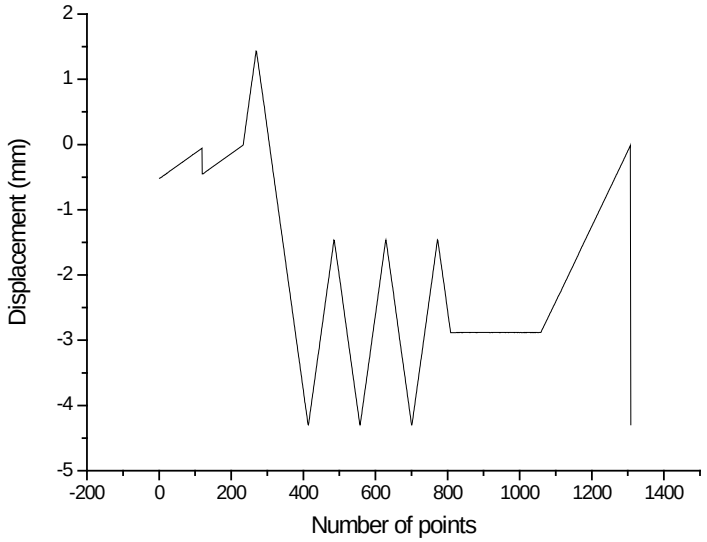

Figure 23. Near-source cycles of dissipators SD1, SD2 and SD3

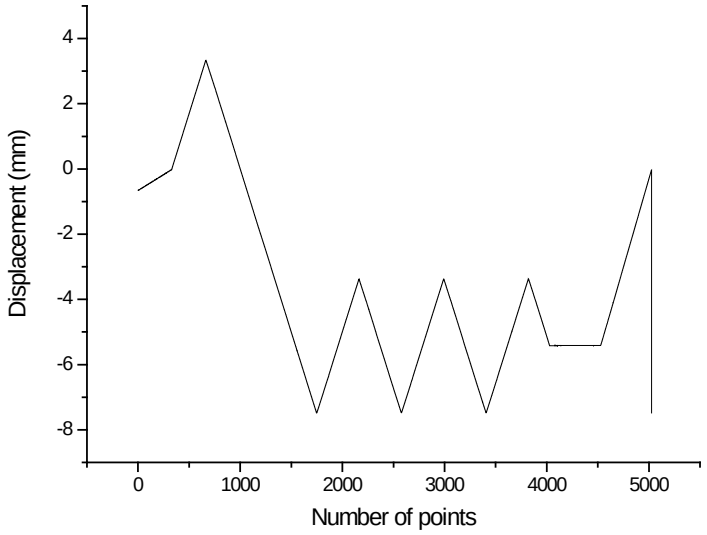

Figure 24. Near-source cycles of dissipators SD4 and SD5

The observation of Figure 23 and Figure 24 shows that the sequence is similar in both cases but the amplitudes are bigger in Figure 24. At Figure 23 the ductility ratio (quotient between the maximum and the yielding displacements) is 11.11 while in Figure 24 it is 19.64; the maximum displacements correspond to the three “lower” peaks (in between points 400 and 800 for Figure 23 and in between points 400 and 800 for Figure 24). For dissipators SD1 and SD3 the total duration of the cycles was 24 s, for dissipator SD2 it was 127 s and for dissipators SD4 and SD5 it was 50 s.

Figure 25, Figure 26 and Figure 27 display the third type of loading histories (constant amplitude cycles) for dissipators SD1, SD2 and SD3 (Figure 25), SD4 (Figure 26) and SD5 (Figure 27).

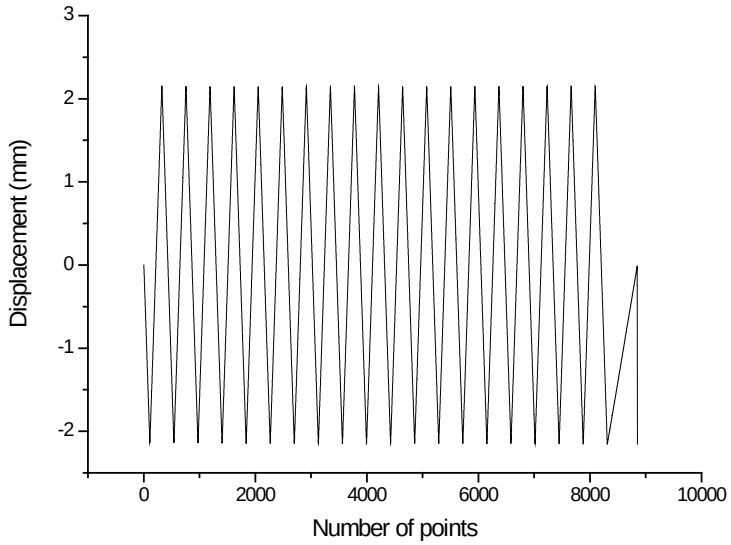

Figure 25. Constant amplitude cycles of dissipators SD1, SD2 and SD3

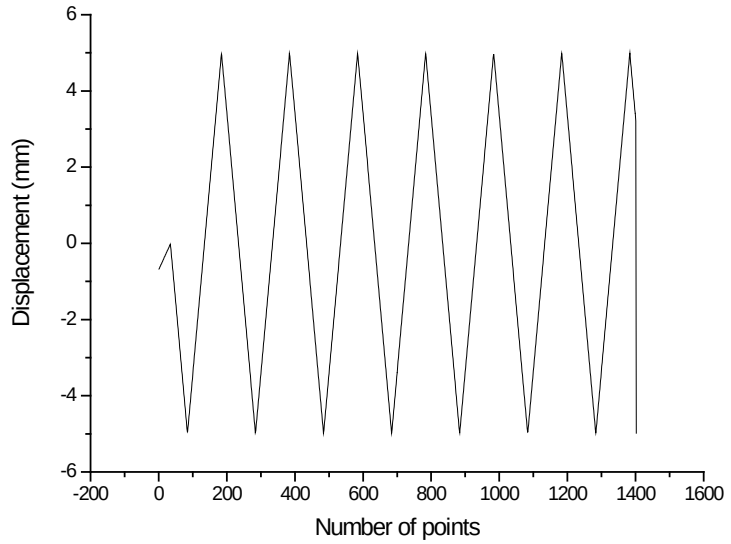

Figure 26. Constant amplitude cycles of dissipator SD4

The observation of Figure 25, Figure 26 and Figure 27 shows that the three sequences are alike but their amplitudes are different. At Figure 25 the ductility ratio (quotient between the maximum and the yielding displacements) is 5.56, in Figure 26 is 12.92 and in Figure 27 it is 7.75. For dissipators SD1 and SD3 the total duration of the cycles was 177 s, for dissipator SD2 was 842 s, for SD4 was 50 s and for SD5 was 177 s. For dissipators SD4 and SD5 the number of cycles is smaller (than for dissipators SD1, SD2 and SD3) because of premature failure of the core.

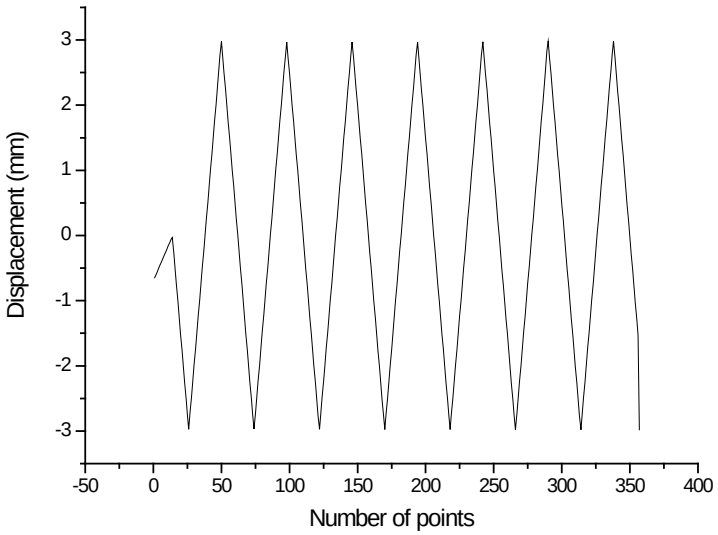

Figure 27. Constant amplitude cycles of dissipator SD5

Table 5 summarizes the maximum displacements in the loading protocols described by Figure 21, Figure 22, Figure 23, Figure 24, Figure 25, Figure 26 and Figure 27.

Table 5. Maximum displacements (mm) in the tests of the short dissipators

Protocol	Nº of cycles	SD1, SD2 and SD3	SD4	SD5
Growing amplitude	2	± 0.05	± 0.12	
	2	± 0.11	± 0.24	
	2	± 0.16	± 0.36	
	6	± 0.25	± 0.60	
	6	± 0.34	± 0.80	
	6	± 0.52	± 1.23	
	4	± 0.69	± 1.65	
	2	± 1.05	± 2.50	
	2	± 1.45	± 3.35	
	2	± 2.15	± 5.00	
Pulse	1/2	+ 1.44	± 3.40	
	3	- 1.45 to - 4.3	- 3.30 to - 7.6	
Constant amplitude	18	± 2.15	± 5.00	± 3.00

All the tubes were filled with grouting (or mortar) by 15th April 2006; dissipators SD1, SD2, SD3, SD4 and SD5 were tested by 24th to 26th April 2006. The (naked) steel cores were tested by 26th April 2006. The mortar was tested by 11th May 2006.

Next subsections display some pictures and most of the experimental results from the tests (of the five short dissipators) carried out at the laboratory of the Centro Atómico de Bariloche. The main

conclusions arisen from these plots are stated.

4.3 Testing of dissipator SD1

This subsection lists the most relevant results for dissipator SD1. The test of this device had no particular circumstances.

The hysteretic behavior (force vs. displacement) of dissipator SD1 for the three loading histories described by Figure 21, Figure 23 and Figure 25, is represented by Figure 28 and Figure 30 (both correspond to Figure 21), Figure 31 (corresponds to Figure 23) and Figure 32 and Figure 33 (both correspond to Figure 25).

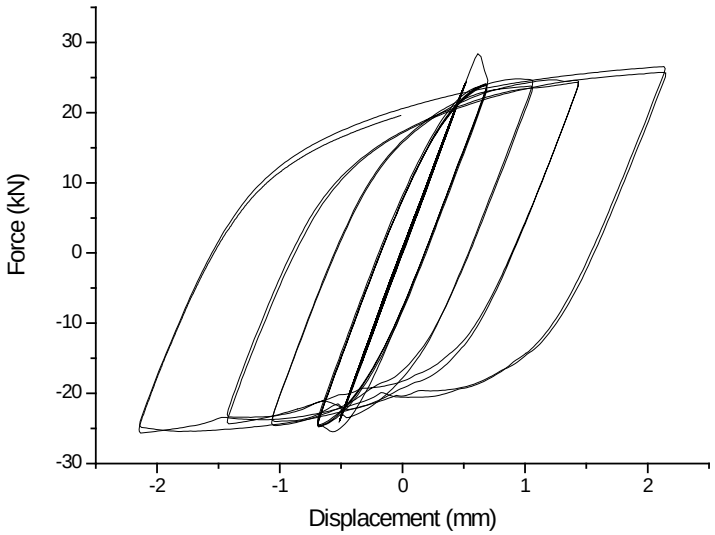

Figure 28. Hysteresis loops of dissipator SD1 for growing amplitude cycles

For a proper interpretation of the plots in Figure 28 (and in other similar figures shown next in this section) it should be kept in mind that, according to Table 4, positive values of force correspond to tension while positive values of displacement correspond to elongation. It implies that the loops in Figure 28 are described clockwise.

Plots in Figure 28 are formed by a number of hysteresis loops; for a better understanding, a sketch of an ideal loop is displayed in Figure 29.

Figure 29 displays a typical ideal hysteresis loop corresponding to constant amplitude steady-state motion of a device made of a material with bilinear (symmetric) elastic-plastic behavior. F_{ey} and Δ_y correspond to the yielding force and to the yielding displacement, respectively; the other symbols refer to the maximum and minimum values of force and displacement. Each loop contains four branches; the steeper ones are elastic while the flatter ones are plastic. The slope of the elastic branches is the initial (elastic) stiffness while the slope of the plastic branches corresponds to the strain hardening. The area encompassed by the loop indicates the amount of dissipated energy. The Bauschinger effect [Akiyama, 1980] has not been taken into account in the ideal plot shown by Figure 29.

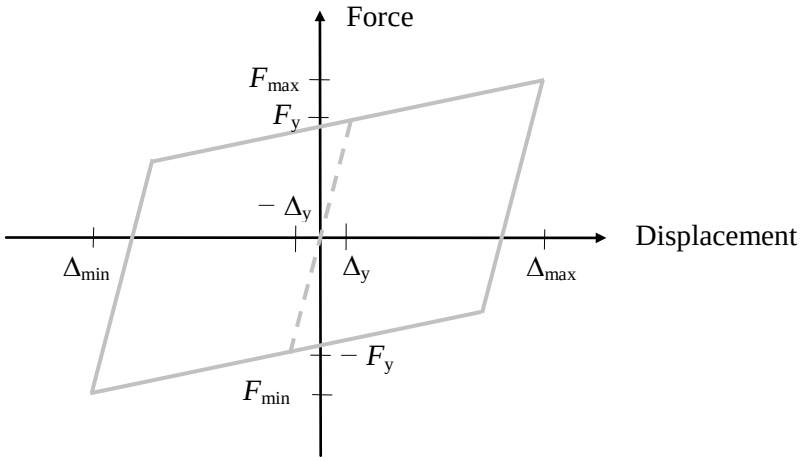

Figure 29. Typical hysteresis loop

Plots from Figure 28 show an irregular behavior in the first loops (in the tension region); to clarify this issue Figure 30 shows the first part of the loops shown in Figure 28 (2500 points out of 4893).

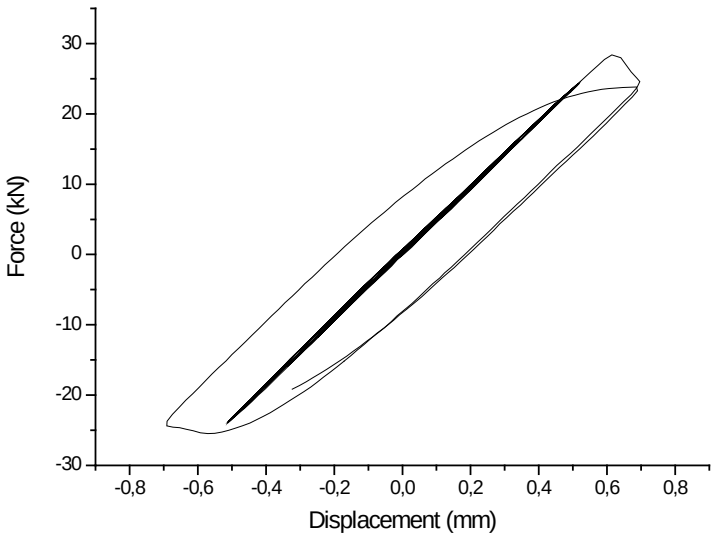

Figure 30. First hysteresis loops of dissipator SD1 for growing amplitude cycles

Plots from Figure 30 show that during the first loops there is no energy dissipation (linear behavior), what is coherent with the value of the yielding displacement (see Eqn. (20), $\Delta_y = 0.387$ mm) and the history of the loading cycles (see Table 5 and Figure 21). Once the force amplitude reaches its maximum value (about 28 kN), a sudden slide appears since the force decreases while the displacement grows; it might correspond to breakage of some bonding between the steel core and the surrounding mortar. It is remarkable that this bonding has to be limited to a rather short segment; otherwise the joint behavior of mortar and steel would increase significantly the (global) stiffness. This fact can be also observed for device SD2 (Figure 34) and, less intensively for devices SD3 (Figure 38), SD4 (Figure 41) and SD5 (Figure 44).

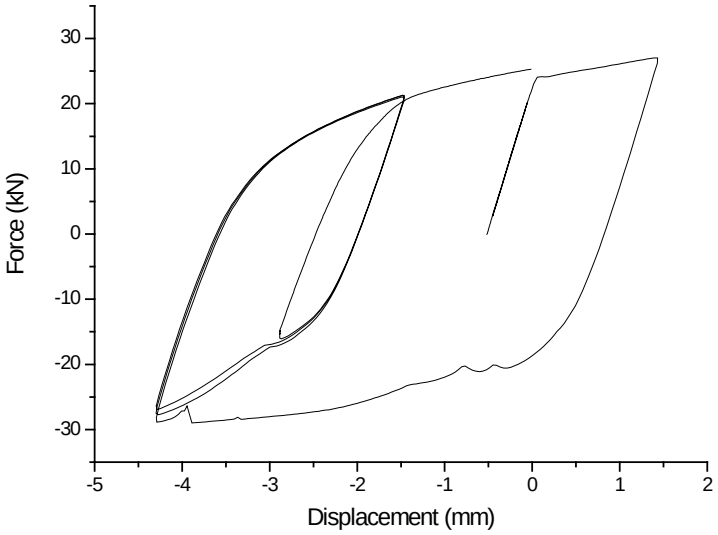

Figure 31. Hysteresis loops of dissipator SD1 for near-source cycles

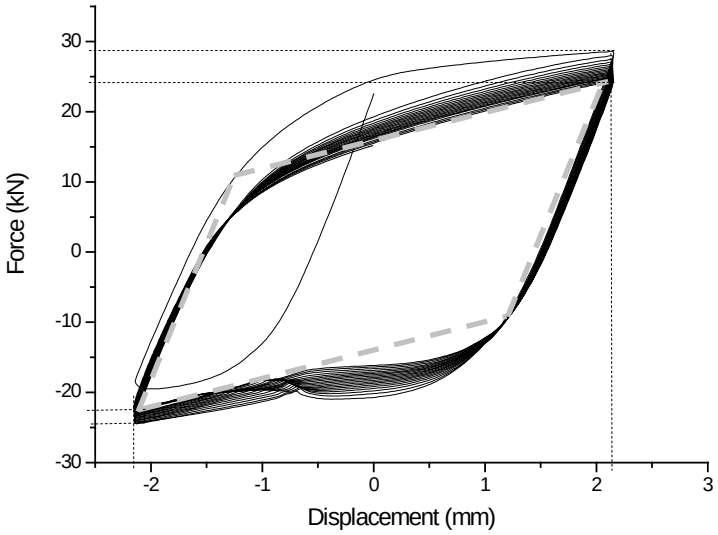

Figure 32. Hysteresis loops of dissipator SD1 for constant amplitude cycles

To facilitate the interpretation of Figure 32 some auxiliary lines have been drawn. The wide dash lines correspond to an ideal bilinear hysteresis loop (see Figure 29) with parallel branches; this loop is intended to fit the inner registered loops. The slope of the plastic branches has been selected to match the lower compressive. The thin dash lines indicate the force and displacement amplitudes of the inner and outer loops.

Figure 32 shows that the force amplitude of the loops is changing along the experiment; in order to determine the main features of this evolution Figure 33 displays the five first loops of Figure 32 (2400 points out of 8850).

Comparison between Figure 33 and Figure 32 shows that the force amplitude of the loops diminishes continuously (both the tension and compression values); it can be understood as a kind of (slight) degradation. The reduction of amplitude is bigger in the tension corner (top) than in the

compression one (bottom). These facts can be also observed for dissipators SD2 (Figure 36), SD3 (Figure 40), SD4 (Figure 43) and SD5 (Figure 46).

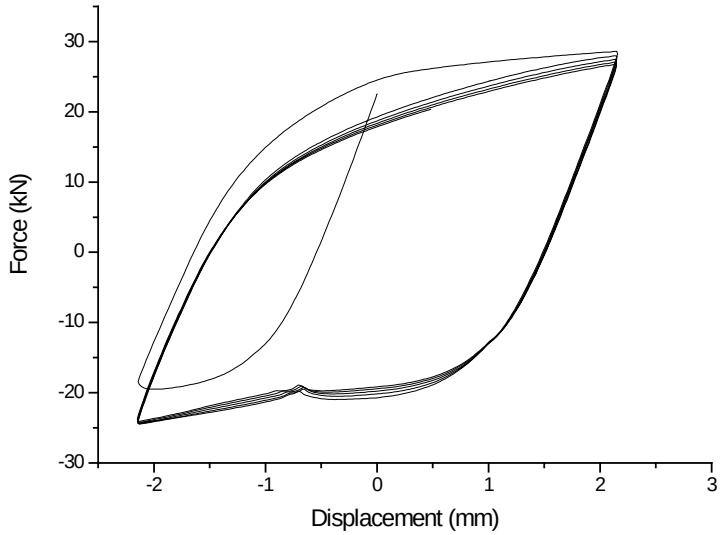

Figure 33. First hysteresis loops of dissipator SD1 for constant amplitude cycles

Figure 28, Figure 31 and Figure 32 show, as expected, a quite regular hysteretic behavior; minor failures (due to buckling of the core) are observed in the compression branches (negative values of the force, see Table 4) generating in Figure 32 smaller (maximum) compression forces than tension ones.

Two common clear trends arise from Figure 28 and Figure 32:

- The (upper and lower) yielding (loading) branches are clearly not horizontal. It is due to the Bauschinger effect [Akiyama, 1980].
- The tension peaks (top right corners) are higher than the compression ones (bottom left corners). In the (plastic) compression domain there are two phenomena that influence oppositely: axial stiffening provided by the casing contribution (because of the friction generated by the compression) and axial softening generated by the buckling of the core. In this case the second effect prevails.

4.4 Testing of dissipator SD2

This subsection lists the most relevant results for dissipator SD2. The test of this device had no particular circumstances.

Figure 34, Figure 35 and Figure 36 show the hysteretic behavior (force vs. displacement) of dissipator SD2 for the three loading histories described by Figure 21, Figure 23 and Figure 25, respectively.

To facilitate the interpretation of Figure 36 some auxiliary lines have been drawn similarly to Figure 32.

Figure 34, Figure 35 and Figure 36 show, as expected, a regular hysteretic behavior; minor failures (due to buckling of the core) are observed in the compression branches (negative values

of the force, see Table 4) except in Figure 36. Comparison with the behavior of the dissipator SD1 (Figure 28, Figure 30, Figure 31 and Figure 32) shows a high similarity; hence, the conclusions are also similar.

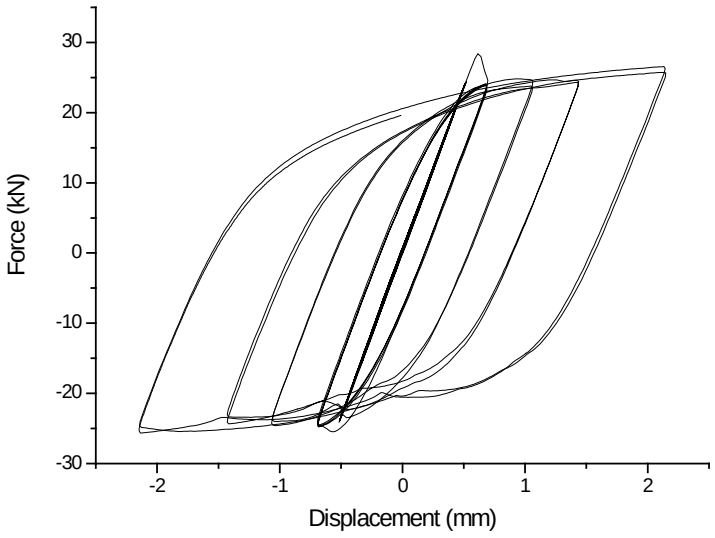

Figure 34. Hysteresis loops of dissipator SD2 for growing amplitude cycles

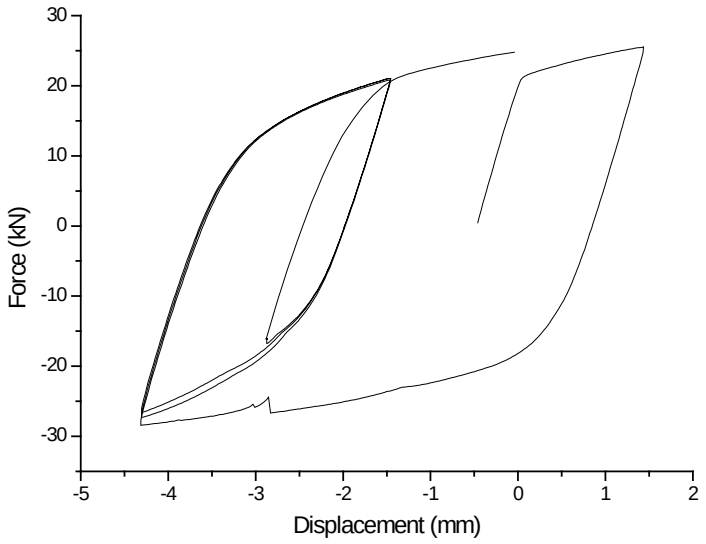

Figure 35. Hysteresis loops of dissipator SD2 for near-source cycles

Figure 37 display comparisons between the force-displacements plots from Figure 18 (for the steel specimen SCS1) and the hysteresis loops for the dissipator SD2 under constant amplitude cycles (see Figure 36).

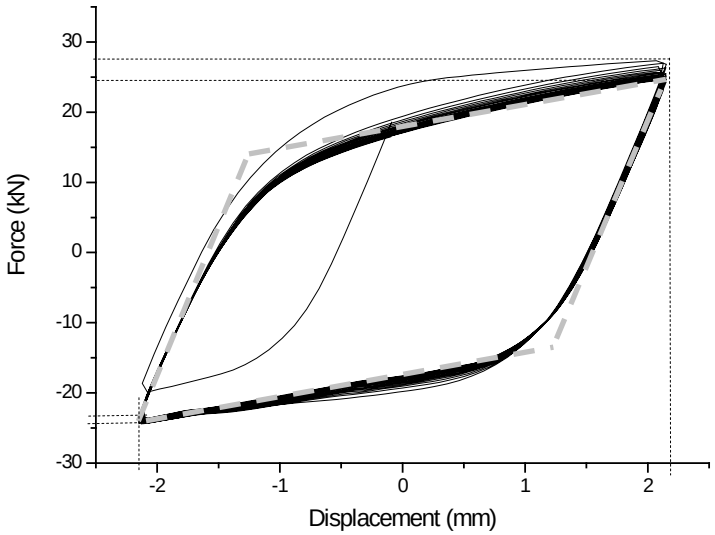

Figure 36. Hysteresis loops of dissipator SD2 for constant amplitude cycles

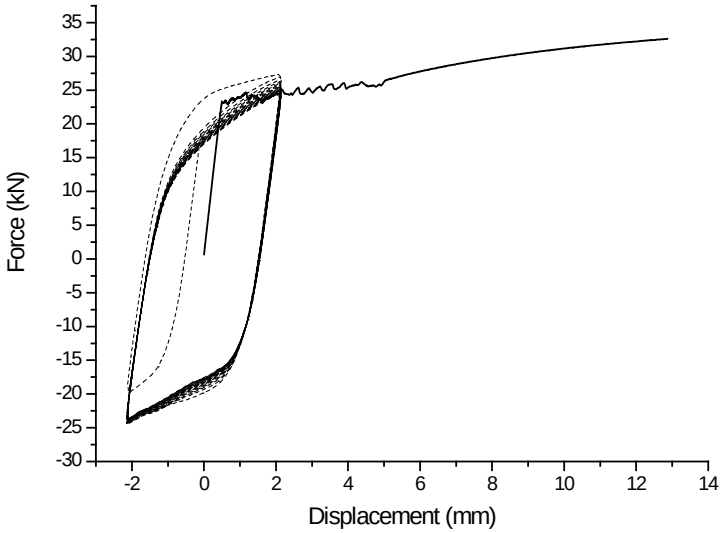

Figure 37. Comparison between stress-strain plots for the specimen core bar CSC1 and for dissipator SD2

Plots from Figure 37 show that the (tension) elastic stiffness of the steel core alone and the one of the dissipator SD2 are almost equal; it shows that the shear stress transfer to the mortar casing is negligible. Comparison among the plots of the core and of the device shows that the amount of consumed skeleton energy [Kato, Akiyama, Yamanouchi, 1973] is rather moderate since the plastic excursion is small (see Figure 18).

4.5 Testing of dissipator SD3

This subsection lists the most relevant results for dissipator SD3. The test of this device had no particular circumstances.

Figure 38, Figure 39 and Figure 40 show the hysteretic behavior (force vs. displacement) of dissipator SD3 for the three loading histories described by Figure 21, Figure 23 and Figure 25, respectively.

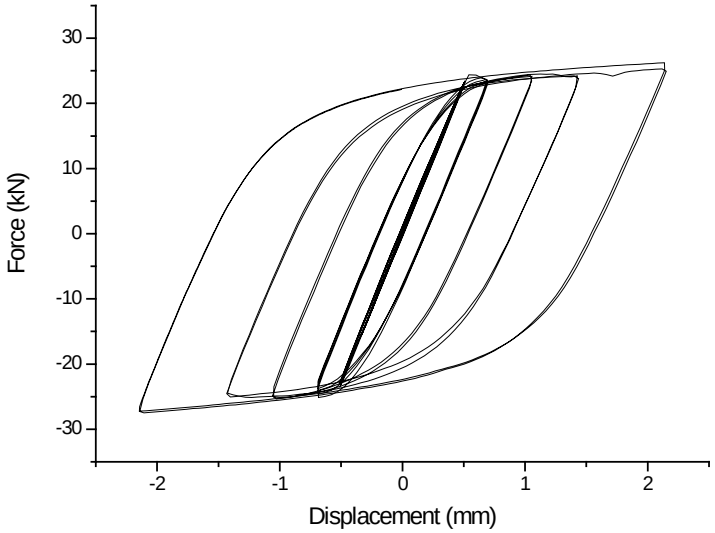

Figure 38. Hysteresis loops of dissipator SD3 for growing amplitude cycles

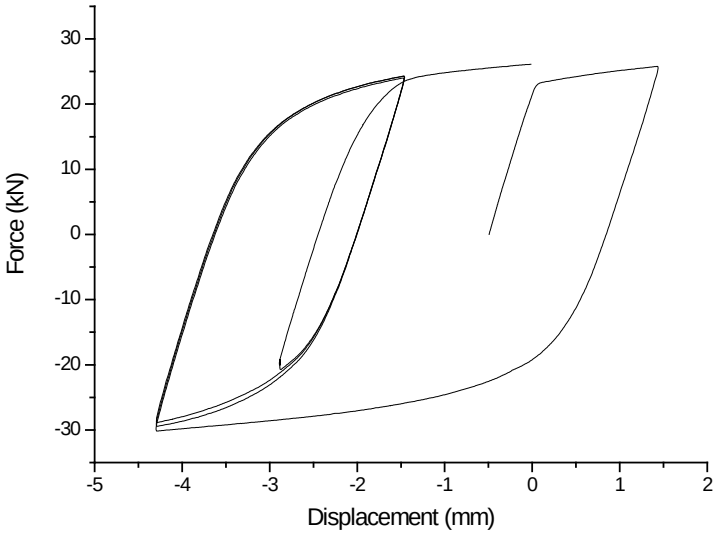

Figure 39. Hysteresis loops of dissipator SD3 for near-source cycles

To facilitate the interpretation of Figure 40 some auxiliary lines have been drawn similarly to Figure 32.

Figure 38, Figure 39 and Figure 40 show, as expected, a regular hysteretic behavior. The (minor) failures (due to buckling of the core) observed in dissipators SD1 and SD2 in the compression branches are not present in this case; consequently, in Figure 40 the tension peaks are not higher than the compression ones. Beyond these differences, comparison with the behavior of the dissipators SD1 (Figure 28, Figure 30, Figure 31 and Figure 32) and SD2 (Figure 34, Figure 35 and Figure 36) shows a high similarity.

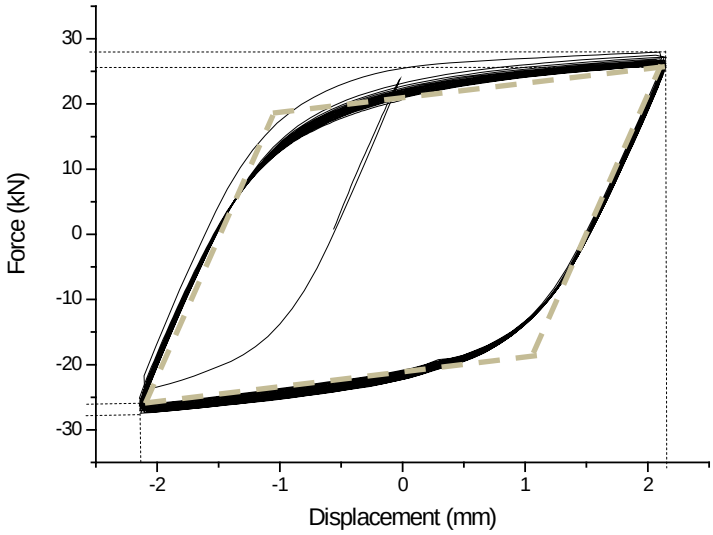

Figure 40. Hysteresis loops of dissipator SD3 for constant amplitude cycles

4.6 Testing of dissipator SD4

This subsection lists the most relevant results for dissipator SD4. The test of this device had no particular circumstances. Conversely to dissipators SD1, SD2 and SD3, the failure came by local buckling of the core.

Figure 41, Figure 42 and Figure 43 show the hysteretic behavior (force vs. displacement) of dissipator SD4 for the three loading histories described by Figure 22, Figure 24 and Figure 26, respectively.

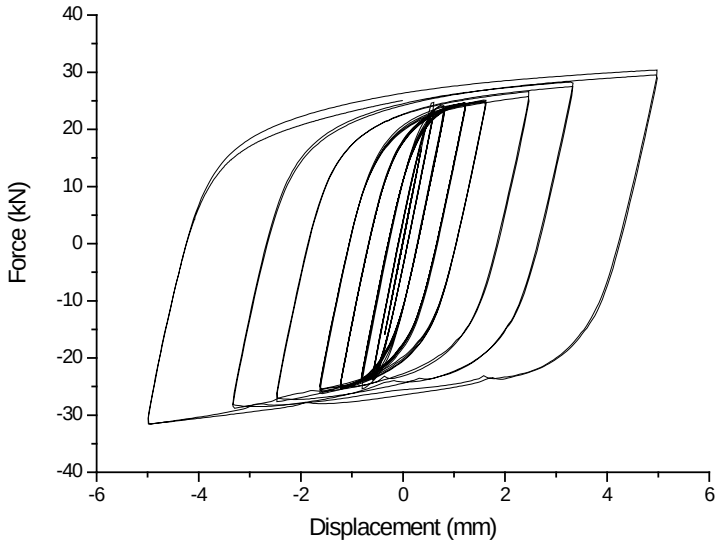

Figure 41. Hysteresis loops of dissipator SD4 for growing amplitude cycles

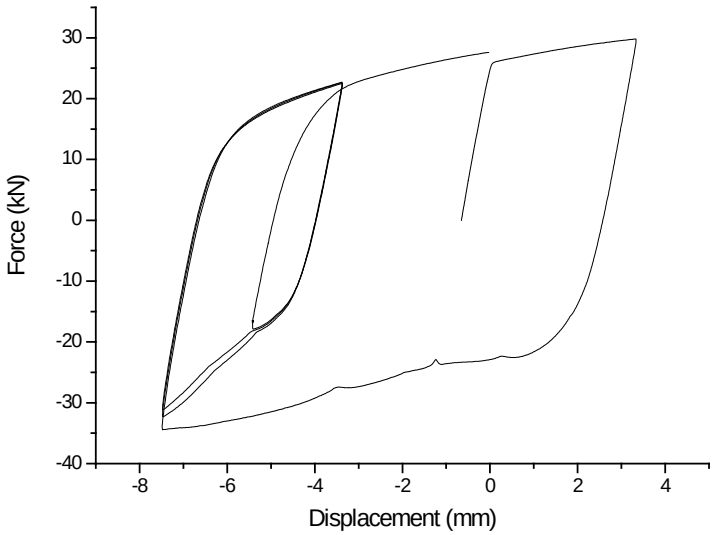

Figure 42. Hysteresis loops of dissipator SD4 for near-source cycles

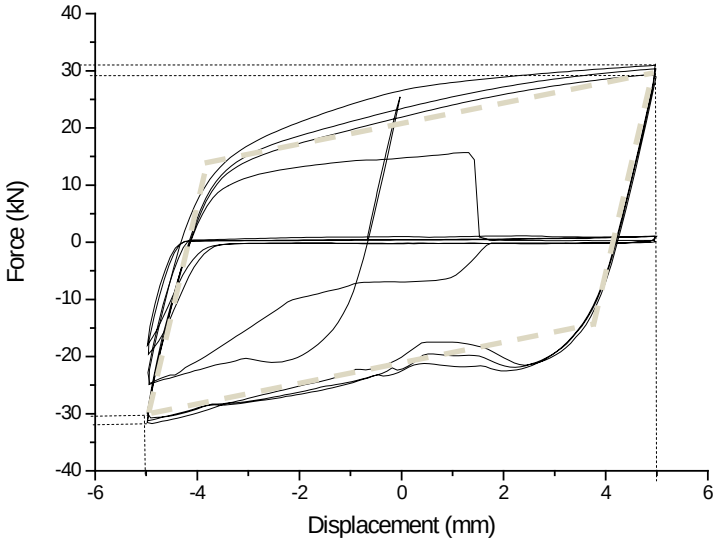

Figure 43. Hysteresis loops of dissipator SD4 for constant amplitude cycles

To facilitate the interpretation of Figure 43 some auxiliary lines have been drawn similarly to Figure 32.

Figure 41, Figure 42 and Figure 43 show, as expected, a regular hysteretic behavior. Minor failures (due to buckling of the core) are observed in the plastic compression branches (negative values of the force, see Table 4) like in dissipators SD1 and SD2; however, Figure 43 does not show relevant differences between the tension and compression peaks. At Figure 43 the final (premature) failure (by local buckling of the core leading to complete breakage as shown by Figure 48) came after 7 cycles and generated a sudden decrease in the compression force. Beyond these differences, comparison with the behavior of the dissipators SD1 (Figure 28, Figure 30, Figure 31 and Figure 32), SD2 (Figure 34, Figure 35 and Figure 36) and SD3 (Figure 38, Figure

39 and Figure 40)shows a high similarity.

4.7 Testing of dissipator SD5

This subsection lists the most relevant results for dissipator SD5. The test of this device had no particular circumstances. Failure came by local buckling of the core.

Figure 44, Figure 45 and Figure 46 show the hysteretic behavior (force vs. displacement) of dissipator SD5 for the three loading histories described by Figure 22, Figure 24 and Figure 27, respectively.

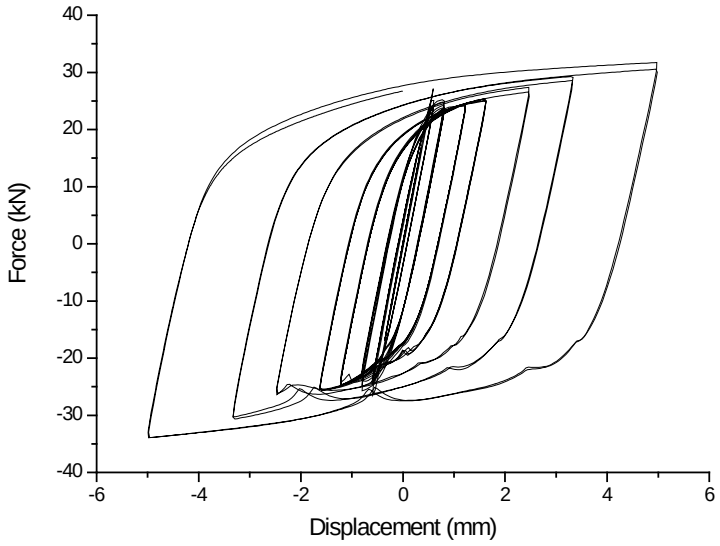

Figure 44. Hysteresis loops of dissipator SD5 for growing amplitude cycles

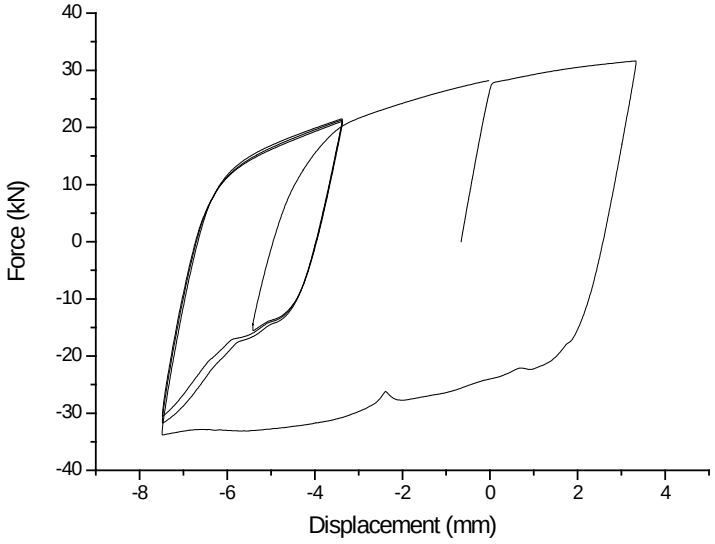

Figure 45. Hysteresis loops of dissipator SD5 for near-source cycles

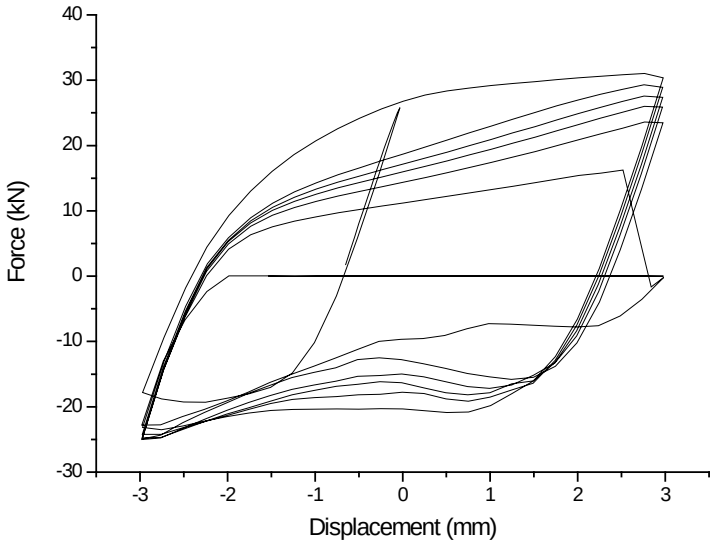

Figure 46. Hysteresis loops of dissipator SD5 for constant amplitude cycles

Figure 44, Figure 45 and Figure 46 show, as expected, a regular hysteretic behavior (except Figure 46). Minor failures (due to buckling of the core) are observed in the compression branches (negative values of the force, see Table 4). At Figure 46 the final failure by local buckling of the core (leading to complete breakage as shown by Figure 48) came after 7 cycles and generated a sudden decrease in the compression force. Beyond these differences, comparison with the behavior of the dissipators SD1 (Figure 28, Figure 30, Figure 31 and Figure 32), SD2 (Figure 34, Figure 35 and Figure 36), SD3 (Figure 38, Figure 39 and Figure 40) and SD4 (Figure 41, Figure 42 and Figure 43) shows a high similarity.

4.8 Summary of results

This subsection presents a summary of the results of tests for dissipators SD1, SD2, SD3, SD4 and SD5. Those results are listed in Table 6. Irregular values corresponding to behavior near or after failure are not accounted for.

At Table 6 the “Ductility ratio” is the quotient between the maximum and yielding displacements for each of the three loading histories (growing amplitude cycles / near field effects / constant amplitude cycles); as well the “Duration of the cycles” refers to them. Conversely, the “No. of cycles” refers only to the constant amplitude stage. The “Dissipated energy” is the sum of the areas encompassed by the three hysteresis loops (corresponding to the three aforementioned stages). Such value has been normalized with respect the elastic energy $\frac{1}{2}\, k\, \Delta_y^2$ where k is the initial stiffness and Δ_y is the yielding displacement; the values of these parameters have been taken alike for the five dissipators. The initial stiffness has been determined after Figure 28 as $k = 47.43$ kN/mm; the yielding displacement is given by Eqn. (20). The “Cumulative plastic ductility” [Black, Makris & Aiken, 2002] is a dimensionless normalized expression of the cumulative plastic deformation defined by

$$\Sigma \frac{\left|\Delta^{+} - \Delta^{-}\right|}{\Delta_y} \qquad \text{Eqn. (21)}$$

At Eqn. (21) Δ^{+} and Δ^{-} are the maximum and minimum values of the plastic displacement, respectively, and Δ_y is the yielding displacement. The sum is extended to all the plastic excursions.

Table 6. Main results of the tests of dissipators SD1, SD2, SD3, SD4 and SD5

Device	L_{di} (mm)	core size (mm × mm)	Tube	Tube filling	Ductility ratio	Duration of the cycles (s)	No. of cycles	Dissipated energy (-)	Cumulative plastic ductility
SD1	175	15.90 × 4.4	PVC	grouting	5.56 / 11.11 / 5.56	98 / 24 / 177	19	875	275.90
SD2	175	15.90 × 4.4	PVC	grouting	5.56 / 11.11 / 5.56	398 / 127 / 842	19	894	275.90
SD3	175	15.90 × 4.4	Steel	grouting	5.56 / 11.11 / 5.56	98 / 24 / 177	19	1016	275.90
SD4	175	15.90 × 4.4	Steel	mortar	12.92 / 19.64 / 12.92	227 / 50 / 50	7	1348	557.14
SD5	175	15.90 × 4.4	Steel	mortar	12.92 / 19.64 / 7.75	227 / 24 / 177	7	1228	501.3

After completing each experiment the tube and the mortar were split to examine the actual condition of the mortar and the core. Figure 47 shows the condition of the mortar of the devices SD4 and SD5 (those which failed) after removing the (external) tube.

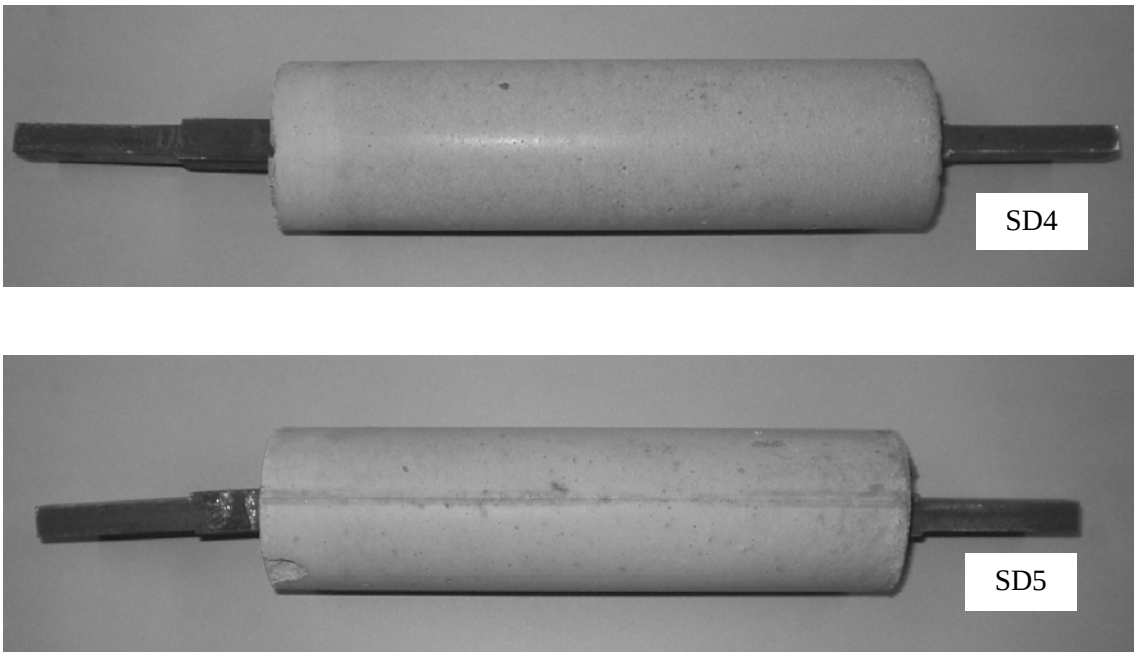

Figure 47. Mortar of dissipators SD4 and SD5 after test

Figure 47 shows no cracks in the mortar of the (broken) devices SD4 and SD5.

Figure 48 displays some views of the split mortar and of the cores of dissipators SD4 and SD5.

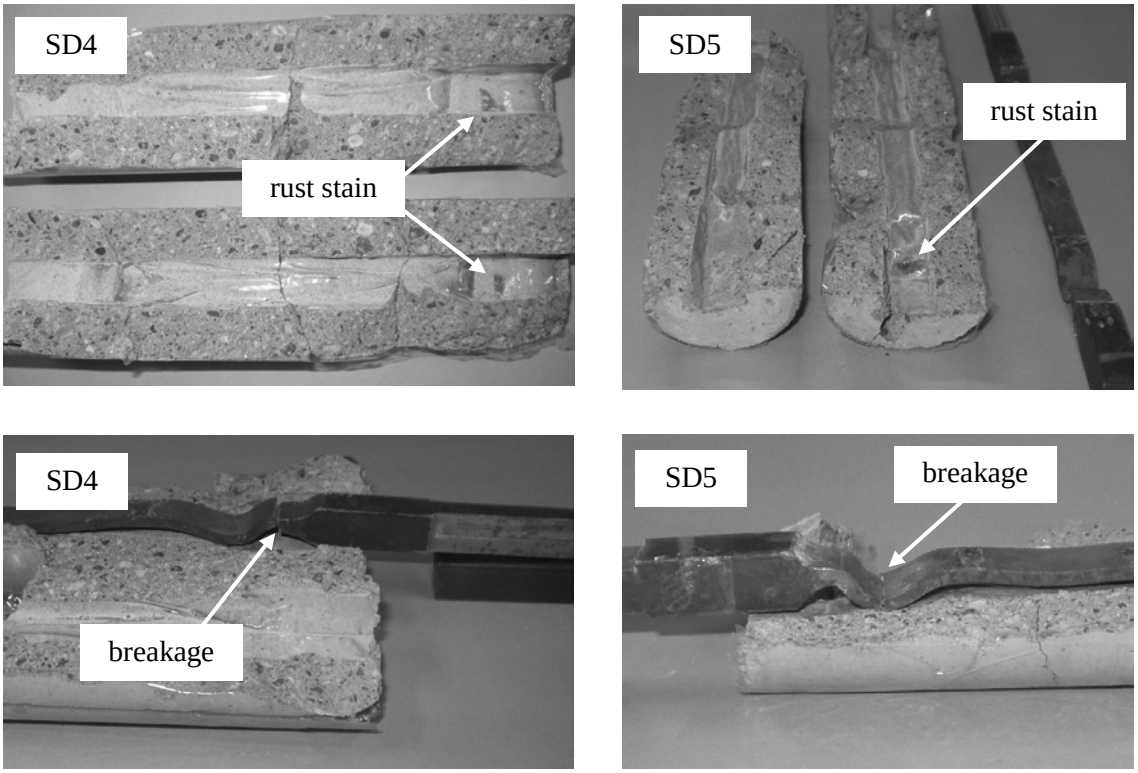

Figure 48. Mortar and cores of dissipators SD4 and SD5 after test

Images in Figure 48 show no cracks in the mortar; those that can be seen were originated during the splitting operation. As well, the surface in contact with the core was not damaged; the two bottom pictures show that the cores were broken due to big (bending) deformations in the zones with bigger gap (between the mortar and the core) because of the porexpan pads (see Figure 6). The core slid with respect to the casing, hence, one of the ends of the central segment of the core buckled inside a hole about 16×16 mm^2 wide; this fact is confirmed by the rust stains shown by the upper pictures in Figure 48.

Figure 49 displays a view of the conditions of the cores of dissipators SD1 to SD5 after the tests.

Images in Figure 49 show permanent deformations corresponding to high buckling modes (rippling, see Figure 15). In the vicinity of the transition zones (where the buckling is unrestrained) the amplitudes are larger; along the whole length of the dissipative zone the wave length is rather constant (about 50 mm). The maximum amplitudes are: 3.1 mm (SD1), 3.4 mm (SD2), 2.3 mm (SD3), 7.7 mm (SD4) and 8.4 mm (SD5). Figure 49 confirm that the failure of the devices SD4 and SD5 (see Figure 48, bottom) was produced by local buckling of the core. It is remarkable that the maximum deformation in dissipators SD4 and SD5 (those that failed, see Table 6) is significantly bigger than in SD1, SD2 and SD3. The comparison among the amplitudes in dissipators SD1, SD2 and SD3 (those which did not fail, see Table 6) shows that the devices with PVC tube (SD1 and SD2) deformed more than the one with steel tube (SD3). About the deformation out of the failure zone (left end of the central segment) it is noteworthy that the cores wrapped with thicker layers (SD2 and SD5) exhibit wider waves; it might allow concluding that to wrap the core with too thick layers is not convenient (since the gap is bigger).

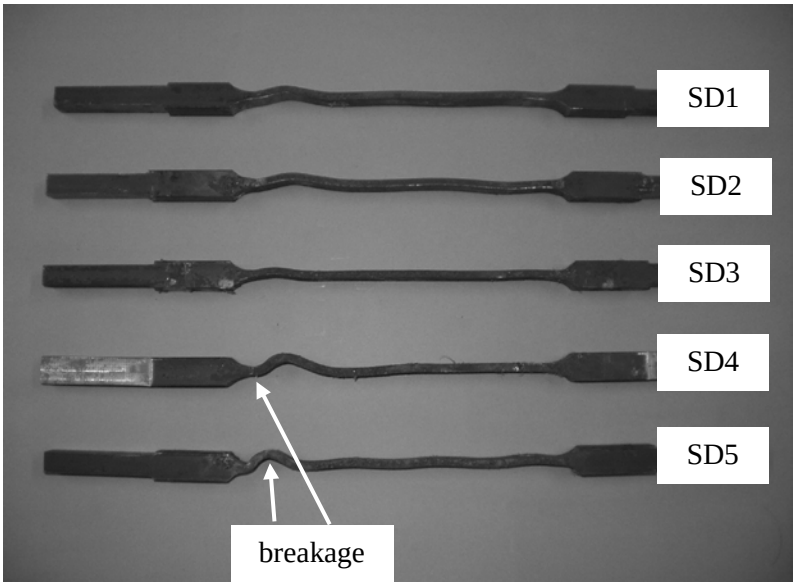

Figure 49. Cores of dissipators SD1, SD2, SD3, SD4 and SD5 after test

5 INDIVIDUAL EXPERIMENTS ON FULL SIZE PROTOTYPES

5.1 Characterization of materials

5.1.1 General description

The steel (of the core) and the mortar were also tested to characterize their most relevant parameters.

5.1.2 Characterization of the steel of the core

The characterization experiments about the steel of the core consisted of conventional tension tests (following [EN 10025, 2002]) on four specimens (coupon testing); two of them had (nominal) 10 mm diameter (termed CS10-1 and CS10-2, accounting for "Core Specimen") and the other two had (nominal) 22 mm diameter (termed CS22-1 and CS22-2). The lengths of each specimen were 230 mm (CS10-1 and CS10-2) and 210 mm (CS22-1 and CS22-2); such measures correspond to the distance among the centers of the parts encased by the jaws. An extensometer was incorporated to specimens CS10-1, CS10-2 and CS22-2 to obtain more accurate results to determine the yielding point and (mainly) the deformation modulus (only the results for specimens CS10-2 and CS22-2 were useful); the effective length of this element is 100 mm (distance between the centers of both ends of the extensometer).

Figure 50 displays three views of the testing rig for the core bars.

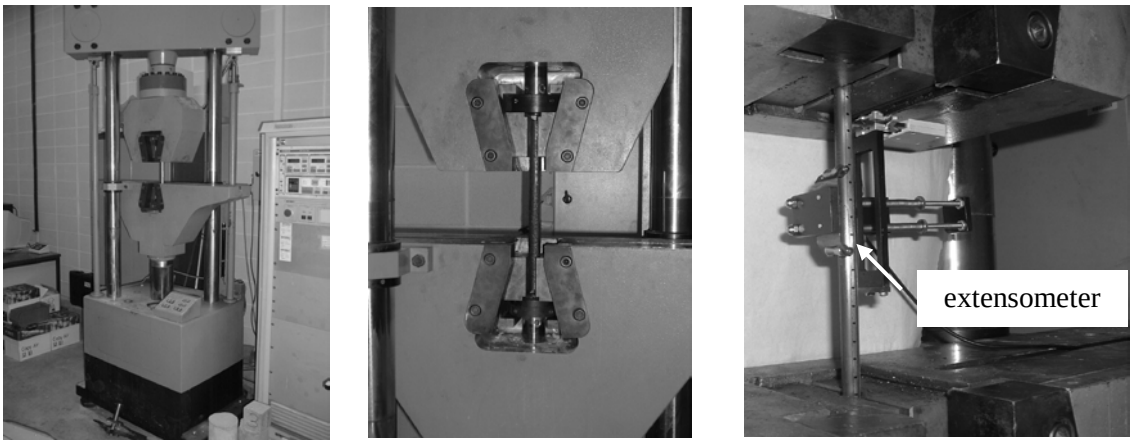

Figure 50. Testing of the steel core

Figure 50 contains three pictures. The left image shows the testing machine. The mid image displays the testing of a 22 mm specimen. The right image shows a 10 mm diameter specimen with the extensometer.

It is remarkable that accurate measurements of the actual diameters showed that the sections are not round and the average values are 10.275 mm (specimens CS10-1 and CS10-2) and 22.54 mm (specimens CS22-1 and CS22-2). These values have been considered next (instead of the nominal ones).

Figure 51 and Figure 52 display the stress-strain plots for the specimens with diameters 10 and 22 mm, respectively.

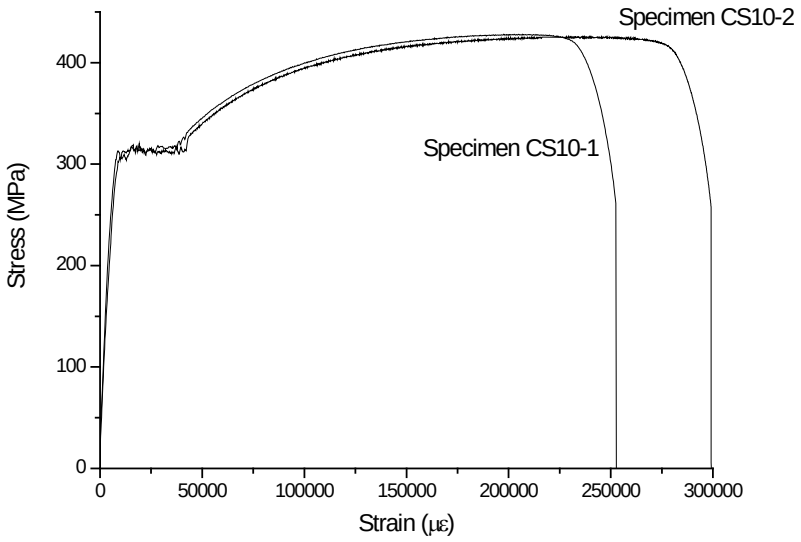

Figure 51. Stress-strain plots for the 10 mm core bar

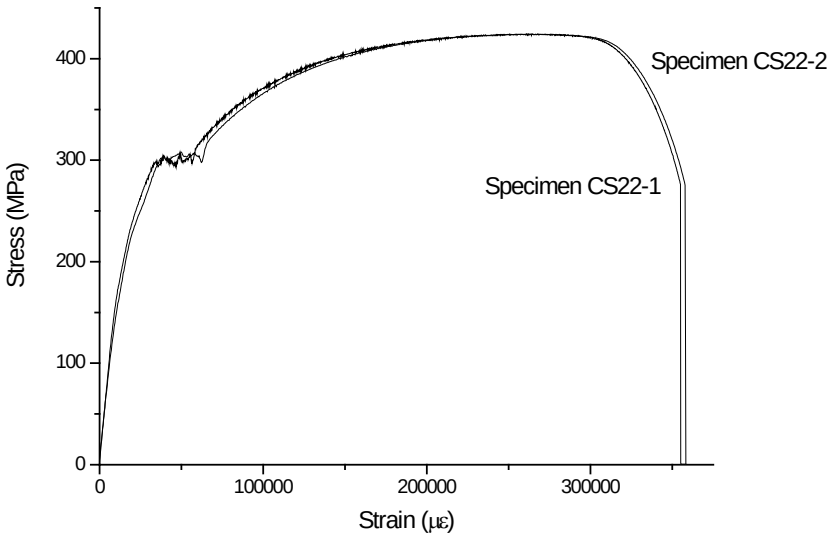

Figure 52. Stress-strain plots for the 22 mm core bar

The observation of Figure 52 shows that the elastic branch is nonlinear; this fact, rather than showing a nonlinear elastic behavior, indicates relevant slides in the jaws. It confirms that the deformation modulus can only be measured with the additional extensometer (see Figure 50, right).

Figure 53 and Figure 54 display the additional stress-strain plots obtained from the extensometers for specimens with diameter 10 and 22 mm, respectively.

The main results of these characterization experiments are shown in Table 7. f_y is the yielding point, E_{co} is the deformation modulus and f_u and ε_u are the ultimate stress and strain, respectively;

f_u and ε_u correspond to the maximum value of the stress-strain plot. It is remarkable that the slides in the jaws impair the accuracy and reliability of ε_u.

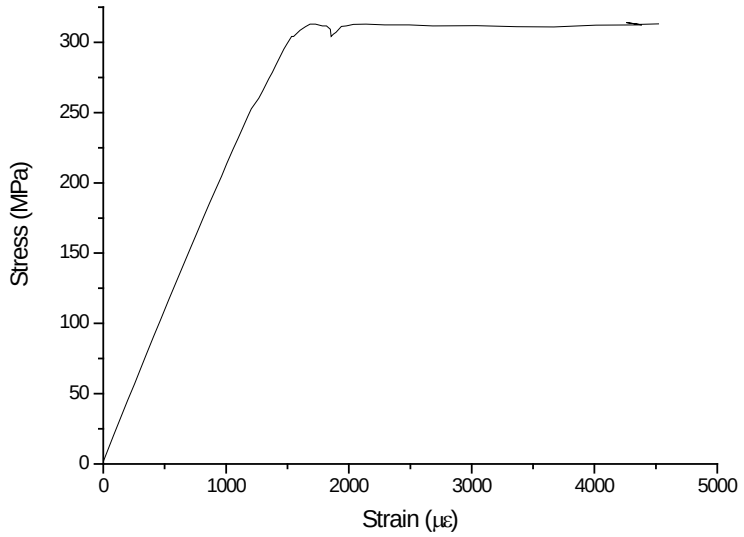

Figure 53. Stress-strain plots from the extensometer for the 10 mm core bar (CS10-2)

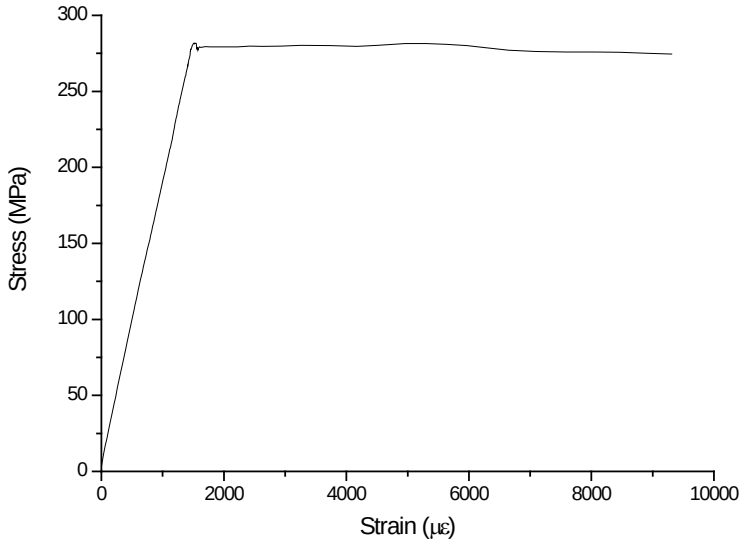

Figure 54. Stress-strain plots from the extensometer for the 22 mm core bar (CS22-2)

In Table 7 the yielding point and the ultimate stress and strain have been obtained from the main stress-strain plots (Figure 51 and Figure 52) and the deformation modulus has been determined from the extensometer measurements (Figure 53 and Figure 54).

Table 7. Measured parameters of the steel of the core

Specimen	f_y (MPa)	f_u (MPa)	ε_u (10^{-3})	E_{co} (GPa)
CS10-1	306	425.96	240	-
CS10-2	308	428.01	207	210.91
CS22-1	298	423.79	262	-
CS22-2	303	423.47	264	186.31

Results from Table 7 show some relevant differences of the yielding points f_y with the nominal value (f_y = 275 MPa) and a slightly better fit with the nominal ultimate strength (f_u = 410 MPa) [EN 10025, 2002]. It should be kept on mind that the nominal values are characteristic ones; for this reason all the values in Table 7 are bigger. It is apparent that the parameters of the 10 mm and 22 mm bars are (slightly) different each other; conversely, less scattering is found among bars with the same diameter. The value of the deformation modulus for dissipator CS22-2 is feasible (agrees with the ordinarily assumed value) but the one for dissipator CS10-2 is generated by slide of the extensometer (see the right image in Figure 50).

5.1.3 Characterization of the mortar

The experiments about the mortar consisted of compressive testing of two specimens cut from the (previously tested) dissipators D1 and D3 (coupon testing); they are termed next MSD1 and MSD3, respectively (accounting for “Mortar Specimen of Dissipator”). The specimen MSD1 has outer and inner diameters 84 and 14 mm, respectively; the section area is $\pi \times (42^2 - 7^2) = 5388$ mm^2. The specimen MSD3 has outer and inner diameters 109 and 26 mm, respectively; the section area is $\pi \times (54.5^2 - 13^2) = 8800$ mm^2. According to European regulations [EN 206-1, 2000] the lengths of both specimens are two times their diameters (i.e. 168 mm and 218 mm for specimens MSD1 and MSD3, respectively).

The test of specimen MSD1 consisted merely of obtaining the compressive strength; for specimen MSD3 the deformation modulus was also determined. These tests were carried out at the Laboratory of Construction Technology of the Technical University of Catalonia (Barcelona) by 11th August 2006.

Figure 55 displays the testing rig for specimen MSD3 and an image of the broken specimen (after failure).

The left picture in Figure 55 shows the specimen mounted on the testing machine; two rigid steel rings are fixed to the specimen to allow for the installation of displacement transducers to determine the deformation modulus.

The obtained compressive strengths were f_c = 41.59 MPa for Specimen MSD1 (the force was 224.09 kN) and f_c = 38.24 MPa for Specimen MSD3 (the force was 336.53 kN). These values, yet high, are slightly lower than the expectable strength (45-50 MPa).

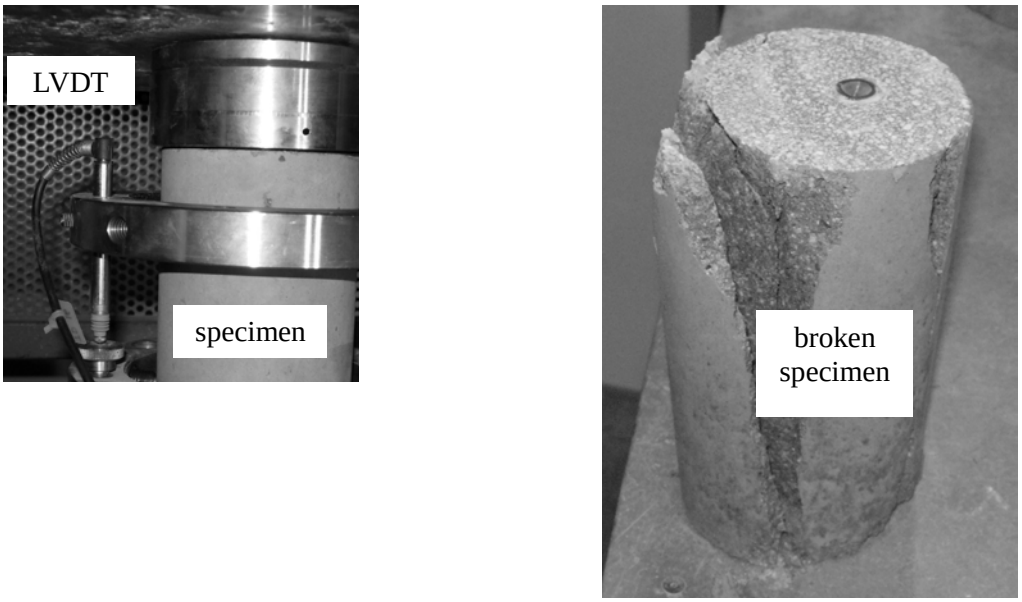

Figure 55. Testing of the specimen MSD3

As discussed previously the deformation modulus was determined from the registers of three displacement transducers (LVDTs) connected to two rigid steel rings fixed to the specimen as shown by the left image in Figure 55. The distance between the centers of both steel rings is 7.5 cm. As only two LVDTs were available (instead of three, as would be desirable) two loading tests were carried out: in the first proof the two displacement transducers were installed as shown by the left image in Figure 55 while in the second proof just one device was connected in the remaining position. To determine the deformation modulus, the average stress (between those in the two proofs) is plotted against the average strain (between the three LVDTs). Such plots are represented in Figure 56.

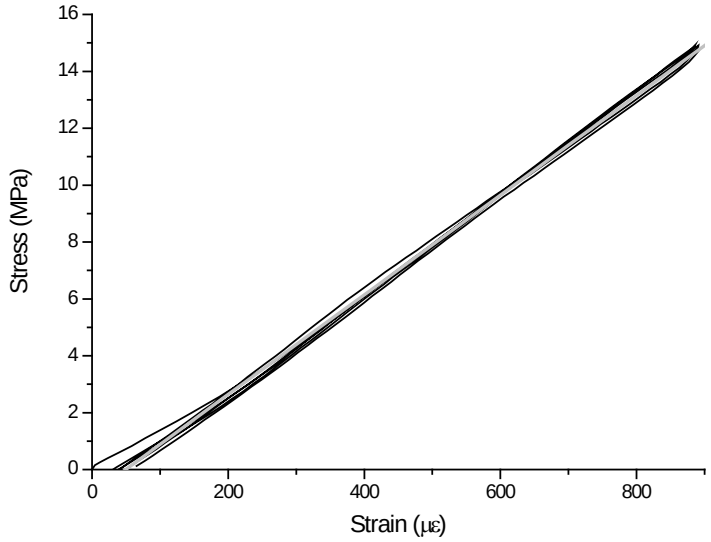

Figure 56. Stress-strain relationship for specimen MSD3

Figure 56 shows the aforementioned stress-strain plots (thin black) and the straight line that fits them best (thick grey). The obtained deformation modulus (slope of this line) is E_m = 17.52 GPa.

The main results of these characterization experiments are shown in Table 8.

Table 8. Measured parameters of the mortar

Specimen	f_m (MPa)	E_m (GPa)
MSD1	41.59	-
MSD3	38.24	17.52

5.2 Testing of dissipators

The four (full size) prototypes have been tested along July 2006 in the University of Girona, Spain. The experiments have consisted of cycling axial loading until failure (individual testing).

The objectives of the tests are (i) to assess the performance of the proposed devices (to validate their design and to investigate their energy dissipation capacity under a certain ductility demand), (ii) to learn deeply about their structural behavior, (iii) to characterize their hysteretic behavior and (iv) to obtain a wide set of experimental results that might be useful to calibrate the numerical models (to be developed). The experiments were designed to reach these goals.

Dissipators D1, D2, D3 and D4 underwent cyclic loading tests until failure. They were placed horizontally, fixed by one of their ends while the other end was connected to a hydraulic jack. Figure 57 contains a sketch (plan view) of the testing rig.

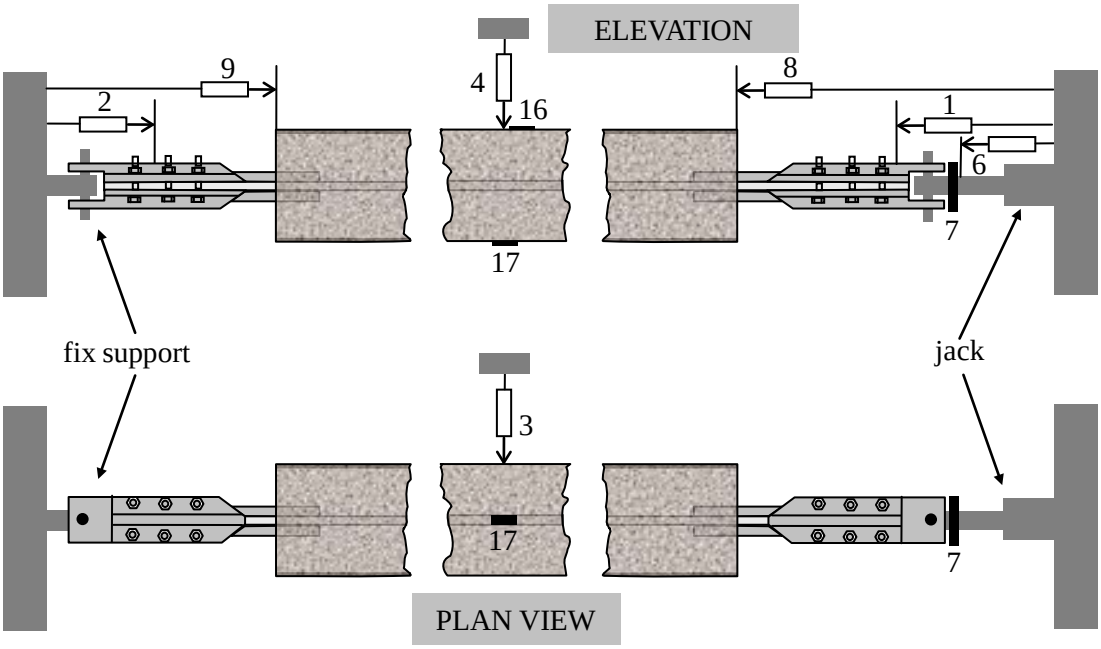

Figure 57. Testing rig for dissipators D1, D2, D3 and D4

It is remarkable that the dissipators were tested horizontally in spite that for real applications they are placed as diagonal or chevron braces (see Figure 1). Since the bending generated by the self weight is not relevant, this difference is not considered important.

Figure 58 displays four views of the testing rig for dissipator D1.

Figure 58 contains three pictures. The upper image depicts a side global view of the testing rig with the fix support on the left and the moving hydraulic jack on the right; the slings on the mid section on the dissipator were placed only for safety reasons (avoiding sudden fall of the device). The lower left image shows only a side view of the central portion of the tube. It is remarkable that the upper and lower right pictures do not show the displacement transducers placed to measure the transverse displacements at the mid section of the tube; they are only shown in the lower left picture. Such image has been taken from the rear of the jack and shows a longitudinal view of the dissipator.

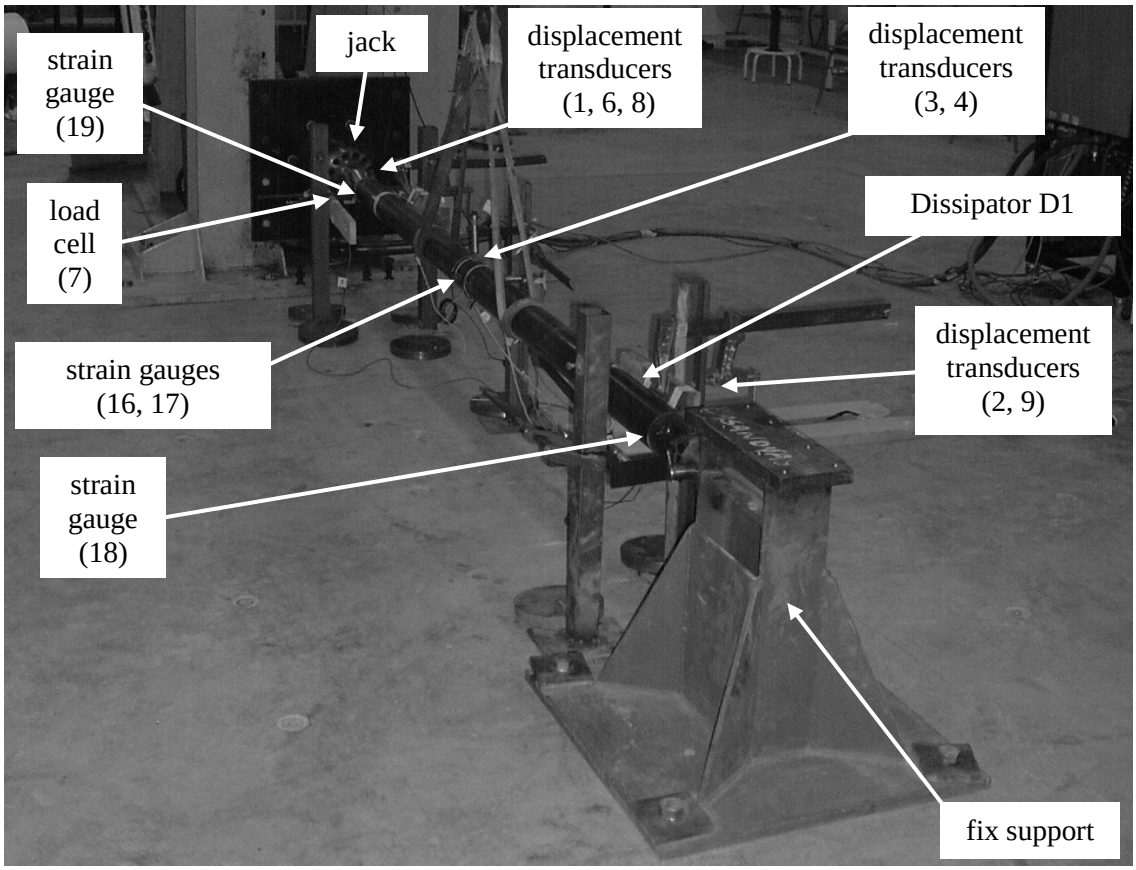

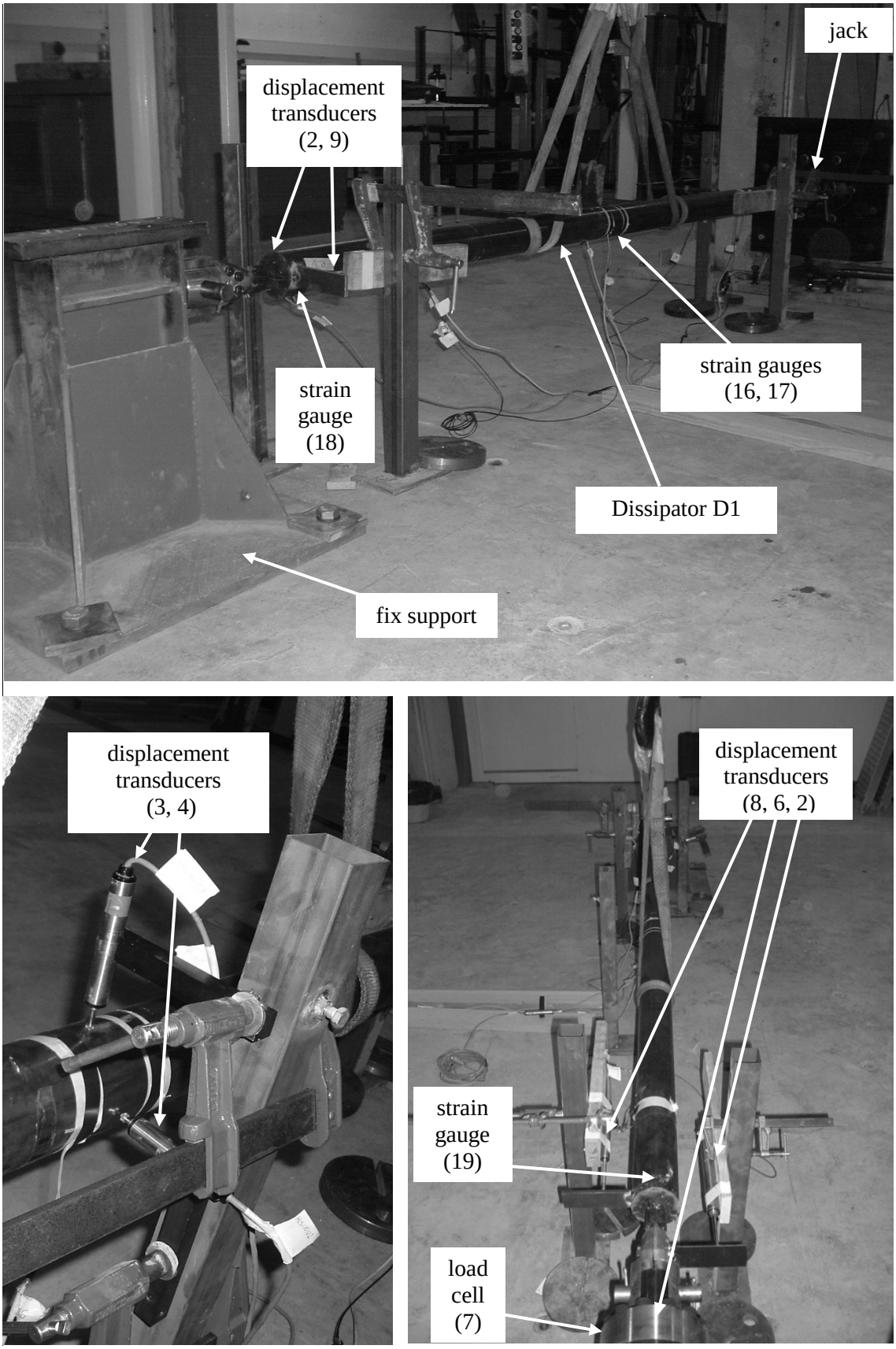

Figure 58. Cyclic testing of dissipator D1

Table 9. Registered magnitudes on the experiments on prototypes

Channel No.	Magnitude	Sensor	Units	Range	Positive sign
1	Right connector displacement	Displacement transducer (APEK HLS-100)	mm	100	Left (in)
2	Left connector displacement	Displacement transducer (APEK HLS-25)	mm	25	Right (in)
3	Mid section vertical displacement	Displacement transducer (APEK HLS-25)	mm	25	Up
4	Mid section transverse displacement	Displacement transducer (APEK HLS-10)	mm	10	Front (come)
6	Displacement of Servo-controlled Actuator	Displacement transducer (Novotechnik LWH-300)	mm	350	Left (out)
7	Actuator axial force	Load cell (AEP TC4/50t)	kN	500	Compression
8	Right section longitudinal displacement (tube)	Displacement transducer (Solartron VS 50 GU)	mm	50	Left (in)
9	Left section longitudinal displacement (tube)	Displacement transducer (Solartron VS 50 GU)	mm	50	Right (in)
16	Mid section longitudinal strain (front)	Strain gauge	με	$\approx \pm 6 \times 10^4$	Elongation
17	Mid section longitudinal strain (rear)	Strain gauge	με	$\approx \pm 6 \times 10^4$	Elongation
18	Left section longitudinal strain	Strain gauge	με	$\approx \pm 6 \times 10^4$	Elongation
19	Right section longitudinal strain	Strain gauge	με	$\approx \pm 6 \times 10^4$	Elongation

Figure 58 shows that the registered magnitudes (at each test) were: axial force in the jack (measured by a load cell, sensor 7), displacement of the jack (measured by a displacement transducer with range 350 mm, sensor 6), longitudinal displacements of the connectors (measured by displacement transducers with ranges 25 and 100 mm, sensors 2 and 1, respectively),

longitudinal displacements of the end sections of the tube (measured by displacement transducers with ranges 50 mm, sensors 8 and 9), transversal horizontal and vertical displacements of the mid section of the tube (measured by displacement transducers with ranges 25 mm in the vertical direction and 10 mm in the horizontal one, sensors 3 and 4, respectively) and axial strains of the tube (measured by two strain gauges fixed opposite each other at a section near the mid of the tube, sensors 16 and 17). Moreover, at dissipator D1 two additional strain gauges were fixed near the end sections of the tube (sensors 18 and 19). Gauges 16 and 17 were placed at opposite ends of a horizontal diameter of a cross section as to be able to obtain the axial forces and (horizontal) bending moments in such section. Table 9 summarizes this information.

At Table 9 the left/right indications correspond to those in Figure 57 and in the upper picture in Figure 58 (from the desk governing the tests). Last column indicates the criteria of signs for the measurements; “out” means the jack is going out, “in” means the jack is coming in and “come” means the device is moving (transverse horizontally) towards the computer governing the experiments (i.e. approaching the camera according to Figure 58, up and low left).

Like in the experiments on the short dissipators (at Argentina), the time was also recorded but it is not considered relevant as the behavior of the dissipator is assumed to be rather rate-independent (for the range of considered velocities).

The imposed displacements were similar for the four prototypes and consisted of two consecutive phases: (i) a series of growing-amplitude cycles and (ii) constant-amplitude cycles until failure. The first phase consists of five pairs of cycles with (approximate) semi-amplitudes 0.25 Δ_y, 0.50 Δ_y, 0.75 Δ_y, 1.00 Δ_y and 2.50 Δ_y, respectively; Δ_y is the yielding displacement. In the second phase the amplitude is (approximately) 5 Δ_y; it means that the final ductility demand on the dissipator is five. The values of Δ_y have been initially estimated as 3.83 mm for dissipators D1 and D2 and 3.37 mm for dissipators D3 and D4. Since the yielding point for the 22 mm bars is slightly smaller than the one for the 10 mm, the actual ductility demands on them are bigger (see Table 10). Figure 59 displays the first fifteen loading cycles (imposed displacements) for dissipators D1 and D2 (for dissipators D3 and D4 the sequence is alike in spite the amplitudes are slightly smaller as discussed previously).

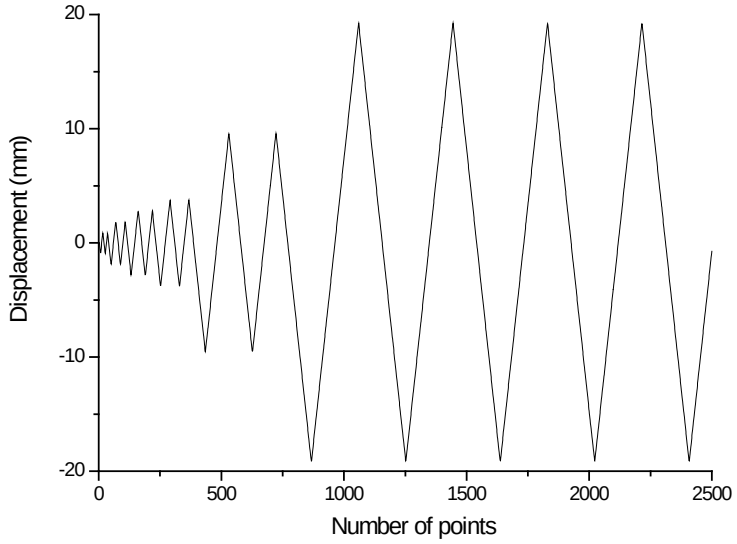

Figure 59. Initial loading cycles of dissipators D1 and D2 (channel 6)

At Figure 59, positive values (in the vertical axis) correspond to elongation.

Conversely to the short dissipators (see Figure 21, Figure 22, Figure 23, Figure 24, Figure 25, Figure 26 and Figure 27), these loading histories are more intended to evaluate the energy dissipation capacity of the devices rather than to investigate the performance for strong seismic inputs.

All the tubes were filled with mortar by 10th July; dissipator 1 was tested 21st July, dissipator 2 was tested 24th July and dissipators 3 and 4 were tested 26th July.

Next subsections display some pictures and the experimental results from the tests (of the four prototypes) carried out at the laboratory of the University of Girona. The main conclusions arisen from these plots are stated. It should be kept in mind that the order of the experiments was: D1, D2, D4 and D3; however, for the sake of understandability, they are presented here in "growing" (natural) order: D1, D2, D3 and D4.

5.3 Testing of dissipator D1

5.3.1 Testing remarks

This subsection lists the most relevant results for dissipator D1. The test of this device had no particular circumstances. Failure came by breaking of the steel core near the central section after 160 cycles (see Table 10).

The testing rig is described by Figure 58. Figure 60 displays the displacement transducers used to register the displacements.

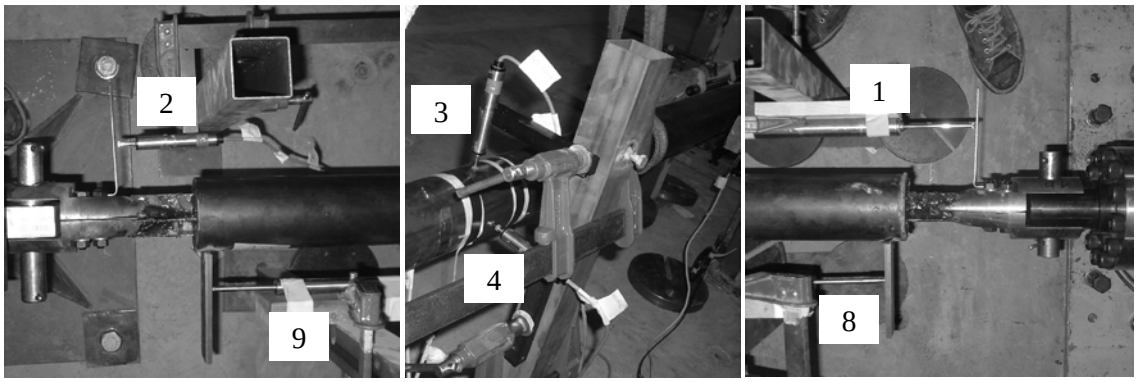

Figure 60. Displacement transducers for dissipator D1

Figure 60 contains three pictures, the left one corresponds to the fix (left) support, the mid one represents the mid portion of the tube and the right one shows the connection with the jack. The information in Figure 60 is complementary of the one in Figure 58.

5.3.2 Testing results for dissipator D1

The most relevant plots are displayed in this subsection. In all the figures, positive values correspond either to elongation (for strain gauges and displacement transducers) or to tension (for the load cell).

Figure 61 shows the time history elongation of the steel core (as measured by channels 1 and 2, see Table 9 and Figure 58) of the dissipator D1.

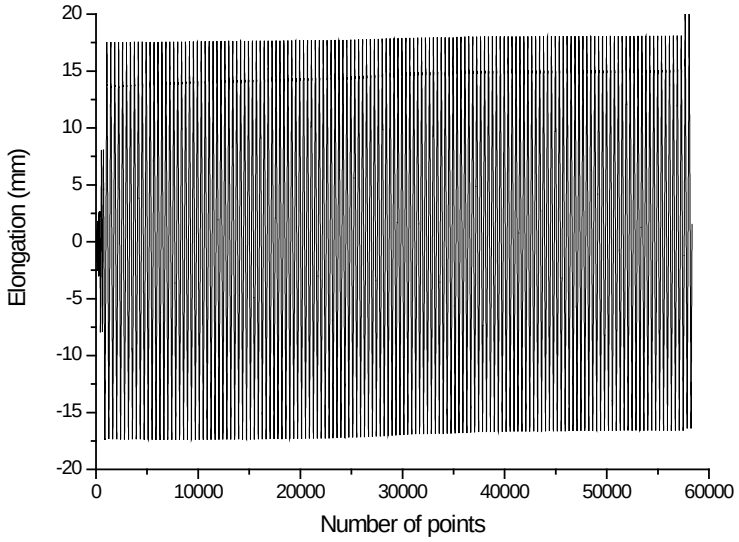

Figure 61. Core elongation for dissipator D1 (channel 1 + channel 2)

Figure 61 shows a rather regular behavior; it confirms the usefulness of the measures taken by these displacement transducers. There is a moderate drift; it is generated by the influence of the rotations (with respect to vertical axis, see Figure 60 left and right) in both ends of the dissipator.

Since a big number of points are involved in Figure 61 (58344), only global conclusions can be drawn. To obtain more precise deductions, two shorter intervals are plotted individually: the initial cycles (1:200) in Figure 62 and a number of cycles (corresponding to the stationary phase of the test) in Figure 63. To assess the feasibility of the displacement measured by the displacement transducer in the jack (channel 6, see Table 9 and Figure 58), such information is also included in these Figures.

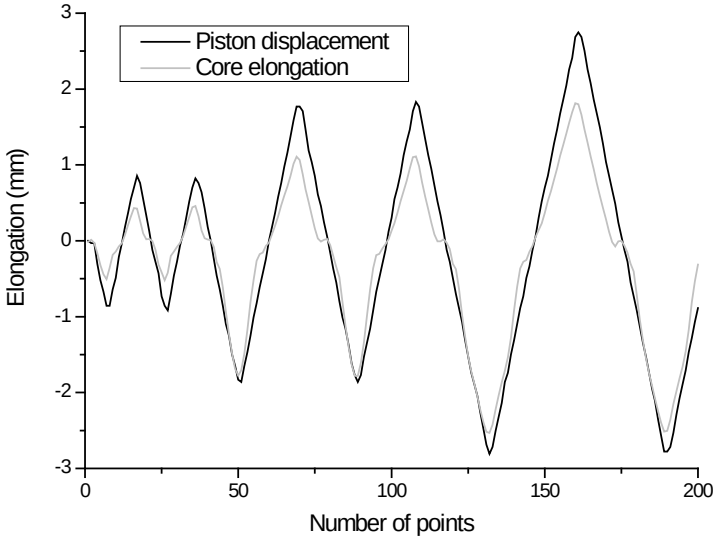

Figure 62. Core elongation for dissipator D1 (channel 1 + channel 2 and channel 6). Initial cycles

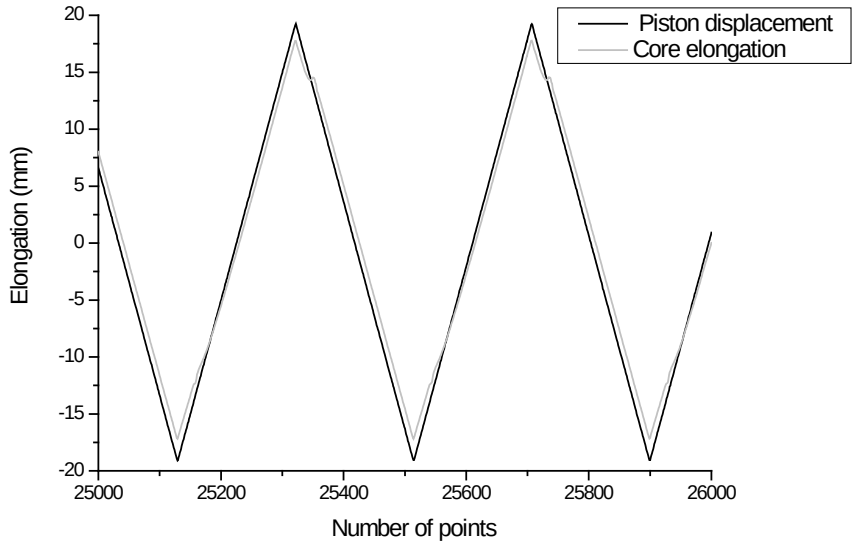

Figure 63. Core elongation for dissipator D1 (channel 1 + channel 2 and channel 6). Mid cycles

The observation of Figure 62 and Figure 63 allows deriving some relevant conclusions:

- Every time the force (in the jack) reverts, the plot of the core elongation (channel 1 + channel 2) exhibits a near horizontal jump (the jack keeps moving but the core does not elongate). This is due to the gap in the pin-joint connections between the dissipator and the end supports (see Figure 57 and Figure 58). At Figure 62 such jumps correspond also to the changes of sign of the jack displacement since the plastification has not yet initiated. Both in Figure 62 and Figure 63, at each cycle the “first” jump (when the force goes from compression to tension) is smoother than the “second” one (when the force goes from tension to compression).
- The jack displacement (channel 6) is bigger than the core elongation (channel 1 + channel 2). This difference is due to the abovementioned gap and to the flexibility of the interposed elements (end connections, supports, etc.). This last is particularly evident by observing the loading branches in the tension domain (without buckling, obviously) in Figure 62: the slopes of both plots are clearly different while they should be near alike.

This last effect is corrected by reducing the slope (in the tension domain) of the measurements from channel 6 (as to match the slope of the loading tension branch of channel 1 + channel 2): the channel 6 is replaced by channel 6 - channel 7 / 15.175 where 15.175 accounts for the stiffness (kN / mm) of the interposed elements. The arising measurement is termed as channel 6’. Figure 64 and Figure 65 show the same plots than Figure 62 and Figure 63 where the channel 6 has been replaced by the channel 6’. The comparison between Figure 64 and Figure 65, by one side, and Figure 62 and Figure 63, by the other side, shows a significantly better agreement between the jack displacement and the core elongation; such fit is particularly tight for the cycles belonging to the stationary phase (Figure 65). Consequently, channel 6’ is used next (instead of channel 6) in relevant plots. It is remarkable than in Figure 65 the corrected jack displacement (channel 6’) is still slightly bigger than the core elongation (channel 1 + channel 2) because of the influence of the abovementioned gap in the end connections.

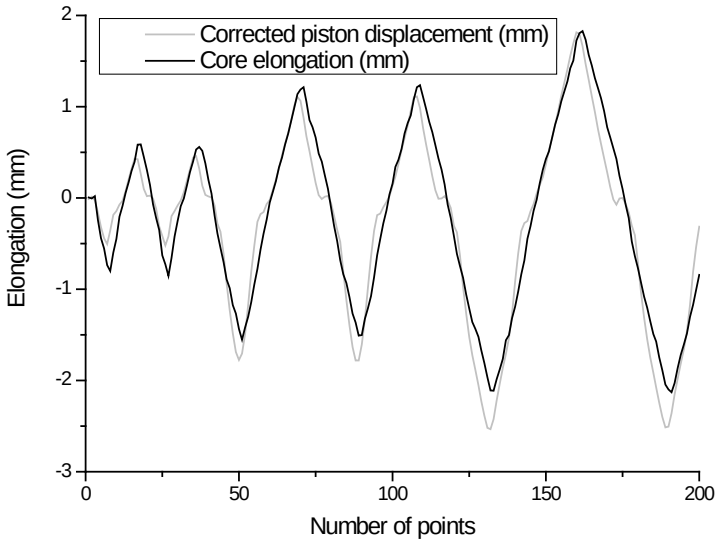

Figure 64. Core elongation for dissipator D1 (channel 1 + channel 2 and channel 6'). Initial cycles

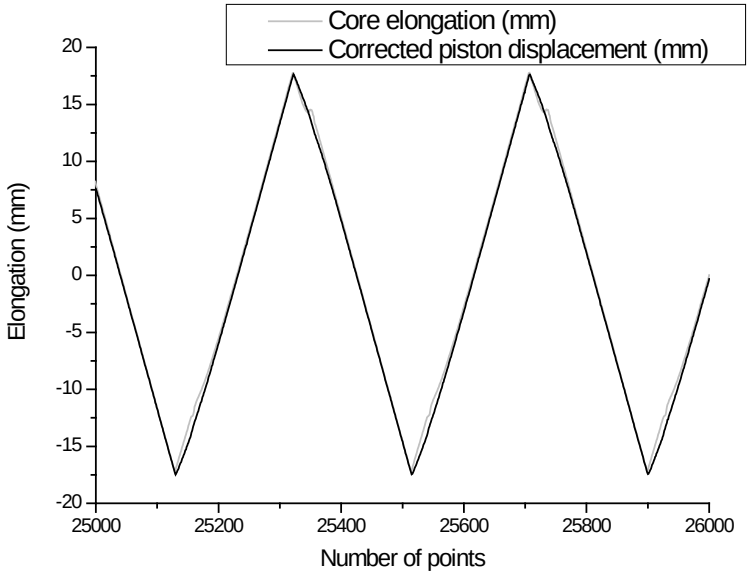

Figure 65. Core elongation for dissipator D1 (channel 1 + channel 2 and channel 6'). Mid cycles

Figure 66 displays the time history of the jack force (for dissipator D1) as measured by channel 7. Plots in Figure 66 show a rather stable hysteretic behavior. Once the maximum amplitude displacement is reached (after about point 850, see Figure 59), the force amplitude tends to decrease rather smoothly until reaching a stationary value (after about point 8000). This is due to a progressive detachment from the inner core and the surrounding mortar. In this stationary phase the maximum positive values (tension, about 25.30 kN) are significantly smaller than the minimum negative ones (compression, about 27.15 kN). This difference can be explained by the contribution of the mortar through the friction forces generated during the compression (when the core tries to buckle against the mortar).

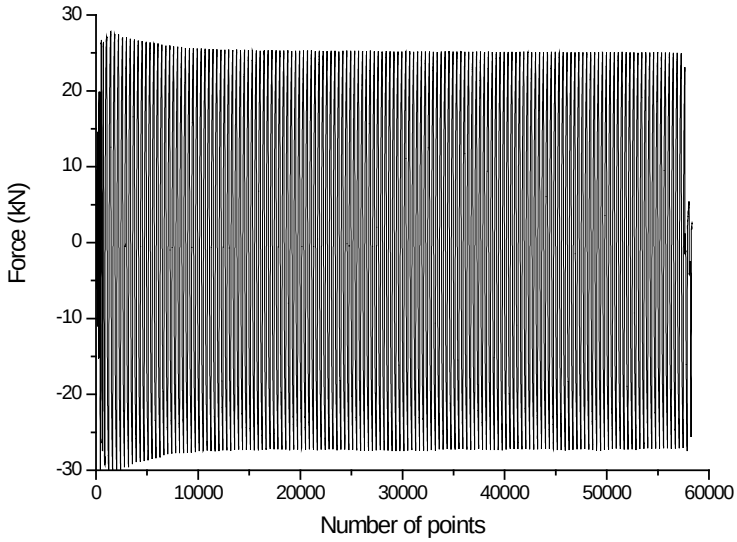

Figure 66. Jack force for dissipator D1 (channel 7)

Since a big number of points are involved in Figure 66 (58344), only global conclusions can be drawn. To obtain more precise deductions, two shorter intervals are plotted individually: the initial cycles in Figure 67 and a number of cycles (corresponding to the stationary phase of the test) in Figure 68.

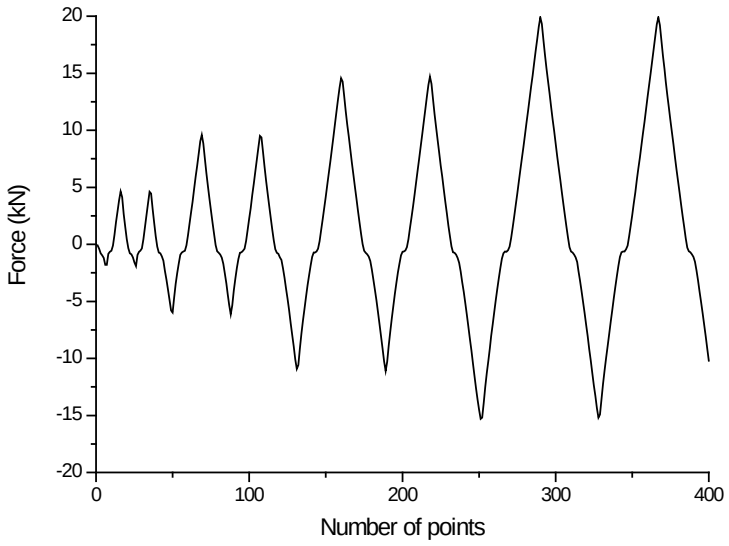

Figure 67. Jack force for dissipator D1 (channel 7). Initial cycles

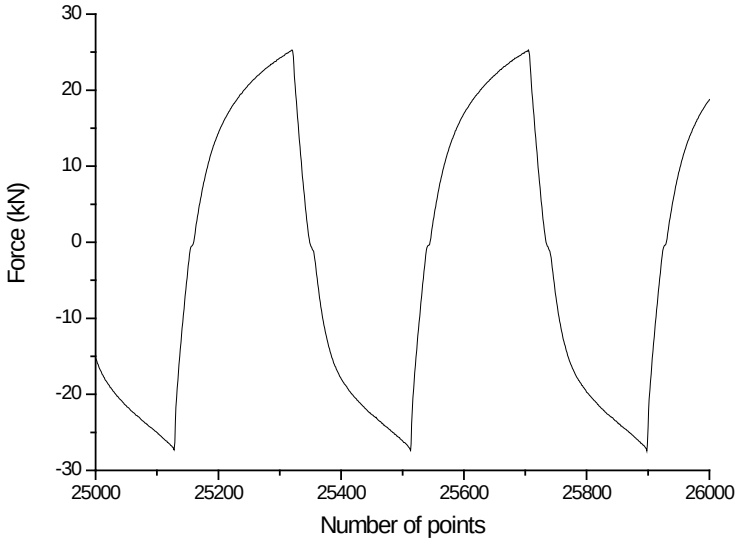

Figure 68. Jack force for dissipator D1 (channel 7). Mid cycles

The observation of Figure 67 and Figure 68 allows deriving some relevant conclusions:

- Every time the force (in the jack) reverts, the plot of the core elongation (channel 7) exhibits a near horizontal jump (the jack keeps moving without any force change). This is due to the gap in the pin-joint connections between the dissipator and the end supports (see Figure 57 and Figure 58). This fact was also observed from Figure 62 and Figure 63.
- The buckling of the core does not affect the force plots.
- In Figure 68 the last segment of the compression (plastic) loading branches exhibit a rather sudden increase leading to a higher peak and a reversal in the curvature. This is due to the mortar contribution and confirms the conclusion derived from Figure 66.

Figure 69 shows the hysteretic behavior (jack force -Channel 7- vs. jack displacement -Channel 6-, see Table 9 and Figure 58) of the dissipator D1.

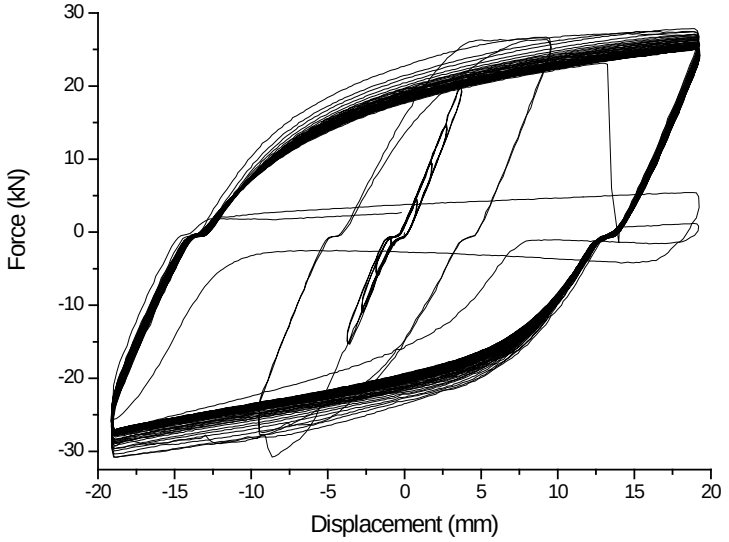

Figure 69. Hysteresis loops for dissipator D1 (channel 7 vs. channel 6)

For a proper interpretation of the plots in Figure 69 (and in other similar figures shown next in this section) it should be kept in mind that positive values of force correspond to tension while positive values of displacement correspond to elongation. It implies that the loops in Figure 69 are described clockwise.

Plots from Figure 69 show a quite stable hysteretic behavior along the whole number of cycles (160). The loops are (roughly) shaped like most of the dissipators based on plastification of metals (see Figure 29) but all the loops exhibit two near horizontal portions in the middle of the elastic left and right branches; they correspond to changes in the sign of the forces and are generated by slides in the connections between the dissipator and the support (left end) and between the dissipator and the jack (right end). In real applications these slides must be avoided (or, in least, strongly diminished) since they increase the "free run", i.e. the value of the interstory drift prior to the onset of yielding (and of dissipation of energy).

The irregular loops correspond to the beginning of the test (see Figure 59) and to its final part (near failure). To confirm this fact Figure 70, Figure 71 and Figure 72 show the cycles in Figure 69 split in three parts: first irregular cycles (Figure 70, points 1 to 1250), stable (regular) intermediate cycles (Figure 71, points 1251 to 57449) and last irregular cycles (Figure 72, points 57500 to 58344).

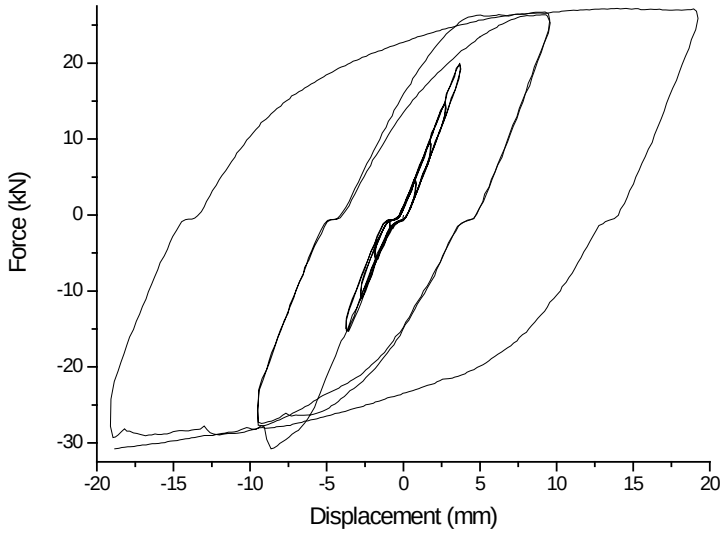

Figure 70. First hysteresis loops for dissipator D1 (channel 7 vs. channel 6)

Figure 70 depicts rather regular (growing) loops. In Figure 70 some minor jumps are observed in the plastic compression branches (generated by the buckling of the core, similarly to the short devices SD1 -Figure 32-, SD2 -Figure 36-, SD3 -Figure 40-, SD4 -Figure 43- and SD5 -Figure 46-).

To facilitate the interpretation of Figure 71 some auxiliary lines have been drawn, similarly to Figure 32. The wide dash (grey) lines correspond to an ideal bilinear hysteresis loop (see Figure 29) with parallel branches; this loop is intended to fit the inner registered loops (the slope of the plastic branches has been selected as to match the compressive one as it is more linear than the tension one as discussed next).

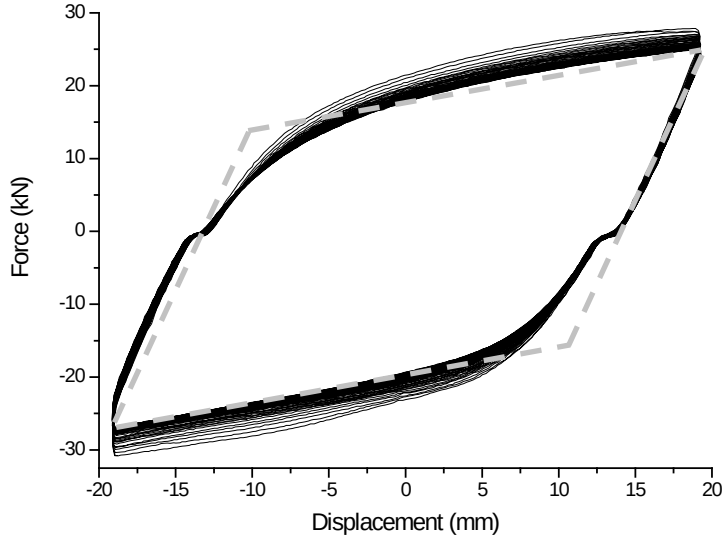

Figure 71. Regular hysteresis loops for dissipator D1 (channel 7 vs. channel 6)

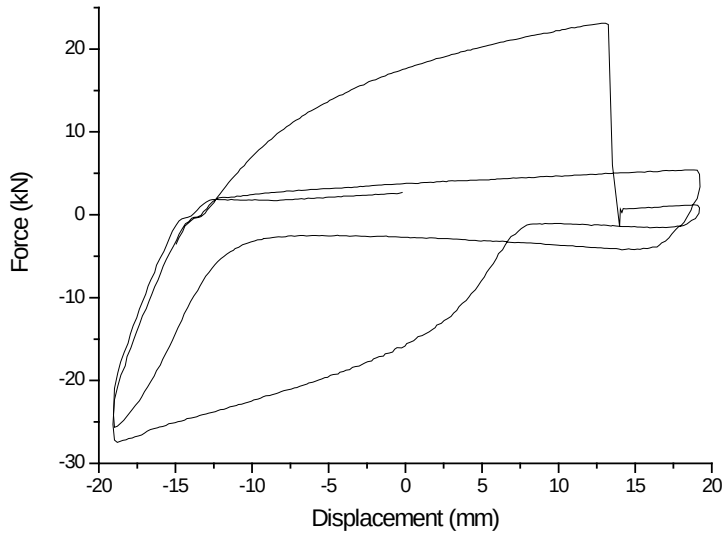

Figure 72. Last hysteresis loops for dissipator D1 (channel 7 vs. channel 6)

The following trends can be observed from Figure 71:

- As shown by Figure 66, the hysteretic behavior is stable. The force amplitude decreases after the first cycles but tends to stabilize quite fast.
- As shown by Figure 68, the lower plastic branch (compression) is more linear and steeper than the upper one (tension); the compression peaks are higher than the tension ones. In fact, the tension behavior is more regular (it is due to the Bauschinger effect [Akiyama, 1980]) while the compression is affected by the mortar contribution (mostly near the peak).
- The horizontal jump due to the gap in the connections that was detected from Figure 68 can be also observed.

Figure 73 displays the stress-strain plots from Figure 53 (for the steel specimen CS10-2) and the hysteresis loops for dissipator D1 (Figure 71) corresponding to the first part of the test after

eliminating the last irregular cycles. The strains for the dissipators have been obtained by dividing the relative displacement between both ends of the core (channel 6') by the length L_{di} (2466 mm) of the core in between both (end) connectors (see Figure 3, Table 1 and Figure 57).

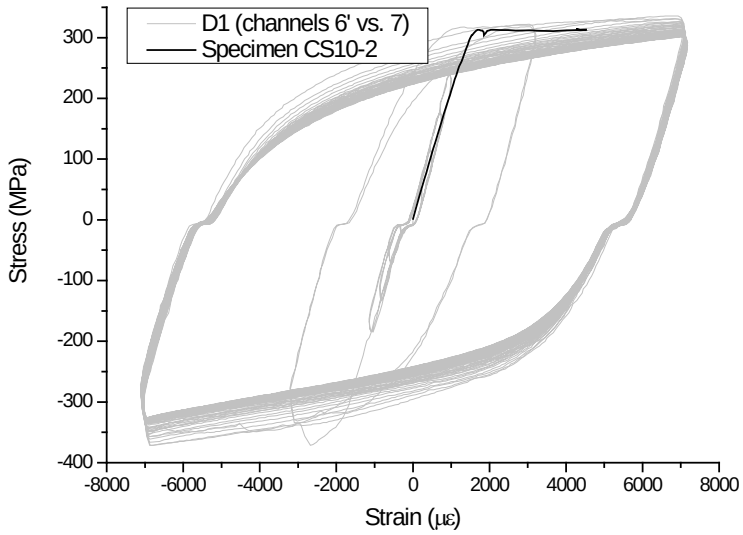

Figure 73. Comparison between stress-strain plots for the 10 mm core bar (CS10-2) and for dissipator D1

Plots from Figure 73 show that the elastic stiffness of the steel core (in tension) is similar to the one of the dissipators. Comparison among the plots of the core and of the device shows that the amount of consumed skeleton energy [Kato, Akiyama, Yamanouchi, 1973] is rather moderate since the plastic excursion is small (see Figure 53). The fit between both yielding points is rather poor (the stress-strain plot for the dissipator exhibits an earlier plastification –in the stationary phase– than the plot for the specimen); a possible explanation for this mismatch is a lack of uniformity along the whole core length.

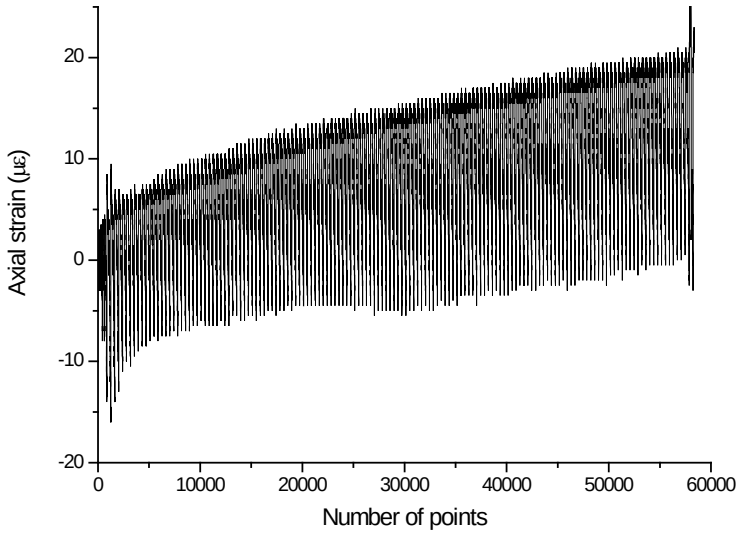

Figure 74. Axial strain of the mid section for dissipator D1 ([channel 16 + channel 17] / 2)

Figure 74 and Figure 75 show the "time histories" of the semi-sum and of the semi- difference,

respectively, of the axial strains measured in the tube by strain gauges 16 and 17 (see Table 9, Figure 60 and Figure 58). The semi-sum represents the strain due to the axial force while the semi-difference represents the strain due to the (horizontal) bending moment.

Plots from Figure 74 show that the strain due to the axial force is not negligible. The average grows continuously, exhibiting positive values (they correspond to axial shortening); apparently this cumulated effect is due to the interaction between the core and the surrounding mortar during compression because of the longitudinal friction forces generated by the contact during the local buckling of the core (see Figure 15). This effect can be considered as a kind of cumulated (slight) damage; it is remarkable that the total number of cycles (160) is significantly bigger than the one in any feasible earthquake.

In Figure 74, near the final failure the average and the maximum (shortening) strains are about 10×10^{-6} and 20×10^{-6}, respectively (forgetting the two last wider cycles). Such strains correspond to stresses 2.1 and 4.2 MPa, respectively; by multiplying by the tube area ($\pi\, d_{tu}\, t_{tu} = \pi \times 90 \times 3 = 848$ mm^2), the axial forces carried by the tube are about 1781 and 3563 N, respectively. By assuming a linear elastic behavior of the tube-mortar assembly, it is concluded that the axial forces carried by such member are about two times these values (3.56 and 7.13 kN, respectively). Comparison with Figure 71 shows that a relevant part of the axial force is transferred to the casing; more than 10% of the maximum compressive force keeps as permanent compression on the casing. However, Figure 74 indicates that the tube keeps permanently tensioned; this conclusion has little feasibility since most of the shear stress transfer from the core to the casing arises during compression (through the friction forces generated while the core tries to buckle). Consequently, a possible explanation is that the tube is initially (i.e. when the gauges are stuck on it) under axial compression because of the mortar shrinkage (in spite it had no shrinkage) and simply “tries” to become “on rest” (with zero axial stress).

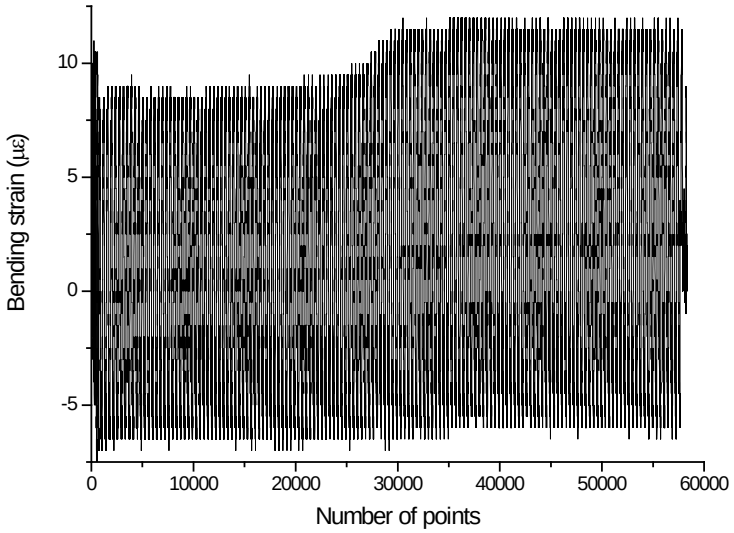

Figure 75. Horizontal bending strain of the mid section for dissipator D1 ([channel 16 – channel 17] / 2)

Comparison between plots from Figure 75 and Figure 74 show that the (horizontal) bending is (about) as relevant as the axial behavior. Such bending is mainly due to the local buckling of the unrestrained end parts of the core.

Since a big number of points are involved in Figure 75 and Figure 74 (58344), only global conclusions can be drawn. To obtain more precise deductions, shorter intervals (corresponding to

the stationary phase of the test) are plotted individually in Figure 76 (axial strain) and Figure 77 (bending strain).

Comparison between Figure 76 and Figure 77 shows that the axial strain behaves significantly more irregularly than the bending strain. This last is produced by the (horizontal) buckling generated during each cycle and has no close relation with the transfer of axial stresses during the compression.

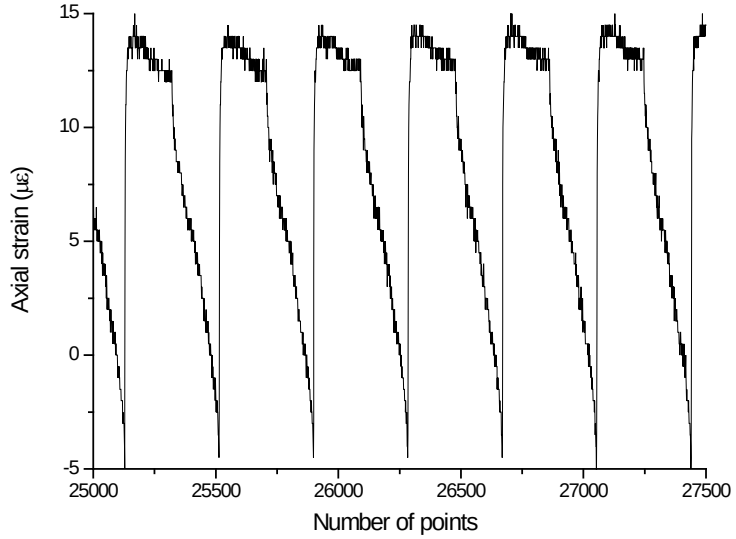

Figure 76. Horizontal axial strain of the mid section for dissipator D1 ([channel 16 + channel 17] / 2). Mid cycles

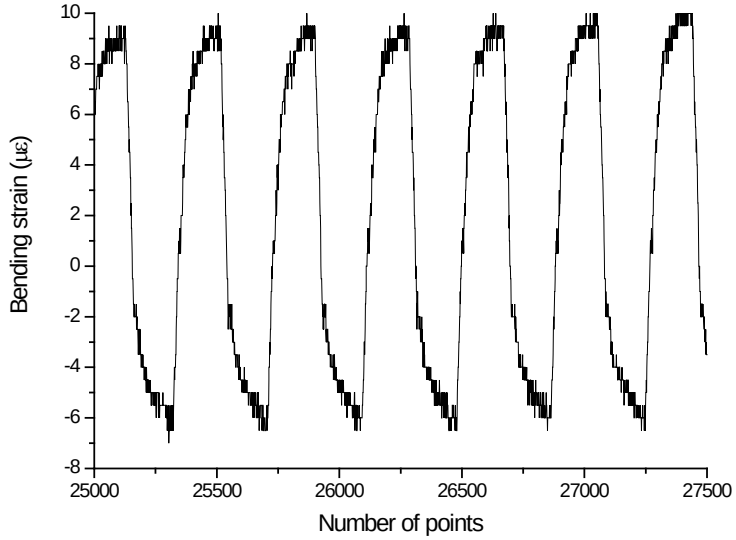

Figure 77. Horizontal bending strain of the mid section for dissipator D1 ([channel 16 – channel 17] / 2). Mid cycles

Plots Figure 76 show that the behaviors in the loading and unloading branches as well as in the elongation and shortening regions are clearly different each other. However, it would be useful to distinguish in between the cases when the dissipator is tensioned or compressed. To further clarify this issue the axial strain is plotted in Figure 78 together with the force in the jack (channel 7, see

Table 9 and Figure 58).

Plots from Figure 78 show that:

- During the loading tension branch, the axial strain in the tube decreases slightly but does not become zero. It indicates that there is a permanent friction (i.e. keeps even during the tension periods) between the mortar and the core.
- During the unloading tension branch, the axial strain in the tube decreases (faster than in the previous phase) but does not become zero. It indicates that there is a permanent friction between the mortar and the core.
- During the loading compression branch, the axial strain grows (towards shortening). Near the peak, the growth is particularly relevant; it confirms that this peak is highly contributed by the shear stress transfer from the core to the mortar.
- During the unloading compression branch, the axial strain decreases (towards elongation) extremely fast (especially at the beginning).

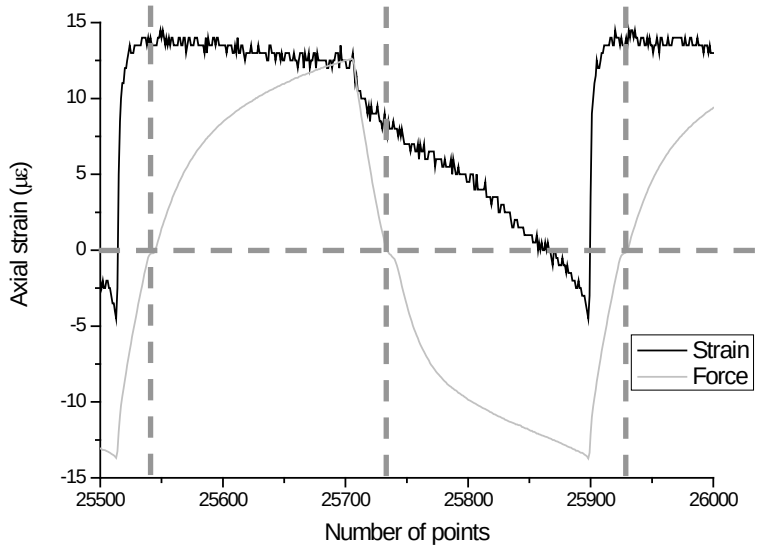

Figure 78. Horizontal axial strain of the mid section for dissipator D1 ([channel 16 + channel 17] / 2) and axial force in the jack (channel 7). Mid cycles

Figure 79 and Figure 80 display the axial strains of the left and right sections of the tube, respectively. These strains are measured by the strain gauges 18 and 19 (see Table 9 and Figure 58).

Comparison between Figure 74, by one side, and Figure 79 and Figure 80, by the other side, shows that at the mid section both the permanent (average) and the maximum strains are bigger than in the end sections. This difference is due to the cumulated effect of the longitudinal friction forces between the core and the mortar. Obviously, this conclusion was clearly expectable. However, it should be kept on mind that the strain gauges 18 and 19 measure only the strains at a single point of the end sections of the tube and cannot provide information neither about the axial force nor about the bending moment in those sections (see Figure 58).

Figure 81 and Figure 82 show the horizontal and vertical displacements of the mid section of the dissipator D1 as measured by the sensors 4 and 3, respectively (see Table 9, Figure 60 and Figure 58).

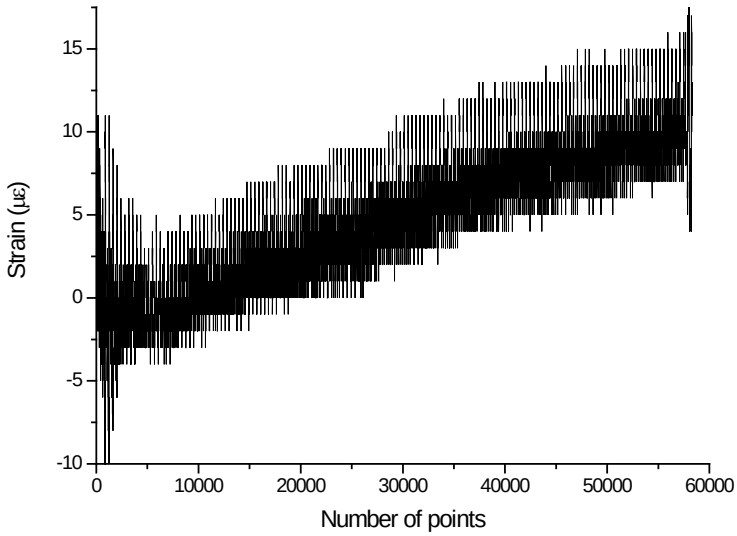

Figure 79. Axial strain of the left section for dissipator D1 (channel 18)

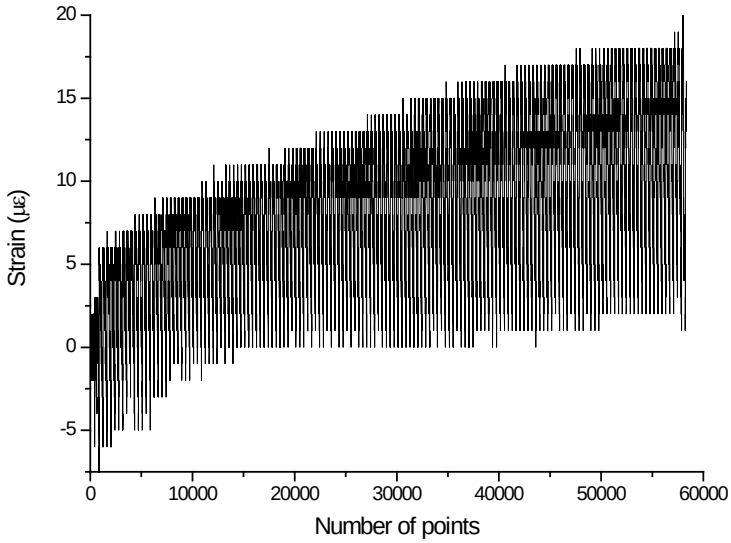

Figure 80. Axial strain of the right section for dissipator D1 (channel 19)

Plots from Figure 81 and Figure 82 show that the mid section experienced relevant transverse displacements, both horizontal and vertical. Comparison between Figure 81 and Figure 82 shows that the vertical displacements are significantly bigger than the horizontal ones.

To assess the correlation between the horizontal and vertical displacements of the mid section, Figure 83 displays the output of channel 4 plotted versus the one from channel 3.

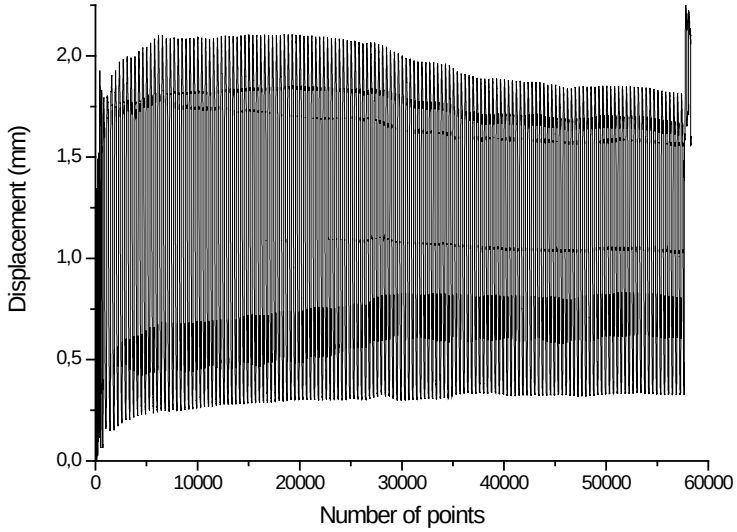

Figure 81. Horizontal displacements of the mid section for dissipator D1 (channel 4)

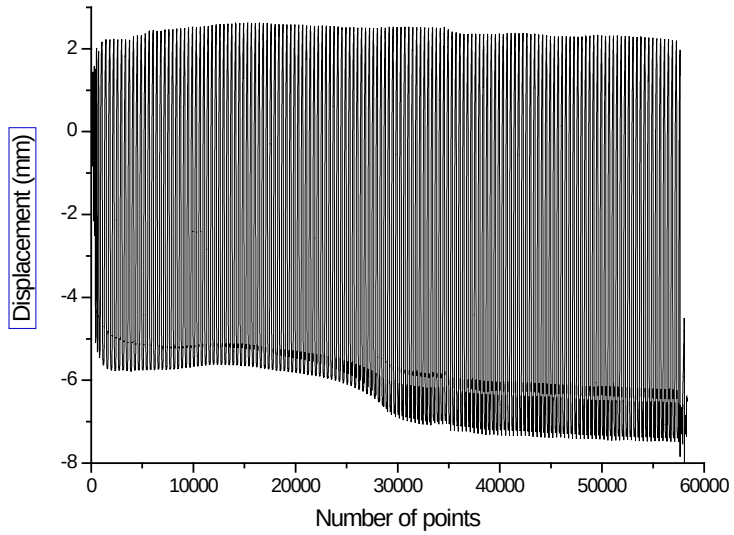

Figure 82. Vertical transverse displacements of the mid section for dissipator D1 (channel 3)

Figure 83 shows that, despite a certain erratic path, the maximum values for horizontal and vertical displacements are near coincident (for each cycle).

Figure 84 displays the difference between the longitudinal displacements of both ends of the encasing tube measured by displacement transducers 8 (right) and 9 (left), respectively (see Table 9, Figure 60 and Figure 58).

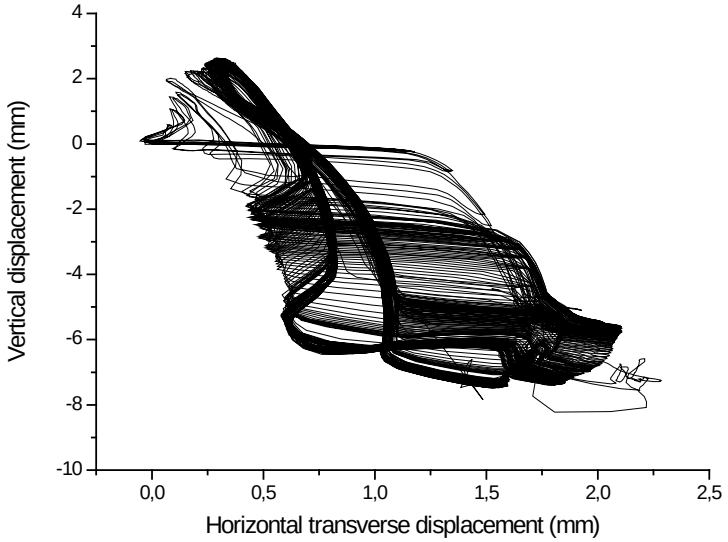

Figure 83. Vertical vs. transverse displacements of the mid section for dissipator D1 (channel 4 vs. channel 3)

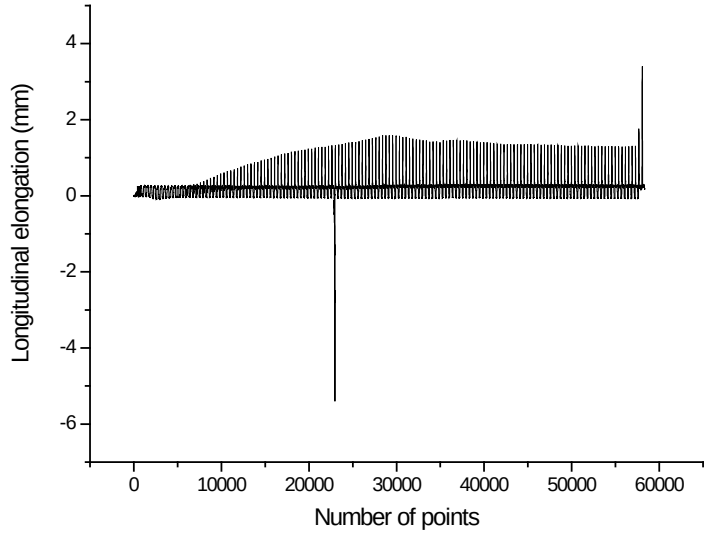

Figure 84. Relative longitudinal displacement between the ends of the casing for dissipator D1 (channel 8 + channel 9)

Plots from Figure 84 aim to represent the elongation experienced by the tube; however, comparison between the relative displacements in Figure 84 and the strains in Figure 74 show that these registered displacements can not correspond to the actual longitudinal displacements of the extremes of the bar as the average strain would be several orders of magnitude bigger than the registered ones. Figure 60 (left and right) show that the displacements in Figure 84 appear to be highly contributed by the (horizontal) rotations experienced by both connectors; this fact could be easily observed during the experiment and is also confirmed by the important transverse displacements shown in Figure 82. For instance, the spike in (about) point 23000 is obviously generated by a sudden rotation.

5.3.3 After-test remarks for dissipator D1

As described previously, final failure came for breakage of the core near the mid section. After concluding this test the broken core was pulled out. Figure 85 displays a representative view during this process.

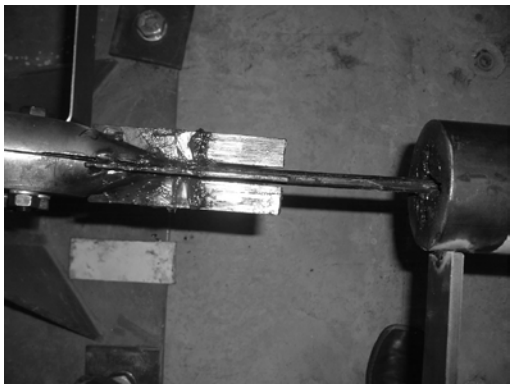

Figure 85. Pulled out core for dissipator D1

Figure 85 shows clearly that the welded trapezoidal plates were unable to restrain the local buckling of the end parts of the core as a significant gap could be observed; this fault was due to a mistake during the welding operation.

After pulling out the broken part of the core (Figure 85), the dissipator was cut longitudinally in two equal halves to observe the actual condition of the mortar. Figure 86 displays views of representative parts of mortar and of the broken core.

Figure 86. Mortar and core of dissipator D1

Left image in Figure 86 shows that the mortar is apparently in good condition, even in the near vicinity of the core; it means that the transversal compressive forces due to high buckling modes (rippling, see Figure 15) were not able to damage locally the mortar. According to the left image in Figure 86 some eccentricity of the core hole was observed; it ranged between 5 and 10 mm. Such values lie inside the range considered for buckling analysis (e_{co} = 20 mm).

The cover of the core (Teflon, grease and rubber) was in good condition. The only observed damages were generated during the after-test manipulation.

Mid and right images in Figure 86 show that the core was permanently bent; it is shaped roughly like a (warped) sinusoidal wave whose wavelength ranges in between 100 and 200 mm and whose

amplitude reaches up to 2 mm. Since the lateral forces exerted by the core were unable to bend significantly the casing (filled tube) and the surrounding mortar is not damaged, is obvious that this permanent curvature is due to the lateral compression of the core cover, particularly the rubber layer.

To investigate the bonding provided by the adhesive, the connector shown in the mid picture in Figure 86 was tested under tension (after eliminating the bolts). The testing rig is shown in Figure 87.

Figure 87. Pull-out test of connectors with adhesive only for dissipator D1

Figure 88 displays the results of the test described in Figure 87.

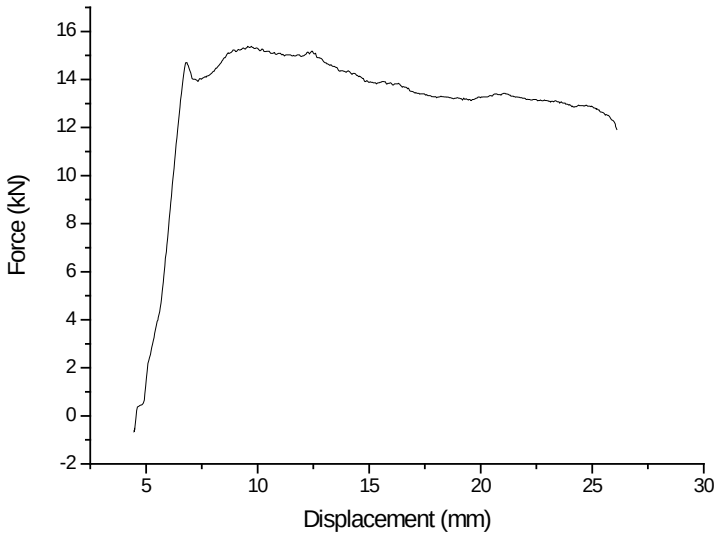

Figure 88. Results of the pull-out test of connectors with adhesive only for dissipator D1

Plots from Figure 88 show that the behavior of the adhesive is unsatisfactory. After a rather linear initial branch, sliding arose when the axial force in the core reached near 15 kN, what is clearly below the maximum values in Figure 71. It must be concluded that most of the strength to sliding is provided by the friction forces generated by the prestressed bolts.

5.4 Testing of dissipator D2

5.4.1 Testing remarks

This subsection describes the most relevant facts for the experiment on dissipator D2.

The test of this device had no particular circumstances. Failure came by breaking of the core near the central section after 131 cycles (see Table 10).

Figure 89 displays the testing rig for dissipator D2.

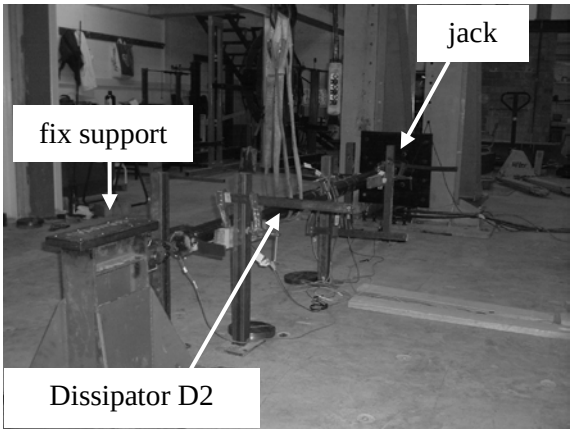

Figure 89. Cyclic testing of dissipator D2

Comparison between Figure 89 and Figure 58 shows a big similarity among both testing rigs. As stated previously, strain gauges 18 and 19 were not installed.

As discussed previously, testing of dissipator D1 pointed out three major inconvenient facts: (i) local buckling of the unrestrained ends of the core (see Figure 85), (ii) relevant rotations in the (hinged) connections (see Figure 82) and (iii) notable slides in such ends (see Figure 69). The two first facts are closely related and lead to important transverse rigid-body displacements of the tube, see Figure 82). To minimize these effects in the experiment about dissipator D2, steel and can wedges were introduced in the (hinged) connections as shown in Figure 90.

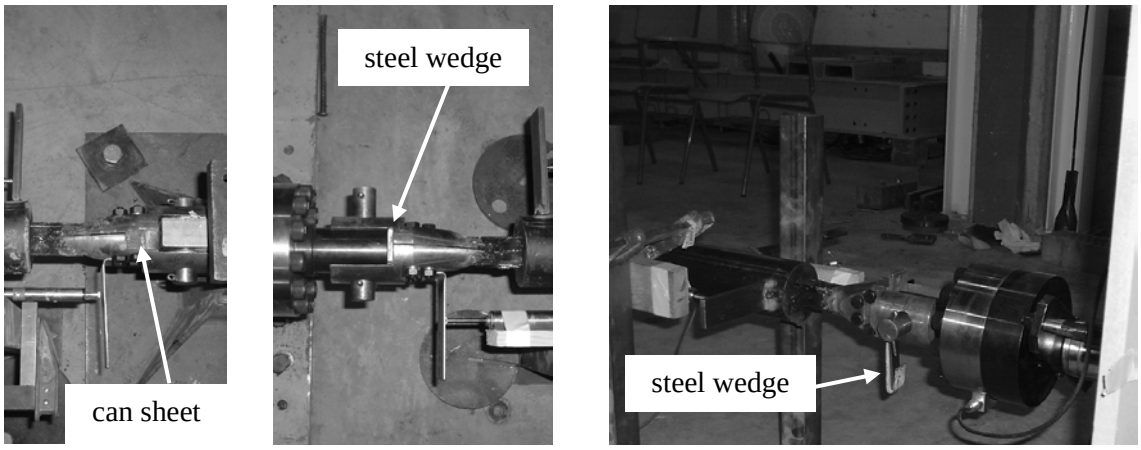

Figure 90. Improved connections for dissipator D2

5.4.2 Testing results for dissipator D2

The most relevant plots are displayed in this subsection. In all the figures, positive values correspond either to elongation (for strain gauges and displacement transducers) or to tension (for the load cell).

Figure 91 shows the time history elongation of the steel core (as measured by channels 1 and 2, see Table 9 and Figure 58) of the dissipator D2.

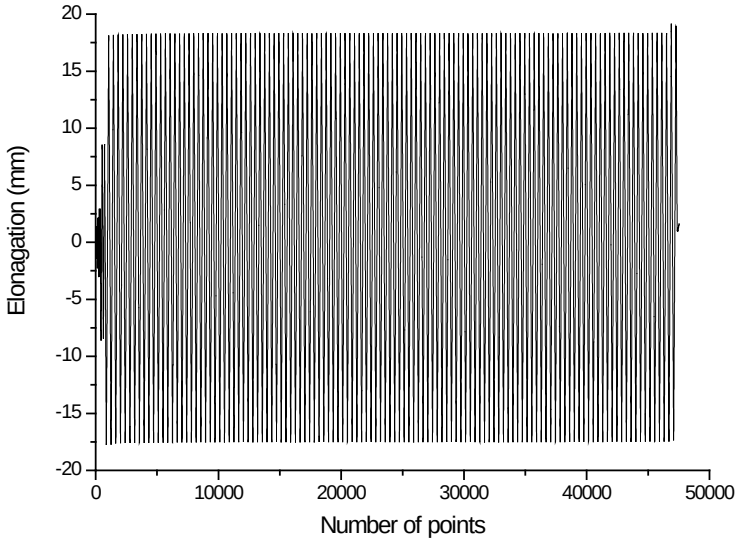

Figure 91. Core elongation for dissipator D2 (channel 1 + channel 2)

Figure 91 shows a rather regular behavior; it confirms the usefulness of the measures taken by these displacement transducers. Conversely to Figure 61 there is no drift; it confirms the effectiveness of the restraints (in both ends of the dissipator) described by Figure 90.

Since a big number of points are involved in Figure 91 (47533), only global conclusions can be drawn. To obtain more precise deductions, two shorter intervals are plotted individually: the initial cycles (1:200) in Figure 92 and a number of cycles (corresponding to the stationary phase of the test) in Figure 93. To assess the feasibility of the displacement measured by the displacement transducer in the jack (channel 6, see Table 9 and Figure 58), such information is also included in these Figures.

The observation of Figure 92 and Figure 93 allows deriving some relevant conclusions:

- Every time the force (in the jack) reverts, the plot of the core elongation (channel 1 + channel 2) exhibits a slight horizontal jump (the jack keeps moving but the core does not elongate). This is due to the gap in the pin-joint connections between the dissipator and the end supports (see Figure 57 and Figure 58). At Figure 92 such jumps correspond also to the changes of sign of the jack displacement since the plastification has not yet initiated. Both in Figure 92 and Figure 93, at each cycle the “first” jump (when the force goes from compression to tension) is smoother than the “second” one (when the force goes from tension to compression). The comparison with the jumps displayed by Figure 62 and Figure 63 shows that the restraints (in both ends of the dissipator) described by Figure 90 have reduced significantly the gap.
- The jack displacement (channel 6) is bigger than the core elongation (channel 1 + channel 2).

This difference is due to the abovementioned gap and to the flexibility of the interposed elements (end connections, supports, etc.). This last effect is particularly evident by observing the loading branches in the tension domain (without buckling, obviously) in Figure 92: the slopes of both plots are clearly different while they should be near alike.

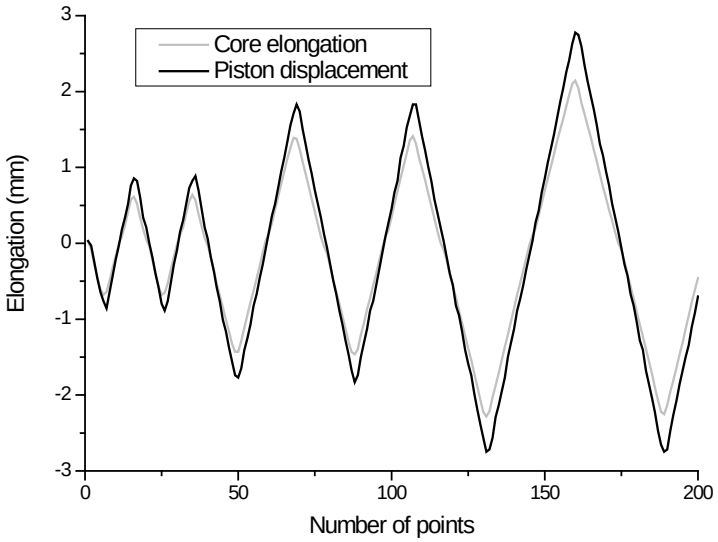

Figure 92. Core elongation for dissipator D2 (channel 1 + channel 2 and channel 6). Initial cycles

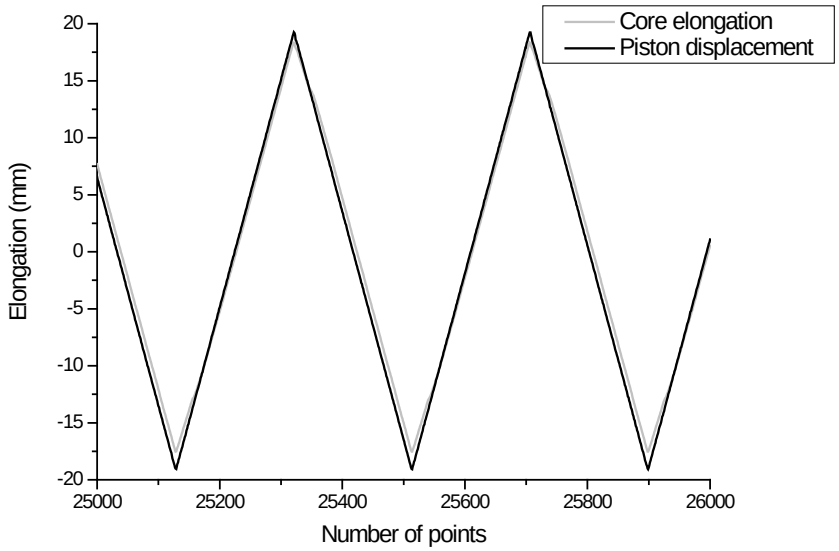

Figure 93. Core elongation for dissipator D2 (channel 1 + channel 2 and channel 6). Mid cycles

This last effect is corrected by reducing the slope of the measurements from channel 6 (as in dissipator D1, see Figure 62 and Figure 63): the channel 6 is replaced by channel 6 - channel 7 / 25 where 25 accounts for the stiffness (kN / mm) of the interposed elements. The arising measurement is termed as channel 6'. Figure 94 and Figure 95 show the same plots than Figure 92 and Figure 93 where the channel 6 has been replaced by the channel 6'. The comparison between Figure 94 and Figure 95, by one side, and Figure 92 and Figure 93, by the other side shows a significantly better agreement between the jack displacement and the core elongation; the fit is

particularly tight for the cycles belonging to the stationary phase (Figure 93 and Figure 95). Consequently, channel 6' is used next instead of channel 6 (for relevant plots). It is remarkable than in Figure 95 the corrected jack displacement (channel 6') is still slightly bigger than the core elongation (channel 1 + channel 2) because of the influence of the abovementioned gap in the end connections.

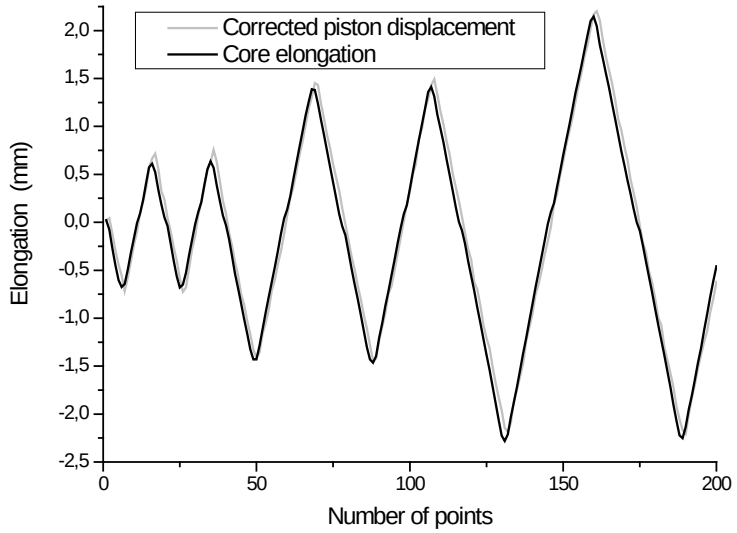

Figure 94. Core elongation for dissipator D2 (channel 1 + channel 2 and channel 6'). Initial cycles

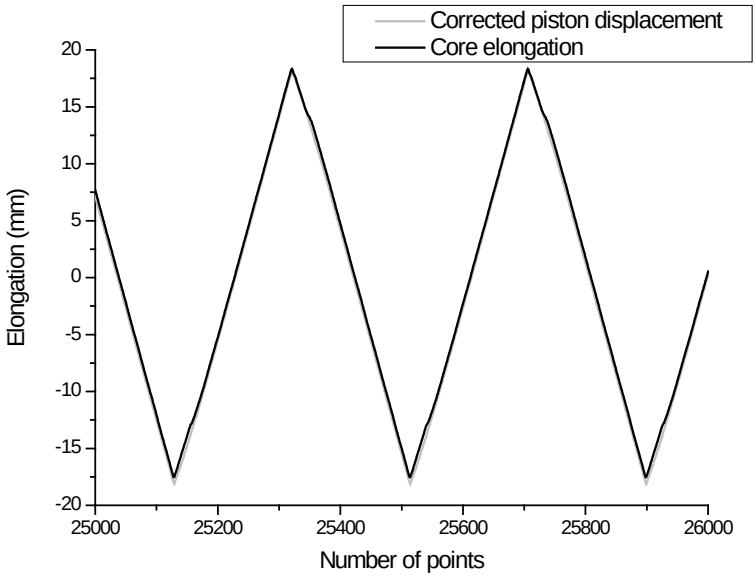

Figure 95. Core elongation for dissipator D2 (channel 1 + channel 2 and channel 6'). Mid cycles

Figure 96 displays the time history of the jack force (for dissipator D2) as measured by channel 7. Plots in Figure 96 show a rather stable hysteretic behavior. Once the maximum amplitude displacement is reached (after about point 850, see Figure 59), the force amplitude tends to decrease rather smoothly until reaching a stationary value (after about point 8000). This is due to

a progressive detachment from the inner core and the surrounding mortar. The difference between the maximum positive and negative values that was observed (for dissipator D1) in Figure 66 (this difference was explained by the contribution of the mortar through the friction forces generated during the compression when the core tries to buckle against the mortar) cannot be seen in Figure 96.

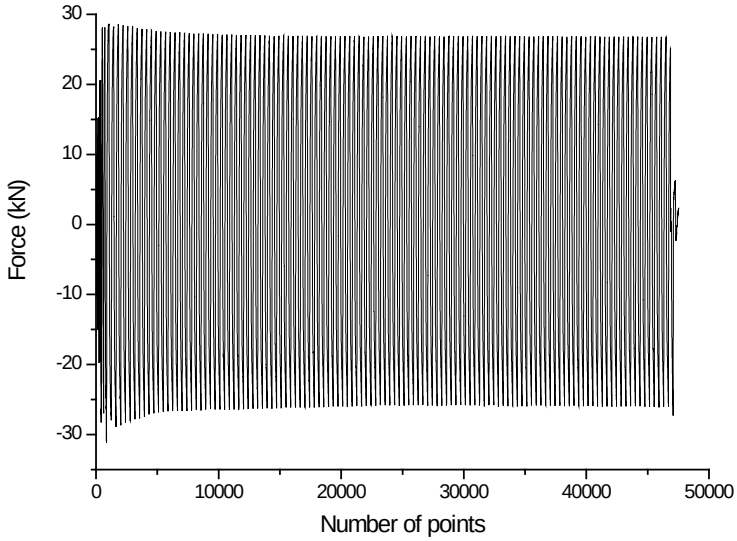

Figure 96. Jack force for dissipator D2 (channel 7)

Since a big number of points are involved in Figure 96 (47533), only global conclusions can be drawn. To obtain more precise deductions, two shorter intervals are plotted individually: the initial cycles (1:400) in Figure 97 and a number of cycles (corresponding to the stationary phase of the test) in Figure 98.

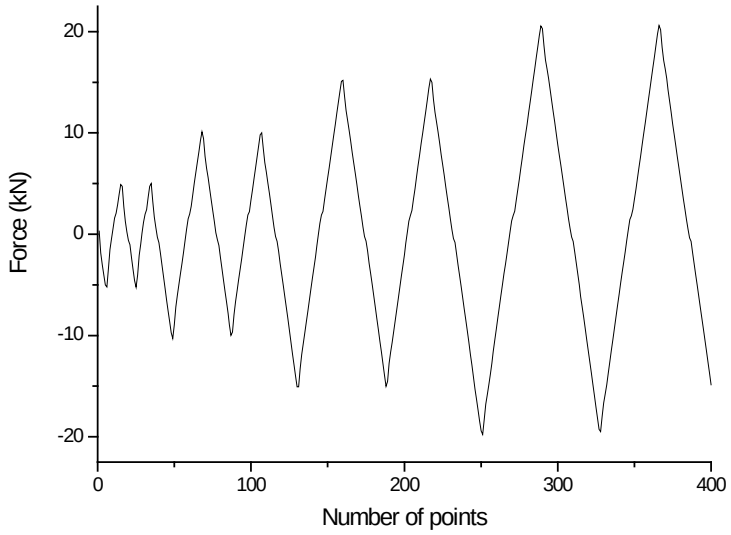

Figure 97. Jack force for dissipator D2 (channel 7). Initial cycles

The observation of Figure 97 and Figure 98 allows deriving some relevant conclusions:

- Every time the force (in the jack) reverts, the plot of the core elongation (channel 7) exhibits a horizontal jump (the jack keeps moving without any force change). This is due to the gap in the pin-joint connections between the dissipator and the end supports (see Figure 57 and Figure 58). This fact was also observed from Figure 92 and Figure 93. The comparison with the jumps displayed by Figure 67 and Figure 68 (for dissipator D1) shows that the restraints (in both ends of the dissipator) described by Figure 90 have reduced significantly the gap.
- The buckling of the core does not affect the force plots.
- In Figure 98 the last segment of the compression (plastic) loading branches exhibit a rather sudden increase leading to a higher peak and a reversal in the curvature. This is due to the mortar contribution and confirms the conclusion derived from Figure 96.

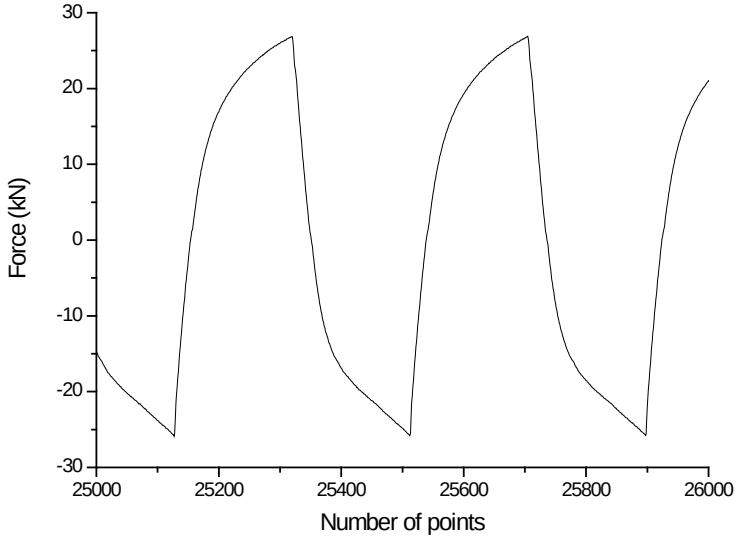

Figure 98. Jack force for dissipator D2 (channel 7). Mid cycles

Figure 99 shows the hysteretic behavior (jack force -Channel 7- vs. jack displacement -Channel 6-, see Table 9 and Figure 58) of dissipator D2.

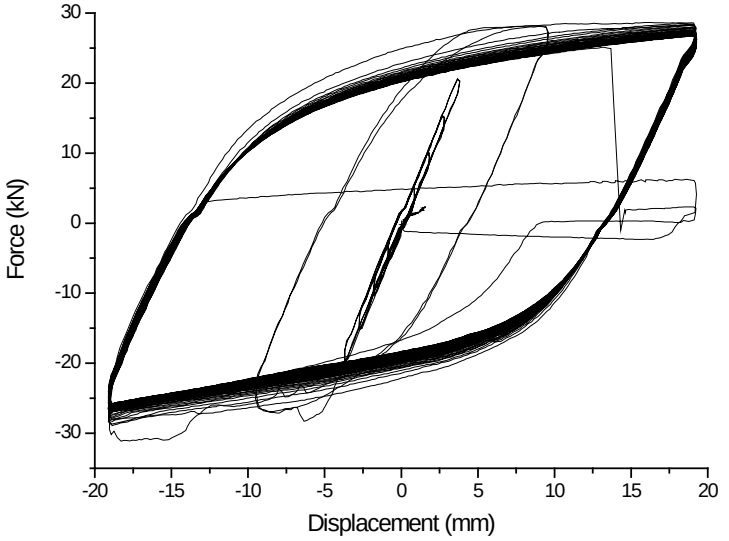

Figure 99. Hysteresis loops for dissipator D2 (channel 7 vs. channel 6)

Plots from Figure 99 show a rather stable hysteretic behavior along the whole number of cycles (131), similarly to dissipator D1 (Figure 69). Comparison between Figure 99 and Figure 69 show that the slides in the connections have been virtually eliminated; it confirms the usefulness of the introduced wedges (Figure 90). As in Figure 69, the irregular loops correspond to the beginning of the test (see Figure 59) and to its final part. To confirm this fact Figure 100, Figure 101 and Figure 102 show the cycles in Figure 99 split in three parts: first irregular cycles (Figure 100, points 1 to 1250), stable (regular) intermediate cycles (Figure 101, points 1251 to 46399) and last irregular cycles (Figure 102, points 46400 to 47533).

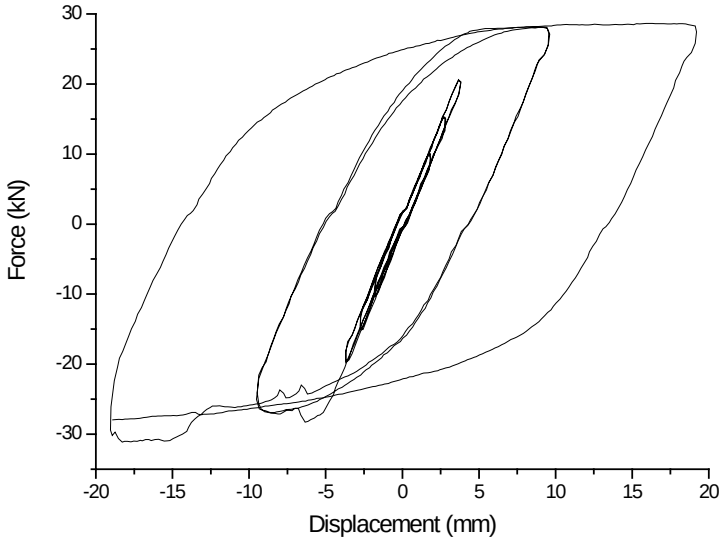

Figure 100. First hysteresis loops for dissipator D2 (channel 7 vs. channel 6)

In Figure 100 some minor jumps are observed in the plastic compression branches (they are generated by buckling of the core, similarly to short devices SD1 -Figure 32-, SD2 -Figure 36-, SD3 -Figure 40-, SD4 -Figure 43- and SD5 -Figure 46-).

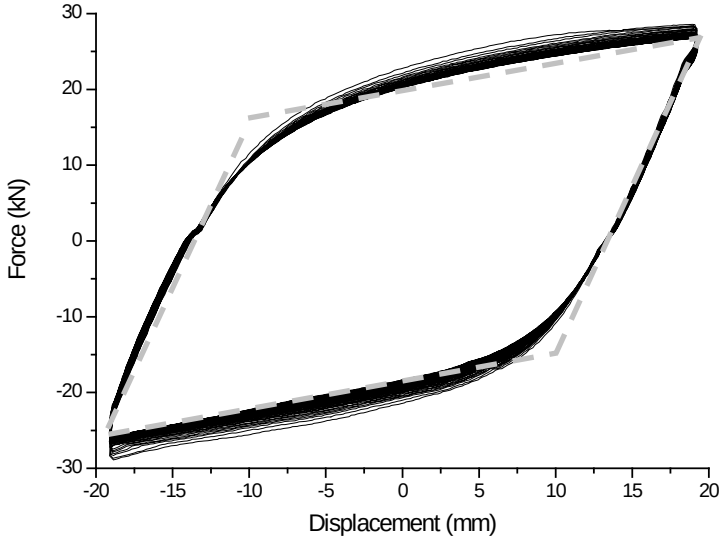

Figure 101. Regular hysteresis loops for dissipator D2 (channel 7 vs. channel 6)

To facilitate the interpretation of Figure 101 some auxiliary lines have been drawn, similarly to Figure 32 and Figure 71. The wide dash (grey) lines correspond to an ideal bilinear hysteresis loop (see Figure 29) with parallel branches; this loop is intended to fit the inner registered loops (the slope of the plastic branches has been selected as to match the compressive one).

Similarly to Figure 71, the following trends can be observed from Figure 101:

- As shown by Figure 96, the hysteretic behavior is stable. The force amplitude decreases after the first cycles but tends to stabilize quite fast.
- As shown by Figure 98, the lower plastic branch (compression) is more linear and steeper than the upper one (tension); the compression peaks are slightly higher than the tension ones. In fact, the tension behavior is more regular (it is due to the Bauschinger effect [Akiyama, 1980]) while the compression is affected by the mortar contribution (mostly near the peak).
- The horizontal jump due to the gap in the connections can be also observed (yet is clearly smaller than in the dissipator D1, see Figure 71).

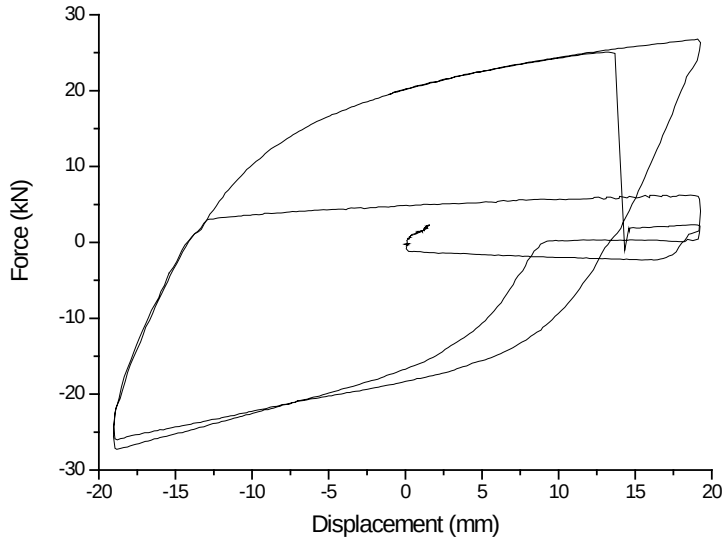

Figure 102. Last hysteresis loops for dissipator D2 (channel 7 vs. channel 6)

Figure 103 displays the stress-strain plots from Figure 53 (for the steel specimen CS10-2) and the hysteresis loops for dissipator D2 (Figure 101) corresponding to the first part of the test after eliminating the last irregular cycles. The strains for the dissipators have been obtained by dividing the relative displacement between both ends of the core (channel 6') by the length L_{di} (2466 mm) of the core in between both (end) connectors (see Figure 3, Table 1 and Figure 57).

Plots from Figure 103 show that the elastic stiffness of the steel core (in tension) is similar to the one of the dissipators. Comparison among the plots of the core and of the device shows that the amount of consumed skeleton energy [Kato, Akiyama, Yamanouchi, 1973] is rather moderate since the plastic excursion is small (see Figure 53). The fit between both yielding points is rather poor (the stress-strain plot for the dissipator exhibits an earlier plastification –in the stationary phase– than the plot for the specimen); a possible explanation for this mismatch is a lack of uniformity along the whole core length. Globally speaking, Figure 73 (for dissipator D1) and Figure 103 (for dissipator D2) allow deriving similar conclusions.

Figure 104 and Figure 105 show the "time histories" of the semi-sum and of the semi- difference,

respectively, of the axial strains measured in the tube by strain gauges 16 and 17 (see Table 9, Figure 60 and Figure 58). The semi-sum represents the strain due to the axial force while the semi-difference represents the strain due to the (horizontal) bending moment.

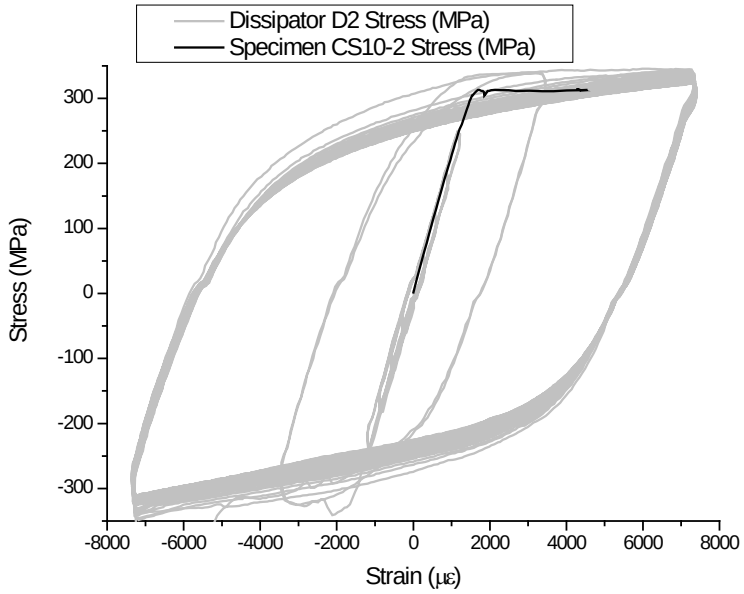

Figure 103. Comparison between stress-strain plots for the 10 mm core bar (CS10-2) and for dissipator D2

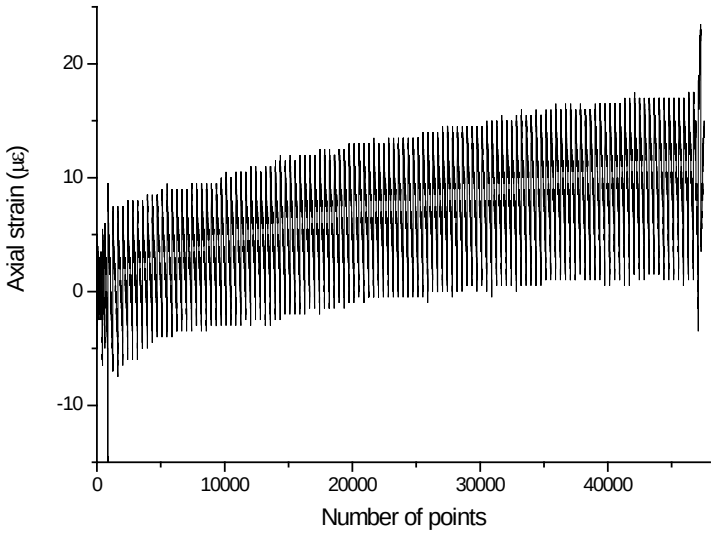

Figure 104. Axial strain of the mid section for dissipator D2 ([channel 16 + channel 17] / 2)

Plots from Figure 104 show that the strain due to the axial force is not negligible. The average grows continuously, exhibiting positive values (they correspond to axial shortening); apparently this cumulated effect is due to the interaction between the core and the surrounding mortar during compression because of the longitudinal friction forces generated by the contact during local buckling of the core (see Figure 15). This effect can be considered as a kind of cumulated (slight) damage; it is remarkable that the total number of cycles (131) is significantly bigger than the one in any feasible earthquake.

In Figure 104, near the final failure the average and the maximum (shortening) strains are about 1 and 17, respectively (forgetting the few last wider cycles). Such strains correspond to stresses 0.21 and 3.57 MPa, respectively; by multiplying by the tube area ($\pi\, d_{tu}\, t_{tu} = \pi \times 90 \times 3 = 848$ mm^2), the axial forces carried by the tube are about 178 and 3026 N, respectively. Assuming a linear elastic behavior of the tube-mortar assembly, it is concluded that the axial forces carried by such member are about two times these values. Comparison with Figure 101 shows that a relevant part of the axial force is transferred to the casing; less than 10% of the maximum compressive force keeps as permanent compression on the casing. Globally speaking, Figure 74 (for dissipator D1) and Figure 104 (for dissipator D2) allow deriving similar conclusions.

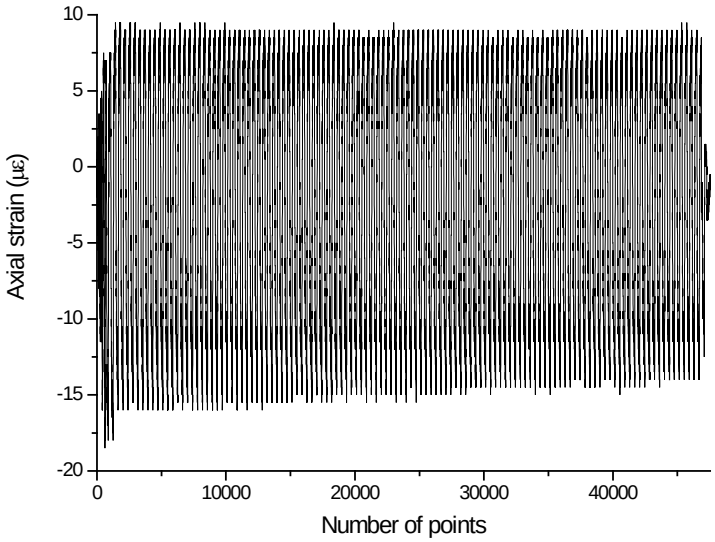

Figure 105. Horizontal bending strain of the mid section for dissipator D2 ([channel 16 – channel 17] / 2)

Comparison between plots from Figure 105 and Figure 104 show that the (horizontal) bending is significantly more relevant than the axial behavior. Such bending is due to the local buckling of the unrestrained end parts of the core as pointed out for Figure 82 (for dissipator D1). Globally speaking, Figure 75 (for dissipator D1) and Figure 105 (for dissipator D2) allow deriving similar conclusions.

Since a big number of points are involved in Figure 105 and Figure 104 (47533), only global conclusions can be drawn. To obtain more precise deductions, shorter intervals (corresponding to the stationary phase of the test) are plotted individually in Figure 106 (axial strain) and Figure 107 (bending strain).

Comparison between Figure 106 and Figure 107 shows that the axial strain behaves significantly more irregularly than the bending strain. This last is generated by the (horizontal) buckling arising during each cycle and has no close relation with the transfer of axial stresses during the compression. Globally speaking, Figure 76 and Figure 77 (for dissipator D1) and Figure 106 and Figure 107 (for dissipator D2) allow deriving similar conclusions.

Plots Figure 106 show that the behaviors in the loading and unloading branches as well as in the elongation and shortening regions are clearly different each other. However, it would be useful to distinguish in between the cases when the dissipator is tensioned or compressed. To further clarify this issue the axial strain is plotted in Figure 108 together with the force in the jack (channel 7, see Table 9 and Figure 58).

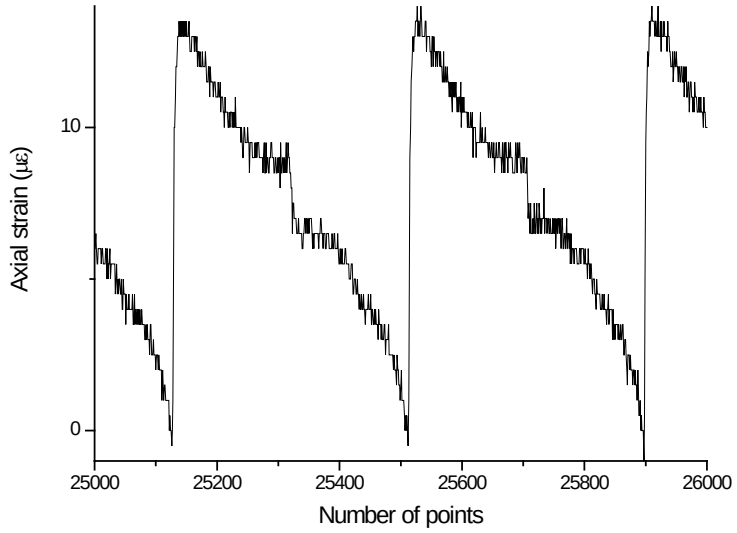

Figure 106. Horizontal axial strain of the mid section for dissipator D2 ([channel 16 + channel 17] / 2). Mid cycles

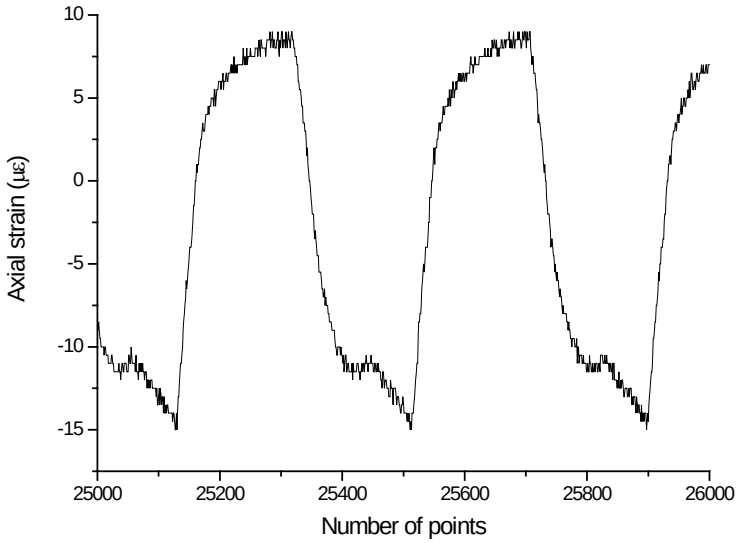

Figure 107. Horizontal bending strain of the mid section for dissipator D2 ([channel 16 – channel 17] / 2). Mid cycles

Plots from Figure 108 show that:

- During the loading tension branch, the axial strain in the tube decreases smoothly but does not become zero. It indicates that there is a permanent friction (i.e. keeps even during the tension periods) between the mortar and the core.
- During the unloading tension branch, the axial strain in the tube decreases (faster than in the previous phase) but does not become zero. It indicates again that there is a permanent friction between the mortar and the core.
- During the loading compression branch, the axial strain decreases (towards shortening). Near the peak, the decreasing is particularly relevant; it confirms that this peak is highly

contributed by the shear stress transfer from the core to the mortar.

- During the unloading compression branch, the axial strain grows (towards more elongation) extremely fast.

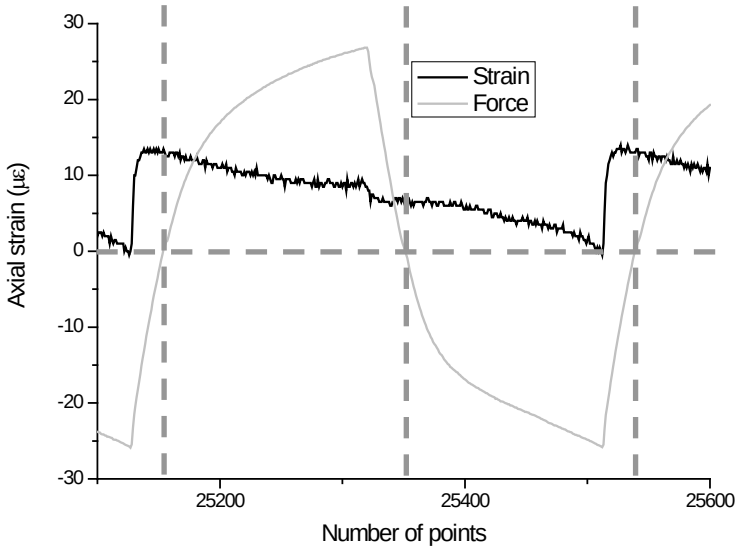

Figure 108. Horizontal axial strain of the mid section for dissipator D2 ([channel 16 + channel 17] / 2) and axial force in the jack (channel 7). Mid cycles

Figure 109 and Figure 110 show the horizontal and vertical displacements of the mid section of the dissipator D2 as measured by sensors 4 and 3, respectively (see Table 9, Figure 60 and Figure 58).

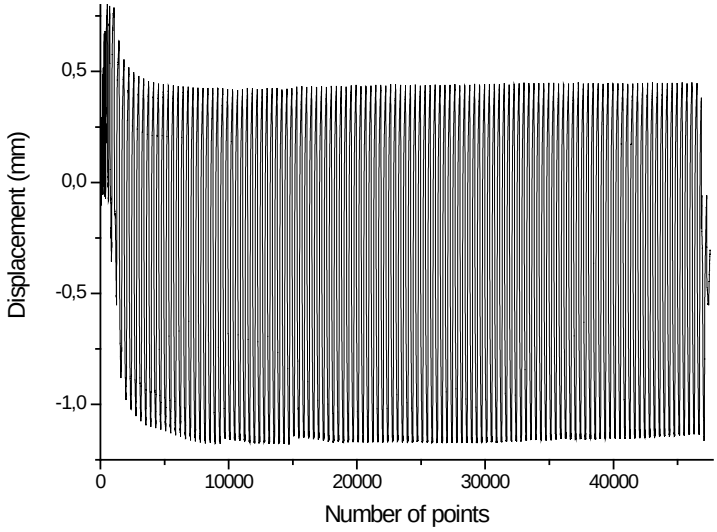

Figure 109. Horizontal displacements of the mid section for dissipator D2 (channel 4)

Plots from Figure 109 and Figure 110 show that the mid section experienced relevant transverse displacements, both horizontal and vertical. Comparison between Figure 109 and Figure 110 shows that the vertical displacements are as big as the horizontal ones. Comparison between Figure 81 and Figure 82 (dissipator D1), by one side, and Figure 109 and Figure 110 (dissipator D2), by the other side, shows that the horizontal displacements are similar for both devices while

the vertical ones are significantly smaller for dissipator D2. This confirms again the usefulness of the introduced wedges (Figure 90).

To assess the correlation between the horizontal and vertical displacements of the mid section, Figure 111 displays the output of channel 4 plotted versus the one from channel 3.

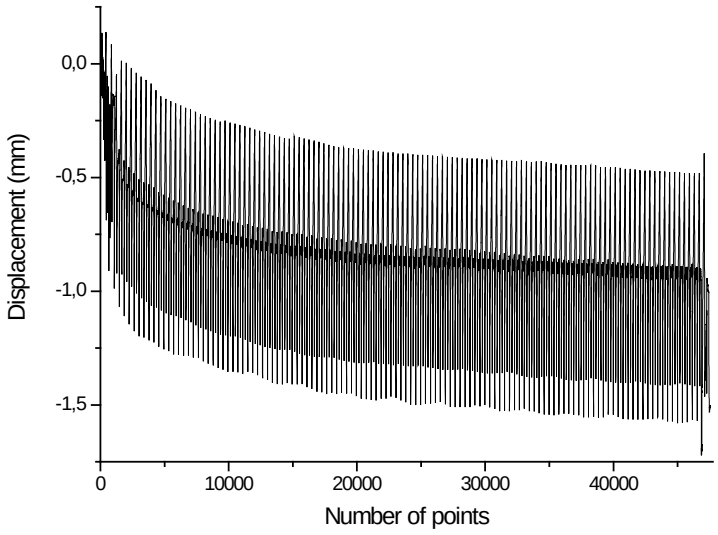

Figure 110. Vertical transverse displacements of the mid section for dissipator D2 (channel 3)

Figure 111 shows that, despite a certain erratic path, the maximum values for horizontal and vertical displacements are near coincident (for each cycle).

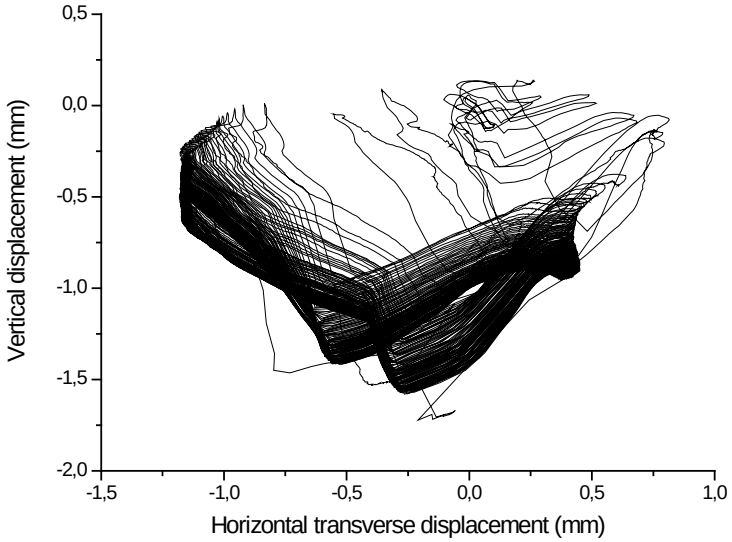

Figure 111. Vertical vs. transverse displacements of the mid section for dissipator D2 (channel 4 vs. channel 3)

Figure 112 displays the difference between the longitudinal displacements of both ends of the encasing tube measured by displacement transducers 8 (right) and 9 (left), respectively (see Table

9 and Figure 58).

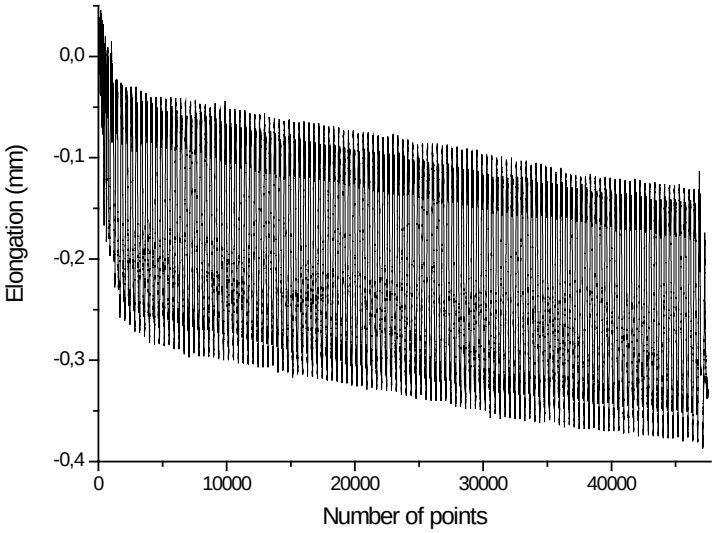

Figure 112. Relative longitudinal displacement between the ends of the casing for dissipator D2 (channel 8 + channel 9)

Plots from Figure 112 aim to represent the elongation experienced by the tube; however, comparison between the relative displacements in Figure 112 and the strains in Figure 104 show that these registered displacements can not correspond to the actual longitudinal displacements of the extremes of the bar as the average strain would be about one order of magnitude bigger than the registered one. Figure 90 shows that the displacements in Figure 112 appear to be highly contributed by the (horizontal) rotations experienced by both connectors; this fact could be easily observed during the experiment. In any case, this effect is less intense than in dissipator D1 (see Figure 84, Figure 74 and Figure 82); this confirms again the positive influence of the wedges.

5.4.3 After-test remarks for dissipator D2

As described previously, final failure came for breakage of the core near the mid section (similarly to dissipator D1). After finishing this test, the broken core was pulled out and the dissipator was cut longitudinally in two (equal) halves to observe the condition of the mortar. Figure 113 displays representative parts of the mortar and of the core.

Figure 113. Mortar and core of dissipator D2

Figure 113 shows that the mortar is apparently in good condition, even in the near vicinity of the

core; it means that the transversal compressive forces due to high buckling modes (rippling, Figure 15) were not able to damage locally the mortar. According to Figure 113, some eccentricity of the core hole was observed as in Figure 86 (for dissipator D1); similar conclusions can be derived.

The cover of the core (Teflon, grease and rubber) was in good condition. Figure 113 shows that the core was permanently bent; it is shaped roughly like a warped sinusoidal wave whose wavelength ranges in between 100 and 200 mm and whose amplitude reaches up to 2 mm. Since the lateral forces exerted by the core were unable to bend the casing (filled tube) and the surrounding mortar is not damaged, is obvious that this permanent curvature is due to the compression of the core cover, particularly the rubber layer. This conclusion is similar to the one for dissipator D1.

The broken core was pulled out like in dissipator D1; Figure 114 displays two views of the naked connector.

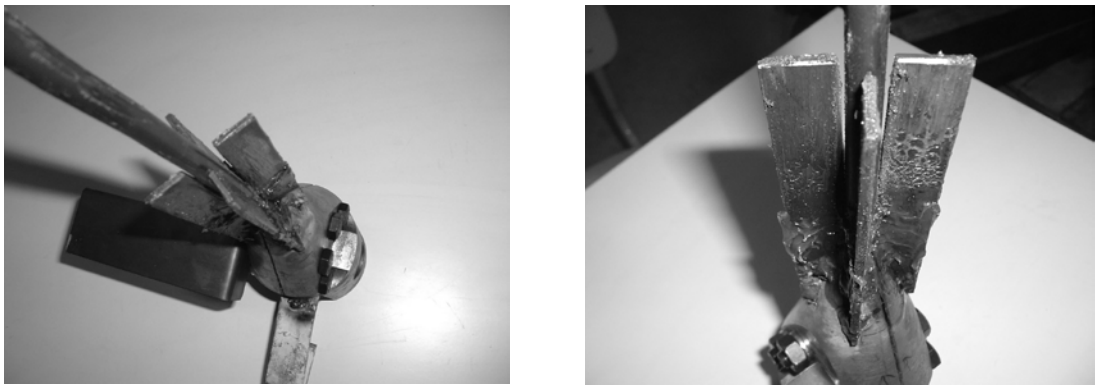

Figure 114. Pulled out core for dissipator D2

Figure 114 shows clearly that, like in dissipator D1 (see Figure 85), the welded trapezoidal plates were unable to restrain the local buckling of the end parts of the core as a significant gap could be observed.

5.5 Testing of dissipator D3

5.5.1 Testing remarks

This subsection describes the most relevant facts for the experiments on dissipator D3.

Figure 115 displays three images of the testing rig for dissipator D3.

As mentioned previously, this test was carried out after the one for dissipator D4 and, hence, some measures were taken to mitigate the observed problems. To reduce the transverse motions and the risk of local buckling of the end portions of the core, steel elements were rigidly anchored to the ground and were incorporated to the tube to prevent the transverse displacements of two sections situated as close to the end ones as possible (marked as left and right supports in Figure 115). These elements prevented the lateral displacements of the tube (in the corresponding sections) but did not restrain its (bending) rotations; therefore, such (intermediate) supports behave as sliding-pinned ones.

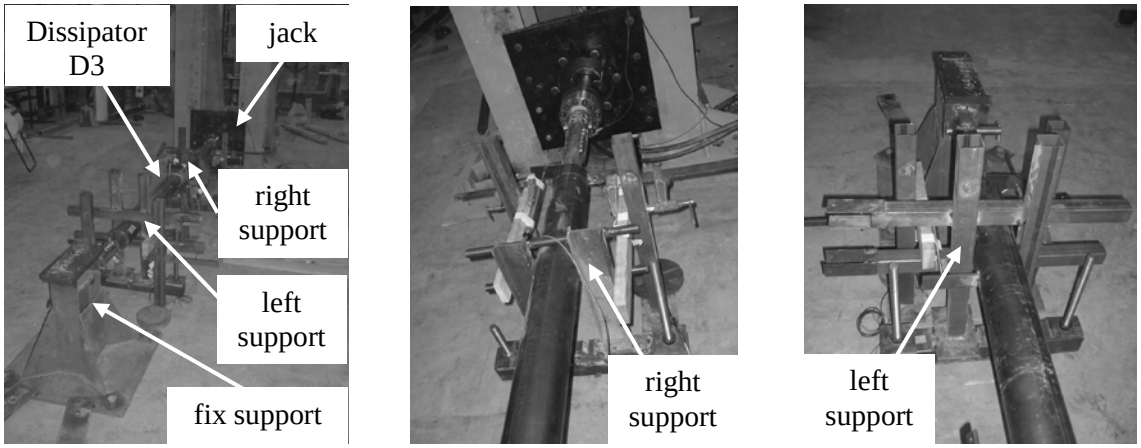

Figure 115. Cyclic testing of dissipator D3

Figure 116 displays three images of particular details of the testing rig for dissipator D3.

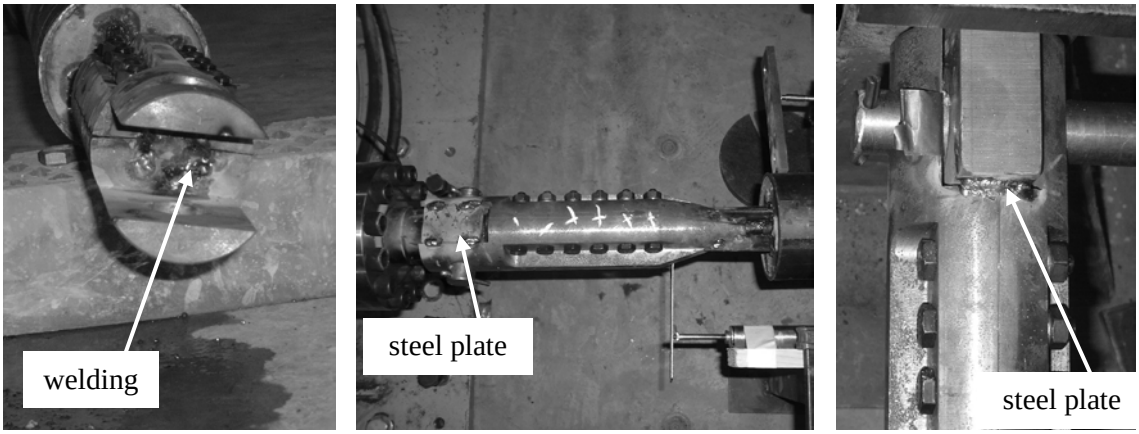

Figure 116. Details of the testing rig for dissipator D3

To avoid further sliding in between the connectors and the core, its end parts were welded to them as shown in the left picture in Figure 116. The ensuing heat impaired the effect of the adhesive and only this welding and the friction generated by the bolts prevented the sliding. Steel plates were welded to both halves of the connectors to restrain the rotation (see Figure 116, mid); moreover, the left connector was welded to the left support for further axial restrain (see Figure 116, right). After a certain number of cycles the bolts were continuously re-tightened up. In spite of these cautions, after 225 cycles a premature failure for sliding of the right connector arose (involving the breakage of the welding as shown by Figure 116, right). At that moment it was not possible to further tighten up the bolts as the gap between both halves of the connectors had disappeared (because of the repeated tightening-up operations); hence, the connectors were dismounted, the intermediate flat surfaces (see Figure 10) were lowered (with a rotating machine), the (curved) contact surfaces (between the two halves and the core) were cleaned from any adhesive product remain, the bolts were again tightened up and the experiment was resumed. Final failure came by breaking of the core (near the mid section) after 162 additional cycles (see Table 10). Next two subsections list the results of the two parts of the test, respectively.

5.5.2 Results for dissipator D3. First part

The most relevant plots of this part of the test are displayed in this subsection. In all the figures, positive values correspond either to elongation (for strain gauges and displacement transducers) or to tension (for the load cell).

This (first) part of the test of dissipator D3 had a minor incidence: following a sudden slide in the left connector (after 40 cycles) the test was interrupted, the bolts were re-tightened up and the experiment continued until failure (by progressive slide of the right connector). This progressive (final) sliding started at cycle 209 and concluded at cycle 225.

Figure 117 shows the time history elongation of the steel core (as measured by channels 1 and 2, see Table 9 and Figure 58) of the dissipator D3 (first part).

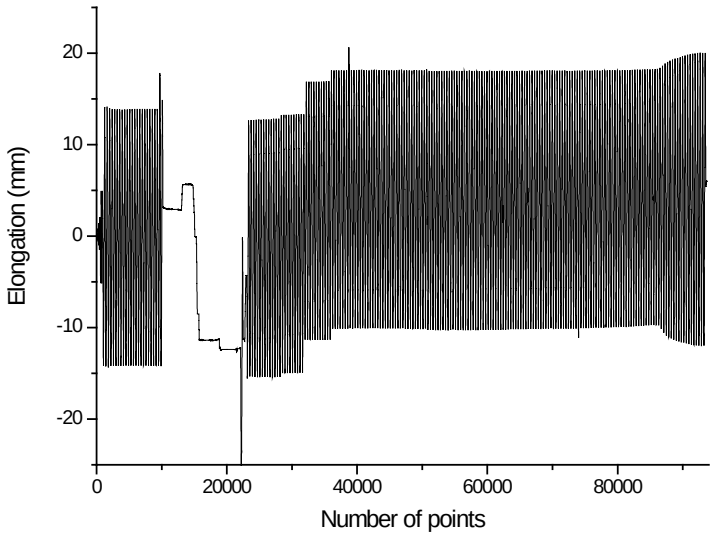

Figure 117. Core elongation for dissipator D3 (channel 1 + channel 2). First part

Figure 117 shows a rather regular behavior. The points between (about) 10500 and 22000 correspond to the abovementioned slide. After this, there are three sudden offsets in the values of the elongation; they correspond approximately to points 28000, 32000 and 36000. By plotting individually the outputs of sensors 1 and 2 it is apparent that only sensor 2 exhibits such discontinuities. Moreover, displacement sensors 8 and 9 (see Table 9 and Figure 58) behave similarly. As well, relevant information is that the jack force (Figure 122) does not have such jumps. Consequently, it can be concluded that the vertical offsets shown by Figure 117 are due to abrupt rotations in the left end of the beam (the fix support, see Table 9 and Figure 58). Beyond these effects, conversely to Figure 61, there is no drift; it confirms the effectiveness of the restraints (in both ends of the dissipator) described by Figure 90. The final amplification (after about point 86000) corresponds to the aforementioned slide: the measurements from channel 6 do not change (since the jack motion was governed by this channel) while a biggest part of such displacement correspond to relative displacement between both end connectors (instead of corresponding to deformation of the connecting elements). To support this conclusion, the amplitudes of channel 1 + channel 2 and of channel 6 are determined prior the onset of sliding and near the final failure: before sliding is 28.31 mm (channel 1 + channel 2) vs. 36.18 mm (channel 6) and after sliding is 32.19 mm (channel 1 + channel 2) vs. 36.18 mm (channel 6). A relevant overall conclusion is that the measures taken by the displacement transducers are useful.

Since a big number of points are involved in Figure 117 (93691), only global conclusions can be

drawn. To obtain more precise deductions, two shorter intervals are plotted individually: the initial cycles (175:575) in Figure 118 and a number of cycles (corresponding to the stationary phase of the test) in Figure 119. To assess the feasibility of the displacement measured by the displacement transducer in the jack (channel 6, see Table 9 and Figure 58), such information is also included in these Figures. In Figure 119 the abovementioned offset has been corrected as to allow proper comparison between the outputs of channel 6 and of channel 1 + channel 2.

The observation of Figure 118 and Figure 119 allows deriving some relevant conclusions:

- Every time the force (in the jack) reverts, the plot of the core elongation (channel 1 + channel 2) exhibits a slight horizontal jump (the jack keeps moving but the core does not elongate). This is due to the gap in the pin-joint connections between the dissipator and the end supports (see Figure 57 and Figure 58). At Figure 118 such jumps correspond also to the changes of sign of the jack displacement since the plastification has not yet initiated. Both in Figure 118 and Figure 119, at each cycle the “first” jump (when the force goes from compression to tension) is smoother than the “second” one (when the force goes from tension to compression).
- The jack displacement (channel 6) is bigger than the core elongation (channel 1 + channel 2). This difference is due to the flexibility of the interposed elements (end connections, supports, etc.). This is particularly evident by observing the loading branches in the tension domain (without buckling, obviously) in Figure 118: the slopes of both plots are clearly different while they should be alike. Comparison between Figure 62, Figure 63, Figure 92 and Figure 93, by one side, and Figure 118 and Figure 119, by the other side, shows that the differences between the outputs from channel 6 and from channel 1 + channel 2 are clearly bigger for the dissipator D3 than for D1 and D2. It is due to the fact that in dissipator D3 the ratio between the flexibility of the interposed elements and the one of the core is higher than in dissipators D1 and D2 (since the interposed elements are similar for all the devices while the cores of dissipators D3 and D4 are thicker than those of D1 and D2, see Table 1).

This last effect is corrected by reducing the slope of the measurements from channel 6 (similarly to dissipators D1 and D2): the channel 6 is replaced by channel 6 - channel 7 / 50 where 50 accounts for the stiffness (kN / mm) of the interposed elements. The arising measurement is termed as channel 6’. The difference between the stiffness of the interposed elements for devices D1 and D2 (respectively, 15.175 and 25 kN / mm) and for device D3 (50 kN / mm) can be explained mainly by the higher robustness of the end connectors (see Figure 116). Figure 120 and Figure 121 show the same plots than Figure 118 and Figure 119 where the channel 6 has been replaced by the channel 6’. The comparison between Figure 120 and Figure 121, by one side, and Figure 118 and Figure 119, by the other side shows a significantly better agreement between the jack displacement and the core elongation; the fit is particularly tight for the cycles belonging to the stationary phase (Figure 119 and Figure 121). Consequently, channel 6’ is used next instead of channel 6 (for relevant plots). It is remarkable than in Figure 121 the corrected jack displacement (channel 6’) is still slightly bigger than the core elongation (channel 1 + channel 2) because of the influence of the abovementioned gap in the end connections.

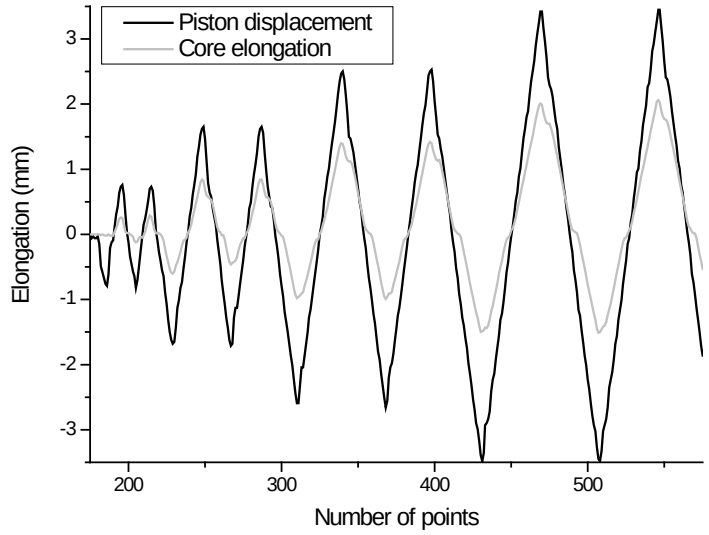

Figure 118. Core elongation for dissipator D3 (channel 1 + channel 2 and channel 6). Initial cycles. First part

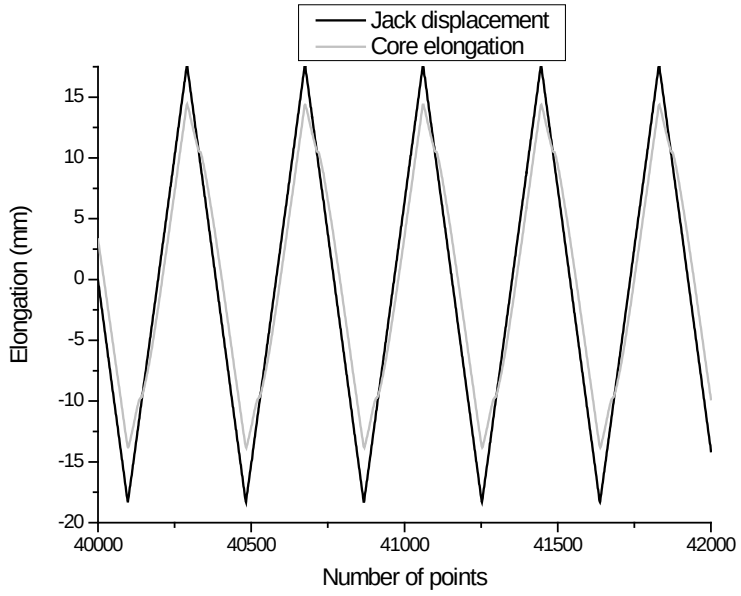

Figure 119. Core elongation for dissipator D3 (channel 1 + channel 2 and channel 6). Mid cycles. First part

Figure 122 displays the time history of the jack force (for dissipator D3) as measured by channel 7. Plots in Figure 122 show a rather stable hysteretic behavior. The difference between the maximum positive and negative values that was observed in Figure 66 (this difference was explained by the contribution of the mortar through the friction forces generated during the compression when the core tries to buckle against the mortar) can also be seen in Figure 122. It is remarkable that this difference grows as the test goes on (after about cycle 53000); it indicates than the mortar collaboration (through friction) becomes more relevant after an important number of cycles. After (about) cycle 86000 the force amplitude reduces as the abovementioned slide progresses.

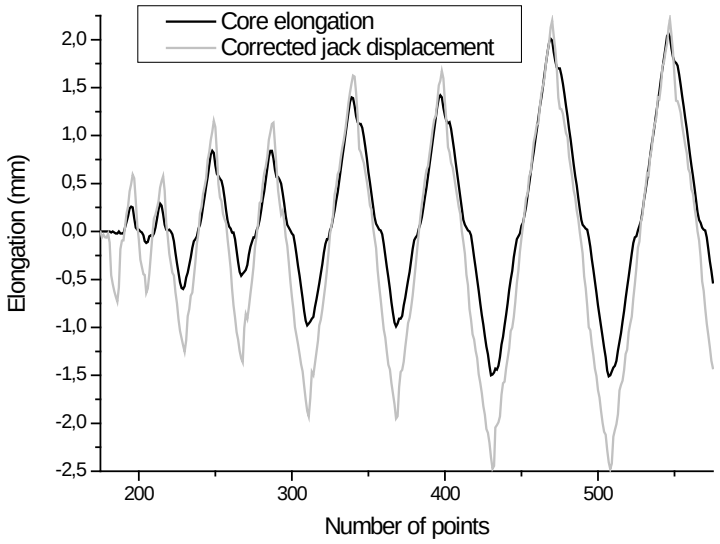

Figure 120. Core elongation for dissipator D3 (channel 1 + channel 2 and channel 6'). Initial cycles. First part

Since a big number of points are involved in Figure 122 (93691), only global conclusions can be drawn. To obtain more precise deductions, two shorter intervals are plotted individually: the initial cycles (175:575) in Figure 123 and a number of cycles (corresponding to the stationary phase of the test) in Figure 124.

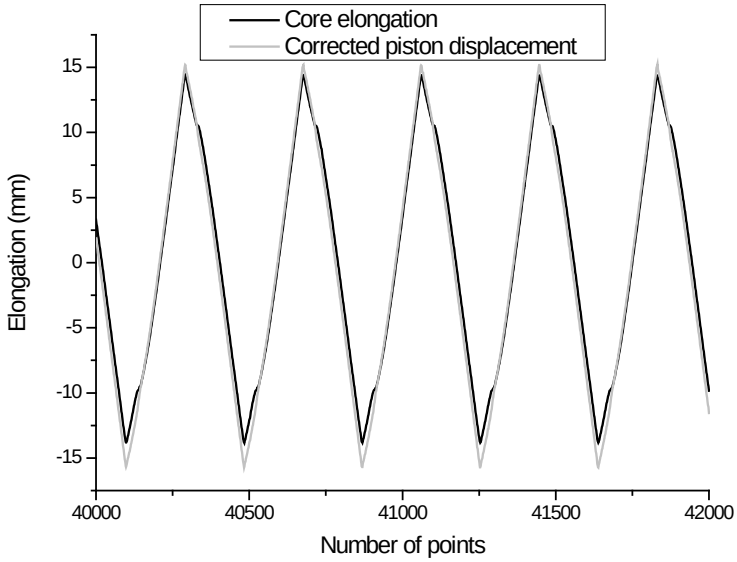

Figure 121. Core elongation for dissipator D3 (channel 1 + channel 2 and channel 6'). Mid cycles. First part

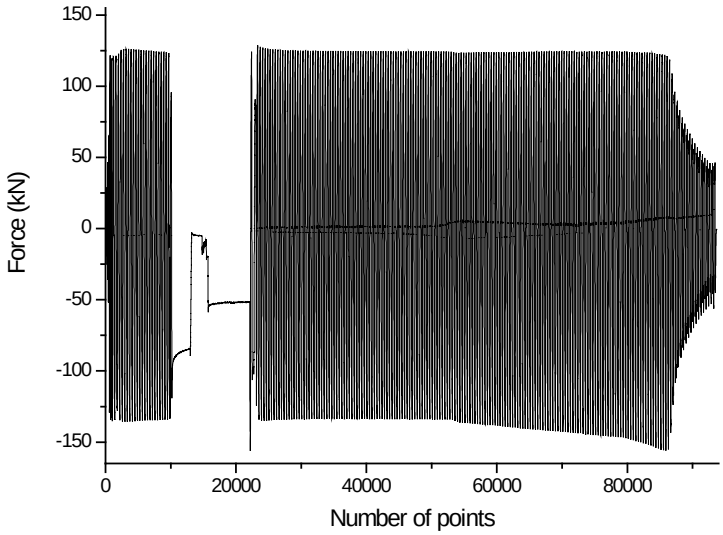

Figure 122. Jack force for dissipator D3 (channel 7). First part

The observation of Figure 123 and Figure 124 allows deriving some relevant conclusions:

- Every time the force (in the jack) reverts, the plot of the core elongation (channel 7) exhibits a horizontal jump (the jack keeps moving without any force change). This is due to the gap in the pin-joint connections between the dissipator and the end supports (see Figure 57 and Figure 58). This fact was also observed from Figure 118 and Figure 119. The comparison with the jumps displayed by Figure 67 and Figure 68 (for dissipator D1) shows that the restraints (in both ends of the dissipator) described by Figure 116 have reduced significantly the gap.
- The buckling of the core does not affect significantly the force plots.
- In Figure 124 the last segment of the compression (plastic) loading branches exhibit a rather sudden increase leading to a higher peak (and even a slight reversal in the curvature). This is due to the mortar contribution and confirms the conclusion derived from Figure 122. If some of the last loops are plotted (e.g. 84000:86000), this effect can be observed even more clearly.

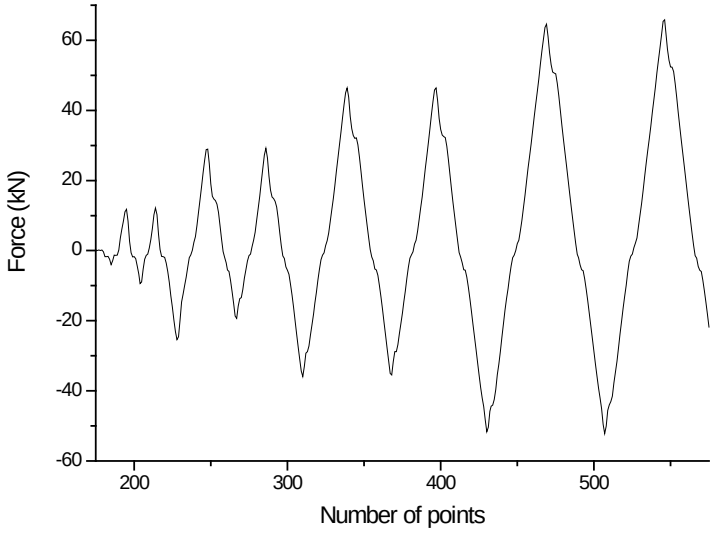

Figure 123. Jack force for dissipator D3 (channel 7). Initial cycles. First part

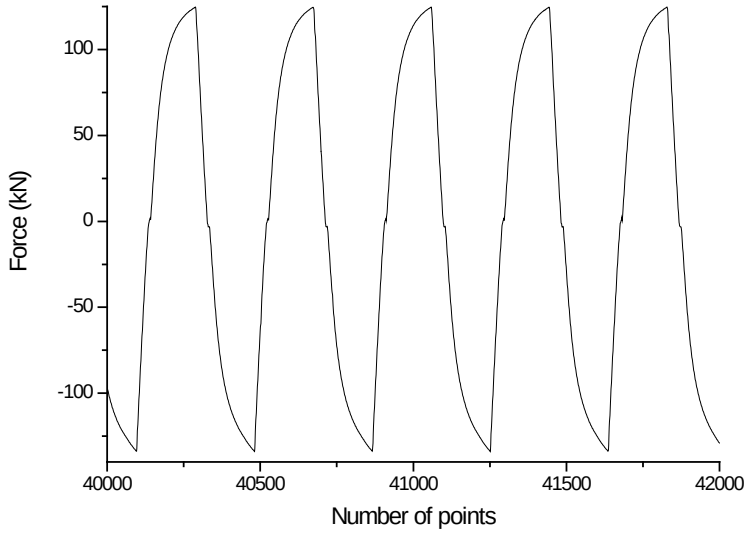

Figure 124. Jack force for dissipator D3 (channel 7). Mid cycles. First part

Figure 125 shows the hysteretic behavior (jack force -Channel 7- vs. jack displacement -Channel 6-, see Table 9 and Figure 58) of dissipator D3 (first part).

Plots from Figure 125 show a rather stable hysteretic behavior along the cycles prior to the onset of sliding (1:209), similarly to dissipators D1 and D2 (Figure 69 and Figure 99). Comparison with Figure 99 and Figure 69 show that the slides in the connections are as relevant as in Figure 69 (dissipator D1) in spite that the same restraining measures than in Figure 99 (dissipator D2) have been taken; this is due to the higher axial forces involved in dissipator D3. As in Figure 69 and Figure 99, the irregular loops correspond to the beginning of the test (see Figure 59) and to its final part; in this case there are also irregularities during the first slide (after 40 cycles). To confirm this fact Figure 126 and Figure 127 show the two sets of regular cycles in Figure 125: prior to the first slide (Figure 126, points 1000 to 9000) and after it (Figure 127, points 23400 to 86200).

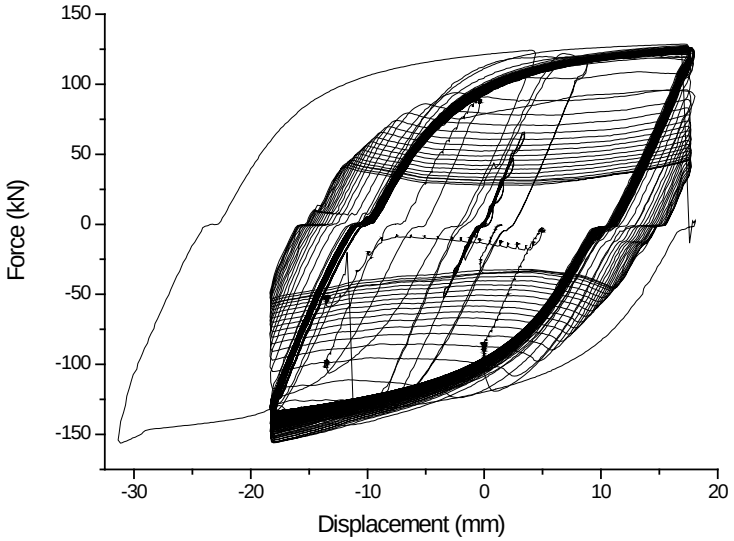

Figure 125. Hysteresis loops for dissipator D3 (channel 7 vs. channel 6) . First part

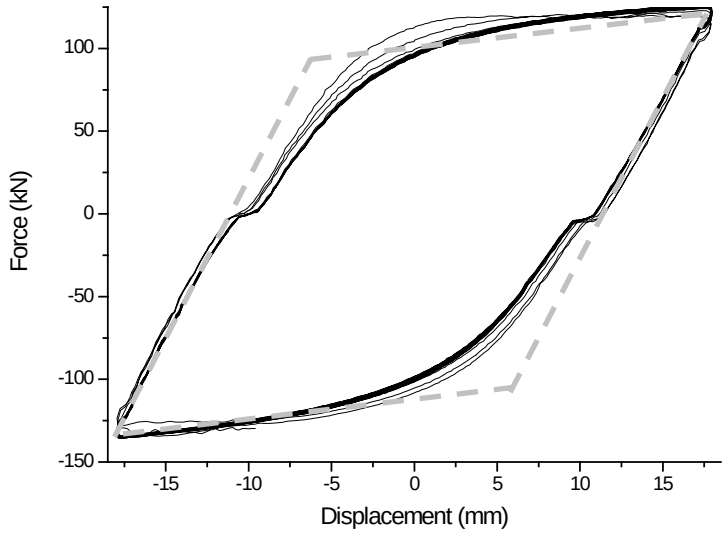

Figure 126. First regular hysteresis loops for dissipator D3 (channel 7 vs. channel 6) . First part

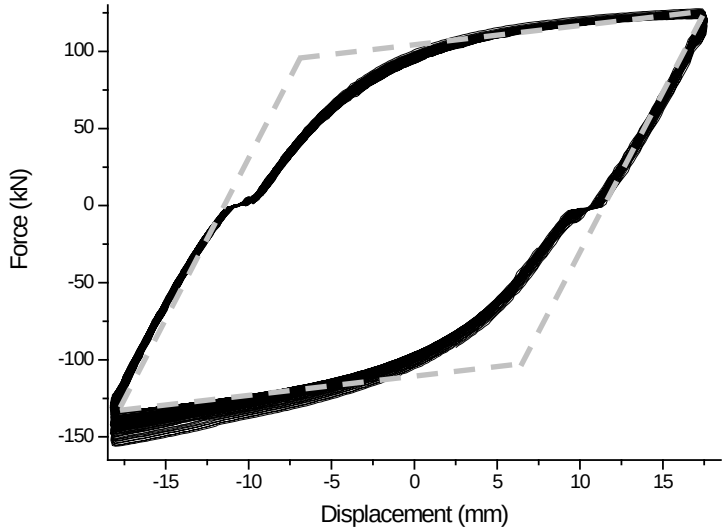

Figure 127. Last regular hysteresis loops for dissipator D3 (channel 7 vs. channel 6). First part

To facilitate the interpretation of Figure 126 and Figure 127 some auxiliary lines have been drawn, similarly to Figure 32, Figure 71 and Figure 101. The wide dash (grey) lines correspond to an ideal bilinear hysteresis loop (see Figure 29) with parallel branches; this loop is intended to fit the inner registered loops (the slope of the plastic branches has been selected as to match the compressive one).

Similarly to Figure 71 and Figure 101, the following trends can be observed from Figure 126 and Figure 127:

- The hysteretic behavior is rather stable.
- The lower plastic branch (compression) is more linear and steeper than the upper one (tension); the compression peaks are higher than the tension ones. In fact, the tension

behavior is more regular (it is due to the Bauschinger effect [Akiyama, 1980]) while the compression is affected by the mortar contribution (mostly near the peak).

- The horizontal jump due to the gap in the connections can be also observed (yet is clearly bigger than in the dissipator D2, see Figure 101).

Figure 128 displays the stress-strain plots from Figure 54 (for the steel specimen CS22-2) and the regular hysteresis loops for dissipator D3 (Figure 127) corresponding to the first part of the test after eliminating the irregular cycles. The strains for the dissipators have been obtained by dividing the relative displacement between both ends of the core (channel 6') by the distance between the centers of both (end) pins (see Figure 3, Table 1 and Figure 57).

Plots from Figure 128 show that the elastic stiffness of the steel core (in tension) is similar to the one of the dissipators. Comparison among the plots of the core and of the device shows that the amount of consumed skeleton energy [Kato, Akiyama, Yamanouchi, 1973] is rather moderate since the plastic excursion is small (see Figure 51 and Figure 52). The fit between both yielding points is satisfactory (in the stationary phase). Globally speaking, Figure 73 (for dissipator D1), Figure 103 (for dissipator D2) and Figure 128 (for dissipator D3) allow deriving similar conclusions. It is remarkable that the maximum strain in the dissipator lies in the horizontal plastic branch of the stress-strain law (far from the hardening branch, see Figure 54).

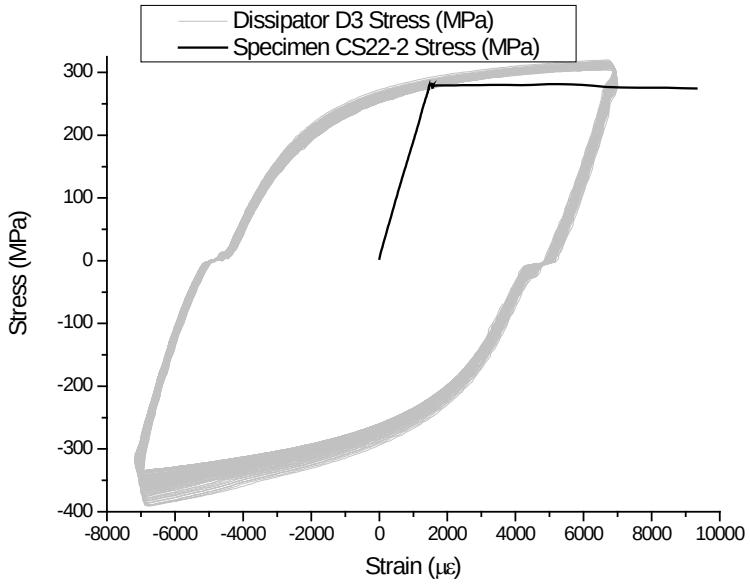

Figure 128. Comparison between stress-strain plots for the 22 mm core bar (CS22-2) and for dissipator D3. First part

Figure 129 and Figure 130 show the "time histories" of the semi-sum and of the semi- difference, respectively, of the axial strains measured in the tube by strain gauges 16 and 17 (see Table 9, Figure 60 and Figure 58). The semi-sum represents the strain due to the axial force while the semi-difference represents the strain due to the (horizontal) bending moment.

Plots from Figure 129 show that the strain due to the axial force is not negligible. As the test goes on, the strain grows; near the failure (initiation of the progressive slide) the maximum (elongation) strain is about 39×10^{-6}. Such strain corresponds to stress 8.19 MPa; hence by multiplying by the tube area ($\pi\, d_{tu}\, t_{tu} = \pi \times 115 \times 3 = 1084$ mm^2), the axial force carried by the tube is 8877 N. Assuming a linear elastic behavior of the tube-mortar assembly, it is concluded that the axial forces carried by such member are about two times this value. Comparison with

Figure 127 shows that about 14% of the tension force is carried by the casing.

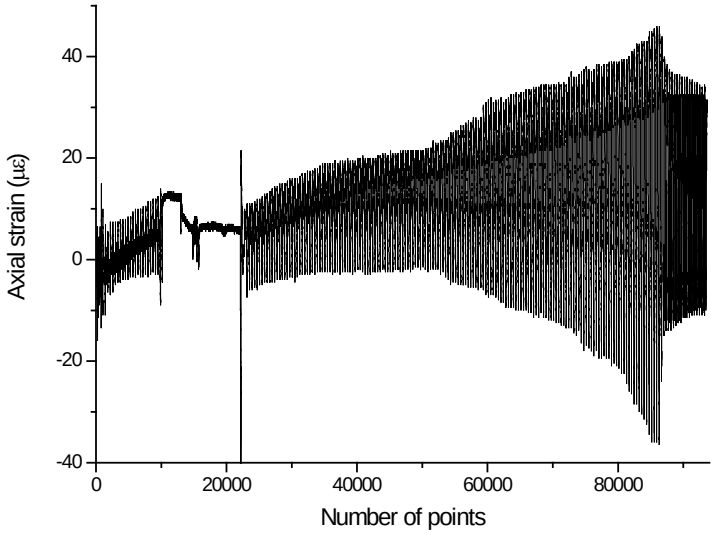

Figure 129. Axial strain of the mid section for dissipator D3 ([channel 16 + channel 17] / 2). First part

Comparison between plots from Figure 129 and Figure 130 show that the (horizontal) bending is less relevant than the axial behavior. It is due to the restrain to the local buckling of the bare end parts of the core by the intermediate supports (see Figure 115).

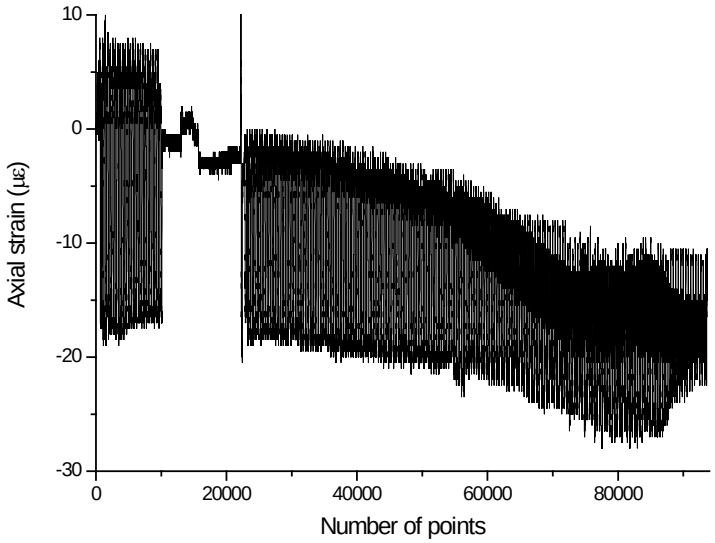

Figure 130. Horizontal bending strain of the mid section for dissipator D3 ([channel 16 – channel 17] / 2). First part

Since a big number of points are involved in Figure 129 and Figure 130 (93691), only global conclusions can be drawn. To obtain more precise deductions, shorter intervals (corresponding to the rather stationary phase of the test) are plotted individually in Figure 131 (axial strain) and Figure 132 (bending strain).

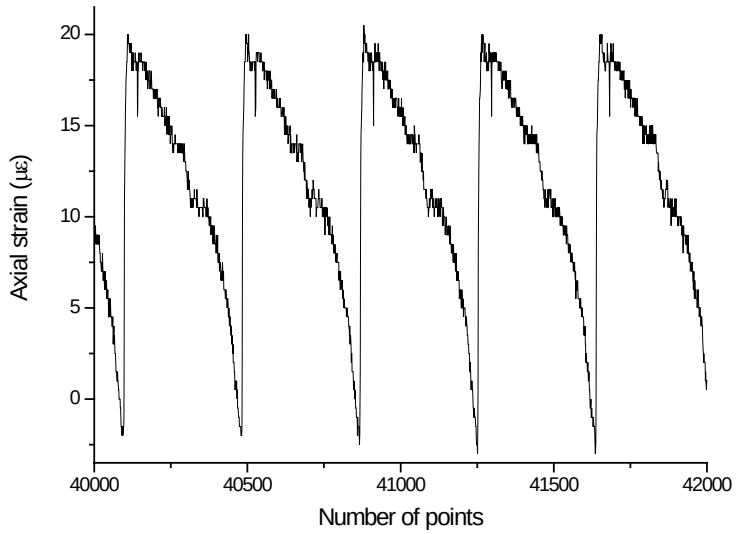

Figure 131. Horizontal axial strain of the mid section for dissipator D3 ([channel 16 + channel 17] / 2). Mid cycles. First part

Comparison between Figure 131 and Figure 132 shows that the axial strain behaves significantly more irregularly than the bending strain. This last is generated by the (horizontal) buckling arising during each cycle and has no close relation with the transfer of axial stresses during the compression. Globally speaking, Figure 76 and Figure 77 (for dissipator D1) and Figure 106 and Figure 107 (for dissipator D2) allow deriving similar conclusions.

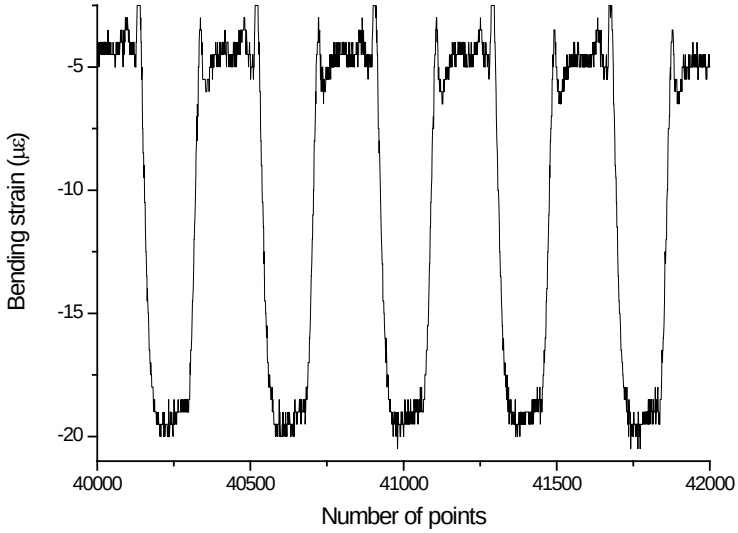

Figure 132. Horizontal bending strain of the mid section for dissipator D3 ([channel 16 – channel 17] / 2). Mid cycles. First part

Plots Figure 131 show that the behaviors in the loading and unloading branches as well as in the elongation and shortening regions are clearly different each other. However, it would be useful to distinguish in between the cases when the dissipator is tensioned or compressed. To further clarify this issue the axial strain is plotted in Figure 133 together with the force in the jack (channel 7, see Table 9 and Figure 58).

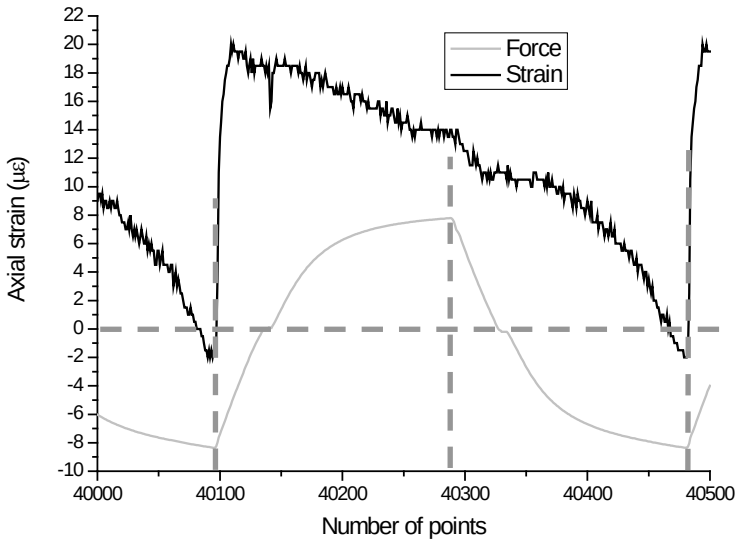

Figure 133. Horizontal axial strain of the mid section for dissipator D3 ([channel 16 + channel 17] / 2) and axial force in the jack (channel 7). Mid cycles. First part

Plots from Figure 133 show that:

- During the unloading compression branch, the axial strain grows (towards elongation) extremely fast (mostly at the beginning).
- During the loading tension branch, the axial strain in the tube decreases smoothly but does not become zero. It indicates that there is a permanent friction (i.e. it keeps even during the tension periods) between the mortar and the core.
- During the unloading tension branch, the axial strain in the tube decreases (faster than in the previous phase) but does not become zero. It indicates again that there is a permanent friction between the mortar and the core.
- During the loading compression branch, the axial strain decreases (towards shortening). Near the peak, the decreasing is particularly relevant; it confirms that this peak is highly contributed by the shear stress transfer from the core to the mortar.

Figure 134 and Figure 135 show the horizontal and vertical displacements of the mid section of dissipator D3 as measured by sensors 4 and 3, respectively (see Table 9, Figure 60 and Figure 58).

Plots from Figure 134 and Figure 135 show that the mid section experienced relevant transverse displacements, both horizontal and vertical. Comparison between Figure 134 and Figure 135 shows that the vertical displacements are bigger than the horizontal ones.

To assess the correlation between the horizontal and vertical displacements of the mid section, Figure 136 shows the horizontal and vertical displacements of such section of dissipator D3 (first part) as measured by sensors 4 and 3, respectively (see Table 9 and Figure 58).

Figure 136 shows that, despite a certain erratic path, the maximum values for horizontal and vertical displacements are near coincident (for each cycle).

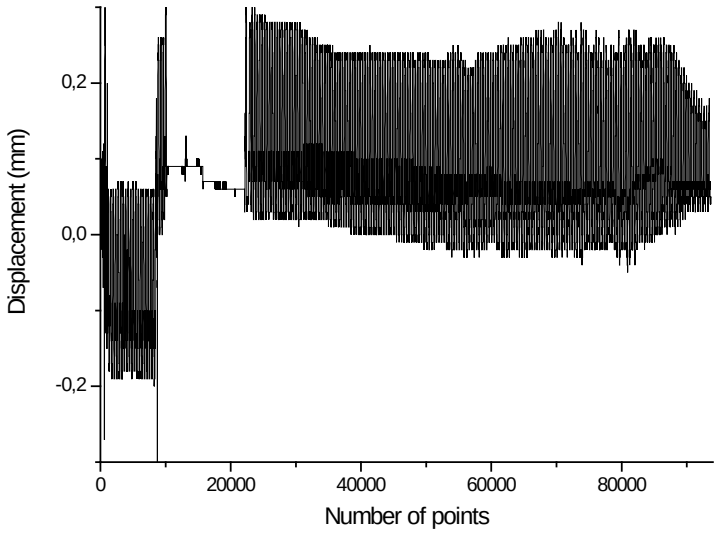

Figure 134. Horizontal displacements of the mid section for dissipator D3 (channel 4). First part

Figure 137 displays the difference between the longitudinal displacements of both ends of the encasing tube measured by displacement transducers 8 (right) and 9 (left), respectively (see Table 9 and Figure 58).

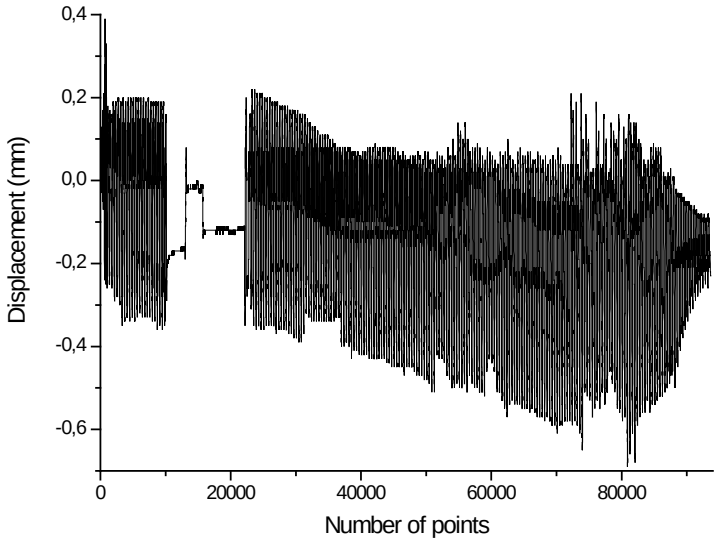

Figure 135. Vertical transverse displacements of the mid section for dissipator D3 (channel 3). First part

Plots from Figure 137 aim to represent the elongation experienced by the tube. Prior to the sudden slide the range lies between about -6 and +8 mm, hence, the maximum (average along the tube) strain would be about $6.38\ 10^{-3}$; this value is two orders of magnitude bigger than the one shown in Figure 129. Therefore, these registered displacements can not correspond to the actual longitudinal displacements of the extremes of the bar; they appear to be highly contributed by the (horizontal) rotations experienced by both connectors (this fact could be easily observed during the experiment).

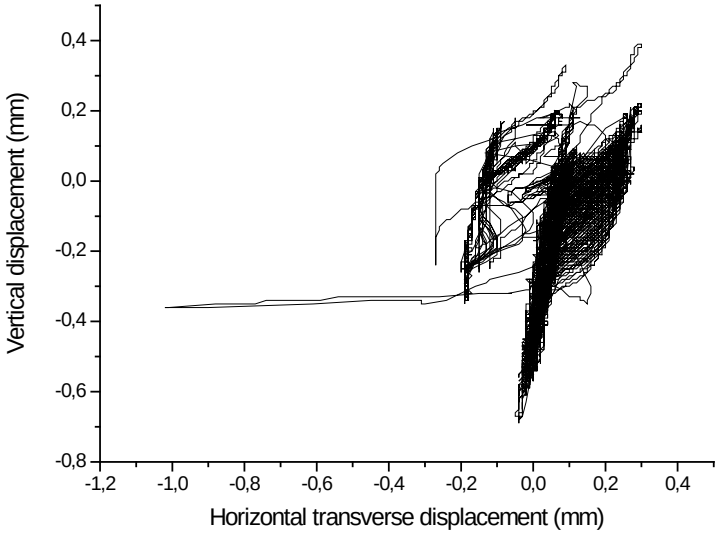

Figure 136. Vertical vs. transverse displacements of the mid section for dissipator D3 (channel 4 vs. channel 3). First part

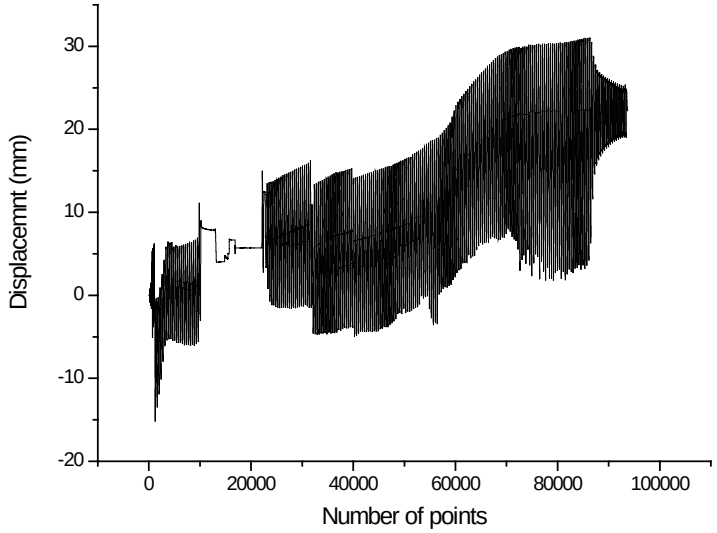

Figure 137. Relative longitudinal displacement between the ends of the casing for dissipator D3 (channel 8 + channel 9). First part

5.5.3 Results for dissipator D3. Second part

The displacement sensors 1, 2, 8 and 9 (see Table 9 and Figure 58) were not installed; hence, only the jack sensors (displacement transducer 6 and load cell 7), the mid section strain gauges (16 and 17) and displacement transducers (3 and 4) provided meaningful results.

Figure 138 displays the time history of the jack force (for dissipator D3) as measured by channel 7. Plots in Figure 138 show a rather stable hysteretic behavior. Once the maximum amplitude

displacement is reached (after about point 850, see Figure 59), the force amplitude tends to decrease rather smoothly until reaching a stationary value (after about point 35000). This is due to a progressive detachment from the inner core and the surrounding mortar. The difference between the maximum positive and negative values that was observed in Figure 66 (this difference was explained by the contribution of the mortar through the friction forces generated during the compression when the core tries to buckle against the mortar) can also be seen in Figure 138. After (about) cycle 60000 there are only compressive forces as the core breaks.

Since a big number of points are involved in Figure 138 (63458), only global conclusions can be drawn. To obtain more precise deductions, a shorter interval is plotted individually in Figure 139.

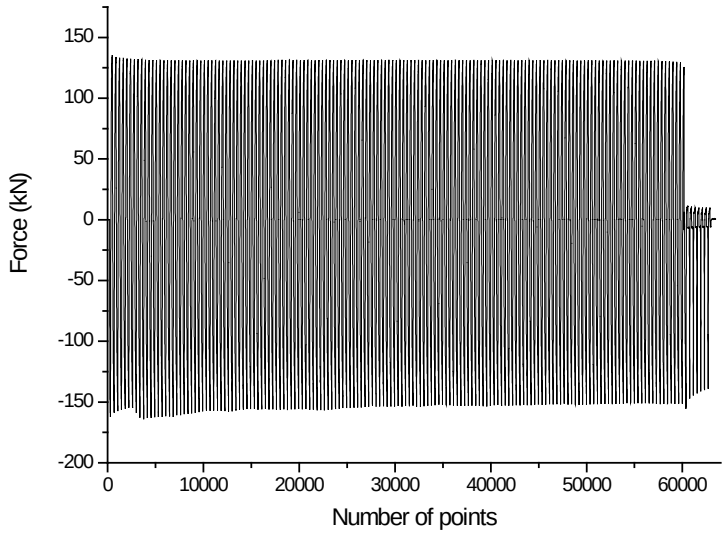

Figure 138. Jack force for dissipator D3 (channel 7). Second part

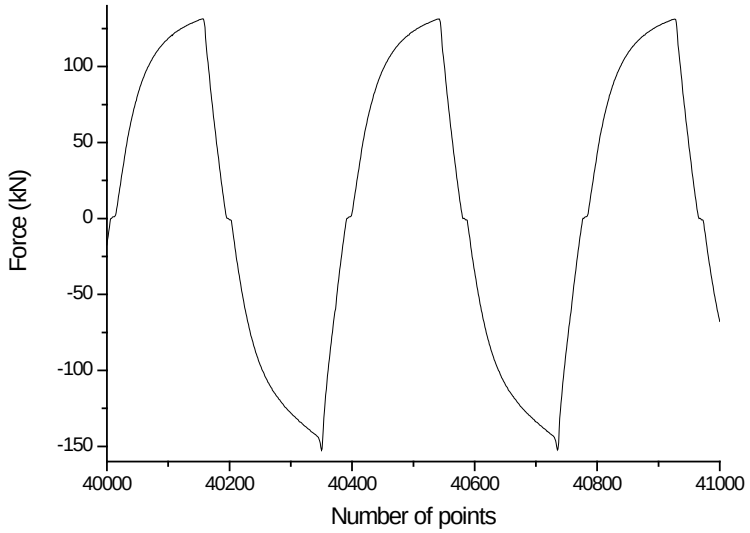

Figure 139. Jack force for dissipator D3 (channel 7). Mid cycles. Second part

The observation of Figure 139 allows deriving some relevant conclusions:

- Every time the force (in the jack) reverts, the plot of the core elongation (channel 7) exhibits a horizontal jump (the jack keeps moving without any force change). This is due to the gap in the pin-joint connections between the dissipator and the end supports (see Figure 57 and Figure 58). This fact was also observed from Figure 118 and Figure 119.
- The buckling of the core does not affect significantly the force plots.
- In Figure 139 the last segment of the compression (plastic) loading branches exhibit a rather sudden increase leading to a higher peak (and even a clear reversal in the curvature). This is due to the mortar contribution and confirms the conclusion derived from Figure 138.

To facilitate the interpretation of Figure 141 some auxiliary lines have been drawn similarly to Figure 71.

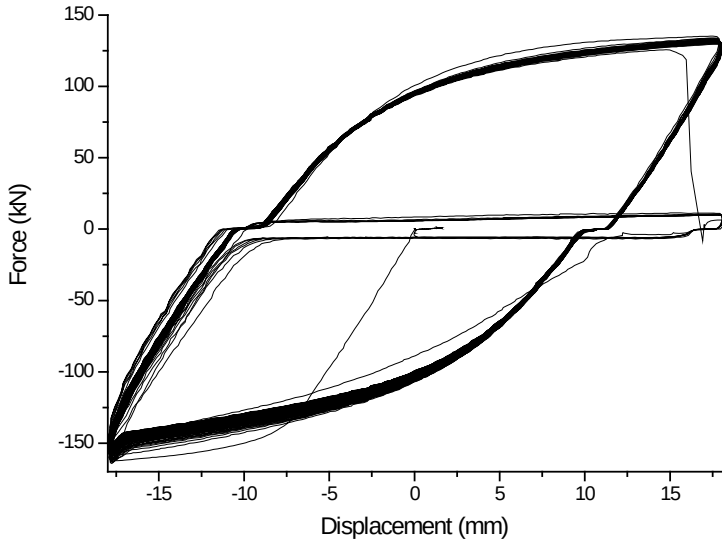

Figure 140. Hysteresis loops for dissipator D3 (channel 7 vs. channel 6). Second part

Figure 140 shows the hysteretic behavior (jack force -Channel 7- vs. jack displacement -Channel 6-, see Table 9 and Figure 58) of dissipator D3 (second part). The irregular loops correspond to the final part of the test (see Figure 59). To confirm this fact Figure 141 shows the regular cycles (points 1 to 60000).

Similarly to Figure 71, Figure 101, Figure 126 and Figure 127, the following trends can be observed from Figure 141:

- The hysteretic behavior is stable. The force amplitude decreases after the first cycles but tends to stabilize quite fast.
- The lower plastic branch (compression) is more linear and steeper than the upper one (tension); the compression peaks are higher than the tension ones. In fact, the tension behavior is more regular (it is due to the Bauschinger effect [Akiyama, 1980]) while the compression is affected by the mortar contribution (mostly near the peak).
- The horizontal jump due to the gap in the connections can be also observed (yet is clearly bigger than in the dissipator D2, see Figure 101).

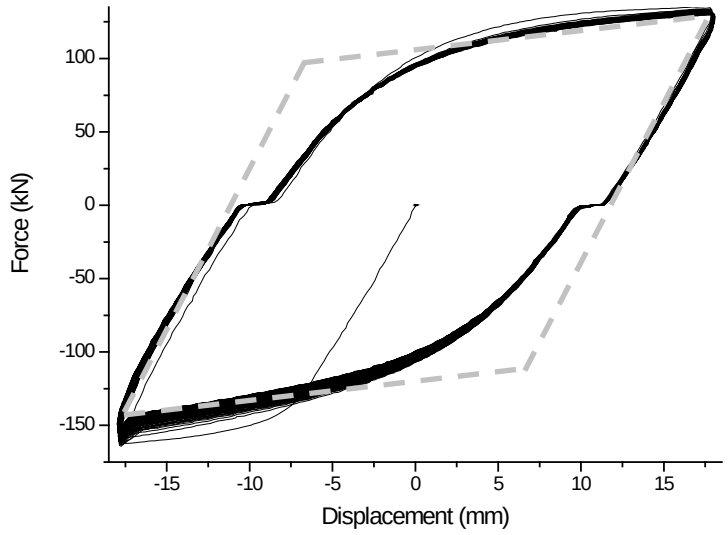

Figure 141. Regular hysteresis loops for dissipator D3 (channel 7 vs. channel 6). Second part

Figure 142 displays the stress-strain plots from Figure 54 (for the steel specimen CS22-2) and the hysteresis loops for dissipator D3 (second part, Figure 140). The strains for the dissipators have been obtained by dividing the relative displacement between both ends of the core (channel 6') by the distance between the centers of both (end) pins (see Figure 3, Table 1 and Figure 57).

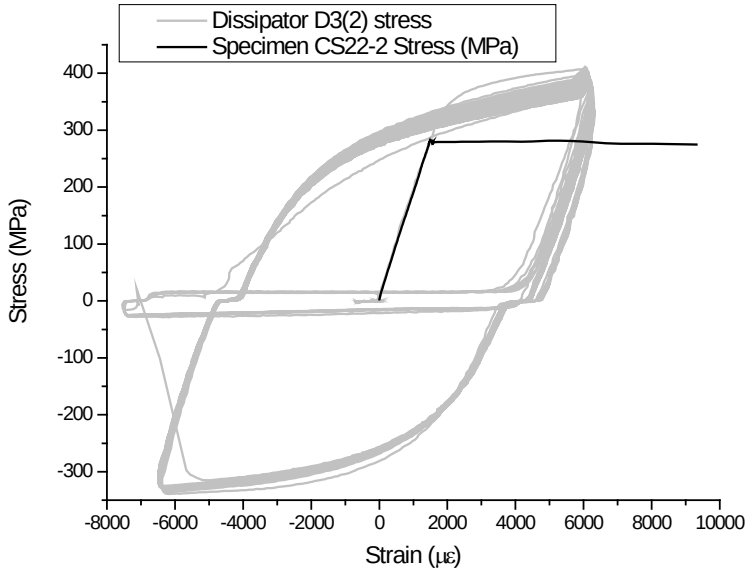

Figure 142. Comparison between stress-strain plots for the 22 mm core bar (CS22-2) and for dissipator D3. Second part

Plots from Figure 142 show that the elastic stiffness of the steel core (in tension) is similar to the one of the dissipators. Comparison among the plots of the core and of the device shows that the amount of consumed skeleton energy [Kato, Akiyama, Yamanouchi, 1973] is rather moderate since the plastic excursion is small (see Figure 51 and Figure 52). The fit between both yielding points (in the stationary phase) is rather satisfactory. Globally speaking, Figure 73 (for dissipator

D1), Figure 103 (for dissipator D2) and Figure 128 and Figure 142 (for dissipator D3) allow deriving similar conclusions. It is remarkable that the maximum strain in the dissipator lies in the horizontal plastic branch of the stress-strain law (far from the hardening branch, see Figure 54).

Figure 143 and Figure 144 show the "time histories" of the semi-sum and of the semi- difference, respectively, of the axial strains measured in the tube by strain gauges 16 and 17 (see Table 9, Figure 60 and Figure 58). The semi-sum represents the strain due to the axial force while the semi-difference represents the strain due to the (horizontal) bending moment.

Plots from Figure 143 show that the strain due to the axial force is not negligible. After (about) point 60000 the core broke and, hence, the amplitude grew as most of the force was carried by the casing. As the test goes on, the maximum elongation strain grows; near the failure (core breaking) the maximum (elongation) strain is about 60×10^{-6}. Such strain corresponds to stress 12.6 MPa; hence, by multiplying by the tube area ($\pi\, d_{tu}\, t_{tu} = \pi \times 115 \times 3 = 1084$ mm^2) the axial force carried by the tube is 13.66 kN. Assuming a linear elastic behavior of the tube-mortar assembly, the axial forces carried by such member are about two times this value. Comparison with Figure 141 shows that about 15% of the tension force is carried by the casing.

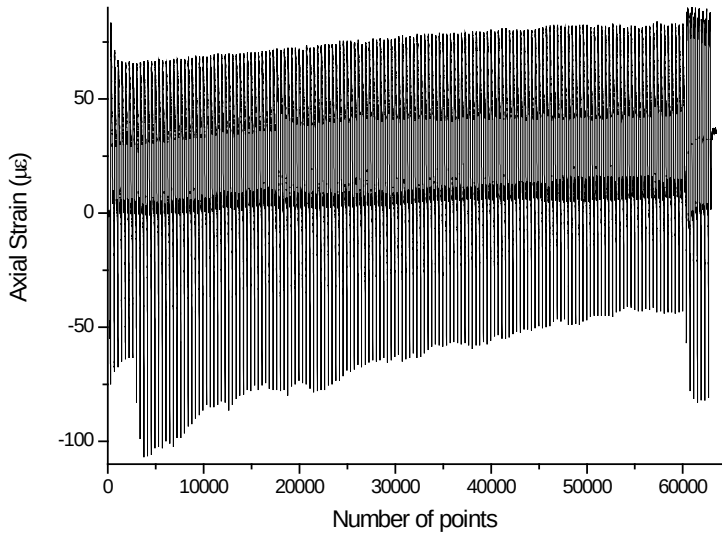

Figure 143. Axial strain of the mid section for dissipator D3 ([channel 16 + channel 17] / 2). Second part

Comparison between plots from Figure 143 and Figure 144 show that the (horizontal) bending is less relevant than the axial behavior. It is due to the restrain to the local buckling of the bare end parts of the core by the intermediate supports (see Figure 115).

Since a big number of points are involved in Figure 143 and Figure 144 (63458), only global conclusions can be drawn. To obtain more precise deductions, shorter intervals (corresponding to the rather stationary phase of the test) are plotted individually in Figure 145 (axial strain) and Figure 146 (bending strain).

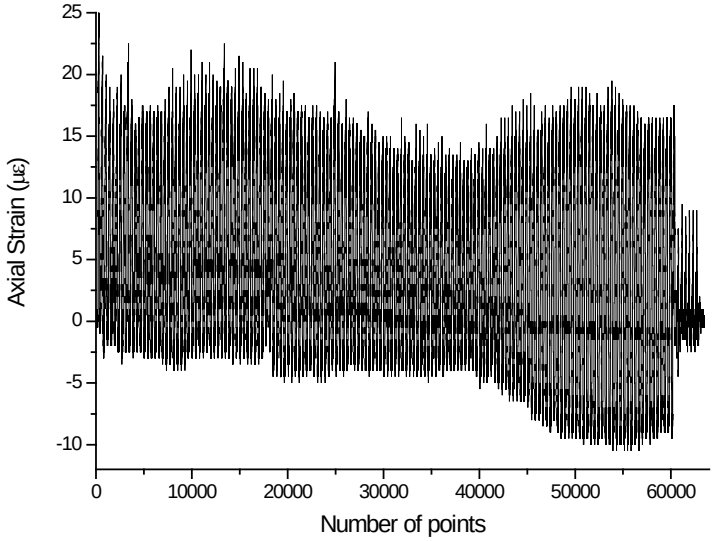

Figure 144. Horizontal bending strain of the mid section for dissipator D3 ([channel 16 – channel 17] / 2). Second part

Comparison between Figure 145 and Figure 146 shows that the axial strain behaves significantly more irregularly than the bending strain. This last is generated by the (horizontal) buckling arising during each cycle and has no close relation with the transfer of axial stresses during the compression. Globally speaking, Figure 76 and Figure 77 (for dissipator D1), Figure 106 and Figure 107 (for dissipator D2) and Figure 129 and Figure 130 (for dissipator D3) allow deriving similar conclusions.

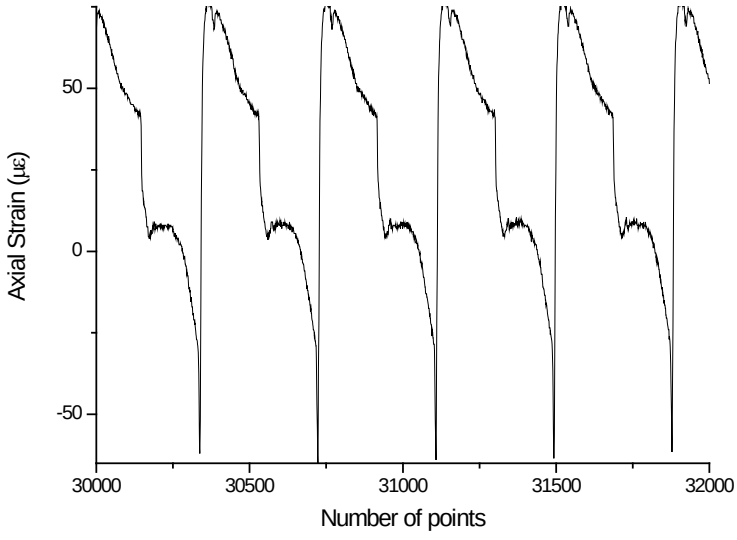

Figure 145. Horizontal axial strain of the mid section for dissipator D3 ([channel 16 + channel 17] / 2). Mid cycles. Second part

Plots Figure 145 show that the behaviors in the loading and unloading branches as well as in the elongation and shortening regions are clearly different each other. However, it would be useful to distinguish in between the cases when the dissipator is tensioned or compressed. To further clarify

this issue the axial strain is plotted in Figure 147 together with the force in the jack (channel 7, see Table 9 and Figure 58).

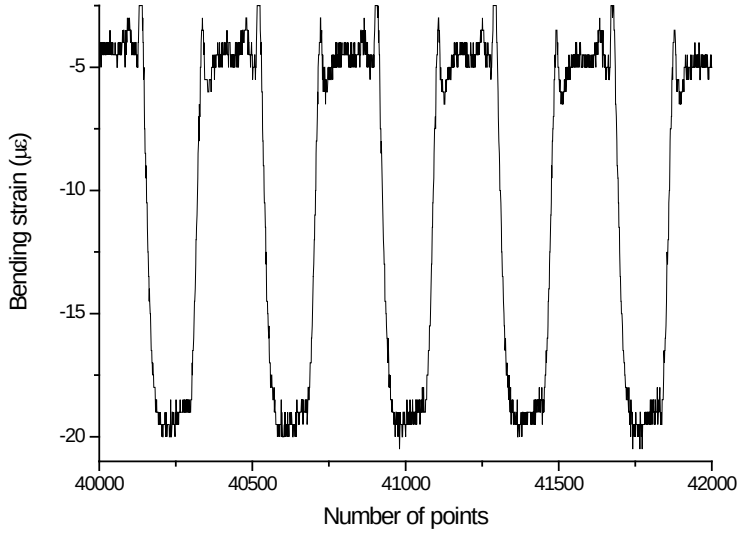

Figure 146. Horizontal bending strain of the mid section for dissipator D3 ([channel 16 – channel 17] / 2). Mid cycles. Second part

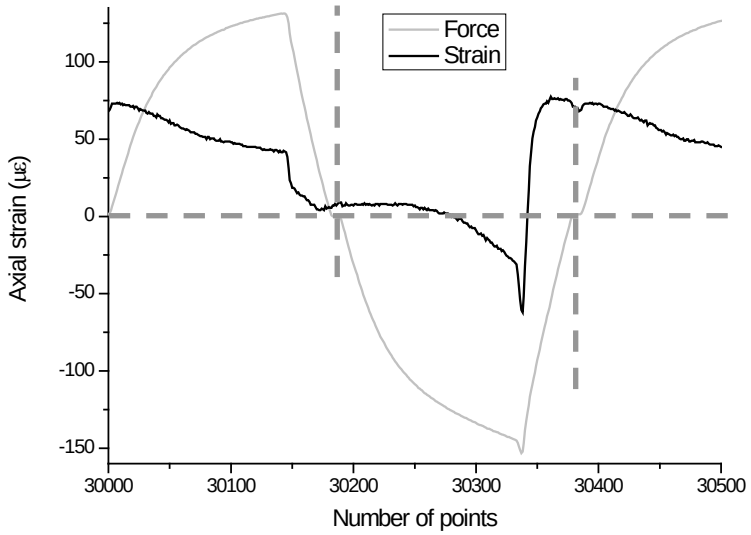

Figure 147. Horizontal axial strain of the mid section for dissipator D3 ([channel 16 + channel 17] / 2) and axial force in the jack (channel 7). Mid cycles. Second part

Plots from Figure 147 show that:

- During the loading tension branch, the axial strain in the tube decreases smoothly but does not become zero. It indicates that there is a permanent friction (i.e. keeps even during the tension periods) between the mortar and the core.
- During the unloading tension branch, the axial strain in the tube decreases (faster than in the previous phase) but does not become zero. It indicates again that there is a permanent friction

between the mortar and the core.

- During the loading compression branch, the axial strain decreases (towards shortening). Near the peak, the decreasing is particularly relevant; it confirms that this peak is highly contributed by the shear stress transfer from the core to the mortar.
- During the unloading compression branch, the axial strain grows (towards elongation) extremely fast (mostly at the beginning).

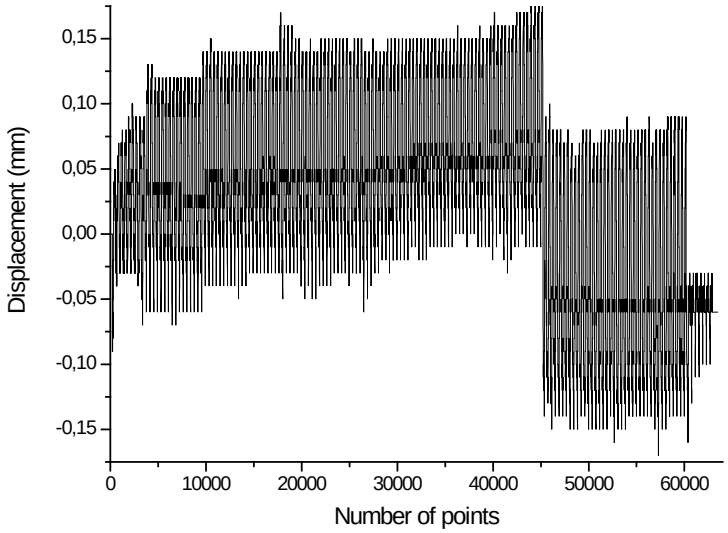

Figure 148. Horizontal displacements of the mid section for dissipator D3 (channel 4). Second part

Figure 148 and Figure 149 show the horizontal and vertical displacements of the mid section of dissipator D3 as measured by sensors 4 and 3, respectively (see Table 9, Figure 60 and Figure 58).

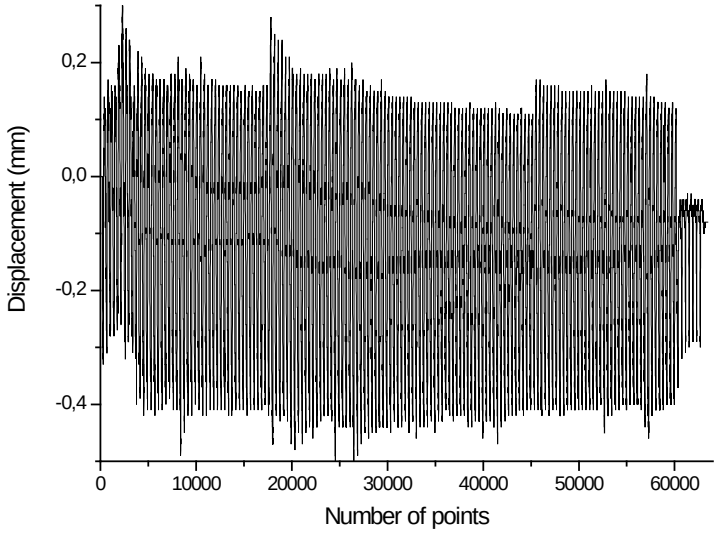

Figure 149. Vertical transverse displacements of the mid section for dissipator D3 (channel 3). Second part

Plots from Figure 148 and Figure 149 show that the mid section experienced relevant transverse displacements, both horizontal and vertical. Comparison between Figure 148 and Figure 149

shows that the vertical displacements are bigger than the horizontal ones.

Figure 150 shows the horizontal and vertical displacements of the mid section of dissipator D3 (second part) as measured by sensors 4 and 3, respectively (see Table 9 and Figure 58).

Plots from Figure 150 show a similar behavior than the one from Figure 136.

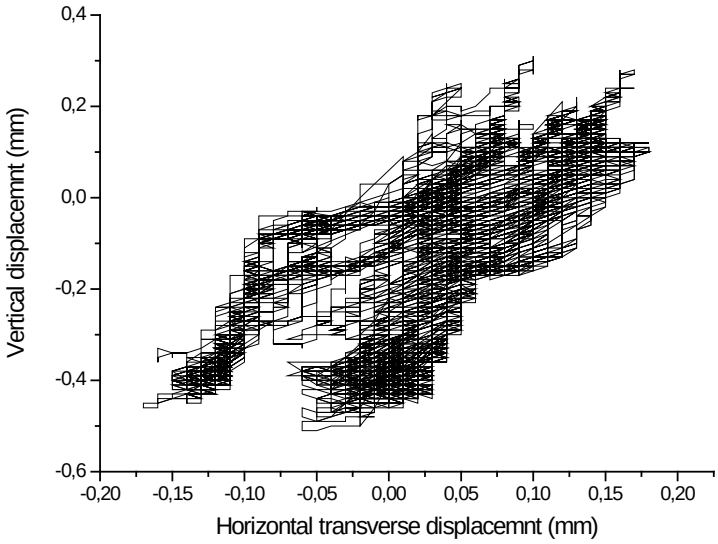

Figure 150. Vertical vs. transverse displacements of the mid section for dissipator D3 (channel 4 vs. channel 3). Second part

5.5.4 After-test remarks for dissipator D3

As described previously, final failure came for breakage of the core near the mid section. After concluding this test, the broken core was pulled out and the dissipator was cut longitudinally in two equal halves to observe the status of the mortar. Figure 151 displays representative parts of the mortar, the rubber and the core.

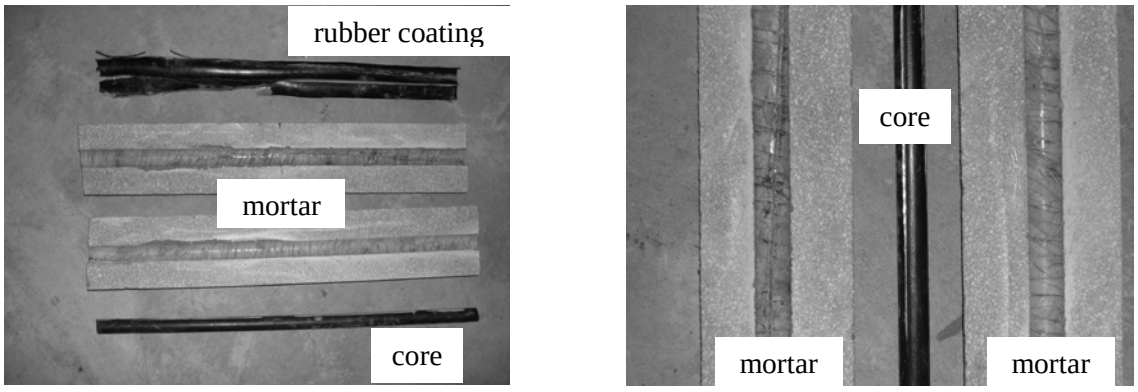

Figure 151. Mortar and core of dissipator D3

Figure 151 shows that the mortar is apparently in good condition, even in the near vicinity of the core; it means that the transversal compressive forces due to high buckling modes (rippling, Figure 15) were not able to damage locally the mortar.

According to Figure 151 some eccentricity of the core hole was observed; it ranged between 2 and 4 mm. Such values lie inside the range considered for buckling analysis (e_1 = 20 mm, see Figure 14). The fact that the bigger eccentricity corresponds to the thinner tube might be due to its higher flexibility. The cover of the core (Teflon, grease and rubber) was in good condition (see Figure 151, upper left). The core was permanently bent; it is shaped like a warped sinusoidal wave whose wavelength ranges in between 300 and 600 mm and whose amplitude reaches up to 3 mm. Since the lateral forces exerted by the core were unable to bend the casing (filled tube) and the surrounding mortar is not damaged, is obvious that this permanent curvature is due to the compression of the core cover, particularly the rubber layer.

5.6 Testing of dissipator D4

5.6.1 Testing remarks

This subsection describes the most relevant facts for the experiments of dissipator D4. As described previously, this dissipator was tested prior to D3.

Figure 152 displays the testing rig for dissipator D4.

Steel and can wedges (similar to the ones in dissipator D2) were used to restrain the slide and the rotation in the (hinged) connections as shown by Figure 153.

After 24 cycles a premature failure for sliding of the right connector arose. This incident was solved by re-tightening up the bolts (exceeding about 20% the recommended pre-stressing force) and the experiment was resumed. Failure came by local buckling of the right end of the core after 49 cycles (see Table 10); the core was not completely broken. Next two subsections present the results of the two parts of the experiment (prior and after that incident), respectively.

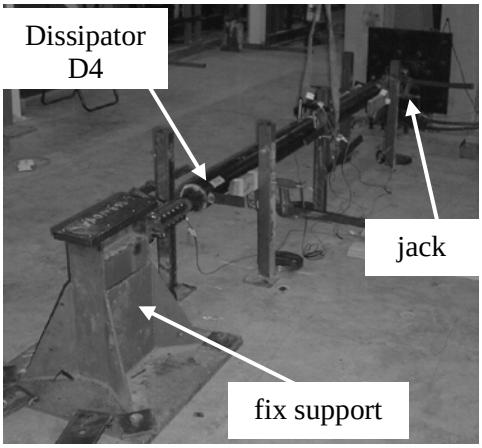

Figure 152. Cyclic testing of dissipator D4

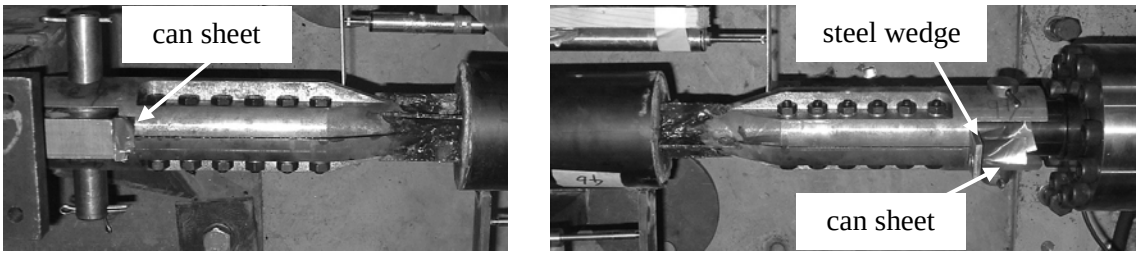

Figure 153. Details of the testing rig for dissipator D4

5.6.2 Results for dissipator D4. First part

The most relevant plots of the first part of test of dissipator D4 are displayed in this subsection. In all the figures, positive values correspond either to elongation (for strain gauges and displacement transducers) or to tension (for the load cell).

Figure 154 shows the time history elongation of the steel core (as measured by channels 1 and 2, see Table 9 and Figure 58) of the dissipator D4 (first part).

Figure 154 shows a rather regular behavior. The last slide generates a sudden (final) increment of elongation. The drift is due to rotations of both ends of the device. A relevant overall conclusion is that the measures taken by the displacement transducers are useful.

Figure 155 displays the time history of the jack force (for dissipator D4) as measured by channel 7. Plots in Figure 155 show a rather stable hysteretic behavior. The difference between the maximum positive and negative values that was observed (for dissipator D1) in Figure 66 (this difference was explained by the contribution of the mortar through the friction forces generated during the compression when the core tries to buckle against the mortar) can be also seen in Figure 155.

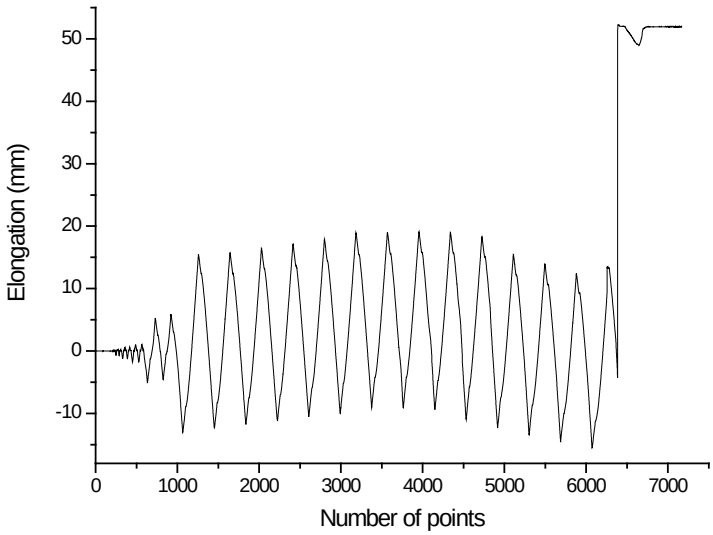

Figure 154. Core elongation for dissipator D4 (channel 1 + channel 2). First part

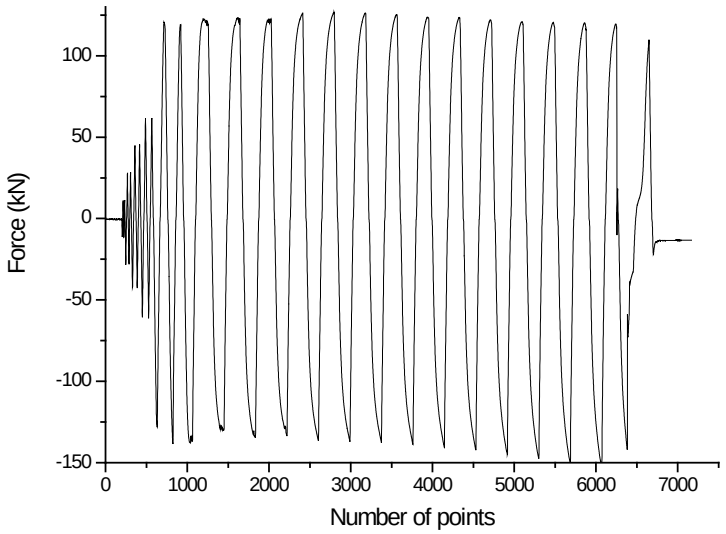

Figure 155. Jack force for dissipator D3 (channel 7). First part

Figure 156 shows the hysteretic behavior (jack force -Channel 7- vs. jack displacement -Channel 6-, see Table 9 and Figure 58) of dissipator D4 (first part).

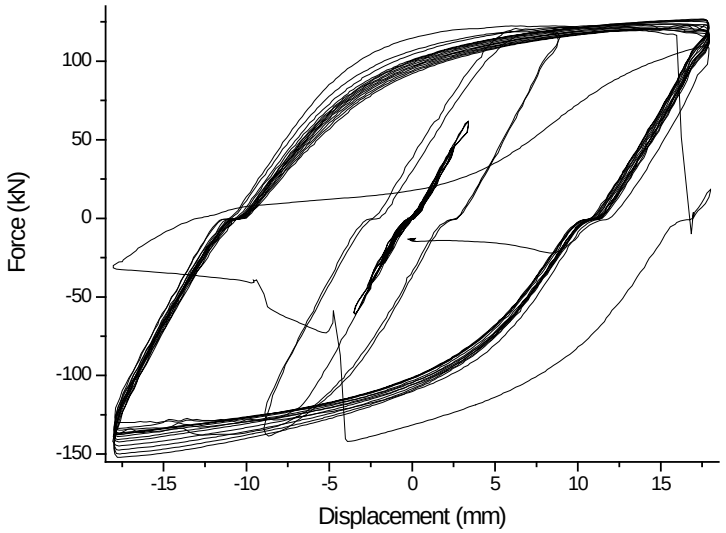

Figure 156. Hysteresis loops for dissipator D4 (channel 7 vs. channel 6). First part

Plots from Figure 156 show a rather stable hysteretic behavior along the whole number of cycles (24). Comparison with Figure 99 (dissipator D2) shows that (as shown by Figure 125 and Figure 140, for dissipator D3) the slides in the connections are larger; it can be due to the greater forces involved (as the diameter of the core is bigger). The irregular loops correspond to the final sliding; Figure 157 displays the remaining regular loops. To facilitate the interpretation of Figure 157 some auxiliary lines have been drawn.

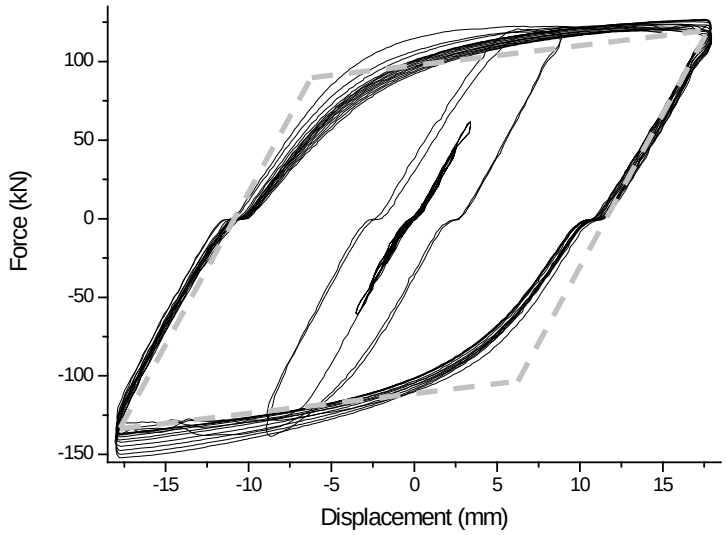

Figure 157. Regular hysteresis loops for dissipator D4 (channel 7 vs. channel 6). First part

Similarly to Figure 71, Figure 101, Figure 126, Figure 127 and Figure 141, the following trends can be observed from Figure 157:

- The hysteretic behavior is rather stable.
- The horizontal jump due to the gap in the connections can be also observed (yet is clearly bigger than in the dissipator D2, see Figure 101).

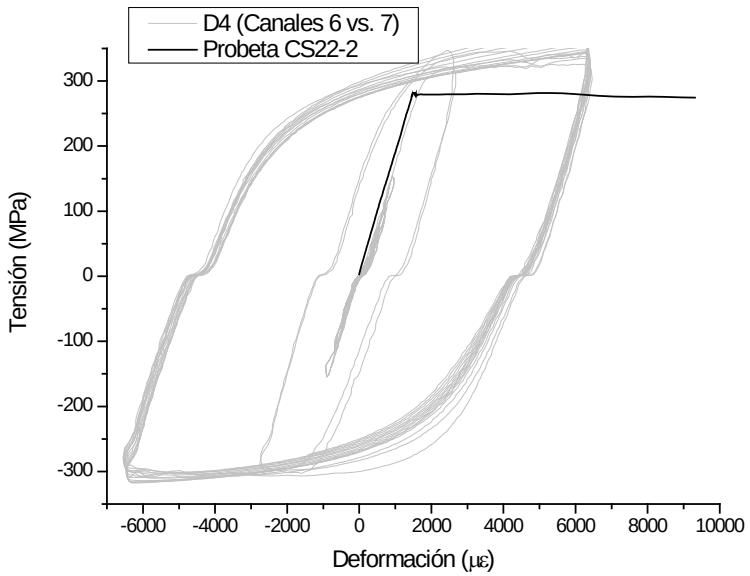

Figure 158. Comparison between stress-strain plots for the 22 mm core bar (CS22-2) and for dissipator D4. First part

Figure 158 display the stress-strain plots from Figure 54 (for the steel specimen CS22-2) and the hysteresis loops for dissipator D4 (Figure 157, corresponding to the first part of the test after eliminating the last irregular cycles). The strains for the dissipators have been obtained by dividing the displacement of the jack (channel 6') by the distance between the centers of both (end) pins (see Figure 3, Table 1 and Figure 57). The values for channel 6' have been calculated

similarly to dissipators D1, D2 and D3 (by eliminating the influence of the flexibility of the interposed elements).

Plots from Figure 158 show that the elastic stiffness of the steel core (in tension) is similar to the one of the dissipators. Comparison among the plots of the core and of the device shows that the amount of consumed skeleton energy [Kato, Akiyama, Yamanouchi, 1973] is rather moderate since the plastic excursion is small (see Figure 51 and Figure 52). The fit between both yielding points is rather poor; a possible explanation is a certain lack of uniformity along the whole core length. Globally speaking, Figure 73 (for dissipator D1), Figure 103 (for dissipator D2), Figure 128 and Figure 142 (for dissipator D3) and Figure 158 (for dissipator D3) allow deriving similar conclusions. It is remarkable that the maximum strain in the dissipator lies in the horizontal plastic branch of the stress-strain law (far from the hardening branch, see Figure 54).

Figure 159 and Figure 160 show the "time histories" of the semi-sum and of the semi- difference, respectively, of the axial strains measured in the tube by strain gauges 16 and 17 (see Table 9, Figure 60 and Figure 58). The semi-sum represents the strain due to the axial force while the semi-difference represents the strain due to the (horizontal) bending moment.

Plots from Figure 159 show that the strain due to the axial force is not negligible. After (about) point 1100, the amplitude decreases suddenly; it corresponds to the initial debonding between core and mortar. As the test goes on, the strain grows; near the failure (initiation of the progressive slide) the maximum (tension) strain is about 22×10^{-6}. Such strain corresponds to stress 4.62 MPa; hence, by multiplying by the tube area ($\pi\, d_{tu}\, t_{tu} = \pi \times 115 \times 3 = 1084$ mm^2) the axial force carried by the tube is 5.01 kN. Assuming a linear elastic behavior of the tube-mortar assembly, the axial forces carried by such member are about two times this value. Comparison with Figure 157 shows that about 4% of the tension force is carried by the casing.

Comparison between plots from Figure 159 and Figure 160 show that the (horizontal) bending is as relevant as the axial behavior.

Comparison between Figure 159 and Figure 160, by one side, and Figure 145 and Figure 146, by the other side, shows a big similarity and, hence, allows deriving similar conclusions.

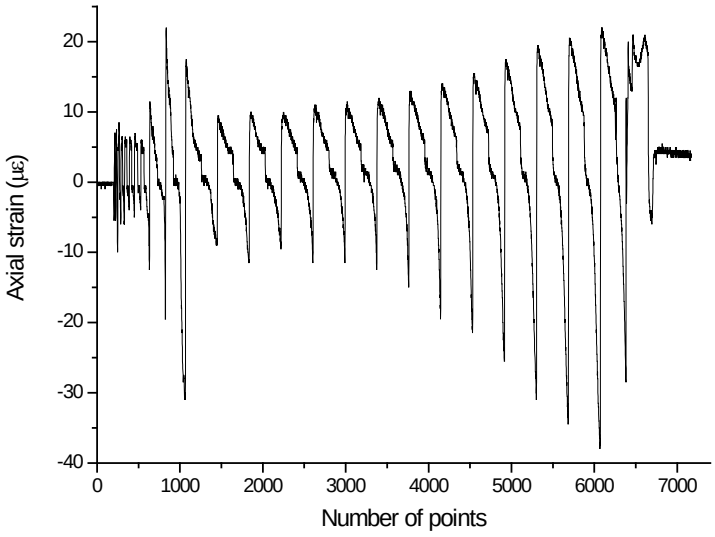

Figure 159. Axial strain of the mid section for dissipator D4 ([channel 16 + channel 17] / 2). First part

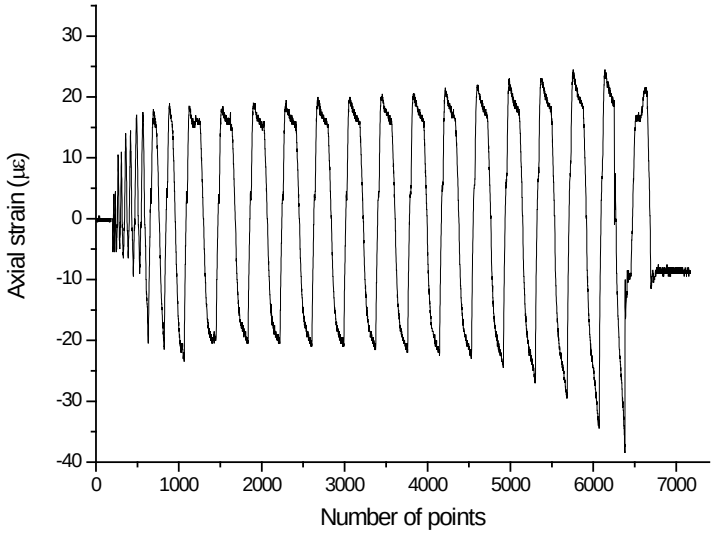

Figure 160. Horizontal bending strain of the mid section for dissipator D4 ([channel 16 – channel 17] / 2). First part

Figure 161 and Figure 162 show the horizontal and vertical displacements of the mid section of dissipator D3 as measured by sensors 4 and 3, respectively (see Table 9, Figure 60 and Figure 58).

Plots from Figure 161 and Figure 162 show that the displacements are significantly bigger than those displayed by Figure 136 and Figure 150 (for dissipator D3); the difference being more relevant for the vertical components. It confirms the usefulness of the intermediate supports (Figure 116). The horizontal displacement transducer (sensor 4) has reached its maximum capacity (see Table 9) during the last cycles; it happened also (but less intensely) to the vertical displacement transducer (sensor 3).

To assess the correlation between the horizontal and vertical displacements of the mid section, Figure 163 shows the horizontal and vertical displacements of the mid section of dissipator D4 (first part) as measured by sensors 4 and 3, respectively (see Table 9 and Figure 58).

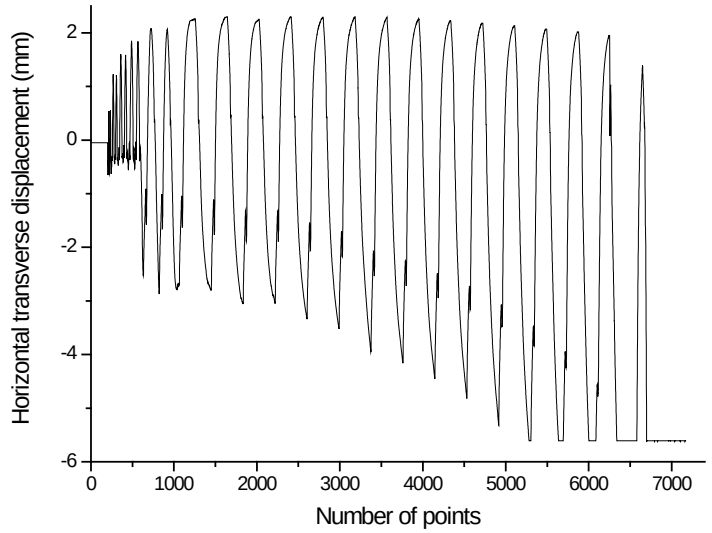

Figure 161. Horizontal displacements of the mid section for dissipator D4 (channel 4). First part

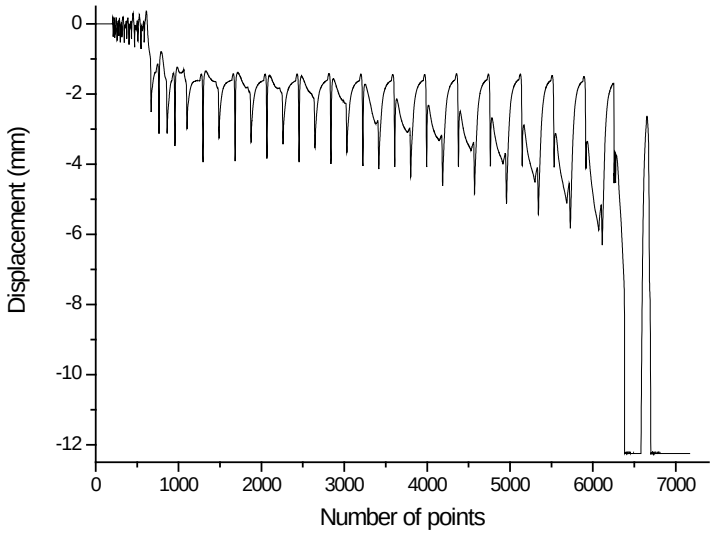

Figure 162. Vertical transverse displacements of the mid section for dissipator D4 (channel 3). First part

Figure 163 shows that, despite a certain erratic path, the maximum values for horizontal and vertical displacements are near coincident (for each cycle).

Figure 164 displays the difference between the longitudinal displacements of both ends of the encasing tube as measured by displacement transducers 8 (right) and 9 (left), respectively (see Table 9 and Figure 58).

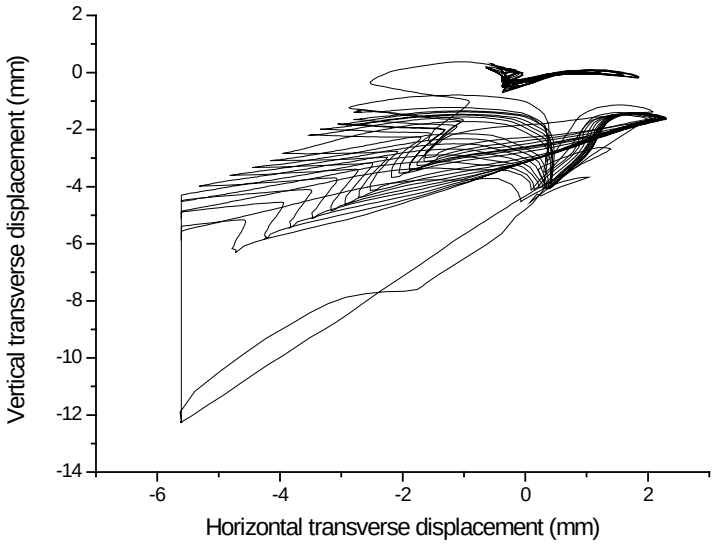

Figure 163. Vertical vs. transverse displacements of the mid section for dissipator D4 (channel 4 vs. channel 3). First part

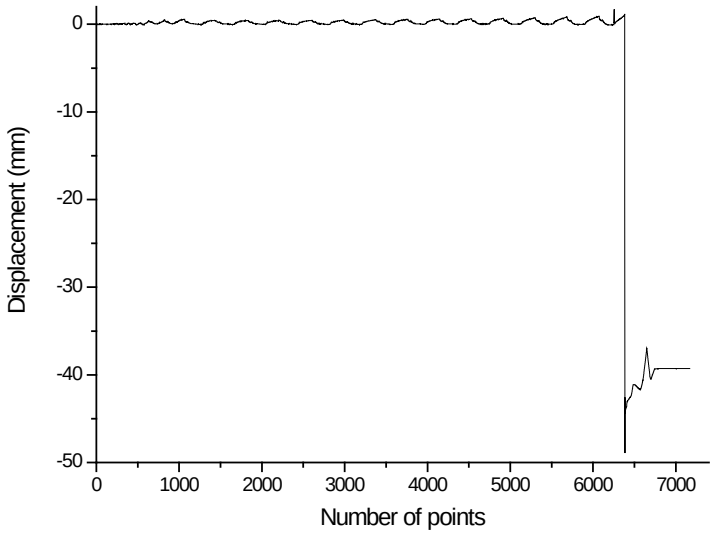

Figure 164. Relative longitudinal displacement between the ends of the casing for dissipator D4 (channel 8 + channel 9). First part

Plots from Figure 164 aim to represent the elongation experienced by the tube. Prior to the sudden slide the range lies between about 0 and 0.7 mm, the maximum (average along the tube) strain would be about 3.19×10^{-4}; this value is one order of magnitude bigger than the one shown by Figure 159. Therefore, these registered displacements can not correspond to the actual longitudinal displacements of the extremes of the bar; they appear to be highly contributed by the (horizontal) rotations experienced by both connectors (this fact could be easily observed during the experiment). This effect is less intense than in dissipator D1 (see Figure 84, Figure 74 and Figure 82).

5.6.3 Results for dissipator D4. Second part

In its turn, this part of the test had another incidence: after a sudden slide in the right connector, the test was interrupted, the bolts were re-tightened up and the experiment continued until the failure (after 49 additional cycles) by local buckling of the right end of the core (see Figure 175). As discussed previously, it is remarkable that the core was not completely broken and some energy dissipation capacity of the device still remained.

The measurements from the two strain gauges at the mid section of the tube (sensors 16 and 17, see Table 9 and Figure 58) were not available during this part of the experiment.

The most relevant plots of the second part of the test of dissipator D4 are displayed in this subsection. In all the figures, positive values correspond either to elongation (for strain gauges and displacement transducers) or to tension (for the load cell).

Figure 165 shows the time history elongation of the steel core (as measured by channels 1 and 2, see Table 9 and Figure 58) of the dissipator D4 (second part).

The relative displacement in Figure 165 aims to represent approximately the axial elongation of the core. Similarly to Figure 154, plots from Figure 165 show a regular behavior except for the sudden slide (about 45 mm) experienced at point 14510; at (about) point 17700 the experiment resumed. A relevant overall conclusion is that the measures taken by the displacement transducers are useful.

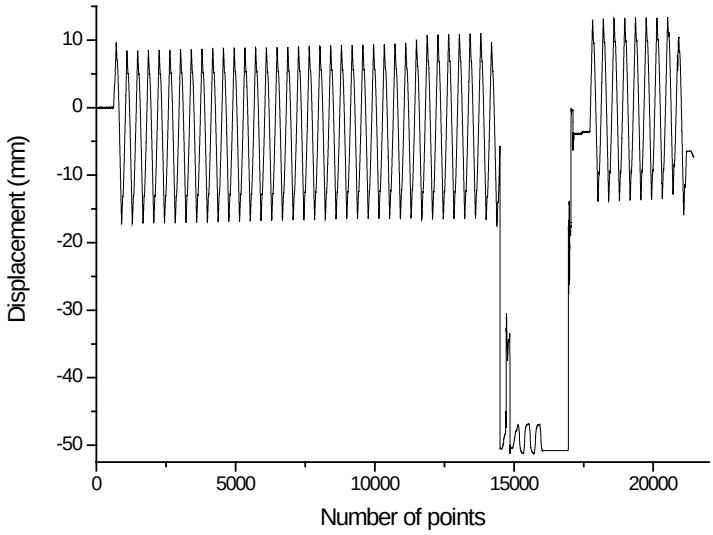

Figure 165. Core elongation for dissipator D4 (channel 1 + channel 2). Second part

Figure 166 displays the time history of the jack force (for dissipator D3) as measured by channel 7. Plots in Figure 166 show a rather stable hysteretic behavior. The difference between the maximum positive and negative values that was observed (for dissipator D1) in Figure 66 (this difference was explained by the contribution of the mortar through the friction forces generated during the compression when the core tries to buckle against the mortar) can also be seen in Figure 166.

Since a big number of points are involved in Figure 166 (21455), only global conclusions can be drawn. To obtain more precise deductions, a shorter interval (corresponding to a stationary phase of the test) is plotted individually in Figure 167.

- Every time the force (in the jack) reverts, the plot of the core elongation (channel 7) exhibits a horizontal jump (the jack keeps moving without any force change). This is due to the gap in the pin-joint connections between the dissipator and the end supports (see Figure 57 and Figure 58). This fact was also observed from Figure 118 and Figure 119. The comparison with the jumps displayed by Figure 67 and Figure 68 (for dissipator D1) shows that the restraints (in both ends of the dissipator) described by Figure 153 have reduced significantly the gap.
- The buckling of the core does not affect significantly the force plots.
- In Figure 167 the last segment of the compression (plastic) loading branches exhibit a rather sudden increase leading to a higher peak (and even a slight reversal in the curvature). This is due to the mortar contribution and confirms the conclusion derived from Figure 166.

The observation of Figure 167 allows deriving some relevant conclusions:

Figure 168 shows the hysteretic behavior (jack force -Channel 7- vs. jack displacement -Channel 6-, see Table 9 and Figure 58) of dissipator D4 (second part).

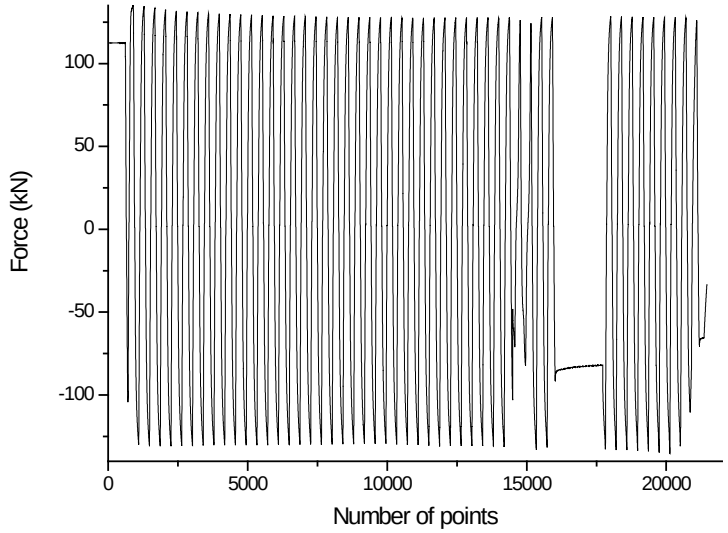

Figure 166. Jack force for dissipator D4 (channel 7). Second part

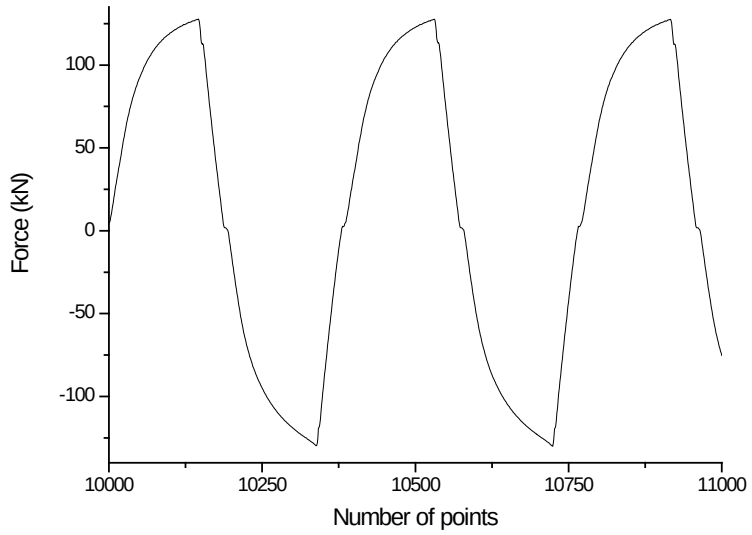

Figure 167. Jack force for dissipator D4 (channel 7). Mid cycles. Second part

Plots from Figure 168 show a rather stable hysteretic behavior along the whole number of cycles (49). The irregular loops correspond to the aforementioned slide and to and to the final part of the test. Figure 169 displays part of the remaining regular loops. To facilitate the interpretation of Figure 169 some auxiliary lines (similarly to Figure 71, Figure 101, Figure 126, Figure 127, Figure 141 and Figure 157) have been drawn.

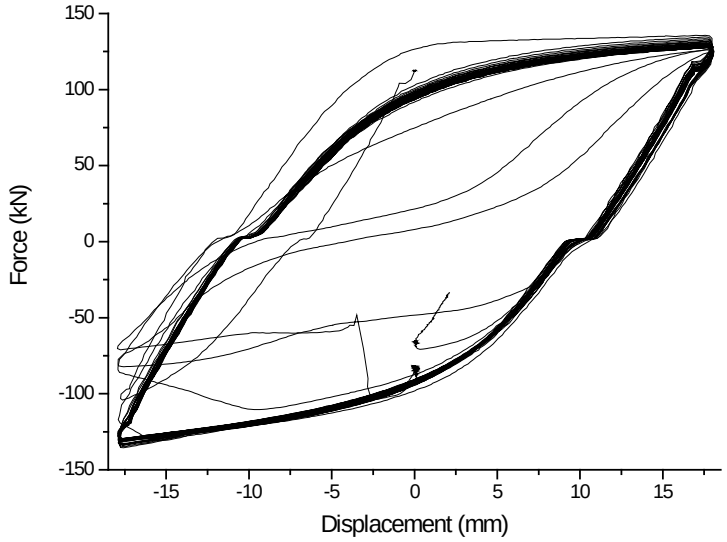

Figure 168. Hysteresis loops for dissipator D4 (channel 7 vs. channel 6). Second part

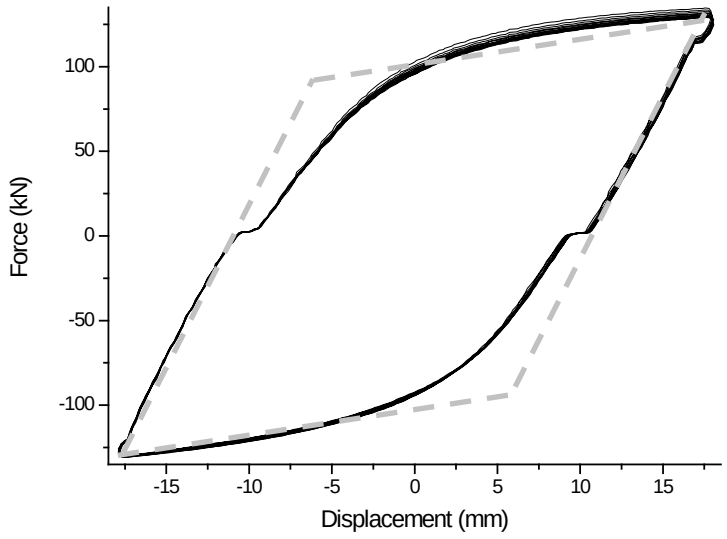

Figure 169. Regular hysteresis loops for dissipator D4 (channel 7 vs. channel 6). Second part

Similarly to Figure 71, Figure 101, Figure 126, Figure 127, Figure 141 and Figure 157, the following trends can be observed from Figure 169:

- The hysteretic behavior is stable. The force amplitude decreases after the first cycles but tends to stabilize quite fast.
- The lower plastic branch (compression) is more linear and steeper than the upper one (tension); the compression peaks are slightly higher than the tension ones. In fact, the tension behavior is more regular (it is due to the Bauschinger effect [Akiyama, 1980]) while the compression is affected by the mortar contribution (mostly near the peak). This conclusion is similar to the one derived from Figure 167.
- The horizontal jump due to the gap in the connections can be also observed (yet is clearly bigger than in the dissipator D2, see Figure 101).

Figure 170 displays the stress-strain plots from Figure 54 (for the steel specimen CS22-2) and the regular hysteresis loops for dissipator D4 (Figure 169) corresponding to the second part of the test after eliminating the irregular cycles. The strains for the dissipators have been obtained by dividing the relative displacement between both ends of the core (channel 6') by the distance between the centers of both (end) pins (see Figure 3, Table 1 and Figure 57).

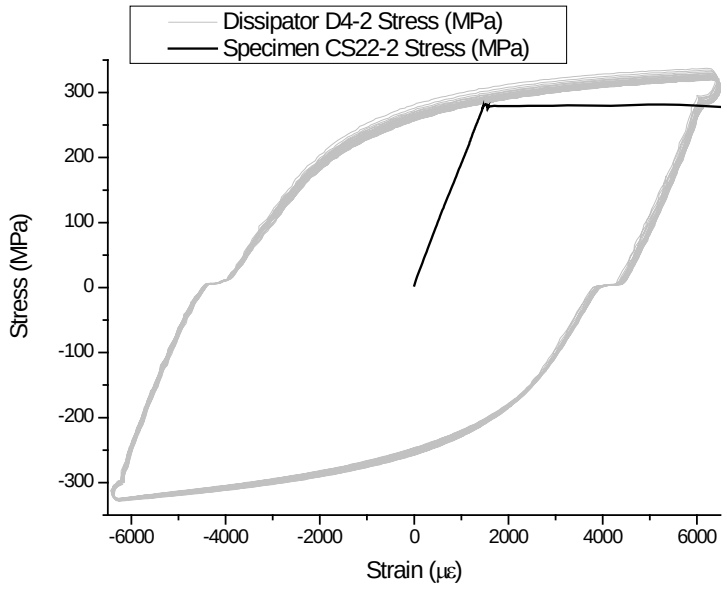

Figure 170. Comparison between stress-strain plots for the 22 mm core bar (CS22-2) and for dissipator D4. Second part

Plots from Figure 170 show that the elastic stiffness of the steel core (in tension) is similar to the one of the dissipators. Comparison among the plots of the core and of the device shows that the amount of consumed skeleton energy [Kato, Akiyama, Yamanouchi, 1973] is rather moderate since the plastic excursion is small (see Figure 51 and Figure 52). The fit between both yielding points (in the stationary phase) is rather satisfactory. Globally speaking, Figure 73 (for dissipator D1), Figure 103 (for dissipator D2) and Figure 128 (for dissipator D3) allow deriving similar conclusions. It is remarkable that the maximum strain in the dissipator lies in the horizontal plastic branch of the stress-strain law (far from the hardening branch, see Figure 54).

Figure 171 and Figure 172 show the horizontal and vertical displacements of the mid section of dissipator D4 as measured by sensors 4 and 3, respectively (see Table 9, Figure 60 and Figure 58).

Plots from Figure 171 and Figure 172 show that the mid section experienced relevant transverse displacements, both horizontal and vertical. In Figure 171 the transducer reached the end of its range and could not register values bigger (yet negative) than about 5 mm. In Figure 172, the enormous displacements (around point 15000) correspond to the abovementioned slide. Comparison between Figure 171 and Figure 172 shows that the vertical displacements are smaller than the horizontal ones (except the huge vertical displacements during the slide).

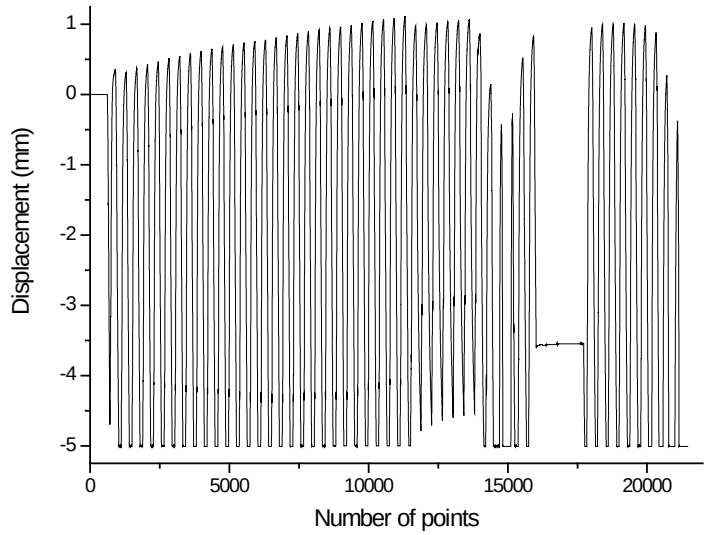

Figure 171. Horizontal displacements of the mid section for dissipator D4 (channel 4). Second part

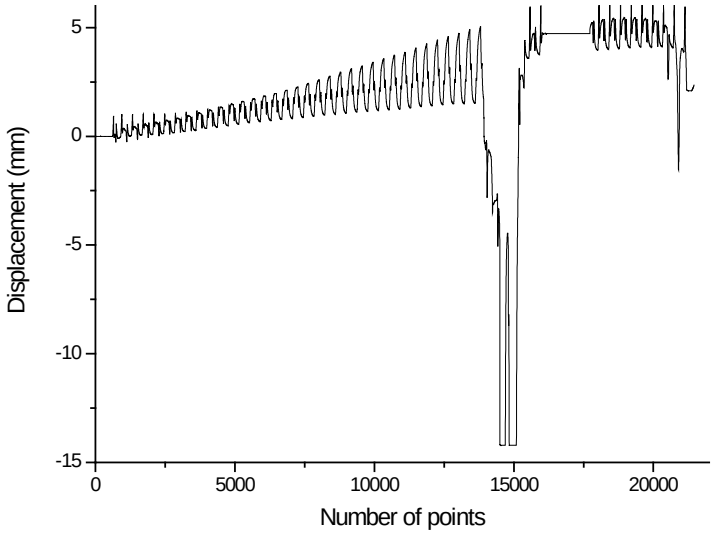

Figure 172. Vertical transverse displacements of the mid section for dissipator D4 (channel 3). Second part

To assess the correlation between the horizontal and vertical displacements of the mid section, Figure 173 shows the horizontal and vertical displacements of the mid section of dissipator D4 (second part) as measured by sensors 4 and 3, respectively (see Table 9 and Figure 58).

Figure 173 shows that, despite a certain erratic path, the maximum values for horizontal and vertical displacements are near coincident (for each cycle).

Figure 174 displays the difference between the longitudinal displacements of both ends of the encasing tube measured by displacement transducers 8 (right) and 9 (left), respectively (see Table 9 and Figure 58).

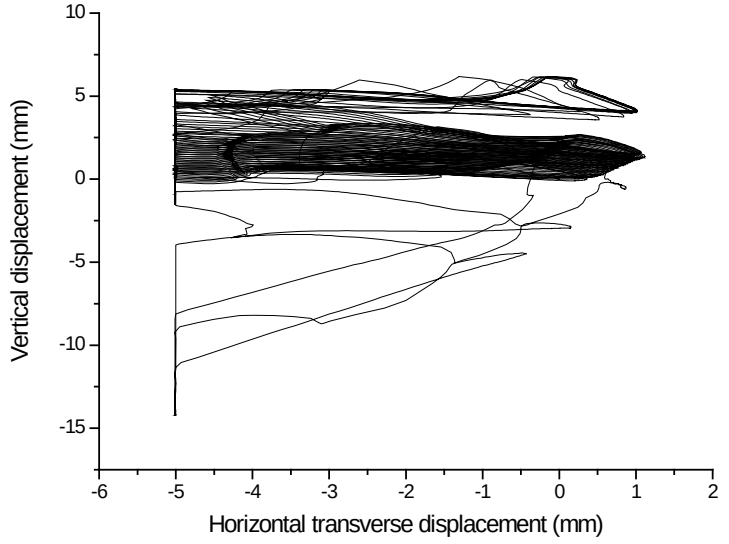

Figure 173. Vertical vs. transverse displacements of the mid section for dissipator D4 (channel 4 vs. channel 3). Second part

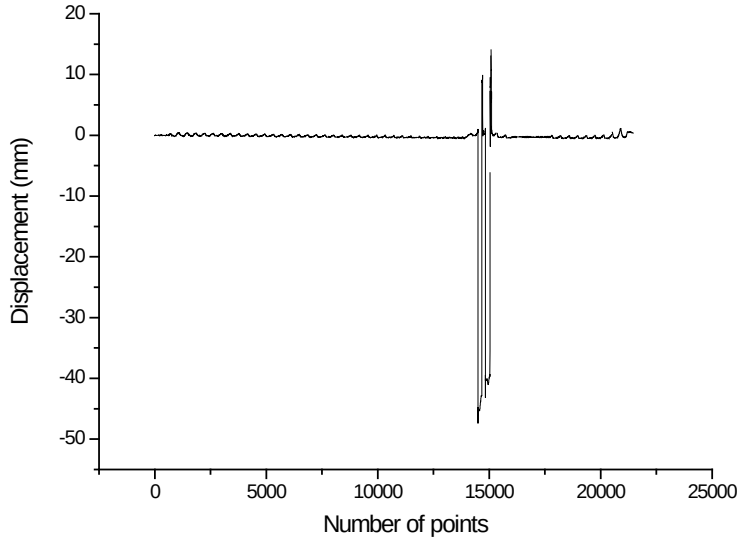

Figure 174. Relative longitudinal displacement between the ends of the casing for dissipator D4 (channel 8 + channel 9). Second part

Plots from Figure 174 allow deriving similar conclusions than those from Figure 164.

5.6.4 After-test remarks for dissipator D4

As described previously, final failure came for local buckling of the right end of the core; Figure 175 displays three images of the damaged connector.

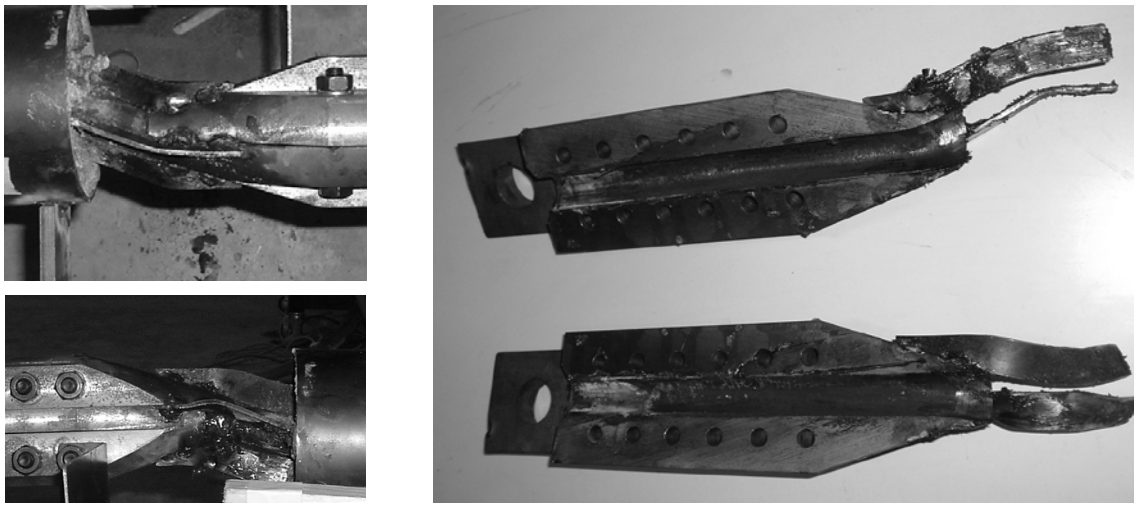

Figure 175. Local buckling of the right connector for dissipator D4

Figure 175 shows clearly that, like in dissipators D1 and D2 (see Figure 85 and Figure 114, respectively), the welded trapezoidal plates were unable to restrain the local buckling of the end parts of the core; they appear both bent and laterally buckled.

After concluding this test, the dissipators were cut longitudinally in two equal halves to observe the status of the mortar and of the core. Figure 176 displays representative parts (mortar and core).

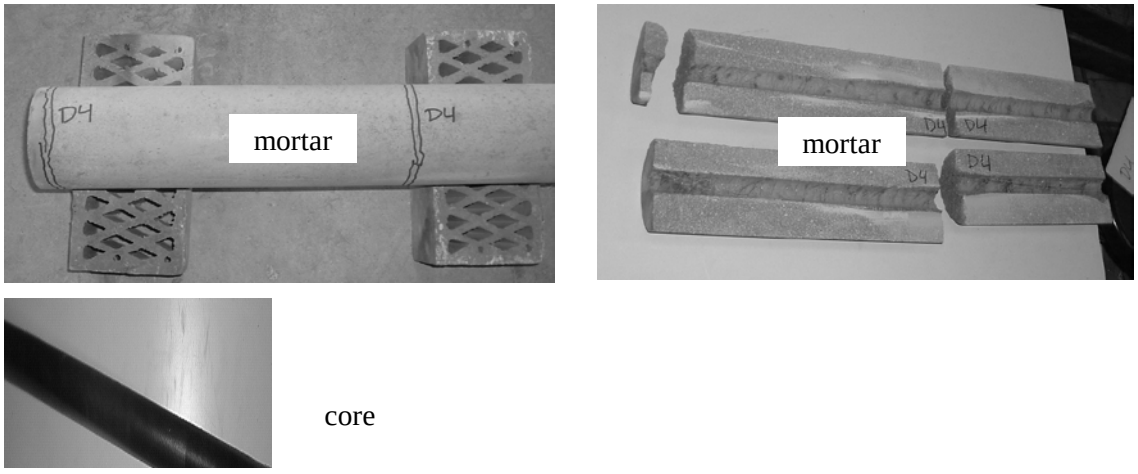

Figure 176. Mortar and core of dissipator D4

Figure 176 shows that, despite the observed cracks (discussed later), the mortar is apparently in good condition, even in the near vicinity of the core; it means that the transversal compressive forces due to high buckling modes (rippling, Figure 15) were not able to damage locally the mortar.

According to Figure 176 some eccentricity of the core hole was observed; it ranged between 2 and 4 mm. Such values lie inside the range considered for buckling analysis (e_1 = 20 mm, see Figure 14). As discussed previously, the fact that the bigger eccentricity corresponds to the thinner tube might be due to its higher flexibility. The cover of the core (Teflon, grease and rubber) was in good condition. The core was permanently bent; it is shaped like a warped sinusoidal wave whose wavelength ranges in between 100 and 200 mm and whose amplitude reaches up to 2 mm. Since the lateral forces exerted by the core were unable to bend the casing (filled tube) and the

surrounding mortar is not damaged, is obvious that this permanent curvature is due to the compression of the core cover, particularly the rubber layer.

Figure 176 shows that the mortar of dissipator D4 is transversally (completely) cracked; an explanation follows. Figure 159 shows that for such device the peak value of the (tension) strain in the steel tube is about 3.8×10^{-5}, the stress is 7.98 MPa and (assuming that the tube and the neighboring mortar do not slide) the stress in the mortar is about 1.39 MPa, which is highly below the tensile strength. Hence, it must be concluded that the mortar was cracked either by concentrated local effects or by the manipulation of the tube after the test. It is remarkable that no more cracks were observed in other dissipators. However, the lack of data about the strain gauges in the second part of the test of dissipator D4 does not allow making final conclusions.

5.7 Summary of results

This subsection presents a summary of the results of tests for dissipators D1, D2, D3 and D4. Those results are listed in Table 10. The irregular values corresponding to behavior near or after failure are not accounted for.

Table 10. Main results of the tests of dissipators D1, D2, D3 and D4

Device	d_{co} / d_{tu} / t_{tu} / L_{tu} (mm)	Axial dispel. (mm)	Ductility ratio	Buckled Ends?	No. of cycles	Dissipated Energy (-)	Tube axial stress range (MPa)	Horizontal maximum transverse displ. range (mm)	Vertical maximum transverse displ. range (mm)	Cumulative plastic ductility
D1	10 / 90 / 3 / 2466	± 19.15	5.31	NO	160	3492	4.6	-0.1 / 2.1	-7.7 / 2.5	2454
D2	10 / 90 / 3 / 2466	± 19.15	5.31	NO	131	2928	3.0	-1.35 / 0.45	-1.6 / -0.05	1976
D3	22 / 115 / 3 / 2196	± 17.85	5.68	NO	387	8856	35.7	-0.2 / 0.3	-0.7 / 0.2	6662
D4	22 / 115 / 3 / 2196	± 17.85	5.68	YES	73	1485	13.0	not available	not available	1124

At Table 10, “Buckled Ends?” refers to the local buckling of the naked core ends. The ductility ratio is the quotient between the maximum displacement and the yielding displacement Δ_y. The values of Δ_y have been estimated from the average yielding points determined from the tests of the 10 mm steel bars (see Table 7) and the length L_{di} of the dissipative segment of the core (see Figure 3 and Table 1) according to the Hooke’s law

$$\Delta_y = \frac{307 \times 2466}{210000} = 3.605 \text{ mm (D1 and D2)} \qquad \text{Eqn. (22)}$$

$$\Delta_y = \frac{300.5 \times 2196}{210000} = 3.142 \text{ mm (D3 and D4)} \qquad \text{Eqn. (23)}$$

In these calculations the contribution of the end connectors (see Figure 57 and Figure 10) has been neglected.

The number of cycles (prior to failure) corresponds to the driving displacement (channel 6). The dissipated energy is the area encompassed by the hysteresis loops (channels 6’ and 7); such value

has been normalized with respect the elastic energy ½ $k\,\Delta_y^2$ where k is the initial stiffness and Δ_y is the yielding displacement. The stiffness has been determined according to the Hooke's law

$$k = \frac{210000 \times \pi \times 5.14^2}{2466} = 7068\,N/\text{mm}\ (\text{D1 and D2}) \qquad \text{Eqn. (24)}$$

$$k = \frac{210000 \times \pi \times 11.26^2}{2196} = 38090\,N/\text{mm}\ (\text{D3 and D4}) \qquad \text{Eqn. (25)}$$

In these calculations the contribution of the end connectors (see Figure 57 and Figure 10) has been neglected.

From Eqn. (22), Eqn. (23), Eqn. (24) and Eqn. (25) the elastic energy is obtained

$$E = \frac{1}{2} 7068 \times 3.605^2 = 47.08\ \text{J}\ (\text{D1 and D2}) \qquad \text{Eqn. (26)}$$

$$E = \frac{1}{2} 38090 \times 3.142^2 = 189.33\ \text{J}\ (\text{D3 and D4}) \qquad \text{Eqn. (27)}$$

The axial stress range in the tube is the maximum amplitude of the oscillations (see Figure 74, Figure 104, Figure 129, Figure 143 and Figure 159). The horizontal and vertical maximum transverse displacement ranges correspond to the mid section of the tube and were registered by sensors 4 and 3, respectively. The type and position of sensors are described by Figure 58 and Table 9. The "Cumulative plastic ductility" [Black, Makris & Aiken, 2002] is a dimensionless normalized expression of the cumulative plastic deformation defined by Eqn. (21).

It is remarkable that the energy dissipated per unit of volume (considering only the dissipative segment of the steel core) is 3.66 J/mm^3 (dissipator D1), 2.99 J/mm^3 (dissipator D2), 7.65 J/mm^3 (dissipator D3) and 1.58 J/mm^3 (dissipator D4). Clearly, the performance is higher for the thicker (diameter 22 mm) bars (except for the premature failure of dissipator D4).

6 CONCLUSIONS AND FURTHER RESEARCH

6.1 Summary

This Monograph presents the results of two series of experiments on buckling restrained braces: five short devices (about 400 mm long) and four full-size (near 3000 mm long) prototype devices. The five short dissipators were tested in Argentina while the proofs on the prototypes were carried out in Spain. All the devices were designed and built by the authors; they consist basically on (central) steel cores embedded in casings formed by a tube filled with mortar. In the short devices the core is a solid square-section bar whose central part has been tapered down to a smaller rectangular section; in the full-size devices the core is a solid circular section. It is remarkable that, as in all the buckling restrained braces, the core must slide with respect to the surrounding mortar. A simplified numerical model of the structural behavior of these dissipators is presented and its usefulness for design is discussed. The final objective of the research is to foster the bulk use of this type of energy dissipators in developing countries located in seismic prone regions. Next two paragraphs present short descriptions of the experiments on the five short devices and on the four full-size prototype devices, respectively.

The five short devices are termed SD1, SD2, SD3, SD4 and SD5. The proofs consisted of applying to each dissipator three protocols of imposed axial displacements; such protocols have been obtained from the technical literature and aim to reproduce the effect of intense earthquakes. Devices SD1, SD2 and SD3 resisted the proofs while SD4 and SD5 exhibited premature failure by breaking of end parts of the core (due to local buckling). The only registered magnitudes were the core displacement and the driving force.

The four full-size prototype devices are termed D1, D2, D3 and D4. Dissipators D1 and D2, by one side, and D3 and D4, by the other side, are alike. Devices D1 and D2 are more slender than D3 and D4 (both about the inner core and the outer tube). The four devices have roughly the same length. For every dissipator, the proofs consisted of constant-amplitude imposed axial displacements until failure. The tests of devices D1 and D2 had no particular circumstances; failure came by breaking of the core after 160 and 131 cycles, respectively. The dissipator D4 was tested prior to D3. For D4, a premature failure (by sliding of one end connection) arose; after fixing that problem, the experiment resumed and the final failure came by local buckling of one of the end portions of the core. For D3, a similar premature failure arose; after fixing that problem the final failure came by breakage of the core (as in D1 and D2).

6.2 Conclusions

The main conclusions arising from this research are listed next. They are classified in three categories: global (those which are most important and that arise from both the experiments on the five short dissipators and on the four full size prototype dissipators) and particular (of the short dissipators and of the prototypes, respectively). In their turn, the conclusions for the full size prototype dissipators are organized in three groups: those arising mainly from the numerical results of the tests, those arising mainly from the observation of the tests and of the tested devices and those arising mainly from the numerical simulation. It is remarkable that in the subsequent list there are some duplicities as some conclusions were confirmed in several ways.

Global conclusions:

- It is feasible to design buckling restrained braces that are easy to produce, robust, cheap, virtually maintenance-free, efficient and durable.
- The fatigue life of buckling restrained braces, even highly uncertain, can be significantly

bigger than expected. It might allow extending the life of these devices after a number of strong seismic inputs.

Particular conclusions for the short dissipators:

- The hysteresis loops were reasonably regular until or near failure.
- In most of the devices (SD1, SD2, SD4 and SD5) there were minor failures (leading to stiffness reduction) in the yielding compression branches; they were generated by the buckling of the core. Conversely, the casing contribution (during compression, because of the friction forces between the core and the mortar) generated an increment of stiffness. Among these two opposing trends, the first one prevailed for dissipators SD1 and SD2 while for the other three the situation was unclear.
- In dissipators SD1 and SD2 a sudden debonding between the steel core and the surrounding mortar follows the first cycles.
- The resistance to fatigue was rather low (the failure for devices SD4 and SD5 arose after little number of cycles).
- The failure came by local buckling of the core near its transition zones (the segments where the square section is lessened; the longitudinal slide of the core inside the casing allowed the central segment of the core to be inside a significantly wider hole (it did not prevent buckling).
- The change of the velocity of the loading cycles has not produced any relevant effect on the response of the dissipators. This fact seems to confirm that their behaviors are basically rate-independent (for the range of considered velocities).
- Some stress concentrations were detected in the corners of the core; they generated minor cracking in the surrounding mortar.
- Some cores were wrapped with thicker layers of polyethylene; they showed bigger permanent (bending) deformations. It shows that the bigger the (surrounding) gap, the bigger the transversal motion (bending).
- In devices SD1 and SD2 the outer tubes were made of PVC while in devices SD3, SD4 and SD5 they were made of steel. The steel tubes performed better than the PVC ones (less permanent deformations of the core).
- No significant shear stress transfer between the core and the casing was observed (the elastic stiffness of the naked core and of the dissipator are similar).

Particular conclusions for the full size prototypes (from the numerical results of the tests). These conclusions are listed next, sorted out according to the corresponding channels (see Table 9 and Figure 58):

- **Channels 1, 2 and 6**. Channels 1 and 2 registered the axial displacements of the end sections of the dissipators (to provide information about the actual core elongation); channel 6 corresponds to the (imposed) displacement. The results of channels 1 and 2 were useful in spite that their measurements were influenced by the rotations in both ends of the devices (mostly for devices D3 and D4). Every time the driving force reverts, the plot of the core elongation (channel 1 + channel 2) exhibits a horizontal jump; this is due to the gap in the connections between the dissipator and the end supports. The axial elongations given by channels 1 and 2 and by channel 6 differ also due to the flexibility of the supports and of the interposed elements; after eliminating such effect, the fit is excellent.
- **Channel 7**. Channel 7 corresponds to the driving (axial) force. This channel shows that the hysteretic behavior is basically stable. Mainly for devices D1 and D2, once the maximum amplitude displacement is reached, the force amplitude tends to decrease until reaching a stationary value; this is due to a progressive detachment from the inner core and the surrounding mortar. In the stationary phase the maximum tension values are generally smaller than the compression ones; this difference can be explained by the contribution of the mortar

through the friction forces generated during the compression (when the core tries to buckle being refrained by the mortar). Every time the driving force reverts, its plot exhibits a horizontal jump; this is due to the gap in the connections between the dissipator and the end supports. The buckling of the core does not affect significantly the force plots. The last segment of the compression (plastic) loading branches exhibit a rather sudden increase leading to a higher peak and a reversal in the curvature; this is due to the mortar contribution. This effect is undesirable (the force increases without any relevant effect on the area encompassed by the hysteresis loop) and most of the buckling restrained braces exhibit it; for these devices, it is rather moderate.

- **Channels 16 and 17**. Such channels correspond to strain gauges stuck to opposite points in the mid section of the tube; in this way the sum of both measurements yields information about the axial forces carried by the tube while its difference yields information about the horizontal bending moment acting on such member. The longitudinal stresses in the tube, yet are not very important, are not completely negligible. In all the dissipators, either a permanent stress or growing range amplitudes (as the test progresses) has been observed. This can be considered as a kind of cumulated damage.
- **Channels 18 and 19**. Such channels correspond to strain gauges stuck to both end-sections of the tube (were used only for dissipator D1). These axial strains are not negligible, yet smaller than in the mid section; this difference is due to the cumulated effect of the longitudinal friction forces between the core and the mortar.
- **Channels 4 and 3**. Such channels correspond to displacement transducers that collect the transversal (horizontal and vertical) displacements of the mid section of the device. The registers showed that these displacements are not negligible, exhibiting a moderately stable and periodic behavior. For dissipator D1 the end rotations (of the core) with respect to horizontal transversal axes were not restrained and, hence, the vertical displacements were significantly bigger than the horizontal ones; conversely, for dissipators D2 and D3, these rotations were prevented and, hence, the horizontal and vertical displacements were similar.
- **Channels 8 and 9**. Such channels registered the axial displacements of the end sections of the tube; their goal was to report about the global axial elongation experienced by the (outer) tube. Unfortunately, these measurements where polluted by the influence of the end rotations of the core; comparison with the axial strains of the tube (channels 16, 17, 18 and 19) shows that these registered displacements can not correspond to the actual longitudinal displacements of the extremes of the bar as the average strain would be several orders of magnitude bigger than the registered ones.

Particular conclusions for the full size prototypes (from the observation during and after the tests):

- The total number of cycles was significantly higher in dissipator D3 than in D1 and D2 (apart from the premature failure of dissipator D4). It might be due to the following reasons: (i) the observed permanent curvatures were smaller and (ii) the local buckling at both ends was better restrained (by the aforementioned intermediate supports).
- The steel core was coated by a Teflon® layer to reduce the friction forces. Such coating was in good condition after the tests.
- The (coated) steel core was wrapped by a rubber layer; its transversal flexibility allowed some transversal motion of the core leading to permanent short-length buckling warped waves. Such observed permanent deformation was bigger for the 10 mm core bars than for the 22 mm ones.
- The mortar performed properly. The parts in contact with the core were not damaged despite the transverse forces (the core pushed the mortar while trying to buckle). Some cracks were observed in dissipator D4 but they neither had any influence in the mortar behavior nor can be attributed to the demands during the experiments (rather to the after test manipulation).
- Some geometrical imperfections (eccentricities of the core with respect to the tube) were observed prior to the tests, mainly in dissipators D1 and D2 (those with the thinner tube).

These values are smaller than those considered for the buckling analysis.

- The steel cores were connected (by their ends) to two-halved steel elements; in their turn they were linked (pinned connections) to a fix support and to a jack (it generated the imposed displacements). Such two-halved elements were attached to the core by a dual mechanism (prestressed) bolts and an adhesive product. Such adhesive could not guarantee a proper bonding between the steel core and the end connectors.
- In dissipator D3, after eliminating the remaining of adhesive product, the friction forces generated by the prestressed bolts were enough to prevent sliding between the core and the connectors.
- The rotation capacity of the two pinned connections (with the left fix support and with the right hydraulic jack) proved to be damaging for the behavior of the devices (dissipator D1) as relevant rotations were observed. The insertion of steel wedges and can sheets improved the situation for dissipators D2, D3 and D4.
- The two pin-ended connections had a relevant longitudinal gap that generated slides every time the force reverted; it could be reduced by placing steel wedges and can sheets.
- Every two-halved steel connector had four trapezoidal steel plates (welded to it) to restrain the local buckling of the (end) naked part of the core, particularly if the side-sway motion of the dissipator was not prevented (dissipators D1, D2 and D4). Such plates were not able to fulfill that requirement. In dissipator D3 two intermediate supports restrained the lateral displacements of the tube and, hence, no local buckling was observed; this measure proved to be very effective to improve the performance of the dissipator.

Particular conclusions for the full size prototypes (from the numerical simulation):

- The buckling design of the casing (filled tube) was over-conservative. Slender tubes (with smaller diameter) might be used. This is particularly true for dissipators D1 and D2.

6.3 Further research

This work has pointed out a number of relevant research needs:

- The structural behavior of the core-casing assembly is rather complicated due to the coexistence of several highly coupled issues: joint operation of four materials (steel core, rubber, mortar and steel tube), plastic behavior of the steel core, partial sliding (friction) between the core and the surrounding mortar, transversal interaction between the core and the mortar (while the core is trying to buckle, being restrained by the mortar), among others. The lack of accurate and reliable numerical models impairs the development of innovative and daring solutions and generates a certain poverty of knowledge about the structural performance of these devices (for example, some of the experimental results discussed in this Monograph, cannot be explained by merely examining them). Moreover, such a model would allow calibrating the simplified models presented in this work. Therefore, to generate a complex algorithm able to simulate the structural behavior of buckling restrained braces is a must.
- In spite that the performance of the four full size prototypes has been highly satisfactory, a number of particular issues require further research: (i) the buckling of the naked (unprotected) end segments of the core was not properly restrained (by the afore mentioned trapezoidal plates), (ii) the bonding between the core and the end steel connectors was guaranteed by a dual mechanism (glue and friction –through the prestressing of the bolts–) while the first one did not perform properly (moreover, both mechanisms are rather incompatible), (iii) the sliding between the core and the mortar was ensured also by a dual mechanism (rubber and grease); it would be useful to discriminate the influence of each of them and (iv) the structural design of the dissipators is clearly over conservative, the use of

the existing and derived numerical models would allow to design slender solutions. Such issues must be investigated in further (individual) experiments.

- To confirm the usefulness of the proposed buckling restrained braces in real applications, a series of comprehensive numerical and experimental studies are required. Particular issues to be considered are: performance for a broad range of buildings (steel-concrete structures, short to tall buildings, shear-wall to shear building, symmetric vs. asymmetric buildings, etc.), performance for a wide set of seismic inputs (soft vs. stiff soil, near source effects, strong to moderate intensity, etc.), impact in the building cost, etc.

ACKNOWLEDGEMENTS

The authors appreciate the cooperation in the tests for the short dissipators of Dr. Yawny and Mr. Soul (Centro Atómico Bariloche, Argentina) and of Mr. Norrito and Mr. Rosales (Laboratorio de Materiales, FRM, Argentina). Mr. O. Montenegro (Technical University of Catalonia, Barcelona) helped testing the mortar of the prototypes, Mr. J.M. Franco (University of Zaragoza, Spain) and Dr. M. Dolce (University of Basilicata, Italy) made relevant suggestions about the design and production issues; these helps are appreciated. The Argentinean “National Technological University” and “Banco Río” (Argentina), supported the stay of Mr. Palazzo in Barcelona and part of the testing cost (“Programa de Becas de Postgrado” and “Proyectos de Investigación Científica para el Perfeccionamiento Docente”). The assistance of the Technical University of Catalonia and of the University of Girona is gratefully acknowledged.

APPENDIX A. NOTATION

a = Initial gap between the core and the surrounding mortar.
A_{co} = area of the core.
A_v = shear area of the tube.
d_{cn} = diameter of the steel connectors.
d_{co} = diameter of the core.
d_{tu} = diameter of the encasing (tube).
e_{co} = initial eccentricity of the core.
e_i = initial eccentricity for the i-th buckling mode.
e_{tu} = initial eccentricity of the casing (tube).
E_{co} = core deformation modulus (steel).
E_m = mortar deformation modulus.
E_{PVC} = deformation modulus of the PVC tube.
E_s = steel deformation modulus.
E_{tu} = casing (filled tube) deformation modulus (mortar and steel tube).
f_c = mortar compressive strength.
f_{ck} = characteristic value of the mortar compressive strength.
f_{cm} = mean value of the mortar compressive strength.
f_u = ultimate strength of steel.
f_y = steel yielding point.
F_i = interaction force for the i-th buckling mode.
F_y = yielding force.
i = number of buckling mode.
I_{co} = moment of inertia of the core.
I_{tu} = moment of inertia of the casing (mortar and steel tube).
k_{tu} = transversal stiffness of the casing (mortar and steel tube).
l_i = wave length for the i-th buckling mode.
L_{cn} = length of the connector (part in contact with the core).
L_{co} = total length of the core.
L_{di} = length of the dissipative segment of the core.
L_{de} = total length of the device.
L_k = buckling (effective) length.
L_{tu} = length of the tube.
M = bending moment.
$M_{pl\,Rd}$ = design value of the bending (plastic) strength of the tube.
n = equivalence coefficient (E_s / E_m).
P = compressive force on the steel core.
P_{cr} = critical value of force P.
P_E = Euler critical value of force P.
P_y = yielding value of force P.
q = distributed interaction force between the core and the casing; distributed load.
q_i = final eccentricity for the i-th buckling mode.
t_{tu} = thickness of the tube.
V = shear force.
$V_{pl\,Rd}$ = design value of the shear (plastic) strength of the tube.
W_{el} = elastic resistance modulus of the tube (moment of inertia divided by the radius).
x = longitudinal coordinate along the length of the device.
y = lateral deflection of the core (and of the casing).
β = distributed spring constant of the mortar casing.
ε_u = ultimate deformation of the steel.

γ = safety factor.
γ_{M0} = material (steel) safety factor.
Δ^+, Δ^- = maximum and minimum values of the plastic displacement.
Δ_y = yielding displacement (of the device).
μ = (dry) friction coefficient.
ν = Poisson's ratio.
ρ = dimensionless coefficient.

APPENDIX B. GLOSSARY

In this appendix some (rather particular) meanings of the terms used in this work are described.

Buckling restrained brace. Passive energy dissipators used for seismic protection of building frames consisting of slender steel bars (core) installed usually either like diagonal or chevron braces. The interstory drift generates axial yielding in such core; its buckling is prevented by a stockiest encasing, it is usually composed of a steel tube filled with mortar.

Casing. A stocky member embracing the dissipative segment of the core to restrain its buckling.

Core. Inner part of the buckling restrained brace. It is a slender steel bar whose buckling is prevented by the casing.

Cumulative Plastic Ductility. Sum of the absolute values of the ratios between the plastic range and the yielding displacement (at each plastic excursion).

CS10-1, CS10-2, CS22-1 CS22-2. Specimens of the steel cores of prototype dissipators D1, D2, D3 and D4. Specimens CS10-1 and CS10-2 have 10 mm diameter and CS22-1 and CS22-2 have 22 mm diameter.

Device. Synonymous of energy dissipator.

Dissipative segment. The part of the steel core intended to yield.

Dissipator. Energy dissipator.

Ductility (ratio). Quotient between the maximum and the yielding deformations.

D1, D2, D3, D4. Full size prototype dissipators (about 3 m long) designed, produced and tested at Spain (Technical University of Catalonia and University of Girona).

Energy dissipator. Member intended to protect a building structure from strong seismic inputs by absorbing and dissipating the input energy. These devices do not participate in the main load-carrying system and can be easily replaced if damaged.

Individual testing. Experiments on dissipators mounted on testing rigs that do not account for the building frames.

MSD1, MSD3. Specimens (coupon) of the mortar of prototype dissipators D1 and D3, respectively.

Specimen. Any element to be tested.

SCS1, SCS2. Specimens of the steel cores of short dissipators SD1, SD2, SD3, SD4 and SD5.

SD1, SD2, SD3, SD4, SD5. Reduced scale (short) dissipators (400 mm long) designed and produced at the National Technological University (Mendoza, Argentina) and tested at the Atomic Center of Bariloche (Argentina).

APPENDIX C. REFERENCES

1. Akiyama H. Earthquake-resistant limit-state design for buildings; University of Tokyo Press, Tokyo, 1980.
2. Akiyama H., (2003), “Metodología de proyecto sismorresistente de estructuras basada en el balance energético”, Ed. Reverté, Barcelona.
3. Araníbar H., Palazzo G., Yazgan U., Franco J.M., López-Almansa F., Crisafulli F. Mass use of energy dissipators for seismic protection and retrofit of buildings. Applications to Bolivia, Argentina and Turkey. 9th World Seminar on Seismic Isolation, Energy Dissipation and Active Vibration Control of Structures, Kobe, Japan, June 13-16, 2005.
4. ASTM A36/A36M “Standard Specification for Carbon Structural Steel”, American Society for Testing of Materials (2005).
5. Astrella M., Whittaker, A. (2005). The Performance-Based Design Paradigm, MCERR Report MCEER-05-0011.
6. Bazant Z.P. & Cedolin L. (1991). Stability of Structures. Oxford University Press.
7. Black C., Makris N. & Aiken L. Component Testing, Stability Analysis Characterization of Buckling-Restrained Unbonded Braces, Pacific Earthquake Engineering Research Center, Report PEER 2002/08, 2002.
8. Black C., Makris N. & Aiken L. Component Testing, Seismic Evaluation and Characterization of Buckling-Restrained Braces, Journal of Structural Engineering ASCE, Volume 130, Issue 6, pp. 329-337 (2004).
9. Bray J.D., Rodriguez-Marek A. Characterization of forward-directivity ground motions in the near-fault region. Soil Dynamics and Earthquake Engineering 24 (2004) 815–828.
10. Brockenbrough R.L., Merritt F.S. Structural Steel Designer's Handbook. McGraw-Hill 2005.
11. Bruneau M., Wang N. Normalized energy-based methods to predict the seismic ductile response of SDOF structures. Engineering Structures 1996; 13-28.
12. Carden L.P., Itani A., Buckle I. and Aiken I. Buckling restrained braces for ductile end cross frames in steel plate girder bridges. 13th World Conference on Earthquake Engineering. Paper No. 503. Vancouver, Canada, 2004.
13. Carden L.P., Itani A.M. and Buckle I.G. Seismic Performance of Steel Girder Bridges with Ductile Cross Frames Using Single Angle X Braces. Journal of Structural Engineering ASCE, Volume 132, Issue 3, pp. 329-337 (2006).
14. Choi H, Kim J. Energy-based seismic design of buckling-restrained braced frames using hysteretic energy spectrum. Engineering Structures 2006; 28:304–311.
15. Clark, P., Aiken, I., Kasai, K., Ko, E., and Kimura, I., 1999, "Design Procedures for Buildings Incorporating Hysteretic Damping Devices," Proceedings 68th Annual Convention, pp. 355-371, Structural Engineers Association of California, Sacramento, CA.
16. CoreBrace, www.corebrace.com.
17. D’Aniello M., Della Corte G., Mazzolani F.M. and Landolfo R. (2006) Steel Buckling Restrained Braces. In: Seismic upgrading of RC buildings by advanced techniques - The ILVA-IDEM Research Project. Polimetrica Publisher, Italy, pp. 179-223.
18. EN 10025. *Hot rolled products of structural steels.* European Committee for Standardization, 2002.
19. EN 206-1. Concrete - Part 1: Specification, performance, production and conformity. European Committee for Standardization, 2000.
20. EN 1993. *Design of steel structures*. European Committee for Standardization, 1996.
21. EN 1994. *Design of steel-concrete composite structures*. European Committee for Standardization, 1996.
22. EN 206-1. *Concrete - Part 1: Specification, performance, production and conformity*. European Committee for Standardization, 2000.
23. EN ISO 4014:2000. *Hexagon head bolts*. European Committee for Standardization, 2000.
24. European Commission, Environment and Sustainable Development Programme of the Research Directorate General. INDEPTH Project (Development of Innovative Devices for

Seismic Protection of Petrochemical Facilities). http://indepth.boku.ac.at.
25. Fahnestock L., Sause R. and Ricles J. “Seismic analysis and design of buckling-restrained braced frames”. 5th International PhD Symposium in Civil Engineering-Walraven, Blaauwendraad, Scarpas & Snijder (eds.), 2004 Taylor & Francis Group, London.
26. Fip Industriale, www.fip-group.it.
27. Hall, J. F, Heaton, T. H., Halling, M. W., and Wald, D. J “Near-source ground motions and its effects on flexible buildings”, Earthquake Spectra 1995; 11, 569-605.
28. Hasegawa, H., Takeuchi, T., Nakata, Y., Iwata, M., Yamada, S., Akiyama, H. (1999). “Experimental Study on Dynamic Behavior of Unbonded Braces,” AIJ J. Technol. Des. No.9, pp.103-106 (in Japanese).
29. Housner G.W., Bergman L.A., Caughey T.K., Chassiakos A.G., Claus R.O., Masri S.F., Skelton R.E., Soong T.T., Spencer B.F. and Yao J.T.P. Structural Control: Past, Present, and Future. ASCE Journal of Engineering Mechanics, Volume 123, Issue 9, pp. 897-971 (1997).
30. Iwata, M., Kato, T., Wada, A. (2000). “Buckling-restrained braces as hysteretic dampers,” Proceedings of Third International Conference on Behavior of Steel Structures in Seismic Areas (STESSA 2000), Montreal, Canada, pp.33-38.
31. Iwata M. Applications-Design of Buckling Restrained Braces in Japan. 13th World Conference on Earthquake Engineering. Paper No. 3208. Vancouver, Canada, 2004.
32. Kanaji H., Hamada N., Ishibashi T., Suzuki N., Mino T., Durán Cárdenas F. and Sakugawa T. Performance of Hysteretic Steel Damper for Seismic Retrofitting of a Long-Span Truss Bridge, Proc. IABMAS’04, Kyoto, 2004.
33. Kasai K., Kibayashi M. JSSI manual for building passive control technology. PART-1 Manual contents and design/analysis methods. 13th World Conference on Earthquake Engineering. Paper No. 2989. Vancouver, Canada, 2004.
34. Kato, B, Akiyama, H, Yamanouchi, H. Predictable properties of structural steels subjected to incremental cyclic loading. IABSE Symposium on Resistance and Ultimate Deformability of Structures Acted on by Well Defined Loads, Lisbon, 1973.
35. Kibayashi, M., Kasai K., Tsuji Y., Kikuchi M., Kimura Y., Kobayashi T., Nakamura H. & Matsuba Y. JSSI manual for building passive control technology. PART-2 Criteria for implementation of energy dissipation devices. 13th World Conference on Earthquake Engineering. Paper No. 2990. Vancouver, Canada, 2004.
36. Kim J. and Choi H. Energy-Based Seismic Design of Buckling-Restrained Braces. 13th World Conference on Earthquake Engineering. Paper No. 2113. Vancouver, Canada, 2004.
37. Konami, S., Sugihara, H., Narikawa, M., Huan, Y.H., Maeda, Y. and Wada, A. (1999). “Seismic performance of moment resisting frames with hysteretic damper,” Annual Meeting of the Architectural Institute of Japan (in Japanese).
38. Lee K. and Bruneau M. Energy Dissipation of Compression Members in Concentrically Braced Frames: Review of Experimental Data. Journal of Structural Engineering ASCE, Volume 131, Issue 4, pp. 552-559 (2005).
39. Lehman D., Roeder C., Yoo J.H. and Johnson S. Seismic response of braced frame connections. 13th World Conference on Earthquake Engineering. Paper No. 1459. Vancouver, Canada, 2004.
40. López W.A., Gwie D.S., Lauck T.W. & Saunders M. (2004). Structural Design and Experimental Verification of a Buckling-Restrained Braced Frame System. Engineering Journal, Vol. 41 No. 4, AISC (American Institute of Steel Construction).
41. Mahin S., Uriz P., Aiken I., Field C. & Ko E. Seismic performance of buckling restrained braced frame systems. 13th World Conference on Earthquake Engineering. Paper No. 1681. Vancouver, Canada, 2004.
42. Martelli A. (2006) Modern seismic protection systems for civil and industrial structures. An advanced approach to earthquake risk scenarios, with applications to different European towns. Downloadable at http://www.samco.org/network/download_area/paper_martelli.pdf.
43. Merritt S., Uang C.-M., Benzoni G. Subassemblage testing of core brace buckling-restrained braces. University of California, San Diego. Report No. TR-2003/01 (2003).

44. Newell J., Uang C.-M., Benzoni G. Subassemblage testing of core brace buckling-restrained braces (G Series). University of California, San Diego. Report No. TR-2006/01 (2006).
45. Nippon Steel Corporation. “Vibration-control and Seismic-isolation Technologies by Nippon Steel”. www0.nsc.co.jp/shinnihon_english/nsnews/pdf/2005100517385506419.pdf (2005).
46. Nishimoto K., Nakata Y., Kimura I., Aiken I., Yamada S. and Wada A. Sub-assembly testing of large buckling-restrained unbonded braces. 13th World Conference on Earthquake Engineering. Paper No. 1133 Vancouver, Canada, 2004.
47. Oller S. (2003), “Simulación Numérica del Comportamiento Mecánico de los Materiales Compuestos”, CIMNE.
48. Palazzo G., Crisafulli F., (2004), “Evaluación de la Eficiencia de Disipadores por Fluencia Usados para la Rehabilitación de Pórticos”, XVIII Jornadas Argentinas de Ingeniería Estructural, Buenos Aires, Argentina.
49. Palazzo G., Crisafulli F. (2004), “Estudio Comparativo de Distintos Disipadores por Fluencia en Base a los Requerimientos Establecidos en Distintas Normas”, XXXI Jornadas Sud-Americanas de Ingeniería Estructural, Mendoza, Argentina.
50. Palazzo, G., Crisafulli, F., López Almansa F. (2006), “Los Disipadores de Energía por Plastificación de Metales en el Diseño por Capacidad”, Encuentro de Investigadores y Docentes de Ingeniería, Mendoza, Argentina.
51. Palazzo, G., Crisafulli, F., López Almansa F., Cahís X. (2006), “Análisis numérico experimental de barras de pandeo restringido”, XIX Jornadas Argentinas de Ingeniería Estructural, Mar del Plata, Argentina.
52. Palazzo G., Rehabilitación de pórticos sismorresistentes de hormigón armado mediante barras de pandeo restringido. Doctoral Dissertation. Universidad Tecnológica Nacional, Facultad Regional Mendoza (2009).
53. Palazzo G., López Almansa F., Cahís X., Crisafulli F. A low-tech dissipative buckling restrained brace. Design, analysis, production and testing. Engineering Structures. Vol. 31, No. 9, Pág. 2152-2161 (2009).
54. Read Jones Christoffersen. www.rjc.ca/cms/files/Buckling Inhibited Braces.pdf.
55. Sabelli R. and Aiken I. “US building-code provisions for buckling-restrained braced frames: basis and development”. 13th World Conference on Earthquake Engineering, Paper No. 1828 Vancouver, B.C., Canada 2004.
56. Sabelli R., Mahin S. and Chang C. (2001) Seismic Demands on Steel Braced Frame Buildings with Buckling Restrained Braces. Pacific Earthquake Engineering Research Center, University of California, Berkeley. http://nisee.berkeley.edu/library/bracedframes.pdf.
57. Sabelli R., Pottebaum W., Brazier J.C. and López W. Design of a Buckling-Restrained Braced Frame Utilizing 2005 Seismic Standards. Metropolis & Beyond 2005 (Proceedings of the 2005 Structures Congress and the 2005 Forensic Engineering Symposium, New York).
58. Sabelli, R., Mahin S., and Chang, C. (2002), “Seismic Demands on Steel Braced Frame Buildings with Buckling-Restrained Braces”, Earthquake Engineering Research Center, University of California, http://nisee.berkeley.edu/library.
59. Seismic Isolation Engineering for Nippon Steel Corporation, 1999. “Tests of Nippon Steel Corporation Unbonded Braces”. Report to Ove Arup & Partners, California.
60. Soong, T. & Dargush G. (1997), “Passive energy Dissipation Systems in Structural Engineering”, John Wiley & Sons.
61. Star Seismic, www.starseismic.net.
62. Structural Engineers Association of Northern California - Seismology and Structural Standards Committee. Recommended Provisions for Buckling-Restrained Braced Frames. SEAONC 2001.
63. Summers P., Jacob P., Martí J., Bergamo G., Dorfmann L., Castellano G., Poggianti A., Karabalis D., Silbe H. and Triantafillou S. Development of new base isolation devices for application at refineries and petrochemical facilities. 13th World Conference on Earthquake Engineering. Paper No. 1036 Vancouver, Canada, 2004.
64. Taranath B.S. Wind and Earthquake Resistant Buildings. CRC Press 2004.

65. Timoshenko S.P. and Gere J.M. 1961. Theory of Elastic Stability. McGraw-Hill.
66. Tremblay R., Ben Ftima M. and Sabelli R. 2004. An Innovative Bracing Configuration for Improved Seismic Response. Proc. Recent Advances and New Trends in Structural Design International Colloquium, Timisoara, Romania, 419-430.
67. Tremblay R., Degrange G., and Blouin J., 1999. “Seismic Rehabilitation of a Four-Storey Building with a Stiffened Bracing System,” Proc. 8th Can. Conf. on Earthquake Engrg., Canadian Association for Earthquake Engineering, Vancouver, B.C., 549-554.
68. Tremblay R., Poncet L., Bolduc P., Neville, R. and De Vall R. Testing and design of buckling restrained braces for Canadian application. 13th World Conference on Earthquake Engineering. Paper No. 2893 Vancouver, Canada, 2004.
69. Tremblay, R., Boldue, P., Neville, R., y De Vall, R. (2006), “Seismic Testing and Performance of Buckling Restrained Bracing Systems”, Canadian Journal of Civil Engineering, Vol. 33 pp. 183-198.
70. Tremblay R, Lacerte M, Christopoulos C. Seismic Response of Multi-Storey Buildings with Self-Centering Energy Dissipative Steel Braces. Journal of Structural Engineering ASCE 2008; 134:108-120.
71. Tsai K.-C., Lai J.-W., Hwang Y.-C., Lin S.-L. and Weng C.-H. Research and application of double-core buckling restrained braces in Taiwan. 13th World Conference on Earthquake Engineering. Paper No. 2179 Vancouver, Canada, 2004.
72. Tsai, K.C. and Lin, S.L. (2003) "Inspection, Non-destructive Testing and Novel Design of Buckling Restrained Braces", Center for Earthquake Engineering Research, National Taiwan University July 2003. (In Chinese).
73. Tsai, K.C., Huang, Y.C. (2002) "Experimental Responses of Large Scale Buckling Restrained Braced Frames", Report No. CEER/R91-03, Center for Earthquake Engineering Research, National Taiwan University, (In Chinese).
74. Tsai, K.C., Loh, C.H., Hwang, Y.C. and Weng, C.S. (2003) "Seismic Retrofit of Building Structures with Dampers in Taiwan", Proceedings, International Symposium on Seismic Retrofit of Buildings and Bridges using Base Isolation and Dampers, Kyoto University.
75. Uang CM, Bertero VV. Use of energy as a design criterion in earthquake–resistant design, Report No. UBC/EERC-88/18. Berkeley: Earthquake Engineering Research Center, University of California, 1988.
76. Usami T., Lu Z. and Ge H. A seismic upgrading method for steel arch bridges using buckling-restrained braces. Earthquake Engineering & Structural Dynamics, Volume 34, Issue 4-5, Pages 471 – 496, 2005.
77. Wada, A., Saeki, E., Takeuch, T., Watanabe, A. (1989). “Development of unbonded brace,” Column (A Nippon Steel Publication), No.115 1989.12.
78. Wada, A., Saeki, E., Takeuchi, T., and Watanabe, A., 1998, "Development of Unbonded Brace" Nippon Steel's Unbonded Braces (promotional document), pp. 1-16, Nippon Steel Corporation Building Construction and Urban Development Division, Tokyo, Japan.
79. Wada A. and Nakashima M. From infancy to maturity of buckling restrained braces research. 13th World Conference on Earthquake Engineering. Paper No. 1732 Vancouver, Canada, 2004.
80. Watanabe, A., Hitomi Y., Saeki, E., Wada, A., and Fujimoto, M., 1988, “Properties of Brace Encased in Buckling-Restraining Concrete and Steel Tube”. Proceedings of Ninth World Conference on Earthquake Engineering, Vol. IV, pp. 719-724, Japan Association for Earthquake Disaster Prevention, Tokyo-Kyoto, Japan.
81. Watanabe, A., Nakamura, H. (1992). “Study on the behavior of buildings using steel with low yield point,” Proceedings of Tenth World Conference on Earthquake Engineering, Balkema, Rotterdam, pp. 4465-4468.

APPENDIX D. TESTING EQUIPMENT

This Appendix contains descriptions of the main instruments used in the experiments on the full size dissipators (D1, D2, D3 and D4) carried out in the University of Girona.

D.1. Hydraulic jack

Hydraulic actuator with 220 kN outer displacement, 300 kN inner displacement. It includes a Load Cell. AEP mod. TC4/50t. Range: 50 tons; sensitivity 2mv/v. Further information can be obtained at http://www.aep.it/. There is also a displacement transducer Novotechnik LWH300. Range: 300 mm. Further information can be obtained at the Internet web site http://www.bollmann-messtechnik.de/Novotechnik/novotechnik.html.

D.2. Data acquisition system

System 5000 (Vishay Measurements Group). Further information can be obtained at http://www.vishay.com/company/brands/measurements-group/guide/inst/5000/5000.htm.

D.3. Displacement transducers

HLS displacement transducers. HLS transducer: Strain gauge based transducers APEK company) http://www.apek.co.uk/. Further information can be obtained at http://www.vishay.com/docs/11350/hs.pdf APEK HLS-10, HLS-25, HLS-100.

LVDT displacement transducers. Solartron VS 50 GU. Range: 50 mm. Type LVDT. Further information can be obtained at the Internet site http://www.solartronmetrology.com/catalogue/datasheets/displacement_transducers_sseries_en.pdf.

D.4. Strain gauges

Reference code: TML FLA-6-11.

APPENDIX E. PREVIOUS TESTS

This Appendix describes a series of tests carried out in the National Technological University at Mendoza (Argentina). These tests were conducted prior to those described in this Monograph; the obtained results and the gained experience were extremely useful. The reference [Palazzo, 2009] contains a deepest description.

E.1. Tested devices

Seven reduced scale devices were produced and tested. Figure E.1 shows a picture of a dissipator (mounted on the testing machine).

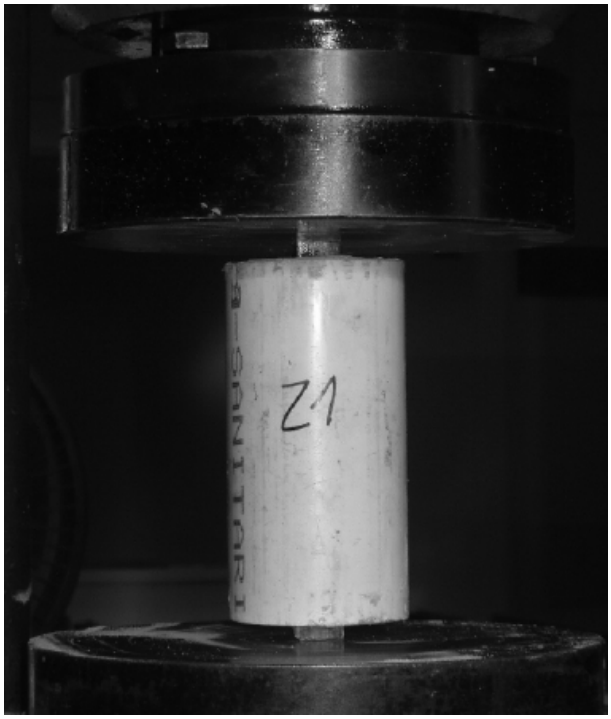

Figure E.1. Tested device

Figure E.1 shows that the devices consists of a steel core surrounded by a casing consisting of a tube (made of either steel or PVC) filled with a mortar-like product. Remarkably, no sliding interface between the core and the mortar was used.

The cores were made of ordinary construction steel, the one possessing the lowest yielding point being available in the local market: f_y = 330 MPa and f_u = 480 MPa. The cores are square cross-section bars (16 mm × 16 mm); the total length is 140 mm while the protruding (“naked”) parts are 8.5 mm long each. Remarkably, the lowest critical value of the axial force (79.71 kN) is lower than the corresponding yielding value (84.48 kN); this means that, without the protection of the casing, the bending instability would arise earlier than the yielding. This value of the critical axial load was confirmed by axial compression testing of individual (e.g. without casing) core members.

In four devices the casing consisted of mortar and in the three other it consisted of concrete. In the dissipators with concrete casing, the outer tube was made of PVC; the thickness was 2 mm. In one of the dissipators with mortar casing, the outer tube was also made of PVC while in the three other it was made of steel; the thickness was 1.2 mm.

E.2. Description of the tests

These experiments were carried out along the first half of 2006 in the laboratories of the National Technological University at Mendoza, Argentina. The objectives of the tests were:

- To gain experience in the definition of the material of the outer tube and of the casing.
- To investigate the convenience of placing a sliding layer between the core and the casing.
- To obtain experimental results useful to calibrate numerical models.

The experiments consisted of three series of quasistatical axial compression tests: (i) proofs on the naked cores, (ii) proofs on the filled tubes (without inner cores) and, (iii) proofs on the completed devices (core, casing and tube). Since the proofs on the cores and the on the tubes have little interest, only the tests on the dissipators are described here. Those seven specimens underwent a monotonic loading branch and an unloading branch, thus completing just half a cycle. The maximum imposed displacements were different for each device.

The testing machine was Möhr & Federhaff; the axial shortening was measured by mechanical meters Mitutoyo, their total stroke (range) is 50 mm and the sensitivity is 0.01 mm. Figure E.2 shows an image of the test of a dissipator.

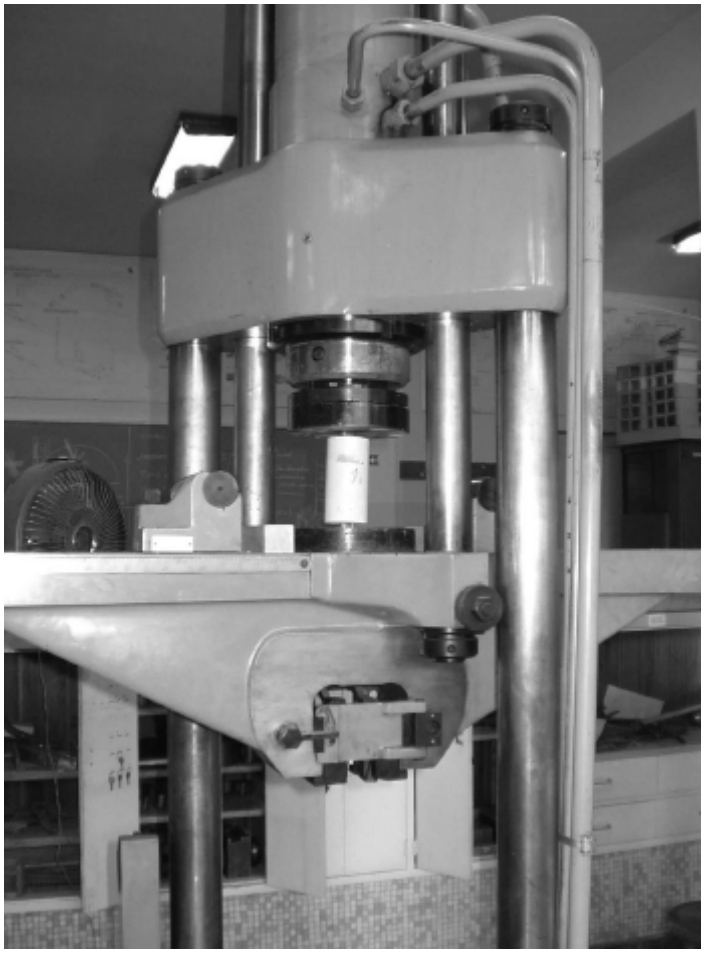

Figure E.2. Testing mock up

Figure E.3 shows the load-displacement plots of the devices equipped with outer steel tubes; as

discussed previously, the casing is made of mortar.

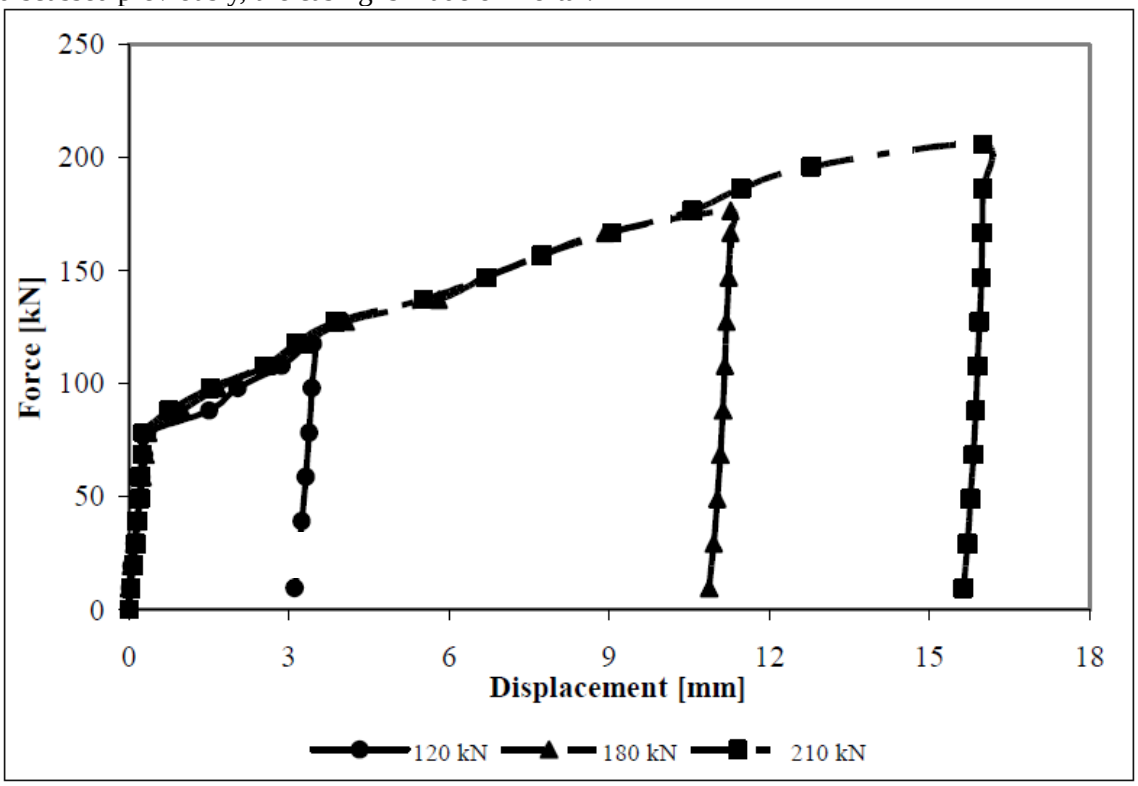

Figure E.3. Testing results of the devices with steel tubes

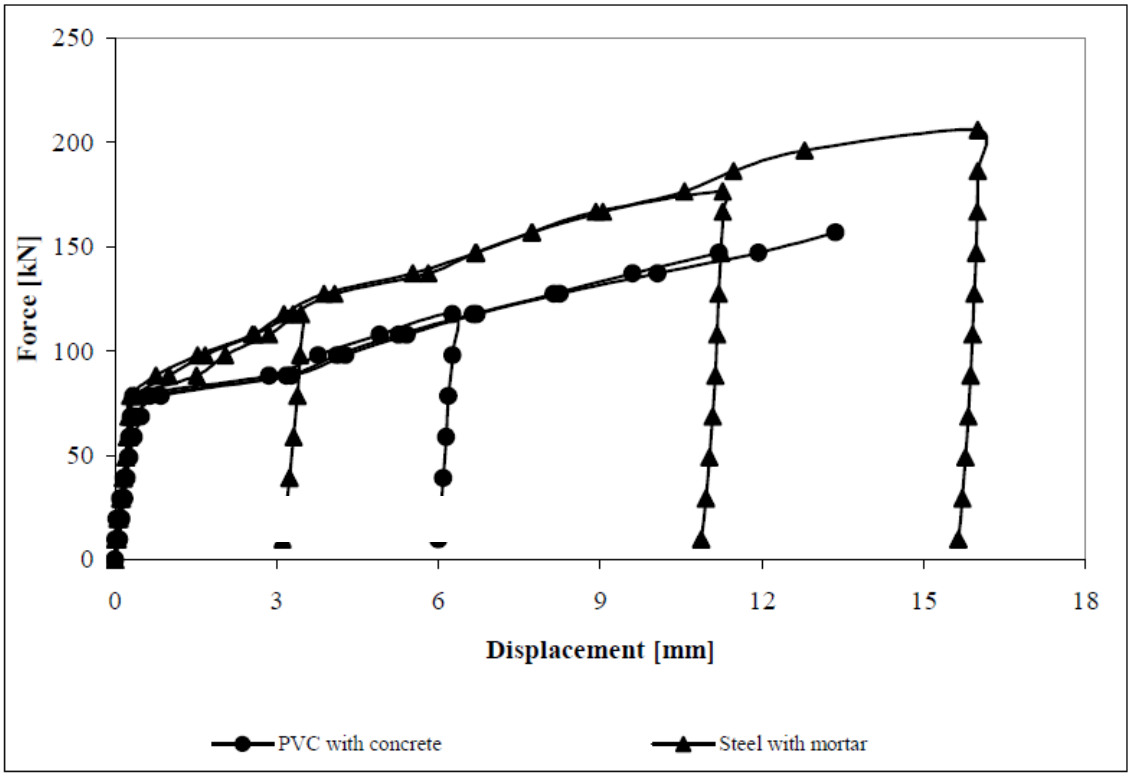

Figure E.4. Comparison among the testing results of the devices with PVC tubes filled with concrete and steel tubes filled with mortar

Comparison among the plots in Figure E.3 and those for the naked cores shows that there is a relevant shear stress transfer from the core to the casing; this confirms the convenience of considering a sliding interface between both members.

Figure E.4 shows a comparison among the load-displacement plots of the devices equipped with outer PVC and steel tubes. As discussed previously, in one of the devices with PVC tube the casing is made of mortar while the three other have concrete casing; only these lasts are shown in this Figure.

Plots in Figure E.4 show that the devices with steel tubes exhibited higher strength than those with PVC tubes.

Figure E.5 shows images of the devices after testing. Figure E.5.a displays a side view of the two halves of a split device; Figure E.5.b depicts the seven tested cores and Figure E.5.c shows a front view of a tested dissipator.

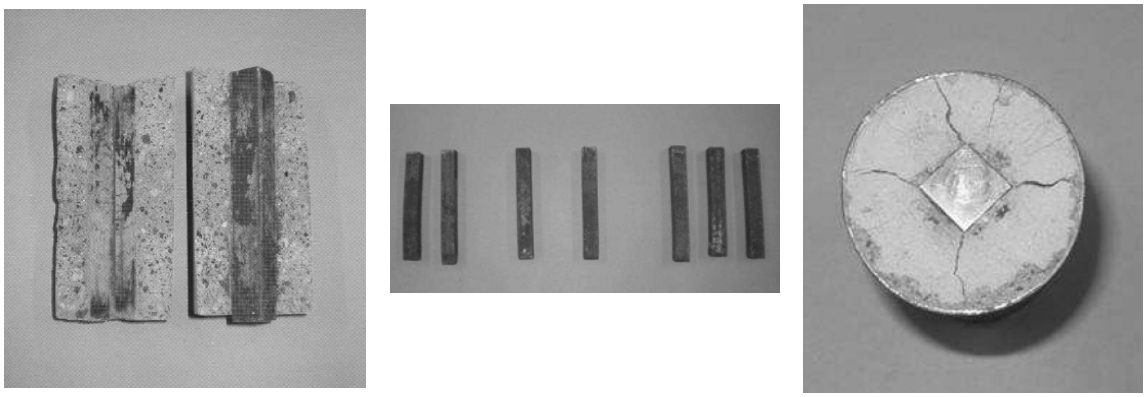

(a) (b) (c)

Figure E.5. Devices after testing

Figure E.5.b shows that none of the inner cores experienced relevant buckling; Figure E.5.c shows that one of the casings exhibited significant cracking starting from the corners of the core.

E.3. Numerical simulation of the tests

The axial compression tests of the naked cores, of the filled tubes (without inner cores) and of the completed devices (core, casing and tube) were numerically simulated with the commercial package Abaqus (finite element software code). Comparisons between the numerical and experimental results for the naked cores and the filled tubes showed a satisfactory agreement. This section describes mainly the results on the completed devices

The core, the casing and the outer tube were discretized with 3-D solid hexahedron (8-node) finite elements as shown by Figure E.6.

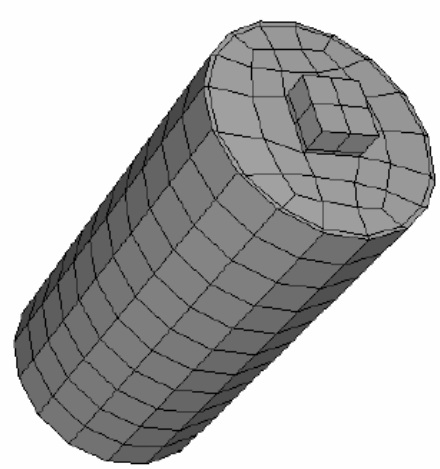

Figure E.6. Finite element mesh of a device

The structural behavior of the outer tube was described with a multiaxial elastic linear model. The sliding between the core and the surrounding mortar was described by a classical dry friction (Coulomb) model; several values of the friction coefficient were considered. The non-linear (plastic) behavior of the steel core was represented by a multiaxial bi-linear constitutive law; the yielding point was estimated as the nominal value (330 MPa), the Poisson's ratio was considered equal to 0.3, the strain hardening was represented by an after-yielding stiffness equal to 0.7% of the elastic one (200 GPa) and the maximum values of the stress and of the strain were 697 MPa and 16.7%, respectively. The structural behavior of the casing (either mortar or concrete) was simulated by a concrete damage plasticity model. The deformation modulus (8802 MPa), the Poisson's ratio (0.15), the limit of the linear range (9.89 MPa), and the compressive strength (17.6 MPa) were estimated after classical testing of ordinary cylindrical specimens. The tension behavior was considered by a damage model whose parameters were selected according the reccomendations of the Abaqus software package.

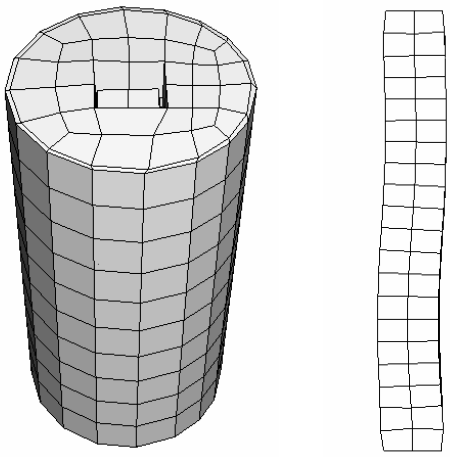

Figure E.7. Result of the numerical simulation without friction and wide gap

The boundary conditions at both ends of the core were modeled as clamped at one end (bottom) and transversal displacement restrained at the other end (top). The imposed displacement was considered in the top end. The quasi-staic analysis was carried out following an explicit formulation.

Figures E.7 and E.8 show results of numerical simulations. In Figure E.7 the friction coefficient in the core-casing interface is assumed to be zero and 1.6 mm gap in the four sides of the core is considered. In Figure E.8 the friction coefficient is equal to 0.3 and the gap is 0.1 mm.

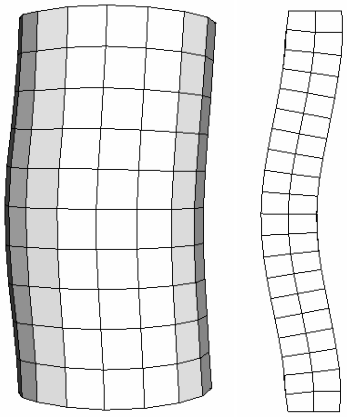

Figure E.8. Result of the numerical simulation with friction and narrow gap. Flexible PVC

Comparison between Figures E.7 and E.8 shows that in this last case the buckling has involved both the core and the casing; it is due to the extreme flexibility assumed for the outer tube since its deformation modulus has been taken as 70 MPa. Figure E.9 shows a comparison between the numerical results and the observed ones for the device in Figure E.8 with a more realistic value of the deformation modulus (700 MPa).

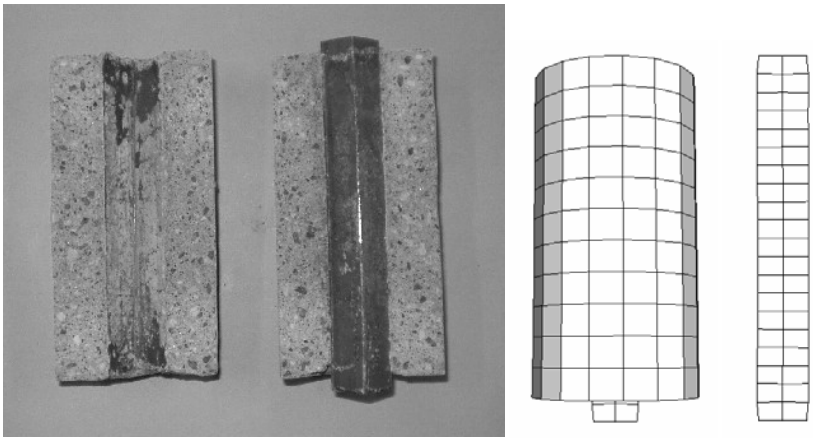

Figure E.9. Comparison between numerical results of the simulation with friction and narrow gap. Rigid PVC

Figure E.9 shows that the higher stiffness of the outer tube has been able to prevent the overall buckling of the device.

CENTRO INTERNACIONAL DE METODOS NUMERICOS EN INGENIERIA
Lista de monografías publicadas en la Serie de Ingeniería Sísmica

Las monograf'as pueden adquirirse dirigiéndose al Departamento de Publicaciones del Centro Internacional de Métodos Numéricos en Ingeniería, Edificio C1, Campus Norte UPC, c/ Gran Capitán s/n, 08034 Barcelona, teléfono: 93-401.60.37, Fax: 93-401-65-17.

IS-1 *Qualitative Reasoning for Earthquake Resistant Buildings,* Luís M. Bozzo, 149 pp., ISBN 84-87867-36-7, 1993

IS-2 *Control predictivo en sistemas de protección sísmica de estructuras,* R. Andrade Cascante, J. Rodellar, F. López Almansa, 143 pp., ISBN 84-87867-37-5, 1993

IS-3 *Simulación numérica del comportamiento no lineal de presas de hormigón ante acciones sísmicas,* M. Galindo, J. Oliver, M. Cervera, 255 pp., ISBN 84-87867-38-3, 1994

IS-4 *Simulación del daño sísmico en edificios de hormigón armado,* A. Hanganu, A.H. Barbat, S. Oller, E. Oñate, 96 pp., ISBN 84-87867-40-5, 1994

IS-5 *Edificios con aislamiento de base no lineal,* N. Molinares, A.H. Barbat, 96 pp., ISBN: 84-87867-41-3, 1994

IS-6 *Vulnerabilidad sísmica de edificios,* C. Caicedo, A.H. Barbat, J.A. Canas, R. Aguiar, 100 pp., ISBN 84-87867-43-X, 1994

IS-7 *Análisis de terremotos históricos por sus efectos,* J. R. Arango González, 119 pp., ISBN 84-87867-44-8, 1994

IS-8 *Control activo no lineal de edificios con aislamiento de base,* A.H. Barbat, N. Molinares, J. Rodellar, 124 pp., ISBN 84-87867-46-4, 1994

IS-9 *Análise estocástica da resposta sísmica nao-linear de estructuras,* A.M. F. Cunha, 199 pp., ISBN: 84-87867-47-2, 1994

IS-10 *Definición de la acción sísmica,* A.H. Barbat, L. Orosco, J.E. Hurtado, M. Galindo, 122 pp., ISBN: 84-87867-448-0, 1994

IS-11 *Sismología y peligrosidad sísmica,* J.A. Canas Torres, C. Pujades Beneit, E. Banda Tarradellas, 87 pp., ISBN: 84-87867-49-9, 1994

IS-12 *Riesgo, peligrosidad y vulnerabilidad sísmica de edificios de mampostería,* F. Yépez, A.H. Barbat, J.A. Canas, 104 pp., ISBN: 84-87867-50-2, 1999

IS-13 *Estudios de ingeniería sismológica y sísmica*, J.A. Canas, ISBN: 84-87867-57-X, 13 pp., 1995

IS-14 *Simulación de escenarios de daño para estudios de riesgo sísmico*, F. Yépez, A.H. Barbat y J.A. Canas, ISBN: 84-87867-58-8, 103 pp., 1995

IS-15 *Diseño sismorresistente de edificios de hormigón armado*, L. Bozzo, A.H. Barbat, ISBN: 84-87867-59-6, 185 pp., 1995

IS-16 *Modelo tridimensional de atenuación anelástica de las ondas sísmicas en la Península Ibérica*, J.O. Caselles, J. A. Canas, Ll. G. Pujades, R.B. Herrmann, ISBN: 84-87867-60-X, 119 pp., 1995

IS-17 *Índices de daño sísmico en edificios de hormigón armado*, R. Aguiar ISBN: 84-87867-43-X, 99 pp., 1996

IS-18 *Experimental study of a reduced scale model seismically base isolated with Rubber-Layer Roller Bearings (RLRB),* D. Foti, J.M. Kelly ISBN: 84-87867-82-0, 112 pp., 1996

IS-19 *Modelos de evaluación del comportamiento sísmico no lineal de estructuras de hormigón armado,* F. Yépez Moya, ISBN: 84-87867-80-4., 96pp., 1996

IS-20 *Evaluación probabilista de la vulnerabilidad y riesgo sísmico de estructuras de hormigón armado por medio de simulación,* F. Yépez Moya, A.H. Barbat, J.A. Canas, ISBN: 84-87867-81-2, 1996

IS-21 *Modelización de la peligrosidad sísmica. Aplicación a Cataluña*, J.A. Canas, J.J. Egozcue, J. Miquel Canet y A.H. Barbat, ISBN: 84-87867-83-9, 101pp., 1996

IS-22 *Evaluación del daño sísmico global en edificios porticados de hormigón armado*, R. Aguiar, A.H. Barbat and J. Canas, ISBN: 84-87867-96-0, 173pp., 1997

IS-23 *Daño sísmico global en edificios con muros de cortante*, R. Aguiar, ISBN: 84-89925-00-3, 101 pp., 1997

IS-24 *Conceptos de cálculo de estructuras en las normativas de diseño sismorresistente*, A.H. Barbat y S. Oller, ISBN: 84-89925-10-0, 107pp., 1997

IS-25 *Stochastic dynamics of histeretic structures*, J.E. Hurtado, ISBN: 84-89925-09-7, 205pp., 1998

IS-26 *Análisis de los acelerogramas de la serie de Adra (Almería). Diciembre 1993 a Enero 1994,* R. Blázquez, A. Suárez, E. Carreño y A.J. Martín, ISBN: 84-89925-11-9,1998

IS-27 *Respuesta de puentes frente a acciones sísmicas*, E. Maldonado, J.A. Canas, J.R. Casas, L.G. Pujades, ISBN: 84-89925-23-2, 107pp., 1998

IS-28 *Estudio de parámetros en la vulnerabilidad sísmica de puentes*, E. Maldonado, J.A. Canas y J.R. Casas, ISBN: 84-89925-16-X, 97pp., 1998

IS-29 *Metodologías para o cálculo sísmico não-linear de barragens de betão*, R. Faria ISBN: 84-89925-25-9, 113pp., 1998

IS-30 *Acciones para el diseño sísmico de estructuras*, R. Aguiar, ISBN: 84-89925-27-5, 122pp., 1998

IS-31 *Avaliação do comportamento sísmico de barragens de betão*, R. Faria, ISBN: 84-89925-28-3, 88pp., 1998

IS-32 *Vulnerabilidad sísmica de hospitales. Fundamentos para ingenieros y arquitectos*, O.D. Cardona, ISBN:84-89925-33-X, 165pp., 1999

IS-33 *Modelación estocástica de la acción sísmica*, J. E. Hurtado, ISBN:84-8925-34-8, 93pp., 1999

IS-34 *Earthquake simulator testing of a steel model seismically protected with friction energy dissipators,* D. Foti and J. Canas, ISBN: 84-89925-40-2, 110pp., 1999

IS-35 *Plasticidad y fractura en estructuras aporticadas, J.* Flórez López, ISBN: 84-89925-46-1, 90pp., 1999

IS-36 *Estimación de efectos locales con movimientos sísmicos y microtembl*ores, V. Giraldo, A. Alfaro, L. G. Pujades, J. A. Canas, ISBN: 84-89925-54-2, 83pp., 1999

IS-37 *Modelo numérico de elastómeros multi-fase y su aplicación al análisis de estructuras con aislamiento sísmico*, O. Salomón, S. Oller y A. H. Barbat, ISBN: 84-89925-54-2, 239pp.,1999

IS-38 *Dinámica de estructuras. Aplicaciones a la Ingeniería Sísmica*, J.E. Hurtado, ISBN:84-89925-59-3,177pp., 2000

IS-39 *Utilización de los conjuntos difusos en modelos de vulnerabilidad sísmica,* E. Maldonado Rondón, J.R. Casas Rius y J.A. Canas, ISBN:84-89925-61-5, 2000

IS-40 *Modelo de vulnerabilidad sísmica de puentes basado en " Conjuntos Difusos ",* E. Maldonado Rondón, J.R. Casas Rius, J. A.Canas, ISBN: 84-89925-64-X, 110pp, 2000

IS-41 *Vulnerabilidad de puentes de autopista. Un estado del arte*, C. Gómez Soberón, A. Barbat, S. Oller, ISBN: 84-89925-64-X, 168pp, 2000

IS-42 *Fuerzas sísmicas en los Países Bolivarianos*, R. Aguiar Falconí, ISBN: 84-89925-74-7, 101pp., 2000

IS-43 *Espectros de input de energía de aplicación en el proyecto sismorresistente estructuras en regiones de sismicidad moderada*, A. Benavent-Climent, L.G. Pujades, F. López-Almansa, ISBN: 84-89925-86-0, 85 pp., 2001

IS-44 *Capacidad límite última de disipación de energía de estructuras de hormigón Armado sometidas a acciones sísmicas,* A. Benavent-Climent, F. López-Almansa, L. G. Pujades, ISBN: 84-89925-88-7, 2001

IS-45 *Evaluación del daño en edificios y desempeño sísmico. Programa de ordenador CEINCI3,* R. Aguiar Falconí, ISBN: 84-89925-87-9, 107pp., 2001

IS-46 *Estudio analítico sobre el comportamiento sísmico de muros de mampostería confinada con aberturas,* J. J. Álvarez, S.M. Alcocer, ISBN: 84-89925-90-9, 119pp., 2002

IS-47 *Seismic vulnerability of bridges using simplified models*, C. Gómez Soberón, S. Oller, A. H. Barbat, ISBN: 84-89925-96-8, 135pp., 2002

IS-48 *Control de vibraciones en puentes. Un estado del arte y de la práctica,* M. Jara, J. R. Casas, ISBN: 84-95999-01-3, 120pp., 2002

IS-49 *Criterio de diseño de puentes con aisladores y disipadores de energía,* M. Jara, J. R. Casas, ISBN: 84-955999-02-1, 115pp., 2002

IS-50 *Ferrocemento: Un acercamiento al diseño sísmico,* D. A. Bedoya, J. Farbiarz, J. E. Hurtado, Ll. G. Pujades, ISBN: 84-95999-23-4, 76pp., 2002

IS-51 *Metodología para la evaluación del desempeño de la gestión del riego,* M. L. Carreño, O. D. Cardona, A. H. Barbat, ISBN: 84-95999-66-8, 2004

IS-52 *Sistema de indicadores para la evaluación de riesgos,* M. L. Carreño, O. D. Cardona, A. H. Barbat, ISBN: 84-95999-70-6, 200

IS-53 *Evaluación "ex-post" del estado de daño en los edificios afectados por un terremoto,* M. L. Carreño, O. D. Cardona, A. H. Barbat, ISBN: 84-95999-76-5, 2005

IS-54 *Identificação modal estocástica de estruturas de engenharia civil,* F. Magalhães, A. Cunha, E. Caetano, ISBN: 84-95999-89-7, 2005

IS-55 *Comportamiento sísmico de puentes articulados y disipación de energia adicional: Un estado del crecimiento,* G. E. Valdebenito, A. C. Aparicio, ISBN: 84-95999-87-0, 2005

IS-56 *Cálculo y diseño sismorresistente de edificios. Aplicación de la norma NCSE-02,* A.H. Barbat, S. Oller, J.C. Vielma , ISBN: 84-95999-89-7, 2005

IS-57 *Evaluación rápida de la deriva máxima de piso para calcular la vulnerabilidad sísmica de estructuras,* R. Aguiar , ISBN: 84-95999-91-9, 2006

IS-58 *Factor de reducción de las fuerzas sísmicas en edificios de hormigón armado sin muros de corte,* R. Aguiar , ISBN: 978-84-96736-40-5, 2007

IS-59 *Herramientas necesarias para la evaluación sísmica de edificios,* R. Moreno, L. Pujades, A.C. Aparicio, A. H. Barbat , ISBN: 978-84-96736-53-5, 2008

IS-60 *Inelastic analysis of geometrically exact rods,* P.L. Mata, A. H. Barbat, S. Oller, R. Boroschek , ISBN:978-84-96736-59-7, 2008

IS-61 *La gestión financiera del riesgo desde la perspectiva de los desastres,* M.C. Marulanda, O.D. Carmona, M.G. Ordez, A. H. Barbat , ISBN: 978-84-96736-60-3, 2008

IS-62 *Seismic protection of cable-stayed bridges applying viscous dampers,* G.E. Valdebenito, A. C. Aparicio ,ISBN: 978-84-96736-84-9, 2010

IS-63 *Reliability problems in earthquake engineering,* J. E. Hurtado , ISBN: 978-84-96736-86-3, 2010

Los autores interesados en publicar monografías en esta serie deben contactar con el editor para concretar las normas de preparación del texto.